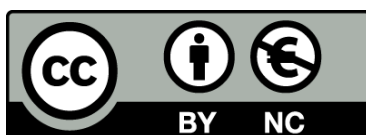UNIVERSITAT DE BARCELONA

Synthesis and Magnetic Studies
of Quasi-Isotropic Coordination Compounds
with 3d and 4f cations

Evangelos Pilichos

PhD program in Nanoscience

Synthesis and Magnetic Studies of Quasi-Isotropic Coordination Compounds with 3d and 4f cations

Evangelos Pilichos

Co-Director: Dr. Albert Escuer Fitè and Dr. Julia Mayans Ayats

Universitat de Barcelona

Tutor: Dr. Albert Escuer Fitè

Universitat de Barcelona

TABLE OF LIGANDS

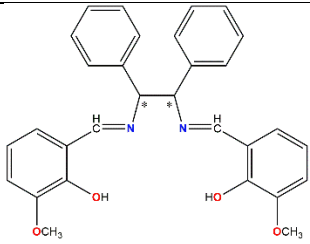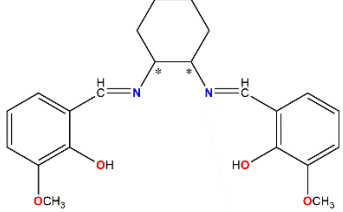| Ligand	Name	Structure
L1	L = N,N'-bis(pyridin-2-ylmethylene)cyclohexane-1,2-diamine	
DppeO₂	DppeO₂ = 1,2-bis(diphenylphosphino)ethane dioxide	
H₂L2	H₂L2 = 2-(((4-(4-((2-(oxido)-3-methoxybenzylidene)amino)phenoxy)phenyl)imino)methyl)-6-methoxyphenolato	
H₂L3	H₂L3 = N-(α-methylsalicylidene)-N'-(salicylidene)-2,2-dimethyl-1,3-propanediamine	
H₂L4	H₂L4 = N,N'-Ethylene-bis(3-methoxysalicylaldiimine)	
H₂L5	H₂L5 = N,N'-cyclohexane-bis(3-ethoxysalicylaldiimine)	
H₂L6	H₂L6 = N,N'-ethylene-bis(3-ethoxysalicylaldiimine)	
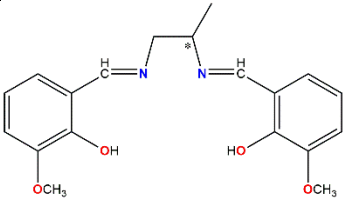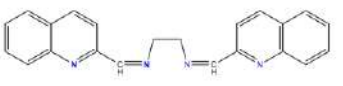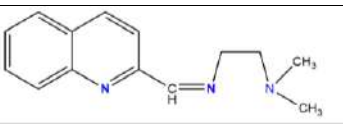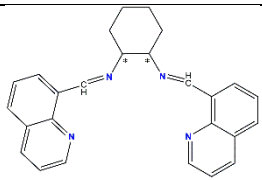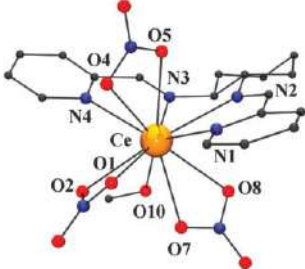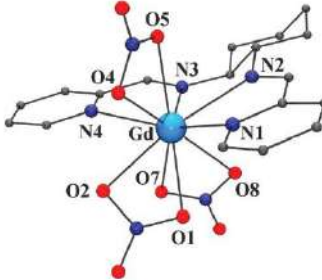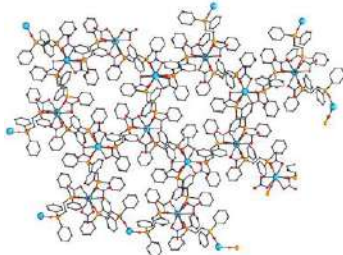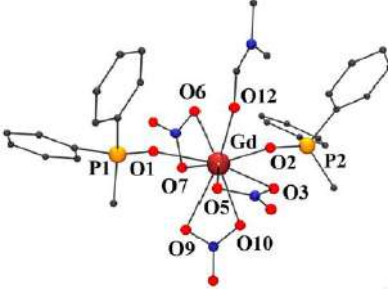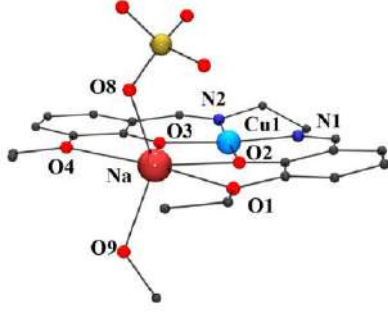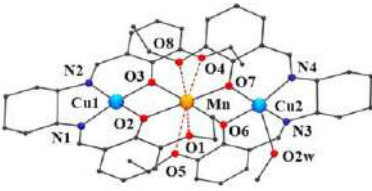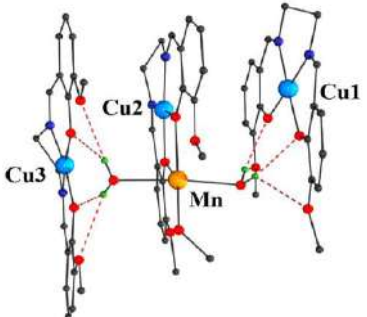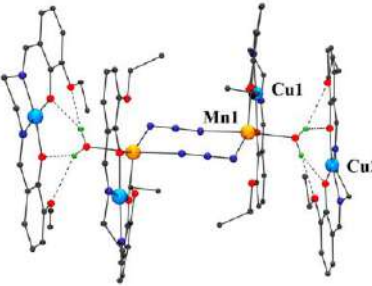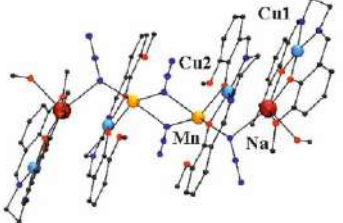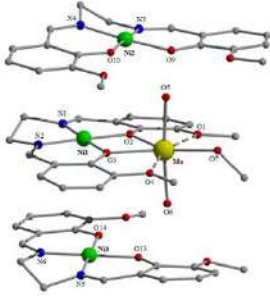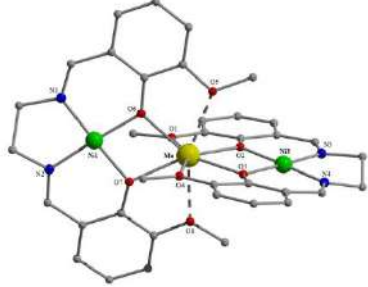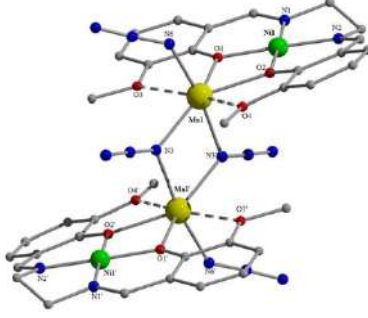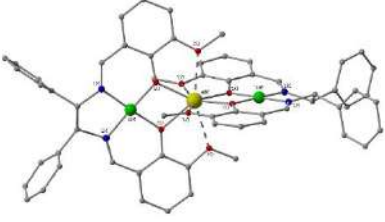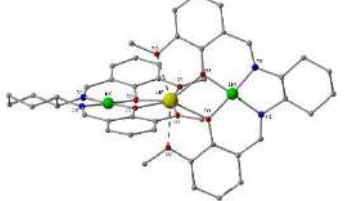
H₂L7	*H₂L7 = N,N'-diphenylethylene-bis(3-methoxysalicylaldiimine)*	
H₂L8	*H₂L8 = N,N'-cyclohexane-bis(3-methoxysalicylaldiimine)*	
H₂L9	*H₂L9 = bis(N, N'-bis(3-methoxysalicylidene)propane-1,2-diamine)*	
L10	*L10 = N-(3-((quinolin-2-ylmethylene)amino)propylidene)quinolin-2-amine*	
L11	*L11 = N,N-dimethyl-N-(quinolin-2-ylmethylene)ethane-1,2-diamine*	
L12	*L12 = 2,2';6',2"-terpyridine*	
L13	*L13 = N,N'-bis(quinolin-8-ylmethylene)cyclohexane-1,2-diamine*	
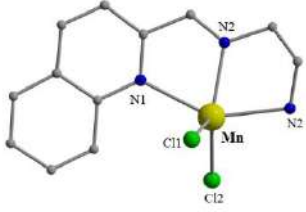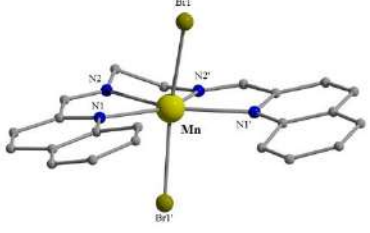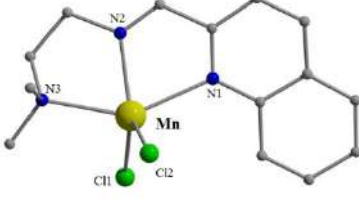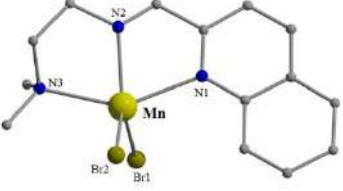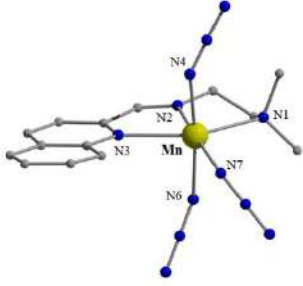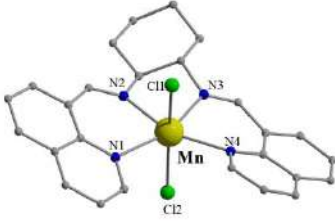
TABLE OF COMPLEXES
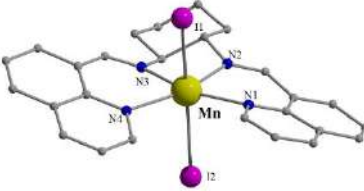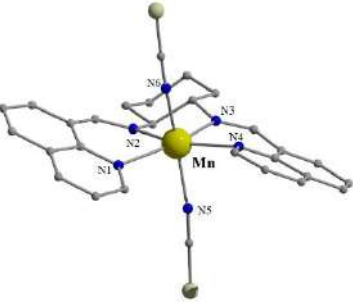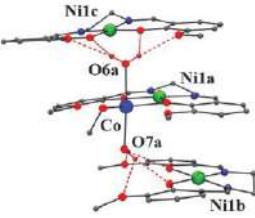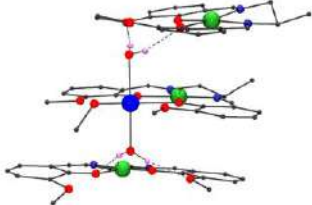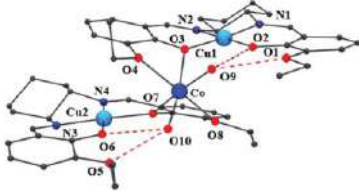
Number, Chapter, Publication id	Ligand	Nuclearity	Structure
[1] appears in Chapter 2 and in *Publication #1* with name (1*SS*)	L1	[Ce^{III}]	
[2] (Gd^{III}) and [3] (Dy^{III}) appears in Chapter 2 and in *Publication #1* with names (2*SS*) and (3*RS*), respectively	L1	[Ln^{III}]	
[4] (Ce^{III}), [5] (Sm^{III}) and [9] (Dy^{III}) appears in Chapter 2 and in *Publication #2* with names (1), (5) and (9), respectively	DppeO$_2$	[Ln^{III}]$_n$	
[6] (Eu^{III}), [7] (Gd^{III}) and [8] (Tb^{III}) appears in Chapter 2 and in *Publication #2* with names (3), (4) and (5), respectively	DppeO$_2$	[Ln^{III}]$_n$	

[10] (La[III]) [11] (Ce[III]), [12] (Pr[III]), [14] (Gd[III]) and [16] (Dy[III]) appears in Chapter 2 and *Publication #3* with names (1), (2), (3), (5) and (7), respectively	H$_2$L2	[Cu$_2$[II]Ln$_2$[III]]	
[13] (Sm[III]) [15] (Tb[III]), [17] (Ho[III]), [18] (Er[III]) and [19] (Yb[III]) appears in Chapter 2 and *Publication #3* with names (4), (6), (8), (9) and (10), respectively	H$_2$L2	[Cu$_2$[II]Ln$_2$[III]]	
[20] appears in Chapter 3 and in *Publication #4* with name (1·2H$_2$O)	H$_2$L3	[Cu[II]Mn[II]]	
[21] in Chapter 3 and *Publication #4* with name (2·MeOH)	H$_2$L4	[Cu$_3$[II]Mn[II]]	
[22] appears in Chapter 3 and *Publication #4* with name (3·MeOH)	H$_2$L4	[Cu$_2$[II]Mn[II]Na[I]]	

[23] appears in Chapter 3 and in *Publication#5* with name (1)	H$_2$L6	[Cu^{II}Na^I]	
[24] appears in Chapter 3 and in *Publication#5* with name (2*SS*·2CH$_2$Cl$_2$·0.5H$_2$O)	H$_2$L5	[Cu$_2^{II}$Mn^{II}]	
[25] appears in Chapter 3 and in *Publication#5* with name (3·MeOH)	H$_2$L4	[Cu$_3^{II}$Mn^{II}]	
[26] appears in Chapter 3 and in *Publication#5* with name (4·2MeOH)	H$_2$L6	[Cu$_4^{II}$Mn$_2^{II}$]	
[27] appears in Chapter 3 and in *Publication#5* with name (5)	H$_2$L4	[Cu$_4^{II}$Mn$_2^{II}$Na$_2^I$]	

[**28**] appears in Chapter 4, Section 4.1	H₂L4	[Ni₃ᴵᴵMnᴵᴵ]	
[**29**] appears in Chapter 4, Section 4.1	H₂L4	[Ni₂ᴵᴵMnᴵᴵ]	
[**30**] appears in Chapter 4, Section 4.1	H₂L4	[Ni₂ᴵᴵMn₂ᴵᴵ]	
[**31**] appears in Chapter 4, Section 4.1	H₂L7	[Ni₂ᴵᴵMnᴵᴵ]	
[**32**] appears in Chapter 4, Section 4.1	H₂L8	[Ni₂ᴵᴵMnᴵᴵ]	

[**33**] appears in Chapter 4, Section 4.2	L10^b	[Mn^{II}]	
[**34**] appears in Chapter 4, Section 4.2	L10	[Mn^{II}]	
[**35**] appears in Chapter 4, Section 4.2	L11	[Mn^{II}]	
[**36**] appears in Chapter 4, Section 4.2	L11	[Mn^{II}]	
[**37**] appears in Chapter 4, Section 4.2	L11	[Mn^{II}]_n	
[**40**] appears in Chapter 4, Section 4.3	L13	[Mn^{II}]	

[**42**] appears in Chapter 4, Section 4.3	L13	[Mn^{II}]	
[**43**] appears in Chapter 4, Section 4.3	L13	[Mn^{II}]	
[**44**] appears in Chapter 5 and in *Publication#6* with name (**1**·MeOH)	H$_2$L4	[Ni$^{II}_3$Co^{II}]	
[**45**] appears in Chapter 5 and in *Publication#6* with name (**2R**·MeOH)	H$_2$L9	[Ni$^{II}_3$Co^{II}]	
[**46**] appears in Chapter 5 and in *Publication#6* with name (**3SS**·MeOH·0.5H$_2$O)	H$_2$L5	[Cu$^{II}_2$Co^{II}]	

CONTENTS

CHAPTER 1
Introduction

Chapter 1: Introduction

1.1 Magnetism

1.1.1   The roots of magnetism

The phenomenon of magnetism has its roots in Ancient Greece; in the province of Magnesia at central Greece, the first discovery of the attraction between lodestone and iron was made. However, this fact is a matter of debate. The first observations were made near the city of "Magnesia" in the old, Asian Minor Greek province of Lydia. This old city was near the modern city Manisa, close to Smirna. There are also strong evidences that around 1088 Chinese sailors were using compasses which were first described by Shen Kua. This knowledge came to Europe one year after and, from that moment, the European sailors were enabled to explore new places accomplishing bigger journeys, like Columbus did with America in 1492 or Vasco de Gama with India.

In 1600, William Gilbert (1544-1603) published the first "modern" scientific results, regarding magnetism, in his monograph "*De Magnete*". In this work, he proved that Earth is a huge magnet by itself and that's the reason behind the movement of the needle of the compass. Until then, it was believed that the needle was moving by the stars. That was the initial point. Before Gilbert's study magnetism was engaged more in philosophy rather than science. Charles Augustin du Coulomb (1736-1806) in his paper entitled "*Du Magnetisme*" pointed out that despite the fact that magnetism and electricity were different phenomena they were related. This work pushed the limits of magnetism further and a huge progress followed. Scientists like Hans-Christian Oersted (1777-1851), Andre-Marie Ampere (1775-1836) and Dominique-François Arago (1786-1853) laid the foundations for the modern principles of magnetism. Michael Faraday (1791-1867) in 1831 showed that voltage can be induced by magnetic flux. This inspired James Clerk Maxwell (1831-1879) and in 1864 he managed to relate electricity, magnetism and light in the, so-called, Maxwell's equations. The discovery of the electron, the seminal ideas of Lewis who wrote simple electronic structures for molecules and ions, and the development of quantum mechanics provided scientists with the appropriate tools for the in-depth understanding of the magnetic properties of the matter. Paul Langevin (1872-1946) introduced paramagnetism and diamagnetism and then, Piere Weiss (1865-1940) explained

magnetism as a collective behavior in the frame of Molecular Field Theory. Until 1960, the most popular magnets consisted mainly of metallic alloys and ceramics, *e.g.*, Alnico and ferrites. At the end of the past century, magnets based on organic radicals were discovered and then coordination compounds picked up the torch. It was obvious that a new field was born.

1.1.2 Magnetometry and Molecular Magnetism

At the end of 1950 chemists entered the field of Magnetochemistry. They used experimentally determined magnetic moments and their variation with temperature to deduce in chemical conclusions and make structural proposals in molecular compounds. In other words, they used the magnetic properties of a compound as a "lance" through which can see the molecule. A famous example is the distinction between the two stereochemistries, square planar or tetrahedral, in 4-coordinate Ni(II) compounds. In particular, Ni(II) in a tetrahedral symmetry has two unpaired electrons. On the other side, when Ni(II) adopts square planar geometry, has no unpaired electrons. Therefore, the former shows paramagnetic susceptibility while the latter has diamagnetic susceptibility. As a result, measuring the magnetic susceptibility of a compound a chemist can identify the coordination geometry of the cation.

Without any doubt, this kind of research was useful. The magnetic measurements, at this point, were performed at room temperature. Thus, the only safe information came from the comparison of the magnetic moment of the molecule with that of the free ion. However, there were some critical aspects that were not taken into consideration: (i) the interaction between the ions and (ii) the symmetry of the complexes. Sooner or later, chemists came up against systems that required to go beyond paramagnetism and tackle with situations where the unpaired electrons interact with other unpaired electrons. That was the first time that chemists turn their head to quantum mechanics. It was the only tool that they had in their hands in order to predict energies and population of different states. Quantum mechanical models were the key and, at the same time, the pathway from Magnetochemistry to Molecular Magnetism.

Molecular Magnetism soon developed as an essential area of interdisciplinary investigation, which produced prototype magnetic materials. The development of a joint interest among chemists (who moved to understand the difficult theoretical and experimental techniques needed to characterize the complex magnetic properties of the new systems) and physicists (who needed help to unravel the complex molecular structures that chemical creativity was able to produce). A NATO ASI was held in Italy in 1983, and the book that was written on that occasion can be considered as the birth of Molecular Magnetism. The title of the ASI was "Magneto-structural correlation in exchange coupled systems" and it stressed the need to work out simple rules to understand how to design molecules capable of interacting ferromagnetically with other molecules. This was at least the goal of the organizers. On the other hand, the physicists who took part in the event were interested in low-dimensional magnets and obscure objects such as solitons or the Haldane gap. Chemists were able to synthesize and isolate desired molecules and physicists had the theoretical background, and that was the cross point. For this reason, ASI is considered as the initial point for the field of Molecular Magnetism.

Molecular Magnetism could be defined as the field which contains the study of the magnetic properties of isolated molecules and/or assemblies of molecules. This is how Professor Olivier Kahn [1] described this field. According to him, is an interdisciplinary field in which chemists synthesize and investigate materials of increasing complexity based on a feedback interaction with physicists who develop sophisticated theoretical models and experimental techniques. Professor Sir Richard Friend explained very well the importance of this collaboration as follows: "*One of the big opportunities in this science is that it crosses traditional divides between subject areas. There's communication between physics and chemistry and materials and divide physics. Managing that communication has been hard work, but it has been really rewarding, as well. It hasn't felt at all like the ordinary mode of activity for a research program in the physics department. In fact, I spend more of my time going to chemistry conferences than I do going to physics conferences. I find what I can pick up at chemistry conferences extremely valuable. I'm constantly trying to better understand what chemists are trying to do.*".

1.1.3 Principles of Molecular Magnetism

At the beginning of the 21st century magnetic materials played a pivotal role in our daily life. Magnets can be found in computer hard disks, credit/debit/ATM cards, televisions, motors, in Magnetic Resonance Imaging (MRI) equipment and in many other technologies that are making our everyday life easier and better [2]. These days' industries are pushing towards greater miniaturization and more digital information storage in computers' hard disks. Thus, the need for smaller and smaller magnets increases. The ability of a single molecule to function as a tiny magnet is thus of great importance because it represents an alternative, 'bottom-up' route to nanoscale magnets. Indeed, it brings all the advantages of molecular chemistry, including crystallinity, solubility (rather than colloid formation), protection by a shell of organic groups that prevents close contact of a molecule's magnetic core with those of neighboring molecules, and the ability to vary this organic shell at will using standard chemical methods. For these reasons magnetism became a major sub-division of nanoscience. Thus, the knowledge of fundamental principles of magnetism is important.

1.1.3.1 Magnetic Susceptibility

Magnetism arises from the movement of electrons. This movement gives rise to two forms of angular momentum: the spin angular momentum, S, and the orbital angular momentum, L. Also, the movement of each electron induces a small magnetic moment. The vector sum of these individual magnetic moments of electrons within an atom combine to give the total magnetic moment of an atom. In atomic and also in the molecular scale there are two types of phenomena that may be exhibited: Diamagnetism and Paramagnetism.

Diamagnetism and Paramagnetism contribute to the overall magnetic susceptibility $[\chi]$[1] as is shown in equation 1:

$$\chi = \chi^D + \chi^P \quad \textbf{(1)}$$

where χ^D and χ^P represent the diamagnetic and paramagnetic susceptibility, respectively. Magnetic susceptibility is traditionally expressed as $cm^3 mol^{-1}$ and represent the

magnetization of a species in the presence of an external magnetic field, as shown in equation 2:

$$\chi = \frac{M}{H} \qquad (\mathbf{2})$$

where M stands for magnetization and H for the applied magnetic field. It is worth noting that equation 2 is valid only when the applied magnetic field is weak or in systems with unpaired electrons that do not interact among themselves, which are called paramagnets.

As mentioned above, magnetic susceptibility is due to two contributions: χ^D and χ^P. The former is due to the presence of paired electrons in the system, which is an intrinsic property of matter. The magnetic moments of paired electrons within an orbital cancel out each other, resulting a net magnetic moment equal to zero. It's a temperature independent behavior, exhibited by all atoms and molecules containing at least one pair of electrons. When χ^D is the dominant phenomenon, then the substance is diamagnetic and it is repelled by the magnetic field. On the other side, when χ^P is the leading contribution, paramagnetism becomes dominant. Paramagneitsm originates from the presence of unpaired electrons in the system. This gives rise to a net magnetic moment, or spin. Paramagnetism results in an attraction of a substance by the applied filed, and it is temperature dependent. In order to get accurate values of χ for a coordination compound, it is necessary to take into consideration both χ^D and χ^P. For determining the diamagnetic contribution, the use of Pascal's tables is the correct strategy. In this approach χ^D is considered as the sum of the diamagnetic contributions of all the atoms and functional groups that are present in the molecule. All these values are reported in the literature [3]. However, there are times that systems with a non-magnetic ground state present a weak paramagnetic behavior. This phenomenon is called temperature independent paramagnetism (TIP) and arises from the mixing into the ground state of the excited states that are not thermally populated [4].

1.1.3.2 Magnetic Behaviors of Bulk Magnets

Bulk magnets are samples that contain multiple paramagnetic centers (molecules or atoms) with interacting spins. The study of magnetic susceptibility shed light on the magnetic behavior of a species. There are four types of behaviors: paramagnetism, ferromagnetism, antiferromagnetism and ferrimagnetism [5] (Fig. 1).
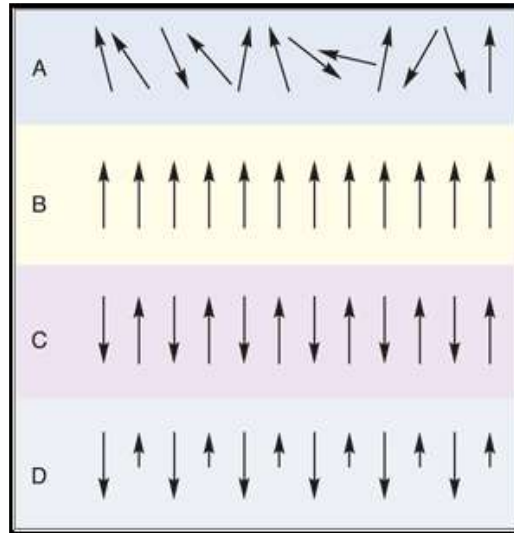
Figure 1: Schematic presentation of different types of magnetic behavior: (A) Paramagnetism, (B) Ferromagnetism, (C) Antiferromagnetism and (D) Ferrimagnetism.

In a bulk solid, paramagnetism (Fig. 1A) occurs when the spins of the paramagnetic atoms or molecules that are contained in this solid do not interact each other but are randomly oriented. When a magnetic field is absent there is no magnetic moment. In the opposite case, when a magnetic field is applied, these spins will align with the field resulting in a weak interaction. The molar susceptibility, χ_M, in this case is both temperature and field dependent. The temperature dependence of χ_M is described by the Curie law:

$$\chi_M = (N_A g^2 \mu_\beta^2 / 3k_\beta T) \cdot S(S+1) \quad \textbf{(3)}$$

where N_A is Avogadro's number, g is the Landè factor, μ_β is Bohr's magneton, k_β is the Boltzmann constant, T is the temperature and S is the spin quantum number [6]. The equation 3 can also be written in a simplified way as follows:

$$\chi_M = \frac{C}{T} \qquad \textbf{(4)}$$

where C ($cm^3 \cdot K \cdot mol^{-1}$) is the Curie constant.

The magnetization (M) of paramagnetic system is also field dependent, (Eq. 2). At low fields (and constant T) the relationship between M and the magnetic field (H) is linear (Fig. 2). At higher fields M approaches, a saturation value M_s. The value of M_s is generally given by equation 5:

$$M_s = \mu_\beta \cdot N_A S \cdot g \qquad \textbf{(5)}$$

If we rearrange the above equation, we obtain:

$$M_s / \mu_\beta N_A = S \cdot g \qquad \textbf{(6)}$$

where the term $M_s/\mu_\beta N_A$ is called "reduced magnetization".
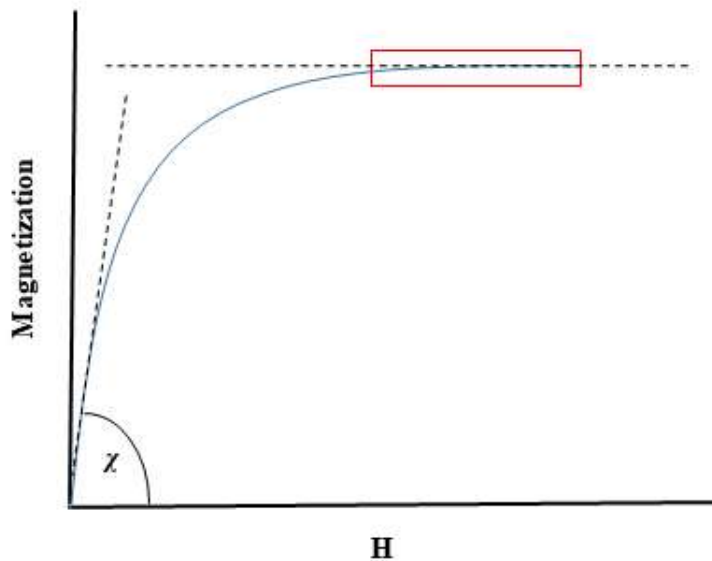
Figure 2: Magnetization vs. Magnetic field plot.

In ferromagnets the magnetic spins are aligned parallel to each other. When a magnetic field is not applied, ferromagnetic species have a large net magnetic moment. Ferromagnets usually exist as groups of domains, where each domain is consisted by a number of aligned

spins. In the absence of a field, the domains are randomly oriented; although each domain has a net magnetic moment the bulk magnet will appear to have a zero magnetic moment. After the application of a field, the domains align and the ferromagnet is attracted strongly by the field. In antiferromagnets, the magnetic spins that have the same magnitude are aligned antiparallel to each other. Thus, the magnetic moments are canceled out, resulting a zero magnetic moment. When a field is applied these kind of materials are repelled by the field.

Ferrimagneitc materials is a "combination" of ferro-and antiferromagnetism. They present an antiparallel align of the spin, but in this case the spins are different in magnitude. They exist also in domains and in the absence of a field the exhibit zero magnetic moment. When the is applied, the domains align and, like ferromagnets, they attracted by the field.

Ferro-, antiferro- and ferrimagnetic behavior happens below a certain temperature. For ferro- and ferrimagnets this temperature is called Curie temperature (T_C) while for antiferromagnets is called Neel temperature (T_N). At higher temperatures, these materials lose their order and act as paramagnets.

1.1.3.3 The Phenomenon of Hysteresis

One of the main features of the bulk magnets is the magnetic hysteresis (Fig. 3). A hysteresis loop is determined by measuring the magnetization M of a system as a function of the applied magnetic field H. This loop is indicative of the memory effect of a molecule. In other words, it shows the "history" of the magnetization.
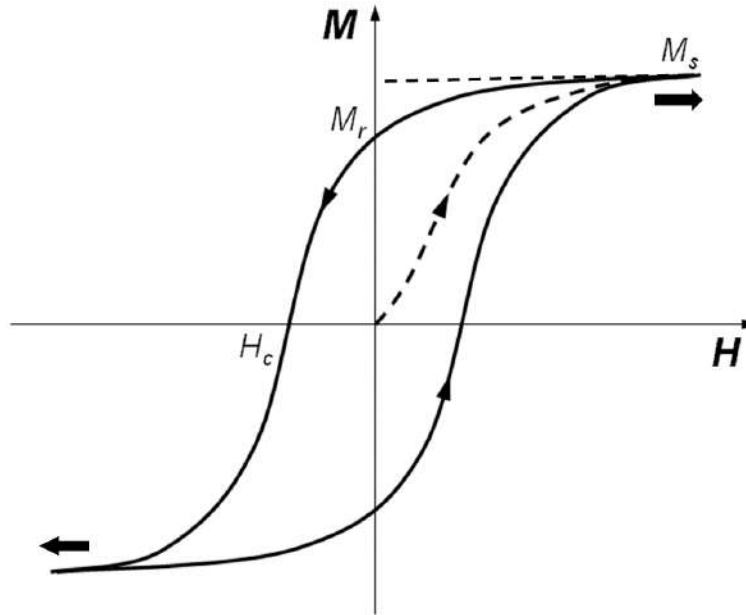
Figure 3: A typical magnetic hysteresis loop.

When a magnetic field is applied to a bulk system, its domains start to align with the field. At higher fields all the domains are magnetically aligned. At this point the magnetization reaches the saturation value, M_s. Decreasing the field, the magnetization also decreases. However, if the field is completely removed then the system is still magnetized. This magnetization is called remnant magnetization, M_r. If we continue to decrease the field, the magnetization turns to zero at a specific field that is called coercive field, H_C. Large coercive fields characterize a hard magnet, while weak fields are characteristic of a soft magnet. Finally, if the magnetic field is applied in the opposite direction, then the magnetization reaches again the M_s value (but with negative sign) resulting a loop. This loop is called hysteresis loop, it is typical of ordered magnets and the overall process corresponds to inversion of the magnetization (Fig. 3).

As mentioned above, at zero field the magnetization is non-zero. In the case of bulk magnets, this is due to irreversible growth of domains with the orientation of the magnetic moments parallel to the field. In molecular nanomagnets the appearance of hysteresis is not for the same reason. In molecular systems, the phenomenon of hysteresis is also present, but has a different of origin; it is a phenomenon intrinsic to the molecule with no communication or interactions between domains. In nanomagnets the magnetization of a

molecule is relaxing too slow compared to the time required to sweep the field. Therefore, the width of the loop is directly related to the dynamics of a single molecule of each system [7].

1.1.3.4 From Bulk Magnets to Molecular Magnets

Traditionally, magnetic materials were consisted by inorganic solids. The presence of unpaired electrons in d- or f- orbitals is responsible for their magnetic behavior. That means those magnets are atom-based magnets. Till very recent years' conventional magnets were metals (Fe, Co, Ni), alloys ($SmCo_5$, $Nd_2Fe_{14}B$) or oxides (Fe_3O_4, Cr_2O_3) [8]. Until today, it is well known that organometallic systems [9a], purely organic systems [9b] and coordination compounds or even a single atom [10] are perfect building blocks for molecular magnets.

Molecule-based magnets present some remarkable advantages over the bulk ones. Molecular magnets can be synthesized in ambient conditions using soft synthetic routes. For this reason, a chemist can control, understand and possibly change or add desired properties. Also, it is feasible the control of the size of the molecule, in contrast with the bulk solids These are the benefits that molecular magnets have due to their easy synthesis. Furthermore, these days' industry demand from the scientist devices that are smaller and smaller. Molecular magnets are the perfect tools for this task, because of the reasons mentioned above, especially for technological investments such as: data storage devices, quantum computing or spintronincs.

1.1.4   Single Molecule Magnets

At the begging of 90's, it was discovered [11-14] that the dodecanuclear mixed-valent manganese compound $[Mn_{12}O_{16}(O_2CMe)_{16}(H_2O)_4]\cdot4H_2O\cdot2CH_3COOH$ (hereafter abbreviated as Mn_{12}), with a ground spin state S = 10, showed slow relaxation of the magnetization (SRM) at 2 K. This compound is consisted by 4 Mn^{IV} and 8 Mn^{III} (Fig. 4), 16 acetate ligands, 16 oxo-bridges and 4 molecules of H_2O. In addition, 4 molecules of water and 2 molecules of acetic acid are cocrystallized in the structure [13].
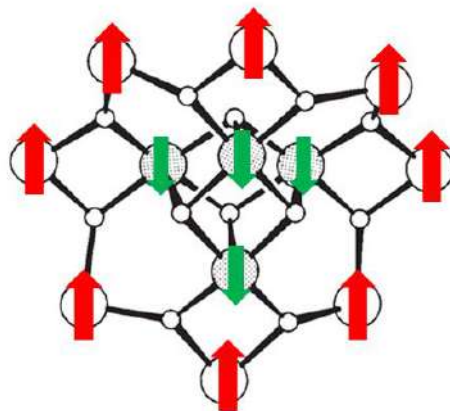
Figure 4: Schematic view of the core of the Mn_{12}. Acetate bridging ligands and water molecules have been omitted for clarity. The big outer spheres represent the Mn^{III} ions while the shaded spheres correspond to Mn^{IV} ions.

In the Mn^{IV} cations of the central cubane, strong ferromagnetic interactions are dominated, resulting a $S_1 = 6$ (Fig. 4, green arrows). In the same way, the 8 Mn^{III} external cations also present ferromagnetic interactions (Fig. 4, red arrows), leading to a $S_2 = 16$. The Mn^{IV} and Mn^{III} are antiferromagnetically coupled and thus, the total spin, S_T, of the molecule is equal to 10. As mentioned above, the main feature of this compound is the slow relaxation of magnetization at very low temperatures. This behavior is of molecular origin and for that reason the Mn_{12} was the 1st Single Molecule Magnet (SMM). The presence of magnetic anisotropy [15], in the form of axial zero-field splitting (ZFS, simplified as D), separate the ground state with S = 10 in 21 microstates. Each microstate is characterized by a quantum number, m_s. The energy of a microstates is given by the equation: $E = m_s^2 |D|$. The negative sign of D, leads to a double-well where the two projections of the spin $\pm m_s$ are separated. This kind of magnetic anisotropy is called Ising type or easy axis (Fig. 5).
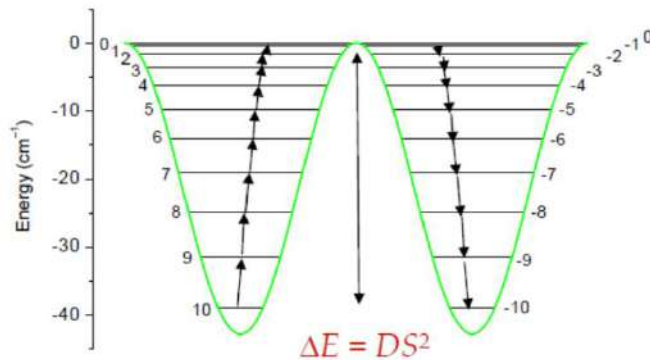
Figure 5: Representation of the double well of Mn_{12} in the absence of an applied magnetic field.

For passing from the one spin projection to the other, energy has to be consumed. This energy is equal to $E = S_T^2 |D|$, and the spin has to pass through the microstate $m_s = 0$. This kind of "relaxation", from $+m_s$ to $-m_s$, is called thermal activation and it has been proved that is of molecular origin. When the complex exposed to a magnetic field, the microstate $m_s = -10$ is stabilized and all the molecules of the complex appear in this microstate (Fig. 6). This is the point of the saturation of the magnetization. When the magnetic is removed, the magnetization of the molecules is "frozen" due to presence of the energy barrier. Finally, if the magnetic field is applied in the opposite direction, the energy barrier becomes lower and the spins are climbing through it. The result of this, is the appearance of the hysteresis loop for the Mn_{12}. Another feature of this compound, is that under a zero magnetic field, its magnetization could be "positive" or "negative" and this depends only from the history of the sample. That kind of molecules present magnetic bistability and they have multiple applications in data storage devices [16,17].
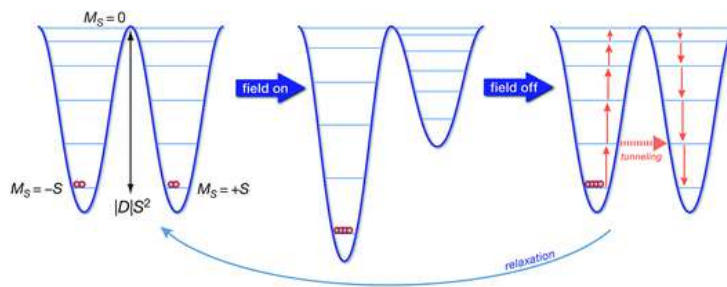
Figure 6: The energy barrier in the absence of a magnetic field (left), after the application of a field (middle) and after the removal of the field (right).

Another remarkable fact for this compound, is the presence of "steps" in the plot of the hysteresis loop (Fig. 7). These "steps" are caused by the abrupt reversion of the magnetization. This phenomenon is called quantum tunneling of magnetization (QTM) [12, 18-20], where at specific values of the external field the spins do not climb above the barrier, but pass through it (Fig. 6, right). This is happening when the microstates have the same energy but they are in the opposite sides of the barrier. For these critical values of the field, the relaxation occurs through the barrier, and thus appear steps in hysteresis loop. QTM takes place at temperatures where the thermal activation is negligible, i.e. at very low temperatures. It is important to mention that, the critical values of the applied field depend only on zero-field splitting parameter D, and also, controlling the applied field we can control the relaxation of magnetization, which is the key-point for technological applications of SMMs.
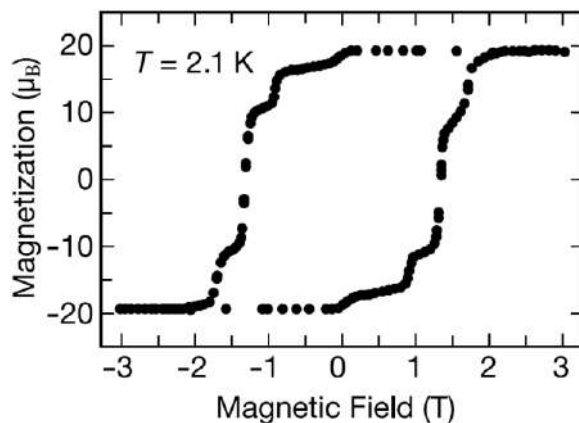
Figure 7: Hysteresis loop for Mn_{12}. The "steps" correspond to the critical values of the magnetic field where QTM occurs.

1.1.5 Mechanisms of Magnetic Relaxation

In order to observe relaxation of magnetization, the system has to exchange energy with its environment. This energy exchange is called spin–lattice relaxation because it is driven by interactions between the spin and the environment, or "lattice", by phonons. The energy is exchanged through phonons, which are collective vibrations in a solid [21]. The availability of phonons in a system is dependent on the temperature of the system and the nature of the

surroundings. As a result, the is a mechanistic diversity in how the relaxation can occur (see below).

1.1.5.1 Orbach Process

Orbach relaxation mechanism [22] may occur when a single lattice phonon excites the spin system and promotes a spin transition to higher energy levels. That means, the spin absorbs energy and then uses it in order to climb at microstates m_s with higher energy. Then, relaxation proceeds from transition of the spin back to the lowest state by releasing energy to the lattice in the form of a phonon. It is self-proved that phonons of appropriate energy must be available in order to occur this process. The Orbach mechanism is not limited to a single transition and can involve multiple steps to a higher energy m_s level before the relaxation via phonon emissions. For example, in Figure 6 the spin climbs (orange arrows) all the way up from the lowest microstate to the highest one and then relaxes. Thus, high-spin metal cations, which present multiple $(2S + 1)$ m_s levels, are good candidates for building blocks of coordination compound that may relax through Orbach mechanism.

The relaxation rate of the Orbach process is described by the following equation:

$$\ln \tau = \ln \tau_0 + U_{eff}/k_\beta T \qquad \textbf{(7)}$$

The above equation mirrors the Arrhenius law, where τ is the relaxation time. In literature the spin-lattice relaxation time is often mentioned as T_1. τ_0 is the microscopic attempt time, *i.e.* the relaxation attempt time for reversal at $T = \infty$. The high of the energy barrier that spin has to overcome before relaxing is denoted U_{eff} and is equal to $|D| \cdot S^2$ or $|D| \cdot (S^2-1/4)$ for integer and half-integer spin values, respectively [23].

1.1.5.2 Direct Process

In contrast with Orbach mechanism, the direct relaxation process does not have an energy barrier. In this case the spins make a direct transition from one microstate to another (Fig.

8). The required energy is taken again by the lattice as a quantum of long-wavelength lattice vibration, *i.e.* an acoustic phonon. Direct process has a characteristic magnetic field and temperature dependence as is shown by the equation 8:

$$\tau^{-1} = AH^nT \qquad (8)$$

where A is a parameter related to the environment of the molecule. H stands for the applied magnetic field and T is the temperature. Furthermore, n can be equal to 2 or 4 for a non-Kramer and a Kramer system, respectively [24]. Also, it has to be noted that the phonons which are participating in the process, have an energy that corresponds to the difference between two crystal-field microstates. The density of states with relevant energies is small (~ 1 cm^{-1}), because Zeeman effect is very small. As a result, the direct mechanism is dominant at low temperatures, where the available phonons from the lattice are low in energy.
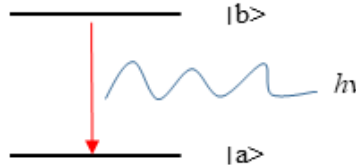
Figure 8: Schematic representation of direct relaxation mechanism.

1.1.5.3 Raman Process

Raman relaxation process is analogous to the Orbach mechanism but in this case the relaxation occurs via a virtual state (Fig. 9). This virtual state is a superposition of lattice vibrations and does not actually exits. Raman process proceeds when the system absorbs and emits phonons of different energies. This action is fundamentally different than the direct process, which is one phonon process, or the Orbach which requires successive absorption and emission of phonons. The rate of relaxation via the Raman process is described by equation 9:

$$\tau^{-1} = CT^n \qquad \textbf{(9)}$$

where C is usually taken as free fit parameter [24], while the exponent n normally takes the values of 7 and 9 for non-Kramers and Kramers systems, respectively. However, this is not strict, since there are examples reported that n can take a lower value. The Raman mechanism occurs at temperatures where there are not available phonons of sufficient energy to excite the spin system to a real microstate and as a result, there is a shortcut of the barrier.
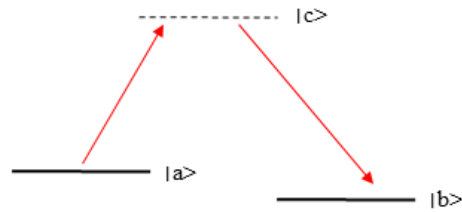
Figure 9: Schematic representation of Raman process.

1.1.5.4 Quantum Tunneling of Magnetization (QTM)

All the above mentioned mechanisms required absorption and emission of energy, in the form of phonons, between the spin system and its environment. However, in the case of QTM the spin passes directly from microstate $+m_s$ to $-m_s$ without exchange of energy (Fig. 10, green arrow). This is happening due to the mesoscopic size of the particles, which give them the possibility to share macroscopic and quantum properties. In paragraph 1.1.4 where the Mn_{12} was described, some key points about QTM were mentioned. In this section QTM will be analyzed with more details.
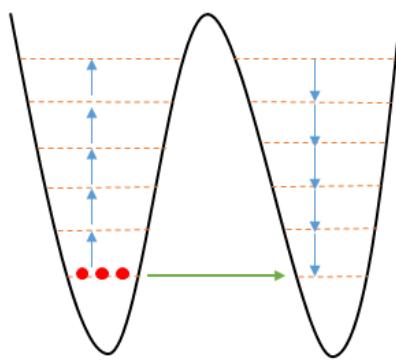
Figure 10: Schematic representation of an energy barrier. Blue arrows represent Orbach process while the green arrow indicate the Quantum Tunneling of Magnetization.

In general, there are two QTM-based processes. The first occurs between the initial and final spin orientation, without any input energy, and it is called "ground-state" QTM. This type of mechanism is operative if there is an interaction between the wavefunctions of the starting and the final spin orientation, which creates a tunnel-splitting energy gap, Δ [25]. It is very similar with what happens to an electron which tunnels because of its spatial wavefunction an exist on both sides of an inaccessible barrier. The spin wavefunction of a spin system can exist on both sides of the energy barrier. It is evident, though, that the stronger the interaction between the states Δ becomes larger and the tunneling is more efficient. Ground state QTM happen regularly at (or near) zero applied magnetic field, because interactions that drive QTM are strongest when the energy difference between the initial and final point is smallest. Regarding the relaxation rate, is temperature independent because tunneling does not require any energy to ascend over a barrier. Thus, QTM is dominant at very low temperatures where the energy of the available phonons is sufficiently low to enable any kind of other processes.

The second type of QTM is called thermal-activated or thermally-assisted QTM (TA-QTM). This process combines two different mechanisms: a thermally- assisted Orbach type one and QTM. At first point, there is an initial promotion (via phonon) of the spin to a higher energy m_s state. This state, however, is below the highest m_s energy level. Once promoted, the system tunnels through the barrier and finally relaxes. This mechanism also, "creates" a barrier that is lower than the theoretical one defined by the zero-field splitting parameter and, thus, is an under-barrier process.

1.1.6 Magnetic Anisotropy

Magnetic anisotropy refers to the preferential alignment of the magnetization along a specific direction. Most of the times, there is an energetically favorable direction for the magnetization in a system, the so-called easy axis. By convention, this axis lies in the *z*-direction. However, if the "easiest" direction for the alignment of the magnetic moment is the *xy* plane, it's denoted as the easy-plane. Therefore, also exists a hard plane and a hard axis, which are perpendicular to the easy plane and easy axis, respectively. The magnetic behavior of SMMs is governed by the anisotropic zero-field splitting parameters, D and E, according to the Hamiltonian:

$$\hat{H} = [D\hat{S}_z^2 - S(S+1)/3 + E(\hat{S}_x^2 - \hat{S}_y^2)] \quad \textbf{(10)}$$

Where D and E stands for axial and rhombic zero-field splitting parameters, respectively. D parameter is associated with distortions in the z axis, while E is describing distortion in the *xy* plane. $\hat{S}$ is the spin operator which describes the projection of the spin in a given axis. The role of zero-field splitting is to remove the degeneracy of the 2S + 1 microstates (for a given S) in the absence of magnetic field. In general, there are two phenomena that contribute to the enhancement of ZFS and consequently to magnetic anisotropy: (a) first order spin-orbit coupling, or in-state spin-orbit coupling) and (b) second order spin-orbit coupling, or out-of-state spin-orbit coupling [1, 7]. In fist order spin-orbit coupling, spin and orbital angular momentum components are mixing directly with the electronic ground state of a system. In second order spin-orbit coupling, the ground state has no orbital angular momentum, but the excited states possess first order orbital angular momentum and thus there is a mixing between these two.

The best example to illustrate the second-order spin-orbit coupling is the case of Ni(II) in an octahedral field (Fig. 11, left). Ni(II) is a $3d^8$ cation with ^{3}F Russell-Saunders free ion ground term. Under an octahedral field the ground term splits and give a ground state with $^3A_{2g}$ as indicated by ligand field theory. For "A" terms no spin-orbit coupling is expected. However, the excited states are described by a "T" term and can mix with the ground state. On the other hand, the best example of first order spin-orbit coupling is the case of Co(II) (Fig. 11, right). In weak octahedral field Co(II) present a T ground state which leads to strong spin-orbit coupling and, as a result, higher magnetic anisotropy [26].

18
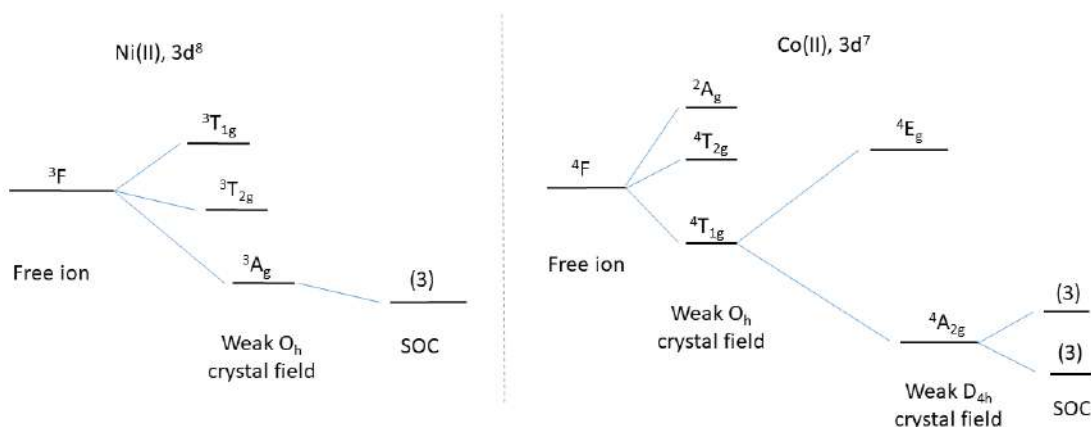
Figure 11: Energy level diagram for Ni(II) (left) and Co(II) (right).

1.1.7 Improving the Energy Barrier

As has been mentioned above, the U_{eff} is determined by the equations: $|D| \cdot S^2$ or $|D| \cdot (S^2 - 1/4)$, depending of the spin value. At first point, one may say that increasing the spin ground state of a system, the higher energy barrier could be obtained. So, at the begging scientists turn their interest to synthesize coordination compounds with spin values, as high as possible. For this reason, they tried to use 3d cations with high spin ground state and negative D, like Mn^{III} (S = 2) and Fe^{III} (S = 5/2), in order to increase the U_{eff} and the T_B, which is the temperature below which an SMM is functional. These attempts led to the isolation of molecules with high nuclearity, such as {Mn19} and {Fe14} (Fig. 12) [27]. For these molecules, the spin ground state is S_T = 83/2 for {Mn19}, and S_T = 25 for {Fe14}. However, the value of D is almost zero because of the high symmetry that these molecules possess. As a result, scientists turn their interest to maximizing the D value instead of S. These two parameters have an inversely proportional relationship [28]. Thus, adding transition metal ions in a compound can be an antagonistic factor in order to induce high magnetic anisotropy. Furthermore, it is important to mention that D is a tensor, and thus, it is an additive factor. That means, that in order to achieve large anisotropy in coordination clusters, all the anisotropy axes have to be aligned which is not always the case. So, the question that arise here, is whether there is a way to include in the same molecule high D and large S. The answer to this, is by using a single ion as a spin carrier which also have large single-ion anisotropy, like lanthanides or even 3d ions (e.g. Co^{II} or Mn^{III}) which

19

present high spin ground states and unquenched orbital angular momentum. This is why the scientists shift their focus from Single Molecule Magnets to Single Ion Magnets (SIMs). In these molecular systems, the properties arise not from the cooperative phenomena but to due to intrinsic properties of the metal ions that are present in the molecular structure. The motivation behind this research is the quest to understand the magnetic anisotropy of these molecules, and how we can cantrol it in order to achive higher energy barriers and blocking temperatures.
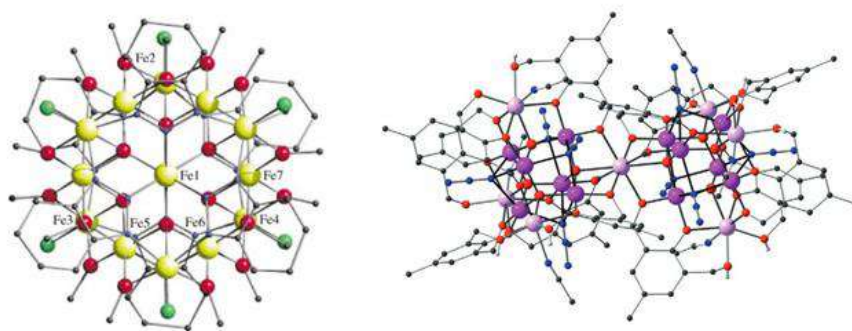
Figure 12: Represantation of molecular stactures of {Fe14} (left) and {Mn19} (right).

These days, that lanthanides are dominating, 3d metal-based Single Ion Magnets may have been put a bit aside. The reasons for this are: (i) they possess smaller magnetic moments than lanthanides, (ii) they have lower spin-orbit coupling costants and, (iii) they present strong coupling between the d orbitals and the ligand field which quench the the orbital momentum. However, after the report of an Fe complex [29] showing magnetic relaxation, the field was gaining ground. Since then, in the literature have been reported examples with Ni(I)/(II), Mn(III), Co(II) or even Cr(II). First-row SIMs are the ideal system to understand the physics that are hidden behind magnetic phenomena, since their chemisty is well-known and relatively simple. Also, they present a major advantage over the lanthanides; they can create strongly coupled systems, in contrast to the lanthanides because of their core 4f orbitals. And why this is helpful? By understanding the behavior of a mononuclear complex, chemists may use this in order to built bigger systems with high spin values, and most importantly, with the desired alignment of the axes of the magnetic anisotropy.

It is obvious that, Single Ion Magnets is a very fruitful field. These systems are more "suitable" for increasing the energy barriers and the blocking temperatures, because scientists can control, apart from the choise of the metal, the enviroment of the molecule, and most importantly, they can drive their synthesis and their systems to an adequate pathway in order to enhance the magnetic properties of the molecule and make SIMs and SMMs real candidates for daily applications.

1.1.8 Lanthanides: Magnetic and Optical Properties

Lanthanides (Ln) (Fig. 13) took their name from the first element of the series, lanthanum. The origin of the name comes from the greek verb "$\lambda\alpha\nu\theta\acute{\alpha}\nu\omega$" (i.e. lanthánein), which means "escaping notice". The explanation for the name, is attributed to the fact that lanthanides were, and still is, very difficult to be isolated because of their similar chemistry. Also, lanthanides, or lanthanoids, are grouped in the category of rare-earth metals together with yttrium and scandium. However, lanthanides are not that rare. In fact, some lanthanides present similar abudance in Earth's crust as some very common metals, like copper, and are more abudant than gold and platinum. In their metallic form, lanthanides have an electronic structure of type: $[Xe]6s^24f^{n+1}$. Exceptionally, Ce, Gd and Lu have one electron in their 5d orbital. Their trivalent form (Ln^{3+}) is the most common oxidation state, with an electronic configuration $[Xe]4f^n$. Some of them also may be found in +2 or +4 oxidation state, depending on how close they are to reach a full, half-filled, or completely empty 4f shell.

Figure 13: Position of lantanides in the periodic table.

Nowadays, lanthanides are among the most important magnetic sources in industry. They are widely used in modern technology and can be found to cell phones, disc drives, computers, cars and wind-power generators to name but a few. Their magnetic properties are dominated by the spin and orbital angular momentum. In contrast with transition metal ions, where the magnetism comes from the spin moment since the orbital contributions are quenched, the lanthanides present strong orbital angular momentum because of their 4f core. So, the initial point is to understand the electronic description of the 4f electrons in free ions.

For better description of electronic structures of lantanides, Russell-Saunders [30] coupling should be adopted. In this scheme, the electron spins are coupled together seperately from the coupling of the orbital angular momenta of the electrons, and the orbital moment is unquenched. The ground state (G.S.) for a given lanthanide ion is unaffected by its coordinated ligands-and thus crystal field (C.F.) splittings are weak- because of the shielding of the 4f electrons by the filled 5s and 5p orbitals.

The spins of the individual electrons are coupled together (added vectorially) to give the spin quantum number, S. The orbital angular momenta (l) of the individual electrons are coupled in the same way. For an f electron, l is equal to 3, so the magnetic quantum number m_l can have any of the seven integral values between +3 and -3. Vectorial addition of the

m_l values of the f electrons for a multi-electrinic system affords the total orbital angular momentun quantum number, L. Vector addition of L and S affords the quantum number J. J can have values of (L+S), (L+S)-1;…(L-S). For any ion, a number of electronic states are "available". The ground state can be determined by using Hund's rules [31], with the following order:

i. The spin multiplicity (2S+1) is as high as possible.

ii. If there is more than one term with the same spin multiplicity, the term with the highest L-value is the ground state.

iii. For a shell less than half-filled, J takes the lowest possible value, while is the opposite for more than half-filled.

Table 1: Representation of states in relation with the quantum number L (top) and electronic configuration of Sm^{3+} (bottom).

L	0	1	2	3	4	5
State	S	P	D	F	G	H

m_l	+3	+2	+1	0	-1	-2	-3
	↑	↑	↑	↑	↑		

As an exapmle, working out the term sumbol for the ground state of Sm^{3+} (f^5 system). The shell is less than half filled, so the J value will take the lowest value. Then:

- $S = \Sigma m_s = (5 \times \frac{1}{2}) = 5/2$; therefore $(2S+1) = 6$.
- $L = \Sigma m_l = +3 +2 +1 +0 -1 -2 = 5$.
- J can have values of (L+S), (L+S)-1;…(L-S) = 15/2, 13/2, 11/2;…5/2.

So, as is shown by Table 1 the state is H. Taking into consideration that J has the lowest value, the term sumbol for Sm^{3+} is $^6H_{5/2}$.

The magnetic moment of the Ln^{3+} is independent of the enviroment, so that one can not distinguish between coordination geometries as is sometimes possible for transition metals. The moments are given by the equation:

$$\mu_{eff} = g_J \sqrt{J(J+1)} \quad \textbf{(11)}$$

where the Landè factor is defined by:

$$g_J = \frac{3}{2} + \frac{S(S+1) - L(L+1)}{2J(J+1)} \quad \textbf{(12)}$$

The strength of spin orbit coupling means that the ground state is well seperated from the excited states, except for Sm^{3+} and Eu^{3+}, where contribution from low-lying paramagnetic excited states contribute to the magnetic moment. Thus, if the magnetic properties of compounds with Eu^{3+} ion ($^7F_0$) should be diamagnetic, there are contributions from thermally accessible levels (e.g. $^7F_1$ and $^7F_2$) which lead to observed room temperature magnetic moments.

Due to their high single-ion anisotropy, lanthanides are very attractive targets for research in the field of single-molecule magnetism [32,33]. However, the description of their electronic structure is always a difficult task. The simplifications and the assumptions made for interpreting the magnetism of trasnition metal ions could lead to massive inaccuracies when applied to lanthanides. This is because the electronic spin is no longer the only source of angular momentum in the compound [34]. The (not complete) degeneracy of the f-orbitals leads to a large unquenched orbital moment which has to be considered. The spin-orbit coupled quantum number J is very important, since the spin-orbit coupling is larger than the crystal field (Fig. 14).
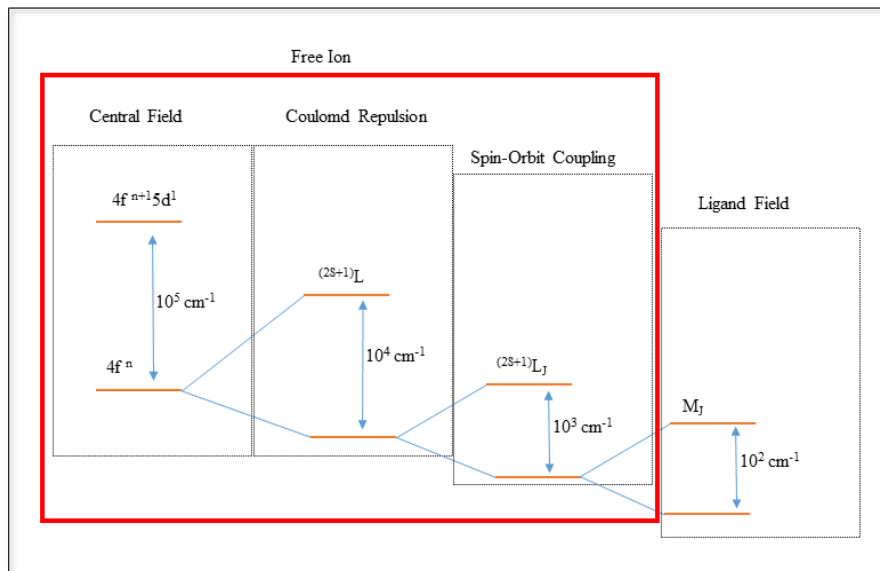
Figure 14: Electronic diagram of free lanthanide ions with the pertubations of electron-electron repulsions, spin-orbit coupling and ligand field.

The projections of the total angular momentum quantum number can be affected by the surrouding ligand field, removing the (2J+1)-fold degeneracy of the ground state. This splitting, in combination with the strong spin-orbit interaction, correlates the orientation of the spin and the symmetry of the ligand field. Having that in mind, we can increase the single-ion anisotropy simpy by choosing the appropriate coordination enviroment of the ion, possibly leading to higher energy barriers. However, the search for electronic structures and configurations that will lead to higher values of single-ion anisotropies has some necessities. First of all, the ground state has to be double degenerate with a high $\pm m_J$ quantum number, making sure that there is a high magnetic moment at temperatures where only the ground state is populated. In the absence of a magnetic field, breaking the m_J degeneracy is forbidden for Krammers ions, due to time-reversal symmetry. Secondly, for achieving strong single-ion anisotropy a large separation between the ground $\pm m_J$ state and the first excited doublet is required. This gap defines the energy needed for spin relaxation, assuming that a temperature dependent relaxation mechanism is taking place [35].

The simplified electronic hamiltonian that describes a lanthanide system is the following:

$$\hat{H} = \hat{H}_{ION} + \hat{H}_{CF} \qquad \textbf{(13)}$$

where H_{ION} is the hamiltonian for the free ion and H_{CF} is the hamiltonian for the crystal field symmetry. As mentioned above, the orbitals are occupied by electrons according to Hund's rules. As a consequence, one can easily estimate the distribution of the free-ion electron density for a given Ln ion. In Fig. 15, the shapes of f orbitals are presented and this is a useful tool in order to visualize the electronic structure for a lanthanide.
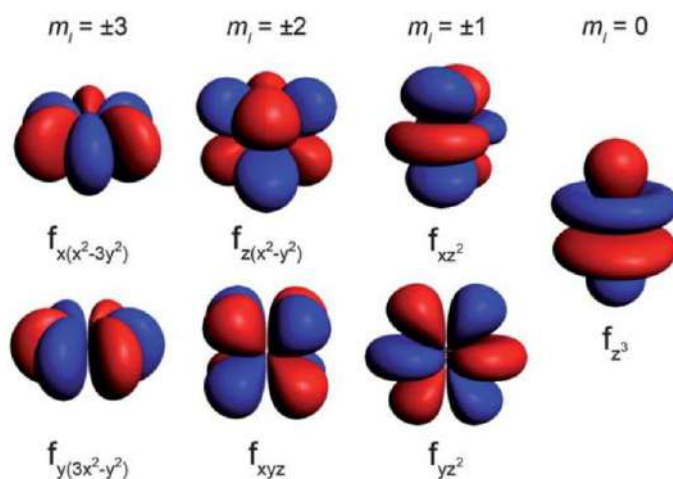
Figure 15: Representation of the 4f orbitals.

Having in mind the shapes of the 4f orbitals, we can "built" the appropriate crystal field around the lanthanide ion which will lead to a more anisotropic ground state. In general, there are two types of ligand fields that have to be consindered depending of the shape of the electron density. Thus, for Ce(III), Pr(III), Nd(III), Tb(III), Dy(III) and Ho(III) we have an oblate electron density, while we have a prolate one for Sm(III), Er(III), Tm(III) and Yb(III). Gd(III) is considered as an isotropic cation and has spherical symmetry. In order to maximize the anisotropy of an oblate ion, we should place it in a crystal field that the donor atoms are located above and below the *xy* plane, as in the case of sandwich-type coumpounds. In the opposite case, for a prolate ion an equatorial geometry is preferable in order to minimize the charge contact between the electron density of the lanthanide ion and the ligand (Fig. 16).
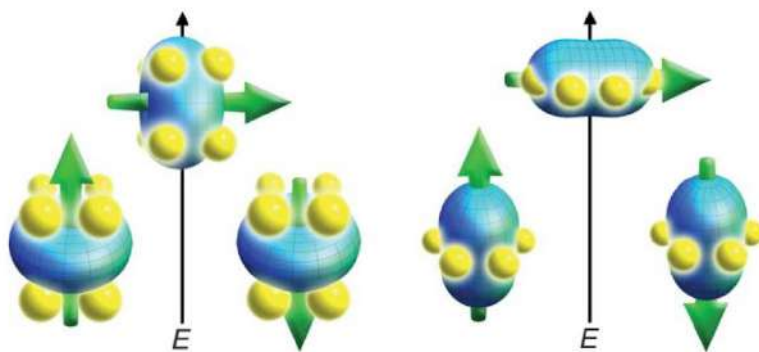
Figure 16: Depictions of energy configurations of the f-orbital electron density with respect to the crystal field for an oblate (left) and a prolate (right) electron density. The green arrow represents the orientation of the spin angular momentum coupled to the orbital moment[35].

Based on the above mentioned, lanthanides may be consindered as the ideal candidates for Single-Molecule Magnets. This model, with the oblate and prolate shaped electronic densities, allows the design of the appropriate coordination enviroment around the lanthanide in order to maximize the single-ion anisotropy. Also, it explains the reason why Dy(III) is so popular in molecular magnetism. First of all, it has a large magnetic moment ($^6H_{15/2}$ in the ground state) with high anisotropy, and secondly it is a Kramer's ion, which means that a double degenerate ground state is ensured. Furthermore, Tb(III) ion present some similarities with Dy(III) but it possesses higher anistropy. The problem in the Tb(III) case is that in order to have a bistable ground state, a strictly axial symmetry has to be maintained due to the fact that Tb is a non-Kramers ion and thus bistability is not guaranteed [35].

An example of this model, is the series of mononuclear complexes $[LnPc_2]^n$ (Ln = Tb, Dy, Ho; H_2Pc= phthalocyanine; n = -1, 0, +1) which were the first lanthanide single-molecule magnets to be identified [36]. At these sandwich-type compounds, passing from highly oblate to higly prolate ions, the ground states shift from higher to lower magnitude m_J states, confirming that the oblate electron densities of Dy and Tb ions can promote the axial single-ion anisotropies and thus, these metals, are ideal building blocks for compounds targeting a Single-Molecule Magnet behavior.

Lanthanide complexes are weakly coloured due to absorptions that are associated with f-f transitions. Their spectra show much narrower and more definite absorption bands than those of 3d metal complexes. The norrowness of the sperctral features and their insensitivity to the enviroment are a consequence of the 4f orbitals which are having a smaller radial extension than the filled 5s and 5p orbitals. These are happening when the oxidation state of the lanthanide is +3. Talking about other oxidation states the things are quite different. Many complexes, where the lanthanide ion is in the +2 or +4 oxidation state, possess intense colour, due to f-d or energy transfer transitions in the visible region of the spectrum.

Lanthanides have a large number of microstates for a given electronic configuration. For example, there are 91 microstates for a f^2 configuration. That means that there is a large number of terms and hence of possible transitions between them. As these terms are derived from f orbitals, there is little mixing between d and f orbitals and thus the transitions are Laporte forbidden.

However, transitions between 4f and 5d orbitals occurs in the higher energy UV region. Since the Laporte rule is relaxed and the 5d orbitals interact with the ligand, these transitions give rise to stronger and broader bands that are more sensitive to the enviroment. Also, many lanthanides compounds are intensively coloured because of the $4f^{(n-1)}5d^1 \leftarrow 4f^m$ transitions which occur in the near-IR and visible region of the spectrum.

Light emission by coordination compounds or materials stems from two different machenisms; the first is the " black-body" emission, which is temperature dependent, and the second mechanism is the luminescence or "cold light" emission [37], that contains specific energy levels of the system. Luminescence can be excisted with many different ways such as: thermoluminescence, photoluminescence, electroluminescnce and chemiluminescence. In lanthanides compounds the emission of light is coming from photoluminescence, through fluorescence and phosphorescence. According to IUPAC fluorescence is a fast, spin-allowed phenomenon, whereas phosphorescence is a slow, spin-forbidden mechanism [38,39]. In the case of lanthanide compounds both mechanisms can be present.

A simple description of lanthanides luminescence mehanism is shown in Fig. 17. Firstly, an electron is promoted to an excited singlet state of a ligand upon absorption of light (e.g. UV radiation). This photon, drops back to the lowest state of the excited singlet, from where it can return to the ground state directly (ligand-based luminescence) or it can follow a non-radiative pathway to a triplet state of the ligand. Thence it may return to the ground state (phosphorescence) or undergo an intersystem crossing, to excited states of Ln^{III} ion, whence it can return to the ground state with non-radiative emission or by metal-based fluorescence involving an f-f transition.
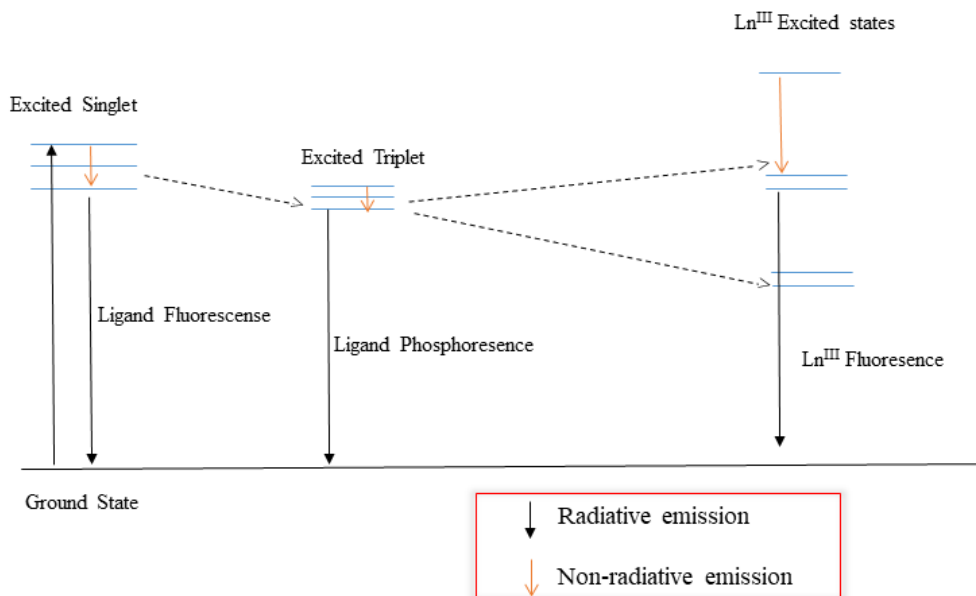
Figure 17: Luminescence machanism for Ln^{III} compounds.

There are certain Ln^{III} ions that have excited states, lying slightly lower in energy than the triplet states of ligands, and present strong metal-based fluorescence. Such ions are Eu^{3+} and Tb^{3+}, which are widely used as building blocks for luminescent compounds. Among other ions, La^{3+} and Lu^{3+} have no excited states; Gd^{3+} has all the excited states above the ligand triplet states while the other Ln^{III} ions posses a large number of excited states and thus energy loss by a non-radiative route may happen. That's why Eu^{3+} and Tb^{3+} are suitable for these kind of studies. For Tb^{3+} the main emissions arise from the $^5D_4 \rightarrow {}^7F_n$ transitions (n = 0-6), where the strongest transition is $^5D_4 \rightarrow {}^7F_5$. For Eu^{3+} the transitions

$^5D_0 \rightarrow {}^7F_n$ (n = 0-4) are responsible for the characteristic nad intense optical properties of its compounds.

As mentioned above, luminescence from Ln^{III} is weak due to Laporte forbidden transitions. In order to enhance their optical properties, chromophores can be used which absord in an appropriate wavelength and transfer the energy to the Ln^{III}, exciting it to the emissive state. This is the so-called "antenna effect" (Fig. 18). Usually, this wavelength ranges between 330-460 nm and most of the times Tb and Eu are the acceptors (their energy levels are located in 20.400 cm^{-1} and 17.200 cm^{-1}, respectively). The triplet state of the ligand has to be above their excited levels, otherwise competing thermally activated back transfer occurs. Exampes of such ligands are calixarenes, substituted macrocycles or phananthidines. The acceptor ligand it is not necessary to be directly bound ti the Ln^{III}, but it has to be close enough.
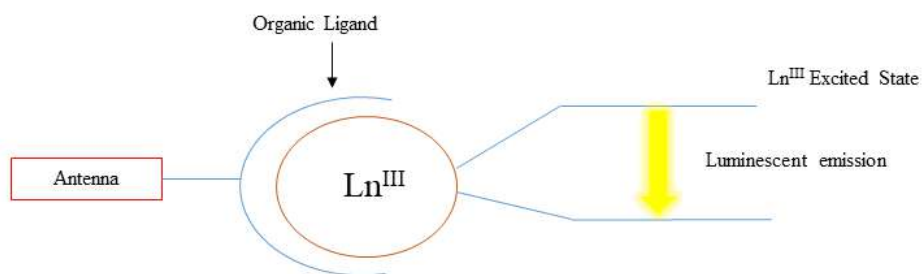
Figure 18: Schematic representation of antenna effect.

1.2. Synthetic Approaches-Strategies

The term "serendipitous assembly" is refered to the lack (or even absence) of systematic control of the synthesis of coordination clusters, where the metal cations may be found in different oxidation states [40]. In these synthetic procedures, simple metal salts or pre-synthesized coordination complexes, with relatively low nuclearity, react with multidentate ligands (most of the times carboxylates) under a variety of conditions [41]. Until today, serendipitous assembly is the most dominant synthetic pathway and the majority of the

complexes with interesting properties has been synthesized by using this strategy. This is attributed to the fact that the precise prediction of the physical properties of a given compound is very difficult and the direct design of systems is only possible with predictable combination of metal-ligands. The idea behind this strategy is based on the connection between the coordination sites (either the number or the type) that are available in a metal cation and the nature of the donor atoms that are contained in a ligand.

The choice of the organic ligand plays a pivotal role since the serendipitous assembly leads to unpredictable results. Ligands with multiple donor atoms are preferable over the ligands that demand complicated synthesis, because it is not possible to predict if they will be useful for the synthesis of new and structurally interesting coordination compounds. In addition, instead of using a single organic ligand, it should be used a series of similar ligands because small changes in the core or in the functional groups of the ligand could affect the nuclearity, the topology and the properties of the compounds [42]. Finally, the molecules that act as ligands should have good solubilities in as many solvents as possible, while the crystallinity of the product in different solvents should be checked as well [43].

On the other side, the "rational design" uses rigid organic ligands, that have strong preferencies for their coordination and metal cations with specific coordination geometries. The rational design has been used successfully by chemists for the synthesis of new compounds that, honestly, showed impressive structures [44]. The rational design approach provides a predictable result at the end of the synthesis. As a result, the structures that are derived are almost habitual and are based on the preferable coordination geometry of the metal cation, on the number of available coordination sites of the ligand and its limited flexebility (Fig. 19). Fujita and Stang [45] developed this strategy for the controlled synthesis of new metallic clusters, called "ligand-directed rational approach". According to this approach, the complexity of the system has to be reduced with the compination of rigid, multi-branched monodentate ligands with partial saturated (i.e. coordination number) of metal ions with specific coordination sites. It is obvious that the rational design approach can not be used in the coordination chemistry of 3d and 4f metal ions, due to the fact that these ions present a plethora of coordination geometries and, in the case of 3d ions, multiple oxidation states.
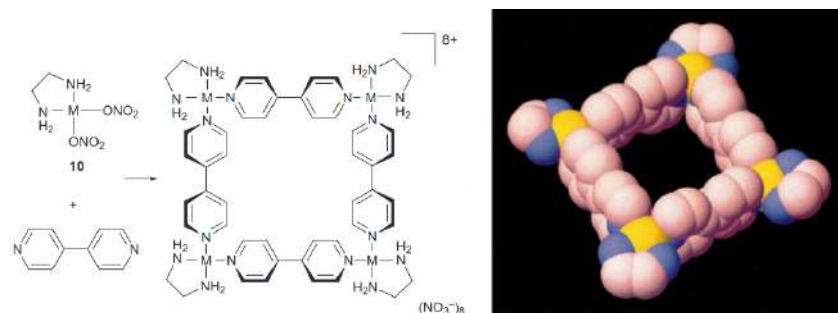
Figure 19: (Left) Represantation of synthesis of a "molecular square" through rational design; (Right) The crystal steucture of this molecule.

An important thing to mention, is the presence or absence of a borderline between these two stategies. In reality, new attractive syntetic procedures are coming to the surface, where the results from the self-assembly approach could be used further through rational design. However, the capabilities of bottom-up approach in the direction of nanoscale are huge. The exclusion of self-assembly from chemists' synthetic toolbox is impossible and sometimes even non-desirabe, when the target is the synthesis of clusters with fascinating magnetic properties.

While the self-assembly approach has contributed with significant results in the chemistry of metal clusters, the rational design approach eliminates the number of accesible structures, e.g. in platonic solids, rings or grids, because these kind of systems demand high symmetry and, most of the times, the same enviroment for each metal center [46]. On the other hand, the self-assembly approach could increase the number of new structures. The unusual structures that can derive the self-assembly strategy, may lead to new molecules with very interesting physical and chemical properties (magnetic, optical, catalytic etc). Despite the fact that chemists do not have the full control of the synthesis in the self-assembly, there are still some parameters that have to be taken into consideration. These parameters are the choise of the organic ligand/the metal cation(s) and also the conditions of the experiment (i.e. ratio of reactans, pH, solvents, temperature, crystallization methods etc).

One of the main goals in magnetochemistry, and in general in coordination chemistry, is the growing of single-crystals. These days, there is a variety of techniques in order to characterize coordination compounds. However, the most precise technique that allow us

to "see" the structure of a complex is the Single-Crystal X-Ray Diffraction. This technique allows the odservation of the crystal lattice, like it would be through a very strong microscope. In 1912 von Laue, Friedrich and Knipping realized experimentally that the X-rays diffracted from the 3D-structure of a crystal with the same way as light does with a diffraction spectrum. This diffraction is the result of the interaction between the X-rays and the electrons of the material.

The main disadvantage of X-Ray Diffraction is the formation and isolation of monocrystals. A monocrystal is a material in which the crystal lattice of the entire system is continuous and no grain boundaries appear. Monocrystals can be obtained, in a appropriate size, in the laboratory under controlled conditions. The methods that are used for formation of such crystals are the following:

- Slow evaporation: with this method, the solvent evaporates, and due to the increase of concentration of the product in the solution, it arrives to a saturated point and the product is formed.

- Vapor diffusion: in this method, a smaller vial with the reaction solution is placed inside a bigger one with the precipitant agent (most of the times is diethylether). The formation of the product is due to solubility and not of concentration.

- Layer crystallization: this method is similar in principal with vapor diffusion. However, in this method at the bottom of the tube there is the reaction solution and at the top is the precipitant agent. This allows the mixing between the two layers in a very slow way.

1.3 Schiff Bases as Ligands

Inorganic materials play an important role in the biological studies and in industry, whereas a lot of organic molecules, used as drugs, are getting activated or are transformed in the presence of metal cations. Many drugs have different properties when they are coordinated with a metal. Schiff bases have a wide spectrum of biological valence, and their complexes has shown antibacterial action too [47].

Schiff bases are called the molecules that contain the functional group (>C=N−). They took their name from Hugo Schiff, who first (1864) described the synthesis of the yellow solids that are the products of the condensation of ketones or aldehydes with primary amines. The formation of these bases is taking place under acidic or basic conditions or under the affection of temperature. The common Schiff bases are crystalline solids, with slightly basic character, and sometimes form insoluble salts with the presence of strong acids. In addition, they can be used in the synthesis of aminoacids or as ligands for the formation of compounds in coordination chemistry [48].

In general, Schiff bases are acting like multidonor ligands and are coordinating via the oxygen atom of the phenol group and/or via the nitrogen atom of the imine group. Also, Schiff bases may act as chelate ligands forming very stable coordination compounds. A lot of complexes with Schiff bases present very interesting catalytic properties and lately there are a lot of referencies with their application in homo- and heterogenious catalysis [49].

The formation of Schiff bases from aldehydes or ketones is a reversible reaction and can lead, relatively easy, to the hydrolysis of the product. The mechanism of this reaction is an "alternative" of the addition mechanism of a nucleophile to a carbonyl. In this case, the nucleophile is the amine and in the first step of the reaction react with the carbonyl group to give an intermidiate unstable molecule that called carbinolamine. In the second step, there is an ejection of a water molecule and the formation of the final product, as depicted in the following equation:

$$\text{(14)}$$
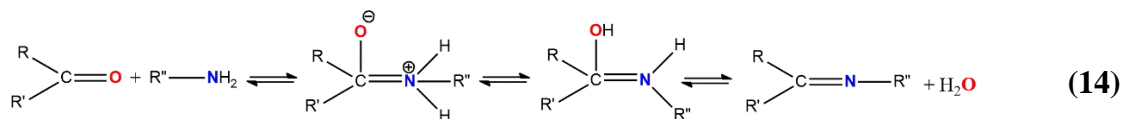
By definition ketones react slower than the aldehydes and they demand higher temperatures and reaction times. The explanation for this, is that the centre of the reaction in the aldehyde is less stereochemically blocked than the one of the ketone. Also, due to the fact that a ketone contains one more carbon atom compare to the aldehyde, the electronic density in the reaction center of the first one will be greater and thus it will be less electrophilic [50].

1.4 Supramolecular Chemistry

The modern verison of Supramolecular Chemistry was introduced by J. M. Lehn [51] and very often is refered as "*the chemistry beyond the molecule*". The term "Supramolecular" appeared for the first time in Webster's dictionary in 1903 and the term "Übermoküle" in 1937, in an attempt to describe molecular structures made up by smaller chemical or molecular species [52]. Supramolecular chemistry is based on weak interactions (H-bonds, π-π stacking, etc) that are developed between two and/or more chemical species for the formation of more complicated structures. In nature, the intermolecular interactions that are responsible for the organization of sub-units, are mainly non-covalent and weak (~0.1-30 kcal/mol) compared with the covalent sp^3 C-C bonds (~80 kcal/mol) that chemists study in clasical chemistry. In addition, the reversible nature of the non-covalent intermolecular interactions often enable the synthesis of thermodynamically stable products without any external stimuli. For example, nature, through its development mechanism, apply this to the self-organization of biological systems, with the most characteristic example of this being the DNA (Fig. 20).
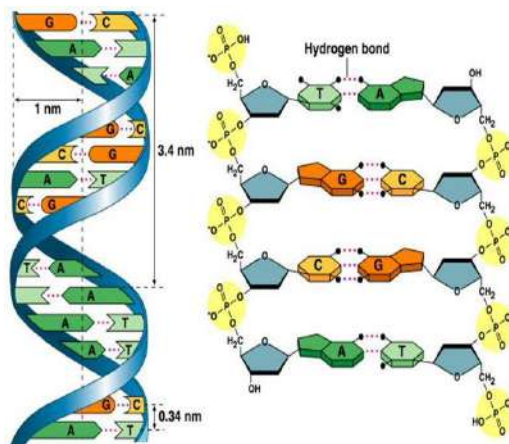
Figure 20: Representation of DNA double helicate; dashed lines represent for the H-bonds.

DNA is a macromolecule, that contains the genetic code of all orgnisms and of some viruses, is consisted by two polymeric strains of nucleotides and useses H-bonds and π-π interactions forming a double helicate. Despite the fact that each of the intermolecular interactions between the stains is weak, the two strains are placed in such a way that they maximize the number of interactions and thus the whole structure is stable. Such complicated self-assembled systems like DNA, inspired the work of D. J. Cram [53], J.M.

Lehn [54] and C. J. Pedersen [55] in the field of supramolecular chemistry. However, the most impressive examples of supramolecular molecules that have been synthesized in the laboratory, are steps behind compared to the ability of nature to use these kind of interactions and drive multiple weak intermolecular interactions to build big and complicated structures. The perspective of using supramolecular structures in daily applications such as microelectronics, medicine, enviroment or even catalysis demand the accurate control and the whole understanding of the way that the non-covalent interactions are working.

When supramolecular chemistry was in its first steps, the inorganic chemists turned their interest to the macrocycled ligands, basically because their coordination compounds were much more stable than the ones with non-macrocycled ligands. This phenomenon is known as "Macrocyclic Effect" and took its name by Cabbines and Margerum in 1969 [56]. In many cases, the metal cations participated in the synthesis of macrocycled ligands through the "template reactions", a strategy that gained a lot of interest from scinetsists from different fields, while this term changed to "self-assembly".

Coordinantion chemistry has, and still play a pivotal role in the growth of supramolecular chemistry. For example, the fact that the metal centers have preferencies and a variety of coordination geometries is a basic knowledge for achieving the steric control in the self-assembly strategy. Alfred Werner was the first who suggested that coordination compounds which contains metel ions should have certain geometries. In 1893 he introduced the idea that the ligands are in certain positions around a metal cation [57]. He named the number of "bonds" between the metals and the ligands coordination number and he noticed that the most frequent coordination numbers were 3, 4, 6 and 8. Also, he noticed that coordination number 6 was very common and he proposed that the arrangement of these ligands around the metal cation should be placed in the apexes of an octahedron. The development of coordination chemistry offered new tools for the understanding of many biological systems and the investment of new molecular materials.

The synthesis of supramolecular structures is based on in the simple model where the metal ion (Lewis' acid) reacts and coordinates with an organic ligand (Lewis' base). The predictable and rigid geometries that can be adopted by the metal ions may allow the easy

synthesis of a plethora of coordination complexes. Furthermore, the metal-ligand bond, that typically are 15-50 kcal/mol in energy [58], offer stability to the final product. This very simple, but effective approach, with normal conditions has been developed during the last decades giving structures with increased complexity. The increase of characterization techniques and structural variations has led to rapid increase of synthetic approaches for the synthesis of new supramolecular coordination compounds such as: weak link, symmetry interaction, directional bonding, molecular paneling, serendipitous self-assembling and designed self-assembling, where the last two are the most common in coordination and supramolecular chemistry.

1.5 Chirality

Chirality took its name from the greek word "χέρι" which means hand. A chiral molecule exists in two different forms, called enantiomers. The word enantiomer is also a word coming from greek; the word "ενάντιος" means opposite. Enantiomers are non-superimposable images of one another. If the two enantiomers are present in the same proportion then the resulting compound is called *racemic*. The important thing is that in a chiral enviroment, the two enantiomers must be considered as chemically different compounds; the enantiomers behave in opposing ways for certain phenomena.

The most studied phenomenon is the interaction of chiral molecules and polarized light. Linearly polarized light is a "racemate" of light, polarized in a clock- and anti-clock manner. Each enantiomer has the ability to rotate the plane of the polarized light; this is known as optical activity. One isomer rotates the light to the right hand direction "x" number of degrees, while the other rotates the light in the opposite direction but with the same number of degrees.. Thus, the enatiomers often are called *optical isomers*. In reality, this is the only difference between the two enantiomers; all the other properties that these complexes could have are the same and this make them extremely difficult to distinguish them.

There are various systems of nomencalture for the chiral compounds. The most widely used is the one based on Cahn, Ingold and Prelog rules. This system uses the letters *R* and

S in order to assign the absolute stereochemistry of the molecules. When the priority of the atoms or groups in a chiral center follows the right-hand side direction the molecule is asigned as *R*, while is asigned as *S* if the atoms or groups are places in a left hand direction.

1.6 Manganese(II) in Molecular Magnetism

Manganese is one of the most important metal ions in the field of molecular magnetism. Apart from the prototype Mn_{12} which opened the field, it has some more worth noting advantages. Firstly, manganese provides a relative easiness of making carboxylates analogues of the Mn_{12}. There are more than 60 [Mn_{12}] complexes that behave as single-molecule magnets. Secondly, it possesses a large spin ground state in various oxidation states and, most importantly, it shows negative magnetic anisotropy of the Jahn-Teller elongated six-coordinated Mn^{III} ions. Thirdly, manganese complexes shows high stability under aerobic conditions, which make it pretty easy on its handling, and finally, there is a large availability of manganese salts/complexes that can be employed as strating materials. Based on the above mentioned, manganese is a very interesting and attractive cation for the field of molecular magnetism.

Manganese(II) is not very "famous" in the field of magnetism. Actually, Mn(II) is considered as a bad candidate for SMMs. This is because it possesses a d^5 ground state (Fig. 21) ($^6A_{1g}$ in octahedral environment), which means that the orbital angular momentum is equal to zero and thus it presents a small zero-field splitting and low magnetic anisotropy. However, there are some examples of Mn(II) complexes in the literature that show single-molecule magnet/ion behavior.

Mn^{II}: S = 5/2; L = 0; $^6A_{1g}$.
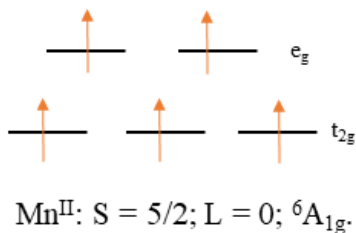
Figure 21: Electronic configuration of Mn(II) cation in octahedral enviroment.

The first example of mononuclear Mn(II) complex that exhibit SMM behavior is a cluster of Ca^{II}-Mn^{II} [59]. This Ca-Mn cluster contains subunits of $[Mn(bipy)_2(OH)_2]^{2+}$ (where bipy = 2,2' bipyridine) and possesses two relaxation pathways; a direct one and a faster relaxation caused by thr resonant phonon trapping. Another example is the tetragonal biramidal $[Mn(4\text{-}bzpy)_4Cl_2]$ (where 4-bzpy = 4-benzylpyridine), which shows single-ion magnetic behavior and the relaxation is dominated by the Raman process [60]. Interestinlgy, this complex shows very high relaxation time; $\tau = 798 \cdot 10^{-3}$ s at 1.9 K and D = 0.6 cm^{-1}. A third compound that shows single-ion magnet behavior is the six-coordinate Mn^{II} complex with formula $[Mn(4\text{-}HOpa)_2(H_2O)_2]$ (where 4-HOpa = N-4-hydroxyphenyloxamate) [61]. In this case the relaxation is dominated by the phonon-bottleneck effect. This effect occurs in a one-phonon direct relaxaton process when the emitted phonons have nowhere to go due to inefficient energy transfer of the lattice to the enviroment and are re-absorbed. A similar behavior was also observed in the complex $[Mn(L)_2(MeOH)_2]$ where the organic ligand in this case is HL = 2,6-bis(pyrazole-1-yl)pyridine-4-carboxylic acid [62]. At this point, it is important to mention that the magnetic behavior of these compounds was observed under an applied magnetic field. When the measurements were taking place at zero field, QTM was present and no magnetic relaxation was observed.

1.7. Gadolinium(III) in Molecular Magnetism

Gadolinium is also a metal that is considered as magnetically isotropic. Its electronic configuration ($4f^7$) implies lack of orbital angular momentum (L = 0) despite the fact that it possesses the highest spin value of all elements (S = 7/2). The absence of orbital contributions lead to almost degenerate enerly levels; their energy difference is within just some wavenumbers (cm^{-1}). Thus, the magnetic relaxation rate is usually very fast due to the quantum tunneling of magentization. However, when an external field is applied this degeneracy can be removed and QTM can be suppressed.

The complexes that behave as SMMs or SIMs present some common features: firstly, they have intramolecular interactions (regarding the dinuclears Gd^{III} complexes); secondly these systems are always field-induced SMMs (or SIMs) and finally no significant anisotropy can be detected by conventional methods because the magnitude of D is very low (~ 0.1

cm^{-1}) and thus Electron Paramagnetic Resonance (EPR) studies are used. Furthermore, the low magnitude of *D* implies that the relaxation phenomenon can not be attributed to overbarrier or tunneling above 2 K.

One of the first examples is the complex [Gd$_2$(fum)$_3$(H$_2$O)$_4$]·3H$_2$O, in which the organic ligand is the dianionic form of fumaric acid (C$_4$H$_4$O$_4$) [63]. In this complex, the Gd cations are placed in a distored tricapped triginal prismatic enviroment. Electron paramagnetic resonance (EPR) studies revealed an S = 7/2 system with uniaxial anisotropy. Magnetic measurements were carried out and the result was that the magnetic relaxation was governed by spin phonon trapping. Another compound that shows single-molecule magnet behavior is the complex [Gd$_2$(phen)$_2$(HCOO)$_4$(HCOO)$_{2-2x}$(NO$_3$)$_{2x}$] where x = 0.52 and phen = 1,10 phenathroline [64]. In this compound Gd is in a distorted tri-capped trigonal prismatic enviroment . The ac measurements were carried out under a static field of 2.75 kOe. Two relaxation pathways were observed; the first pathway is a spin lattice relaxation characterized by a $\tau_1 = 10^{-1}$ s; the second one is a fast relaxation, probably due to spin-spin interactions, characterized by a $\tau_2 = 10^{-5}$-10^{-4} s.

The first chain-like structure of Gd that presents SMM behaviour is a complex of Gd and EDTA (EDTA = Ethylenediaminetetraacetic acid) [65]. The asymmetric unit of this compound is shown in Fig. 22. Also in this case Gd cation is nonacoordinated; the ac measurements were carried out under an applied field of 0.45 T in order to suppress QTM. Two relaxation pathways were observed; the first is characterized by $\tau_0 = 4 \times 10^{-2}$ s and U$_{eff}$ = 6.1 K; and the second one is characterized by $\tau_0 = 8 \times 10^{-7}$ s and U$_{eff}$ of 84 K. The energy barriers and relaxation times were obtained by using the Arrhenius equation: $\tau = \tau_0 \exp(U_{eff}/kT)$.
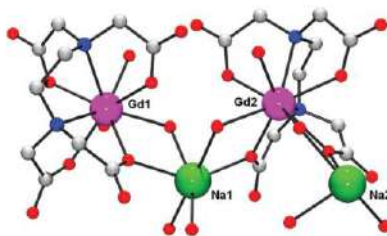
Figure 22: Single crystal X-ray structure of [Gd-EDTA], displaying the asymmetric unit within the chain. Colour code: pink (GdIII), green (Na), red (O), blue (N), grey (C). Hydrogen atoms and water molecules within the lattice omitted for clarity [65].

A similar system with the above mentioned, is the case of the 1D-coordination polymer with formula $\{[Gd_2(CNCH_2COO)_6(H_2O)]\}_n$ [66]. Here, Gd adopts a tricapped trigonal prism coordination geometry. As normal, under zero field no magnetic relaxation was observed. With the applciation of an external field of 0.2 T, magentic relaxation was taking place and two different relaxation processes were present; one fast characterized by a relaxation time $\tau_f = 10^{-3}$ s, and a slower one characterized by a relaxation time of $\tau_s = 0.1\text{-}1$ s and an activation barrier of 5.5 K.

Another breakthrough result was the case of the tetranuclear complex $[Pd_2Gd_2(H_2O)_2(OAc)_{10}] \cdot 2OAc$ reported by the group of Yamshita [67]. In this complex Gd forms a bond with Pd cation; by theoretical calculations it was found that the $4d_z^2$ orbital of the Pd^{2+} forms the highest occupied molecular orbital (HOMO) with the hybridized $6p_z$, $5d_{xz}$ or $5d_{yz}$, which are matched in symmetry and energy. As a result there is a permanent electron density donation from Pd to Gd cation, affecting the magnetic properties. Ac measurements under an applied magnetic field of 3 kOe revealed that the relaxation occurred via Orbach and Direct processes. The pre-exponential factors are 1.03×10^{-6} s for the fast relaxation whereas for the slow one is 6.02×10^{-2} s which was the slowest reported value. Some years later the same group presented a triple decker compound abbreviated as **GdGd**, **GdY** and **YY** (Fig. 23). The first one indicates the presence of two Gd cations in the complex, the the second one the presence of one Gd and one Y cation. The **YY** stands for the fully diluted compound [68]. In this complex the Gd adopts a distorted square antiprism geometry; the distance between the two Gd cations is 3.538 Å indicating that there is a intramolecular interaction. DC magnetic mesurements affirms the ferromagnetic interaction between the Gd centers with a $J = 0.034$ cm^{-1}. In this work, they show that the intramolecular interactions between the Gd cations affects the magnetic behavior of the complexes in a way that the more diluted the compound is the higher relaxation times can appear.
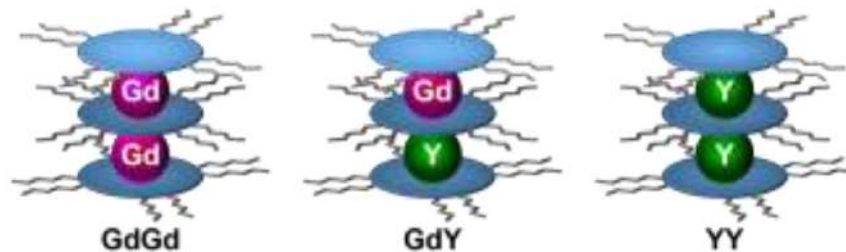
Figure 23: Represantation of GdGd, GdY and YY complexes. The blue discs correspond to the organic ligand employed in this work [68].

Apart from the above mentioned clusters, a vey important work is the one reported by the group of F. Luis [69]. In this work, they tried to study the affection of coordination geometry around Gd in terms of magnetism. For this reason they synthesize two polyoxometalate clusters; GdW_{10} and GdW_{30}. The first pocesses an axial symmetry while the second cluster has an equtorial one. Both compounds behave as Single-Ion Magnets at low temperatures, but in this case this is happening without the application of an applied magneitc field. From ac magnetic studies it is revealed that GdW_{10} has slower magnetic relaxation than GdW_{30} which indicates the importance of local geometry in their magnetic behavior.

Nowadays, there is an increasing interest in the field of magnetism about Gd single-molecule or single-ion magnets. Much attention is paid in correlating the enviroment of the cation and the affection it has on its magnetisation [70], how the intramolecular interactions or exhange couplings are working [71] and most importantly if this knowledge could be useful in materials such as Metal-Organic Frameworks [72]. In any case, Gd magnets and "isotropic" SMMs can be an new fruitful field of research and investigation.

At this point it should be pointed that SMM/SIM response is not expected for isotropic systems containing Gd^{III} or Mn^{II} as spin carriers. The small value of D that they present is due to the strongly distorted enviroment, and thus EPR measurements become crucial in the determination of the magnetic anisotropy magnitude. Low D values, are not able to generate conventional SIM/SMM systems because the energy barrier derived from the double well takes very low values that are orders of magnitude lower than the calculated ones. Thus, quantum tunneling and Orbach relaxation should be excluded menaning that the "unusual" magnetic response could be related to their weak anisotropy that break the degeneracy of the ground state under external magnetic fields. Also, QTM and over-barrier

relaxation should be exluded for the systems ttat possess a ground state S = ½; the absence of excited m_s states does not allow the these kind of relaxation and thus, Direct and Raman mechanisms should be considered as the dominated mechanisms.

1.8 Experimental Methothology

All the complexes that are presented in this thesis, have been characterized dy means of classical characterization techniques; Infrared spectroscopy (IR), single-crystal or powder X-ray diffraction and electronic circular dichroism (ECD). Magnetic properties were performed using a Superconducting Quantum Interference Device (SQUID), for the study of dynamic and static properties for all the complexes in this work.

1.8.1 Superconducting Quantum Interference Device (SQUID) [73]

A superconducting quantum interference device is a very sensitive instrument for measuring very weak magnetic fields; it can measure magnetic fields as low as 5 aT (5 x 10^{-18} T). Due to this sensitivity, SQUIDs are widely used in biological research and others ultrasensitive electronic and magnetic measurements where poor signals can not be detected using conventional instruments. There are two different types of SQUID; the radio frequency (RF) SQUID consisitng of one Josephson junction, and the direct current (DC) SQUID with two ot more juctions. RF SQUID is cheaper in contsruction but less sensitive compared to the DC.

A typical DC SQUID has two parallel junctions inserted in a superconducting loop (Fig. 24). Without a magnetic field, the input current splits equally between the branches. This maintains an externally connected tank circuit at resonance. Any external magnetic field causes a change in the resonant frequency in the tank circuit, and a current imbalance that leads to a voltage across the Josephson junction. The voltage is a function of the magnetic flux and can therefore be measured and used to calculate the magnetic flux.
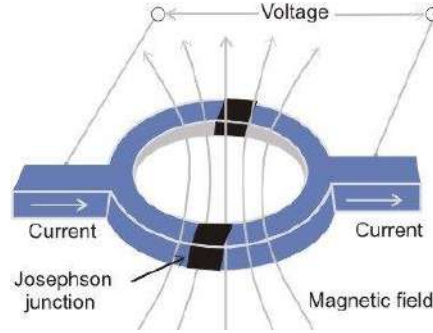
Figure 24: Schematic represantation of a SQUID.

The magnetization (*M*) measurement is carried out at a temprature window of 1.5 to 300 K. Temperature dependent measurements are important because while the temperature (*T*) decreasing, the excited states are depopulated and the ground state becomes populated, according to Boltzman distribution. In general, the representation of ($M/N_{\mu B}$) vs. the field is used; $N_{\mu B}$ is the magnetic moment of a mol of electrons. With this representation, when *g* value is close to g_e, the value at which $M/N_{\mu B}$ tends, is the number of unpaired electrons, which determine the fundamental state of the system, *S*. Furthermore, plotting the field-dependence of *M* at different temperatures, *i.e.* the reduced magnetization, we can extract information about the anisotropy of the system.

Magnetic susceptibility (χ) measurements, are carried out at a costant field and variable temperatures. Most of the times the χT vs *T* representation is used; this representation is useful to extract informations about the deviations from paramagnetic behavior, at low temperatures, for the non-interacting spins that should follow the Curie law. Also, this representation is helpful for understanding the nature of the magnetic exchange interactions between coupled electrons.

With SQUID it is possible to get information about *spin dynamics*; it allows time-depedent measurements, which consists in measuring the time decay of the remnant magnetization by applying a strong magnetic field at a temperature that the dynamics are fast. The next step is to cool down the system, remove the field and measure the magnetization as a function of the elapsed time. The magnetization follows an exponential law:

$$M(t) = M(0)\exp(-t/\tau) \quad \textbf{(15)}$$

where τ is the relaxation time. The time window for these experiments ranges from 100s to days or even weeks and months, depending on the experimentalist.

Another way to get information about the spin dynamics is the alternating current (ac) measurements. With this technique, we can realize if the sample can behave as an SMM or not, the number and the relaxation mechanisms that the molecule pocess. The measurement can be done in a static magnetic field H_0 parallel to the oscillating filed h so the applied magneitc field becomes:

$$H = H_0 + h\cos\omega t \quad \textbf{(16)}$$

where ω is the angular frequency of the ac current. In the simple case of a $S = \frac{1}{2}$, the equilibrium population between the two states, $m_s = \pm \frac{1}{2}$, oscillates following the equation:

$$p_1/p_2 = \exp[-g\mu_B(H_0 + h\cos\omega t)/k_\beta T] \quad \textbf{(17)}$$

while the establishment to thermal equilibrium requires time τ. If the frequency of the ac field ω is low, i.e. $\omega\tau \ll 1$, the susceptibility that is measured is the isothermal one, $\chi = \chi_T$. On the other limit, when $\omega\tau \gg 1$, the system does not have time to exchange energy with its enviroment, and then the adiabatic susceptibility is measured, χ_S. In the intermediate regime, Casimir and de Prè [74] proposed that:

$$\chi(\omega) = \chi_S + (\chi_T - \chi_S/1 + i\omega\tau) \quad \textbf{(18)}$$

And if we separate the real and the imaginary compounts of the susceptibility we have:

$$\chi' = [(\chi_T - \chi_S)/ 1 + \omega^2\tau^2] + \chi_S; \quad \textbf{(19)}$$

$$\chi'' = [(\chi_T - \chi_S)\omega\tau/1 + \omega^2\tau^2] \quad \textbf{(20)}$$

The above mentioned treatment of the magnetic data is known as the "*Debye Model*", because mathematically analogous relations have been used in the field of dielectric materials.

Another "tool" that has been taken from dilectrics is the Cole-Cole plots [75], or kown as Argand plots [76] in magnetism, where χ'' vs χ' is used. Equation (19) and (20) transform in semicircle where its centre is on the x-axis. At the top of the semicircle the relaxation time τ is equal to $\tau = \omega^{-1}$ (Fig. 25).
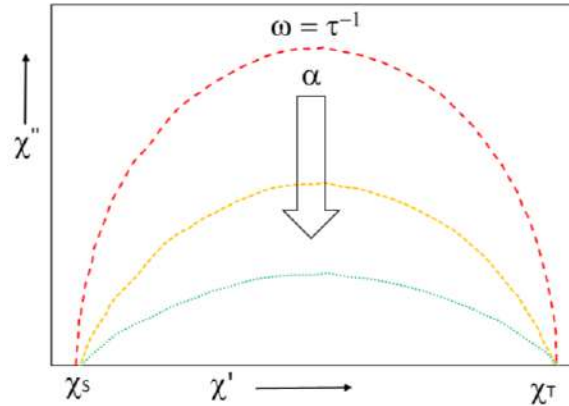
Figure 25: Argand (or Cole-Cole) plots where at a given temperature χ" vs χ' is plotted for each frequency.

If the relaxation process is not characterized by a sinlge relaxation time τ, but there is a distribution of relaxation times, then the following empirical law is used:

$$\chi(\omega) = \chi_S + [(\chi_T - \chi_S)/1 + (i\omega\tau)^{1-\alpha}] \quad \textbf{(21)}$$

The wider the distribution in relaxation times the larger the α. This parameter is very important in molecular magnetism and it can be easily extracted by the experimental ac data, because the semicircle in the Argand plots becomes an arc of a circle as the α parameter increases (Fig. 25 white arrow). The possible values that α can take is between 0 and 1, where 0 stands for a single relaxation time. Also, it is possible that different relaxation processes can be occurred, and then more semicircles can be obtained.

1.8.2 Electron Paramagnetic Resonance (EPR)

Electron paramagnetic resonance (EPR), or electron spin resonance (ESR), spectroscopy is a technique that is used to study chemical entities with unpaired electrons. EPR spectroscopy plays a crucial role in the study and in the understanding of organic or inorganic radicals, coordination compounds and biological membranes. Like most of the spectroscopic techniques, EPR spectometers measure the absorption of electromagnetic radiation.

EPR permits the observation of any molecule having unpaired electrons. Examples of such molecules are:

- Molecules that have an odd number of electrons in the outer shells (e.g. ClO_2).

- Molecules with an even number of electrons but they present a magnetic moment (e.g. O_2).

- Organic or inorganic radicals and coordination compounds of transition metlas or lanthanoids.

The EPR spectrum of a free radical (S = ½) is the simplest of all the forms. In the absence of an external field, the two electron spin states, $m_s = \pm 1/2$, are degenerate. By the application of an external magnetic field, this degeneracy is lifted and transitions between the electron spin levels can be induced by radiation at the matching frequency. When a magnetic field is applied, atoms with unpaired electrons align parallel (spin-up) or antiparallel (spin-down) with the direction of the field. These two alignments have different energies due to Zeeman effect (Fig. 26). By increasing the magnetic field, the energy gap between the states is widened until it matches the microwaves' energy, as represented by the blue dashed line in Fig. 26. At this point the electrons can move between the two states. Since there are more electrons in the lower state, according to Boltzmann distribution, there is a net absorption of energy, and it is this absorption that is monitored and converted into a spectrum.

$$m_s = 1/2$$

$$\Delta E = h\nu = g\mu_B B_0$$

$$m_s = -1/2$$
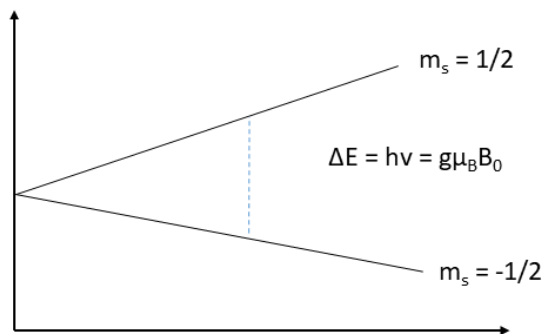
Figure 26: Energy levels for a S = ½ in an applied magnetic field B_0.

When the system has a single electron, then the EPR spectrum would only consists of a single line; since the source of an EPR spectrum is a change in an electron's spin state, it might be thought that all EPR spectra for systems that have one electron would consist of one line. However, this is not always the case. The interactions of the unpaired electrons

with nearby nuclear spins, results in additional allowed energy states and, as a result, multilined spectra[77]. In this scenario, the spacing between the EPR spectral lines is indicative for the degree of interaction between the unpaired electron and the nuclei. The interaction between nuclear and electronic spins is called hyperfine interaction.

EPR, fundamentally, is similar to more widely familiar NMR spectroscopy. However, there are some important differencies. Both spectroscopies deal with the interaction of electromagnetic radiation with magnetic moments of particles, although there are many distinctions:

- EPR focuses on the interactions between an external magnetic field and the unpaired electrons.
- The radiation which is used in NMR is typically between 300 and 1000 MHz, whereas EPR is typically performed in the range of 3-400 GHz.
- Due to the sort relaxation times of electron spins in comparison to nuclei, EPR experimetns are performed at very low temperatures, often below 10 K.
- EPR specrtoscopy is approximatelly three orders of magnitude more sensitive than NMR due to the higher frequency of electromagnetic radiation used in EPR compare with NMR.

1.8.3 Electronic Circular Dichroism (ECD)

Circular Dichroism (or simply CD), is the difference between the absorption of left or right circularly polarized light; it is strictly associated to chirality. It is very popular and applicable in the research field of biomolecules such as nucleic acids and to the investigation of secondary structures of biopolymers.

Electronic Circular Dichroism (ECD) is very useful technique in order to prove the absolute configuration of a given compound. ECD is a spectroscopic technique based on circular dichroism and the absorption occurs in the region of UV-Vis electromagnetic spectrum (800-200 nm). ECD is based in the so-called Cotton effect, on account of the discoverer of the phenomenon; the spectra can display a maximum or a minimum, or even both, in the region under study. These curces are characterized as positives or negatives depending on the sign of the first extreme observed at the longest wavelength (Fig. 27).
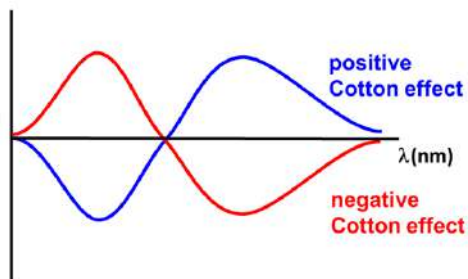
Figure 27: Blue line represents a positive Cotton effect while the red one a negative.

When we are working with enantiomers, their ECD has to be identical; the region that deviates is the region where the transitions n → π* are taking place which are of opposite signs for a each enantiomer. Simply, the two enantiomers exhibit identical but opposite sign spectra. When an ECD spectrum is recording, the molecule gets excited from the ground to the an excited electronic state via absorption of a photon. The chiral coumpounds have the ability to rotate the plane of polarization, so the initial beam that passes through the sample exits in a different orientaiton.

1.9 OBJECTIVES

- Synthesis and structural characterization of 3d and/or 4f coordination compounds derived from Schiff bases.

- Design of lanthanoid complexes with large anisotropy in the search of Single Molecule Magnet response.

- Design of molecular systems derived from isotropic cations, able to exhibit slow relaxation of the magnetization (SMR).

- In depth study of magnetic properties of Gd(III) and Mn(II) complexes that present SRM, using EPR and standard staticmagnetometry.

- To elucidate the decive factor that determines the SRM in Mn(II) complexes. Study of the magnetic properties of these compounds.

CHAPTER 2

SMR in Lanthanide(III) Complexes: The case of Gd(III)

Chapter 2: SMR in Lanthanide(III) Complexes: The case of Gd(III)

Chapter 2 comprises **Publication #1**, **Publication #2**, **Publication #3**

Lanthanides are very common building blocks for SMMs or SIMs due to their large single-ion magnetic anisotropy. However, their magnetic behavior is affected by the ligand field provided by the ligands that are coordinated to the metal cation. Thus, it would be interesting to study the way how different classes of ligands can affect the properties, not only magnetic but also in supramolecular level, of Ln(III)-based compounds.

Publication #1 *"Structural and magnetic studies of mononuclear lanthanide complexes derived from N-rich chiral Schiff bases"* describes a new family of mononuclear lanthanide complexes with formulas $[Ce^{III}(L1)(NO_3)_3(MeOH)]$ (**1**) and $[Ln^{III}(L1)(NO_3)_3]\cdot MeOH$ in the case of Ln = Gd (**2**) or Dy (**3**). The organic ligand that employed in this work is a multidentate Schiff base (L1, Fig. 28) derived from the condensation of two equivalents of 2-pyridinecarboxaldehyde and one equivalent of (*1R/S,2R/S*)-1,2-diamino cyclohexane; it's a neutral, N-rich molecule which is "unusual" in the coordination chemistry of Ln(III). In the majority of the cases o-vanillin or salicylic precursors are used due to the oxophilic character of Ln ions, following the Hard and Soft Acids and Bases model. As a result, complexes with N_4L type ligands are less studied in the field of molecular magnetism and that was the initial motivation in order to investigate this kind of systems.
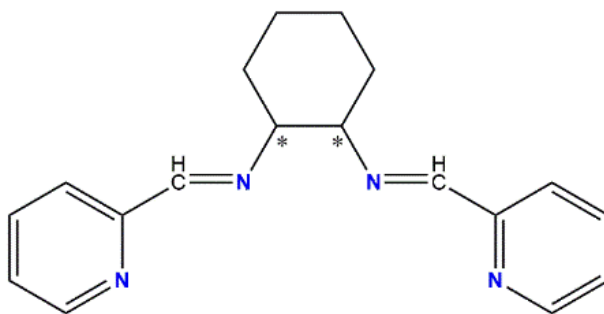
Figure 28: Structural formula of the chiral organic ligand L1 employed in **Publication #1**.

The organic ligand L1 was not isolated as solid. Instead its solution was used directly for the syntheses of complexes (**1**), (**2**) and (**3**). The corresponding lanthanide nitrate salt was added in the methanolic solution of the ligand, resulting the isolation of two different kind

of complexes. In case of (**1**) the coordination sphere of Ce^{III} is fulfilled by one neutral ligand, three bidentate nitrato ligands and one methanol molecule, whereas in the cases of (**2**) and (**3**) the methanol is not in the first coordination sphere of the cations, but is cocrystallized in the lattice. Also, the diluted complexes of (**2**) and (**3**), (**2d**) and (**3d**), with Eu^{III} were synthesized in order to study the effect of magnetic dilution. Partially labelled plots of the three complexes are shown in Fig. 29.
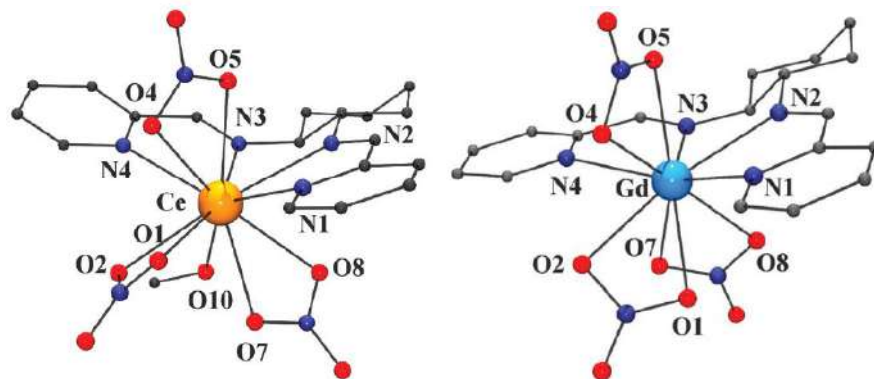
Figure 29: Partially labelled plots for (**1**) (left) and (**2**) (right). Complex (**3**) is isostructural to (**2**).

The three complexes were studied in terms of electronic circular dichroism and magnetism. Due to the fact that the ligand employed in this work is chiral, it could be interesting to realize if this chirality is transferred to the cations. However, this is not happening in this case and the chiroptical properties are related to ligands.

Static magnetic measurements were performed in the temperature range of 2-300 K. For (**1**) and (**3**) the $\chi_M T$ product decreases on cooling due to the de population of Stark sublevels. Complex (**2**) showed a Curie law response with a constant value of 7.6 $cm^3mol^{-1}K$, as expected for an isotropic Gd^{III} cation ($^8S_{7/2}$ and $g = 2.00$). EPR measurements were recorded for (**2**), and its diluted analogue, showing several absorptions at $g = 6.8$, 3.1 and 1.69 exposing the presence of a $D = 0.07$ cm^{-1}.

Dynamic magnetic measurements were performed for all the complexes. No out-of-phase signals were observed at zero field. However, under different applied fields all the complexes revealed well-defined peaks. For (**1**) a dc field of 0.2 T was used in the frequency range of 500-1500 Hz. Fitting of the data revealed that the magnetic relaxation is governed by the Orbach process. For (**3**) an applied field of 0.1 T was used in the 10-

1500 Hz range of frequency. At low temperatures the relaxation is governed by quantum tunneling whereas for higher frequencies the Arrhenius fit yielded an energy barrier equal to 30.6 K. Also, its diluted analogous was studied and the result was that tunneling of magnetization was suppressed yielding a slightly higher relaxation barrier equal to 34.6 K. Finally, for (**2**) ac measurements were recorded at 0.4 T in the frequency range of 1-1488 Hz. In this case, two HF/LF processes were observed with an intermediate region with a minimal signal being present. The HF signal is temperature dependent, while the LF peaks were poorly dependent on the frequency. Measurements in the diluted compound (**2d**) showed similar response. The fit of the relaxation time vs. temperature for (**2**) and (**2d**) yielded similar energy barriers with magnitudes of 13.3 K and 10.6 K, respectively.

Taking into consideration the magnetic behavior for compounds **2**, **2d**, **3** and **3d**, there are some important facts to mention. In the case of Dy^{III} compounds the dilution suppressed the quantum tunneling by the reduction of the dipolar interactions; however, the energy barriers and the relaxation times were practically unaffected ($\tau_0 = 9.7 \times 10^{-7}$ s for **3** and $\tau_0 = 4.9 \times 10^{-7}$s for **3d**, as extracted from the fit of the corresponding Argand plots). In contrast, in the case of Gd^{III} systems the fit of Argand plots showed similar magnitudes of the energy barrier but a clear enlargement of the relaxation times ($\tau_0 = 2.9 \times 10^{-12}$ s for **2** and $\tau_0 = 1.9 \times 10^{-8}$s for **2d**).

Publication #2 *"Magnetic and optical studies of a new family of multidimensional and multiproperty PO-lanthanide(III) derived systems"* describes a new family of Ln(III) compounds, using an O-donor ligand which should be more suitable for the coordination of lanthanides. The ligand employed in this work, is 1,2-bis(diphenylphosphino)ethane dioxide depicted as $DppeO_2$ (Fig. 30). The use of the corresponding lanthanide nitrate salts in a mixture of MeOH/DMF in the presence of the ligand allowed the isolation of two different topologies, depending on the lanthanide; two-dimensional structures were isolated for Ce (**4**), Sm (**5**) and Dy (**9**) with formula $[Ln^{III}(dppeO_2)_{1.5}(NO_3)_3(H_2O)_{0.5}]_n$, while one-dimensional structures were isolated for Eu (**6**), Gd (**7**) and Tb (**8**) with formula $[Ln^{III}(dppeO_2)(NO_3)_3DMF]_n$.
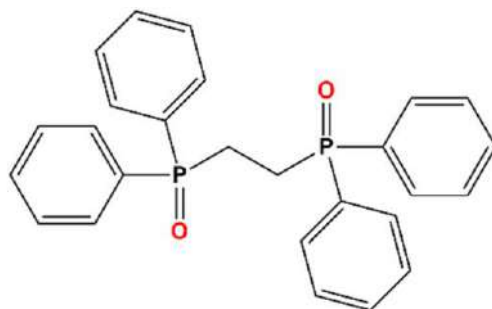
Figure 30: Structural formula of the ligand DppeO$_2$.

The structures of **4**, **5** and **9** consist of a 2D layer Ln^{III} cations linked by bis-monodentate phosphine oxide ligands. The coordination sphere of the Ln^{III} cations are completed by three chelating nitrato ligands, three O-donor atoms from the dppeO$_2$ ligands and one terminal water molecule. The coordination geometry of the cations is an intermediate between a capped octahedron and a capped trigonal prism, as revealed from SHAPE measurements. On the other side, the structures of **6**, **7** and **8** consist of a 1D arrangement of Ln^{III} cation bridged by bis-monodentate dppeO$_2$ ligands. Three chelating nitrato ligands, two O-donors from two dppeO$_2$ ligands and one DMF molecule complete the coordination environment of the cations, leading to a coordination number of nine. Partially labelled plot for the coordination environment of Ce^{III} and for the Gd^{III} complex is shown in Fig. 31.
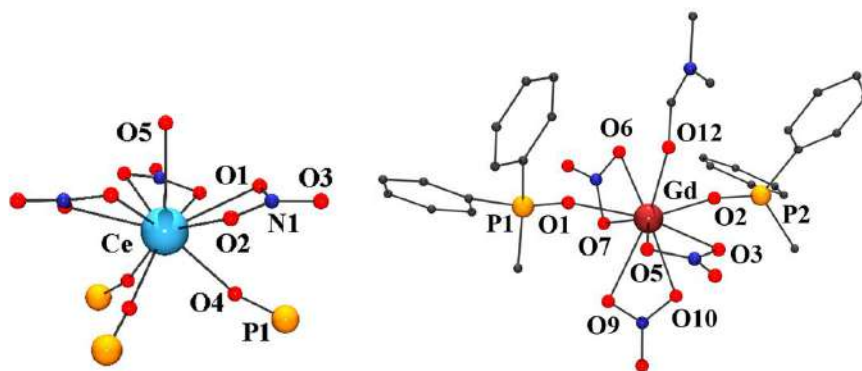
Figure 31: Partially labelled plot for the coordination environment of Ce^{III} (left) and for the structure of Gd^{III} complex (right).

Magnetic measurements were carried out for compounds **4**, **7**, **8** and **9**. The topology of the above mentioned structures dictated that the treatment of the data should be done by considering the complexes as mononuclear compounds. The $\chi_M T$ product for **4**, **8** and **9**

were close to the corresponding values for the isolated lanthanide cations: $^2F_{5/2}$ (Ce^{III}, 0.80 cm^3 mol^{-1} K), $^7F_6$ (Tb^{III}, 11.82 cm^3 mol^{-1} K), and $^6H_{15/2}$ (Dy^{III}, 14.17 cm^3 mol^{-1} K), respectively. The decay of the susceptibility at lower temperatures that observed for these compounds was due to the depopulation of the Stark sublevels. A more pronounced decay was observed below 50 K probably due to intramolecular antiferromagnetic interactions. For complex **4**, the $\chi_M T$ product follows a Curie law, as expected for the isotropic Gd^{III} cation.

Alternate current measurements revealed that none of the complexes behave as SIM in the absence of magnetic field. Complexes **4** and **8** showed weak tails of out-of-phase signals, but well defined peaks were present for complex **9** in the range of 0.1-0.6 T. Thus, **9** could be considered as a field-induced SIM. Analysis of the data using the generalized Debye model revealed that two different relaxation pathways were present: Orbach and Raman. The energy barrier was found to be 21.77 K while $\tau_0 = 2.0 \times 10^{-7}$ s, while the α parameter was 0.06 indicating a narrow distribution of relaxation times. Also, in order to demonstrate the lattice intervention in the magnetic relaxation, ultra-low Raman measurements have been performed and the spectrum evidenced the presence of low frequency vibrations which were compatible with the energy required the spin-phonon relaxation path. Finally, complexes **5**, **6** and **8** were measured in terms of luminescence showing good emission properties in the visible range.

Publication #3 *"Field-Induced Slow Magnetic Relaxation in a New Family of Tetranuclear Double-Stranded Cu_2^{II}-Ln_2^{III} Metallohelicates"* describes the synthesis and characterization of a series of tetranuclear $Cu_2^{II}Ln_2^{III}$ double-stranded metallohelicates using a bis-bidentate ligand derived by the condensation of o-vanillin and 4,4'-oxydianiline. In this case, the chosen organic ligand is the Schiff base 2-(((4-(4-((2-(oxido)-3-methoxybenzylidene)amino)phenoxy)phenyl)-imino)methyl)-6-methoxyphenolato abbreviated as H_2L2 (Fig. 32); it contains two sets of three donor atoms separated by a flexible spacer. Also, it provides two coordination pockets at each end, enable the coordination of two cations that can be bridged by the phenolato bridges. Thus, the reaction of H_2L2 with [$Cu_2(CH_3COO)_4(H_2O)$] and further with nitrate salts of Ln(III) led to the isolation of a series with {$Ln_2^{III}Cu_2^{II}(L2)_2$} skeleton, where Ln = La (**10**), Ce (**11**), Pr (**12**),

Sm (**13**), Gd (**14**), Tb (**15**), Dy (**16**), Ho (**17**), Er (**18**) and Yb (**19**). Complexes **10**, **13**, **14**, **18** and **19** were determined by single-crystal X-ray diffraction. The other members of this family were characterized by means of XRPD and two different kind of complexes were identified: the first consist of complexes **10**, **11**, **12**, **14** and **16** while the other consist of complexes **13**, **15**, **17**, **18** and **19**.
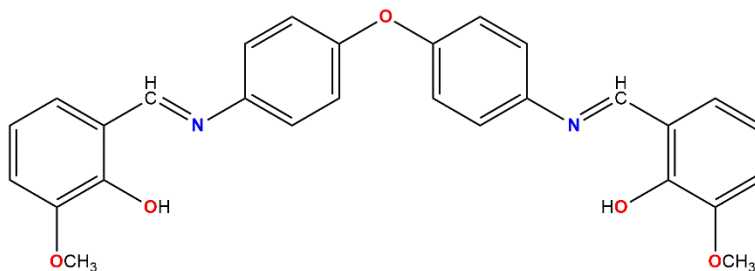
Figure 32: Structural formula of ligand H_2L2.

The formula for complex **10** (Fig. 33) is $[Cu_2La_2(L2)_2(MeOH)_2(NO_3)_6]\cdot 1.5CH_3CN\cdot C_4H_{10}O$. It consists of {$Cu_2La_2$} tetranuclear double-stranded helicate where the four metal ions are held together by two deprotonated $(L2)^{2-}$ ligands. Each Cu^{II} cation is coordinated by one N-iminic atom and one O-phenoxo donor from each ligand, forming a square planar coordination geometry around the cation. Also, La^{III} and Cu^{II} are bridged by the $O_{phenoxo}$ donors. In addition to this, each La^{III} cation is coordinated to two $O_{methoxo}$ donors, three bidentate nitrate anions and one methanol molecule. That leads to a coordination number eleven and a capped pentagonal antiprism coordination geometry, as revealed from continuous shape measurements. Similar structures were observed for **13** (Sm), **14** (Gd), **18** (Er) and **19** (Yb) complexes, however there are some differences which are attributed to lanthanide contraction.
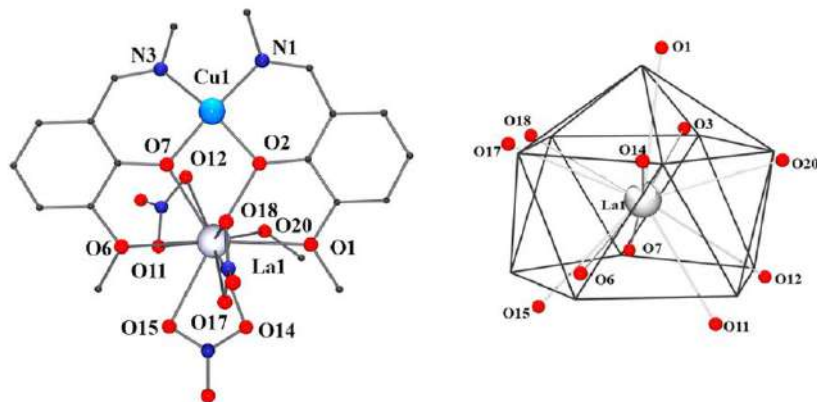
Figure 33: Labeled plot for complex **10** (left) and ideal polyhedron for La cation (right).

Along the series a concomitant decrease of the coordination number was observed. For **10** (La), **11** (Ce) and **12** (Pr) the coordination number is 11 whereas for **13** (Sm) and **14** (Gd) the coordination number decreases to 10, and also the nitrate ligands present a different coordination mode. Furthermore, the case of **18** (Er) present intense interest. The two cations appear in the structure show different environments; Er1 is 10 coordinated while Er2 is 9 coordinated. For Yb derivative, the cation shows similar enneacoordination with Er2.

Direct magnetic measurements were carried out for complexes **11** (Ce), **13** (Sm), **14** (Gd), **15** (Tb), **16** (Dy), **18** (Er) and **19** (Yb). The $\chi_M T$ values were in good agreement with the expected values for two Cu^{II} and two Ln^{III} non-interacting cations. Upon cooling, the susceptibility for **14** and **15** is roughly constant, showing a maximum at 7 K 10 K, respectively. This behavior indicates ferromagnetic interactions. For the other complexes, the $\chi_M T$ values decreases lowering the temperature due to depopulation of the corresponding Stark levels. The exchange interaction J between Cu^{II}-Ln^{III} is positive for Gd, Tb, Dy, Er and Yb analogues and negative for Ce and Sm complexes.

Ac measurements for complexes **14**, **15** and **16** revealed out-of-phase signals under a field of 0.6, 0.3 and 0.5 T, respectively. For complex **14** the energy barrier was found to be 22 K and $\tau_0 = 6 \times 10^{-7}$ s, while the relaxation time for low frequencies and temperature is close to 0.1 s. Fitting of Argand plots for **15** and **16** revealed an energy barrier of 18.8 K for Tb complex with $\tau_0 = 1.2 \times 10^{-8}$ s, and a barrier of 10.9 K with $\tau_0 = 3.46 \times 10^{-7}$ s for Dy.

PUBLICATION #1

"Structural and magnetic studies of mononuclear lanthanide complexes derived from N-rich chiral Schiff bases"

Check for updates

Structural and magnetic studies of mononuclear lanthanide complexes derived from N-rich chiral Schiff bases†

E. Pilichos,[a] M. Font-Bardia, [ID][b] A. Escuer [ID] *[a] and J. Mayans [ID] *[c]

A new family of mononuclear lanthanide complexes with the formula [Ce^{III}(L)(NO$_3$)$_3$(MeOH)] (**1**) and [Ln^{III}(L)(NO$_3$)$_3$]·MeOH where Ln = Gd (**2**) or Dy (**3**) and L = *N,N'*-bis(pyridin-2-ylmethylene)cyclohexane-1,2-diamine has been obtained with the use of enantiomerically pure Schiff bases. Dynamic magnetic studies indicate that **1–3** present field-induced slow relaxation of the magnetization and their response has been compared with the magnetically diluted complexes **2d** and **3d**. Structural studies have been carried out by single crystal X-ray and powder diffraction.

Introduction

The coordination chemistry of lanthanide(III) ions has recently attracted the interest of the scientific community for different reasons like their ability to form oligo- and polynuclear metal complexes (coordination clusters) with unique and aesthetically attractive structures, their unusual luminescence properties resulting from the forbidden f–f electronic transitions that emerge when organic ligands are coordinated with 4f metal ions, the so-called antenna effect, and their essential role in the development of efficient single-molecule magnets (SMMs) due to their single-ion anisotropy.[1–3] The discovery by Ishikawa and co-workers[4] that a terbium–phthalocyaninate complex is magnetically bistable up to 30 K opened a new horizon in the field of molecular magnetism and offered a wide pathway for new studies. It was soon realized that this remarkable magnetic behaviour is attributed to the large magnetic moment of Tb^{III} ($^7F_6$ in the ground state) and to the strong easy axis type single ion anisotropy which it assumes in a specific coordination environment. This leads to a large effective anisotropy energy barrier, U_{eff}, for the reversal of the magnetization. However, in the past few years, many reports

pointed out that the presence of a large anisotropy barrier is not enough to increase the relaxation time in all the temperature range, because of the competition between relaxation processes, *e.g.* Raman and direct one.[5,6]

Among this, the capricious geometries around the lanthanide(III) spin carrier in these molecular systems result in the apparition of rhombic anisotropy (*E*) which allows the occurrence of quantum tunneling of magnetization (QTM) relaxation which compromises their efficiency as SMMs.[7–9]

To date, many lanthanide coordination complexes have been reported to show slow relaxation of the magnetization, as probed by ac measurements using a SQUID magnetometer, either with or without the presence of an external applied field. Among lanthanide-derived systems, complexes based on Dy^{III} have been the most studied cases due to its large magnetic moment ($^6H_{15/2}$ in the ground state) and due to its Kramers ion nature, which ensures the degeneracy of the two lowest lying levels and reduces the possibility of QTM.[9–13] However, any paramagnetic lanthanide(III) ion (Eu^{III} is the exception because of its non-magnetic ground state, $^7F_0$) can show slow relaxation of the magnetization under appropriate conditions as was proposed recently by Rinehart *et al.*,[14] who postulated a qualitative model where the electronic density around the lanthanide ion plays a pivotal role which could effectively enhance the single-ion anisotropy. Following this approach, many publications can be found in the literature with the so called "uncommon lanthanides" in molecular magnetism, which include the light lanthanides Ce^{III} and Nd^{III} with low magnetic moments, but also the non-Kramers Ho^{III} or Yb^{III}, for which, even its high anisotropic character, a scarce number of SMMs have been reported.[15]

Taking into advantage our previous experience on the chemistry of compartmental and tetradentate Schiff bases with lanthanides,[16,17] we synthesized a new family of mononuclear

[a]*Departament de Química Inorgànica i Orgànica, Secció Inorgànica and Institute of Nanoscience (IN²UB) and Nanotecnology, Universitat de Barcelona, Marti i Franques 1-11, Barcelona-08028, Spain. E-mail: albert.escuer@qi.ub.edu*
[b]*Departament de Mineralogia, Cristal·lografia i Dipòsits Minerals and Unitat de Difracció de R-X, Centre Científic i Tecnològic de la Universitat de Barcelona (CCiTUB), Universitat de Barcelona, Solé i Sabarís 1-3, 08028 Barcelona, Spain*
[c]*Instituto de Ciencia Molecular (ICMol), Universidad de Valencia, Catedrático José Beltran 2, 46980 Paterna, Valencia, Spain. E-mail: julia.mayans@uv.es*
†Electronic supplementary information (ESI) available: Structural and magnetic data. CCDC 2043144–2043146. For ESI and crystallographic data in CIF or other electronic format see DOI: 10.1039/d0dt04224b
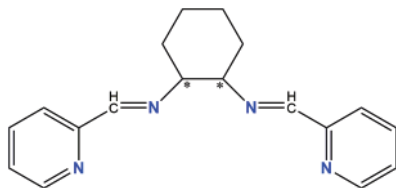
Chart 1 Structural formula of the L ligand employed in this work. Asterisks denote the chiral centres.

lanthanide complexes with the formula $[Ce^{III}(L)(NO_3)_3(MeOH)]$ (**1**) and $[Ln^{III}(L)(NO_3)_3]\cdot MeOH$ for Ln = Gd (**2**) and Dy (**3**) in which L = N,N'-bis(pyridin-2-ylmethylene)cyclohexane-1,2-diamine (Chart 1), obtained by the reaction of the L Schiff base with lanthanide nitrates in methanolic solution. The magnetic dilutions of **2** and **3** Gd@Eu (**2b**) and Dy@Eu (**3b**) were also performed to compare the effect of dilution with Eu^{III} of an isotropic and an anisotropic lanthanide(III) ion in a Ln^{III}/Eu^{III} ratio of ~ 0.2 : 0.8.

The organic chiral ligand L was synthesized by the condensation of two equivalents of 2-pyridinecarboxaldehyde and 1 equivalent of (1R/S,2R/S)-1,2-diamino cyclohexane in methanolic solution. Neutral N-rich Schiff bases (N_4L) have been less employed than the more usual O-rich Schiff bases derived from salicylic or o-vanillin precursors and complexes with the general formula $[Ln(N_4-L)(NO_3)_3]$ or $[Ln(N_4-L)(Cl)_3]$ have been studied from structural,[18–21] catalytic[22] and luminescence[23,24] points of view. However, their magnetic properties remain practically unexplored.[17,25]

Complexes **1–3** have been magnetically studied and the dynamic magnetic measurements revealed that they present field-induced slow relaxation of the magnetization. These results were expected for the highly anisotropic Dy^{III} derivative with a high magnetic moment, but demonstrate that Ce^{III}, with its lonely 4f electron ($^2F_{5/2}$ in the ground state), which yields a low magnetic moment, allows enough spin–orbit coupling to present relevant magnetic anisotropy of its ground $J = 5/2$ state, is not that "uncommon" as a building block for field-induced SMMs[15,25–27] and that also the non-anisotropic member of the lanthanide family, Gd^{III}, is becoming a regular source of SMM systems.[28–34] The effect of magnetic dilution on the relaxation mechanisms for an isotropic cation (Gd^{III} (**2**)) and one isostructural anisotropic system (Dy^{III} (**3**)) has been studied by comparison of the out-of-phase response of the diluted compounds **2d** and **3d**.

Experimental

X-ray crystallography

Single crystal structural determination was selectively performed for the complexes that exhibit ac response. Colourless prism-like specimens of **1SS**, **2SS** and **3RS** were used for the X-ray crystallographic analysis. The X-ray intensity data were collected using a D8 Venture system equipped with a multilayer monochromator and a Mo microfocus (λ = 0.71073 Å).

Table 1 Crystal data, collection and structure refinement details for the X-ray structure determination of complexes **1SS**, **2SS** and **3RS**

	1SS	2SS	3RS
Formula	$C_{19}H_{24}CeN_7O_{10}$	$C_{19}H_{24}GdN_7O_{10}$	$C_{19}H_{24}DyN_7O_{10}$
FW	650.57	667.70	672.95
System	Monoclinic	Triclinic	Triclinic
Space group	$P21$	$P1$	$P\bar{1}$
a/Å	8.5057(6)	9.5580(9)	9.5045(8)
b/Å	15.531(1)	11.459(1)	11.409(2)
c/Å	9.3697(7)	11.665(1)	11.664(1)
α/°	90	108.182(3)	108.073(3)
β/°	101.896(3)	90.985(3)	90.811(3)
γ/°	90	91.903(3)	92.020(4)
V/Å^3	1211.2(2)	1212.6(2)	1201.2(2)
Z	2	2	2
T, K	100(2)	100(2)	100(2)
Θ range/°	2.447–30.647	3.612–30.624	2.145–30.579
Reflex. collected	24 066	36 000	43 858
Reflex. indep.	7171	13 994	7383
Parameters	335	634	329
λ(MoKα), Å	0.71073	0.71073	0.71073
ρ_{calc}, g cm^{-3}	1.784	1.829	1.861
μ(MoK$_\alpha$), mm^{-1}	1.948	2.803	3.180
Flack parameter	0.007(6)	0.036(1)	—
R	0.0204	0.0183	0.0402
ωR^2	0.0374	0.0429	0.0937

The frames were integrated with the Bruker SAINT software package using a narrow-frame algorithm. The structure was solved and refined using the Bruker SHELXTL Software Package.[35] Crystal data and refinement details are summarized in Table 1. Further crystallographic details can be found in the corresponding CIF files provided in the ESI.†

Powder X-ray diffraction was performed with a PANalytical X'Pert PRO MPD θ/θ powder diffractometer of 240 millimetres of radius, in a configuration of convergent beam with a focalizing mirror and a transmission geometry with flat samples sandwiched between low absorbing films and Cu Kα radiation (λ = 1.5418 Å). Comparison between the calculated spectrum from the single crystal structure of **2** and the experimental spectra for the diluted compounds **2d** and **3d** confirms the isostructurality among them, Fig. S1.†

Physical measurements

Magnetic susceptibility measurements were carried out on pressed polycrystalline samples with a MPMS5 Quantum Design susceptometer working in the range 30–300 K under a magnetic field of 0.3 T and under a field of 0.03 T in the 30–2 K range to avoid saturation effects at low temperature. Diamagnetic corrections were estimated from Pascal tables. Infrared spectra (4000–400 cm^{-1}) were recorded from KBr pellets on a Bruker IFS-125 FT-IR spectrophotometer. ECD spectra were recorded in methanolic solutions using a Jasco-815 spectropolarimeter.

Syntheses

L ligand. The synthesis was accomplished by reaction of 2-pyridincarboxaldehyde (0.107 g per mmol) and the corresponding isomer of 1,2-diaminocyclohexane (0.057 g per

0.5 mmol) dissolved in 10 mL of MeOH and kept with continuous stirring for 30 minutes at room temperature. The dissolution was employed directly to synthesize the derived complexes without isolation of the solid ligand. Similar syntheses were previously reported.[17,36]

[Ce(L)(NO$_3$)$_3$(MeOH)] (1) and **[Ln(L)(NO$_3$)$_3$]·MeOH, Ln = Gd (2) and Dy (3)**. The corresponding lanthanide nitrate salt (0.5 mmol) was added to the previously prepared ligand. The resulting solution was left under stirring for two hours at room temperature. The complexes precipitate as a yellow powder that was collected in high yield (~70%), filtered and washed with cold diethylether (2 × 3 mL). Yellowish prism-like crystals suitable for X-ray diffraction were obtained after a few days by layering the filtrate with diethylether.

The diluted complexes **2d** and **3d** were prepared following the same procedure but starting from europium nitrate and gadolinium or dysprosium nitrate (0.4 : 0.1 mmol).

The cation ratio for the diluted complexes was determined from the comparison of their magnetic moments resulting in Eu$_{0.84}$Gd$_{0.16}$ and Eu$_{0.82}$Dy$_{0.18}$ for **2d** and **3d**, respectively. Calculated/found elemental analysis for **1** C, 35.08/35.2; N, 15.07/15.1; H, 3.72/3.8%; for **2** C, 34.17/34.0; N, 14.68/14.5; H, 3.62/3.7%; for **3** C, 33.91/34.1; N, 14.57/14.4; H, 3.59/3.6%. Selected IR peaks for all compounds (KBr, cm^{-1}): 3400(b), 2937(w), 1647(m), 1595(s), 1483(s), 1384(s), 1017(m), 782(m), 636(m), ESI, Fig. S2.†

Results and discussion

Description of the structures

The structures of the complexes **1SS**, **2SS** and **3RS** were determined by single crystal X-ray diffraction. The Gd^{III} and Dy^{III} complexes are isostructural and to avoid repetitive text only the Gd^{III} compound will be described.

[Ce(L)(NO$_3$)$_3$(MeOH)] (1SS). A partially labelled plot of **1SS** is shown in Fig. 1 top. Selected bond parameters and angles are summarized in Table 2. The structure of **1SS** consists of a neutral mononuclear complex of Ce^{III}, in which the cation links one neutral tetradentate L ligand, three bidentate nitrato ligands and one methanol molecule, resulting in an 11-coordinated environment.

The four N-donor atoms from the organic ligand L are coordinated to the central cation with Ce–N bond distances in the narrow 2.657(3)–2.721(3) Å range. Three bidentate chelate nitrato and the methanol ligands complete the coordination sphere of the cation with Ce–O bond distances comprising between 2.555(2) and 2.733(2) Å. The Ce^{III} environment is severely distorted due to the low bite angle of the organic ligand and the nitrato groups: the N–Ce–N bond angles between the neighbouring N-donors show values comprised between 62.30(9) and 59.99(8)° and the O–Ce–O bond angles for each nitrate are close to 48°. SHAPE[37] calculations indicate that the closer coordination polyhedron around the Ce^{III} cation is an intermediate between the ideal C_{5v} capped pentagonal prism and antiprism (Fig. 1 and Table S1†) with a large
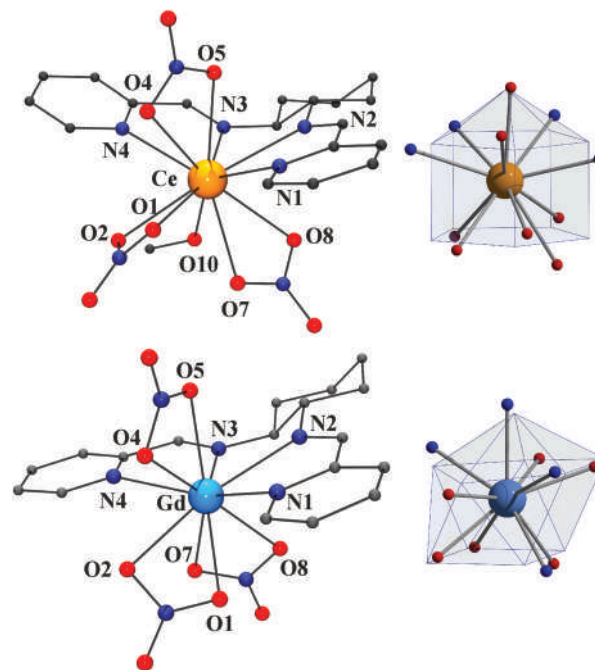
Fig. 1 Partially labelled plots and the ideal coordination polyhedron *vs.* real donor sites for the Ce^{III} (**1**) (top) and Gd^{III} (**2**) (bottom) complexes. The Dy^{III} complex **3** is isostructural to **2**. Colour key for all figures: Ce^{III} orange, Gd^{III} light blue, O red, N navy and C grey.

Table 2 Selected bond distances (Å) and angles (°) for complexes **1SS**, **2SS** and **3RS**

	1SS Ln = Ce	**2SS** Ln = Gd	**3RS** Ln = Dy
Gd(1)–O(1)	2.684(2)	2.540(4)	2.535(5)
Gd(1)–O(2)	2.583(2)	2.525(4)	2.487(4)
Gd(1)–O(4)	2.601(2)	2.454(5)	2.441(3)
Gd(1)–O(5)	2.733(2)	2.496(5)	2.458(4)
Gd(1)–O(7)	2.625(2)	2.481(4)	2.449(3)
Gd(1)–O(8)	2.656(2)	2.479(5)	2.475(3)
Ln(1)–O(10)	2.555(2)	—	—
Gd(1)–N(1)	2.657(3)	2.578(5)	2.551(4)
Gd(1)–N(2)	2.706(3)	2.562(5)	2.503(4)
Gd(1)–N(3)	2.657(3)	2.506(4)	2.473(5)
Gd(1)–N(4)	2.721(3)	2.604(6)	2.554(4)
O(1)–Gd(1)–O(2)	48.35(6)	51.1(1)	50.2(1)
O(4)–Gd(1)–O(5)	47.56(6)	51.6(2)	51.9(1)
O(7)–Gd(1)–O(8)	48.34(7)	51.2(2)	51.4(1)
N(1)–Gd(1)–N(2)	62.30(9)	63.3(2)	64.2(2)
N(2)–Gd(1)–N(3)	59.99(8)	64.8(2)	64.8(2)
N(3)–Gd(1)–N(4)	61.03(9)	64.8(2)	65.4(1)

CShM due to the strong distortion generated by the low bite of the nitrato ligands and the neighbour N-donor atoms from the Schiff base.

The molecules are well isolated in the network (a minimum Ce···Ce distance of 8.506(1) Å), the only intermolecular contacts being the weak CH···O H-bonds established between the aromatic rings and the O-atoms from the nitrato ligands of the neighbouring molecules.

[Gd(L)(NO$_3$)$_3$]·MeOH (2SS) and **[Dy(L)(NO$_3$)$_3$]·MeOH (3RS)**. A partially labelled plot of **2SS** is shown in Fig. 1, bottom.

Selected bond parameters and angles for **2SS** and **3RS** are summarized in Table 2. The structure of **2SS** consists of a mononuclear neutral Gd^III complex which crystallized in the *P*1 triclinic system. The unit cell contains two crystallographically non-equivalent molecules (labelled A and B) with slight deviations in bond parameters and angles. The discussion of the structural details will be referred to molecule A. The structure of **2SS** consists of neutral mononuclear complexes of Gd^III, in which the cations link one tetradentate L ligand and three bidentate nitrato ligands, resulting in a decacoordinated environment. The four N-donor atoms from the organic ligand L are coordinated to the central metal ion with Gd–N bond distances ranging from 2.506(4) to 2.604(6) Å. Gd–O bond distances are comprised between 2.454(5) and 2.540(4) Å, slightly shorter than the Gd–N ones. The Gd^III environment is also distorted: the N–Gd–N bond angles between the neighbouring N-donors show values around 64° and the O–Gd–O bond angles for each nitrate are close to 51°. SHAPE[37] calculations indicate that the closer coordination polyhedron around the Gd^III cation is an ideal sphenocorona (Fig. 1) (C_{2v}, CShM = 3.05, Table S1†) with a relatively large CShM.

Because of the presence of methanol solvent and the accessible O-donors from the nitrate groups, there are intermolecular H-bonds promoted by MeOH···$O_{nitrate}$ contacts with O···O distances in the range of 2.8–2.9 Å. The structure does not present direct contacts between the complexes and the minimal intercluster Gd···Gd distance is 8.085(1) Å showing a good isolation of the clusters.

The comparison between the three structures shows the gradation of the bond distances according to the reduction of the cationic radius from Ce^III to Dy^III. For complexes **2** and **3**, two nitrato ligands are placed in an axial arrangement, roughly perpendicular to the Schiff base main plane, whereas the addition of an extra ligand (MeOH) in the coordination sphere of the Ce^III complex displaces one of the nitrato ligands and this steric hindrance induces the folding of the ligand resulting in a dihedral angle of 145.9(3)° between the aromatic rings, Fig. 2. This distortion displaces the Ce^III cation 0.878(1) Å out of the plane defined by the four N-donors of the organic ligand.

Electronic circular dichroism

Chirality transfer is a common feature when using enantiopure chiral ligands in coordination compounds;[38–40] however, transference of chirality from the chiral ligand to the metallic centres is poor in this case and the differences around the lanthanide cation are limited to the relative torsion of the nitrato groups and thus, the chiroptical properties must be mainly related to the ligands due to the π–π* transitions of the aromatic rings as was reported for the related complexes [Ln(L′)Cl₃] (L′ = *N,N′*-bis((1,2-diphenyl-(pyridine-2-yl)methylene)-(*R,R/S,S*)-ethane-1,2-diamine).[17] ECD spectra in methanolic solution were recorded for the representative enantiomeric pairs of **2RR** and **2SS**, respectively, Fig. 3 and their mirror image confirms the enantiomeric nature of the reported complexes. The spectrum exhibits a positive Cotton effect at λ_{max} =
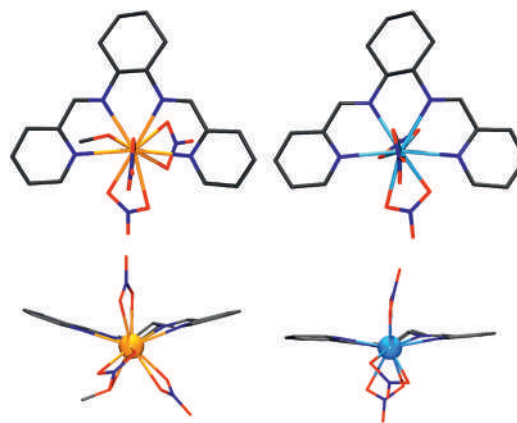
Fig. 2 Axial view of complexes **1** (left) and **2** (right) showing the relative position of the nitrato ligands as a function of the coordination number and the arrangement of the Schiff base.
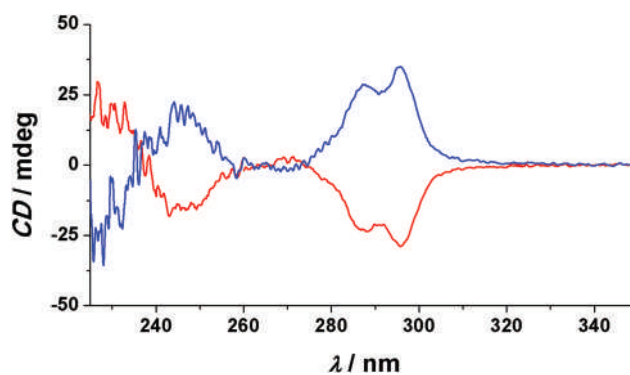
Fig. 3 Solution ECD spectra for the Eu^III pair of complexes **2RR** (red line) and **2SS** (blue line).

295, 287(sh) and 246 nm and a negative band at 270 nm for **2RR** and the same bands with opposite sign for **2SS**.

Magnetic properties

Static measurements. The magnetic susceptibility measurements for the compounds in the form of $\chi_M T$ product *vs.* temperature were performed on polycrystalline samples in the range of 2–300 K. On cooling, the $\chi_M T$ values decrease from room temperature for the Ce^III complex **1** and below 50 K for the Dy^III (**3**) derivative due to the depopulation of the Stark sublevels of the anisotropic Ln^III cations. Magnetization measurements show unsaturated values at the maximum explored field of 5 T, which are in good agreement with the corresponding *J* and *g* values, Fig. S3.†

The isotropic Gd^III complex (**2**) (⁸S_{7/2}, *g* = 2.00, 7.875 cm³ mol⁻¹ K) shows a Curie law response with a constant $\chi_M T$ value of 7.6 cm³ mol⁻¹ K in the full range of temperatures that agrees with the expected value for an *S* = 7/2 spin. Magnetization tends to the expected value of 7.04*N*μ_β Fig. 4, left. Reduced magnetization measurements between 1.8 and
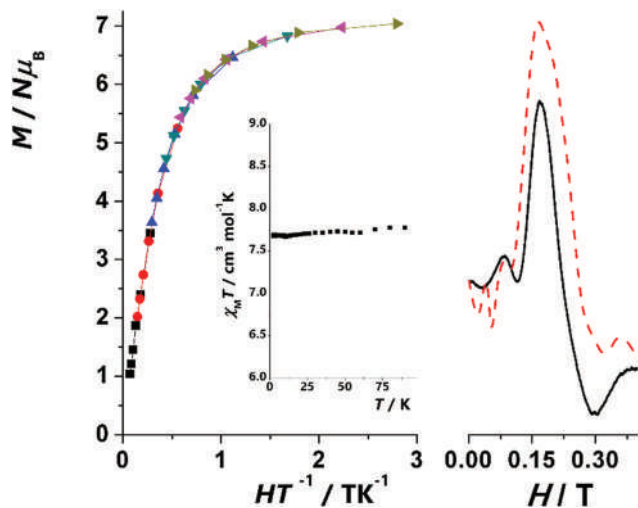
Fig. 4 Left, reduced magnetization for complex **2** measured between 1.8 and 6.8 K with increments of 1 K. Inset, $\chi_M T$ *vs.* temperature. Right, the X-band EPR spectrum for complex **2**. The dashed line shows the simulated spectrum.

Fig. 5 Left, $\chi''_M f(T)$ plots for compound **1**. Right, Argand plot for **1**, (solid lines show the fit of the experimental data).

6.8 K show superimposable plots indicating negligible anisotropy.

However, susceptibility or magnetization measurements are not adequate to determine weak anisotropy for low spin values as is the case of Gd^{III} ($S = 7/2$) that in contrast can be precisely determined by means of the more sensitive EPR spectroscopy. The X-band spectra of complex **2** are far from the single $g \approx 2.00$ band characteristic of an isotropic cation, showing several absorptions at $g = 6.8$, 3.1 and 1.69 that can be simulated with a zero field splitting parameter of 0.07 cm^{-1}, Fig. 4, right. The spectrum for the diluted compound **2d** shows the same absorptions with a sharper linewidth as a result of the reduction of the dipolar interactions, confirming the identical environment around the Gd^{III} cation between the pure and diluted complexes, Fig. S4.†

Dynamic measurements. Preliminary alternate current measurements showed that any of the complexes exhibits out-of-phase response in zero field. Scan of the response under different applied dc fields (Fig. S5†) revealed defined peaks for the Ce^{III}, Gd^{III} and Dy^{III} complexes.

Frequency-dependent susceptibility for the Ce^{III} compound **1** was analysed by applying a dc field of 0.2 T in the 500–1500 Hz range of frequencies at which complete maxima were defined (Fig. 5 and S6†). An Arrhenius dependency fit was firstly used to calculate the relaxation time (τ_0) and the effective relaxation energy barrier (U_{eff}) by means of the equation

$$\ln(2\pi\omega) = \ln(1/\tau_0) - U_{eff}/K_B T$$

which supposes the so-called Orbach relaxation which involves two phonons in the spin–lattice relaxation through real states and yield the best fitting values of U_{eff} of 17.0 K and a τ_0 value of 3.9×10^{-8} s. Using the data extracted from the fitting of the Argand plot for **1**, the relaxation parameters yield a value of
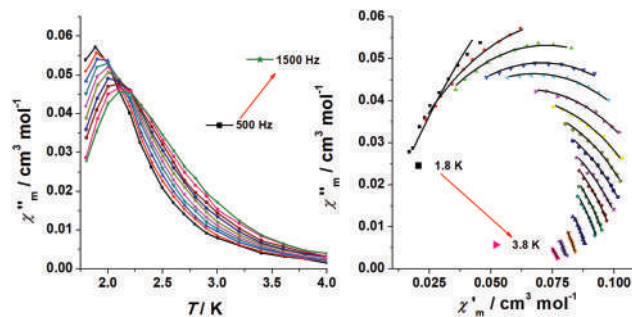
13.6 K and a τ_0 value of 3.2×10^{-7} s, confirming the occurrence of only one relaxation process in this temperature range (Fig. 5 and S7†) with alpha values ranging from 0.16 to 0.34 between 2 and 4 K indicating a wide distribution of the relaxation times of the observed relaxation process.

Alternate current susceptibility measurements for the dysprosium derivative **3** were performed under a field of 0.1 T in the 10–1500 Hz range of frequencies showing well-resolved $\chi''_M(T)$ peaks for frequencies above 39 Hz, Fig. 6 left. At low temperature, the χ''_M peaks overlap with a relaxation process effective below 2 K that corresponds to a QTM relaxation. The Arrhenius fit of the peak maxima for the larger frequencies yielded $U_{eff} = 30.6$ K and $\tau_0 = 7.2 \times 10^{-7}$ s.

The $\ln(\tau)$ *vs.* T^{-1} plot shows an almost linear Arrhenius dependence that deviates from linearity at low temperatures in agreement with the presence of a different process. Analysis of the semi-circular Argand plot gives α values ranging between
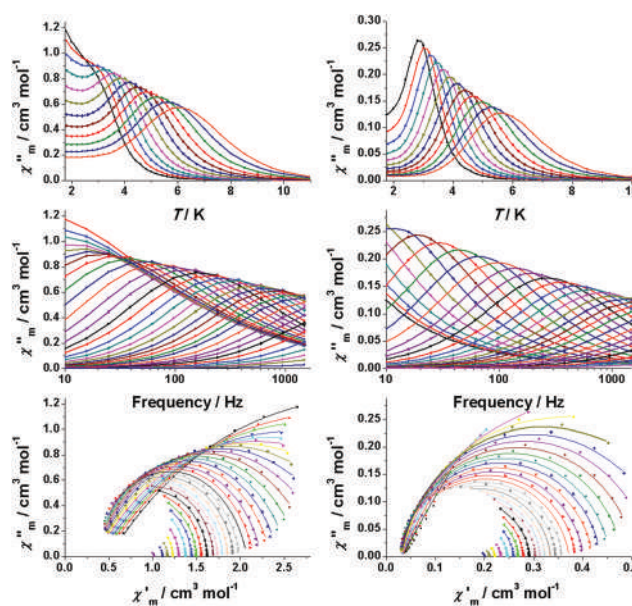
Fig. 6 Dependence of out-of-phase susceptibility for complexes **3** (left) and the diluted compound **3d** (right) measured under a dc field of 1000 Oe.

0.04 and 0.46 (1.8–7.6 K), suggesting a wide distribution of the relaxation times in this temperature range.

Generalized Debye fitting of the relaxation times obtained for the larger temperatures gives the close values of U_{eff} = 30.6 K and $\tau_0 = 9.7 \times 10^{-7}$ s.

In order to analyse the effect of the dipolar interactions in **3**, the diluted sample **3d** in a $Eu^{III}_{0.82}/Dy^{III}_{0.18}$ ratio was studied under the same conditions (field 0.1 T, 10–1500 Hz), Fig. 6, right. It is noteworthy that the only difference between the pure and diluted samples was the better definition of the out-of-phase peaks in the $\chi''_M(T)$ plot for the whole range of frequencies, including the lower ones, due to the suppression of the low T QTM process. The Arrhenius fit of the $\chi''_M(T)$ peak position of the larger frequencies yielded U_{eff} = 34.6 K and $\tau_0 = 2.4 \times 10^{-7}$ s in agreement with the fit of relaxation times obtained from the $\ln(t)$ fit for the larger temperatures of the Argand plot, that gives U_{eff} = 32.4 K and $\tau_0 = 4.9 \times 10^{-7}$ s. The α values varying between 0.05 and 0.32 show a shorter variation range than complex **3**.

It is important to note that the values of the effective relaxation barrier for complexes **1**, **3** and **3d** are by far lower than the usual first excited state of the Ln^{III} cation, and an over-barrier relaxation is not allowed which is a common feature in field-induced SMM lanthanide systems meaning that the Orbach process parameters given above can only be taken as a first approach.

It is noteworthy that the Gd^{III} complex **2** and its diluted analogous **2d** exhibit strong out-of-phase signals despite its spherical electronic distribution and its *a priori* isotropic character.

The response of the two systems as a function of the transverse field was studied between 0 and 1 T for selected low (LF, 10 Hz) and high (HF, 1488 Hz) frequencies to choose the optimal field for the $\chi''_M(T)$ measurements.

The complexes do not show signals in zero field but the measurements reveal a strong field-dependence, and a continuous shift of the signals for the increasing field with a fast increase of intensity with a maximum around 5000 G, decreasing gradually for larger fields, Fig. 7. Remarkably, this continuous shift differs from the usual response of anisotropic systems for which the shift and intensity of the out-of-phase signals have a limit corresponding to the optimal QTM suppression.

The $\chi''_M(T)$ measurements for **2** in the frequency range of 1–1488 Hz were performed under a field of 4000 G. The $\chi''_M(T)$ plot clearly shows two HF/LF processes with an intermediate region with a minimal signal intensity at around 100 Hz, Fig. 8, left. The HF signal is clearly temperature dependent following an Arrhenius law with a short $\tau_0 = 2.9 \times 10^{-12}$ s and a U_{eff} barrier of 82 K that overcome in orders of magnitude the barrier ($DS^2 - 1/4 = 0.6$ cm^{-1}) derived from the small D value calculated from EPR measurements. In contrast, the LF peaks are poorly dependent on the frequency. Peak maxima in $\chi''_M(\omega)$ are out of the limits of the recorded frequencies indicating a short relaxation time for the HF process and a large relaxation time for the LF process.
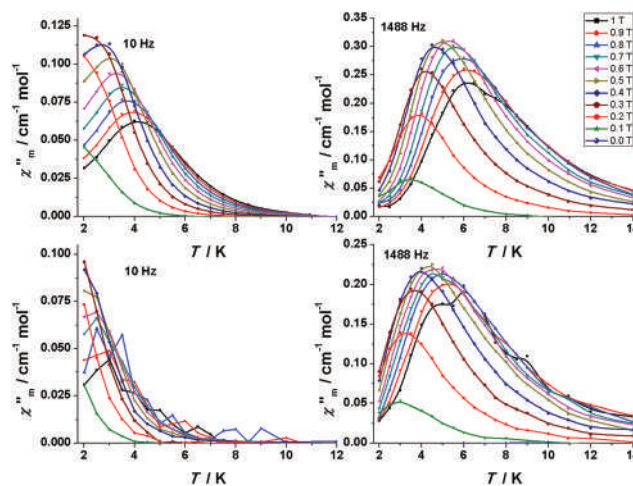
Fig. 7 Dependence of LF and HF out-of-phase susceptibility for complex **2** (top) and the diluted compound **2d** (down) measured in the field range 0–1.0 T.
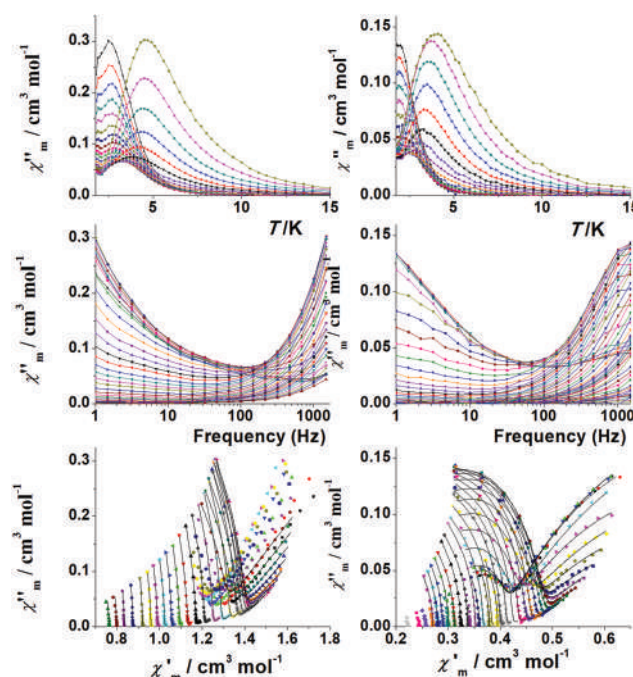
Fig. 8 Dependence of out-of-phase susceptibility for complexes **2** (left) and the diluted compound **2d** (right) measured under a dc field of 4000 Oe.

Measurements for the diluted compound **2d** show a similar response: HF/LF processes also appear in the $\chi''_M(T)$ plot but shifted to a lower temperature, Fig. 8, right. The temperature dependence of the HF process gives $\tau_0 = 1.9 \times 10^{-8}$ and an U_{eff} barrier of 34 K. As a consequence of the peak shift, the HF process is better defined in the $\chi''_M(\omega)$ plot suggesting larger relaxation times than the concentrated Gd^{III} complex **2**. The fit of the relaxation time *vs.* temperature effectively yields larger τ values for similar U_{eff} values of 13.3 K (**2**) or 10.6 K (**2d**).

The isostructurality between the compounds **2**, **2d**, **3** and **3d** allows the comparison in a rigorously identical coordination and network environment between one anisotropic Dy^{III} complex and the analogous Gd^{III} isotropic complexes. Summarizing the above results, Fig. 9, we observed that for the Dy^{III} complex **3** QTM is efficiently suppressed by a magnetic dilution due to the reduction of the dipolar interactions and due to the application of a transverse dc field, whereas the U_{eff} barrier and the relaxation times remain practically unaltered as could be expected for the cation in the same environment.

In contrast, the response of the Gd^{III} system is completely different: the apparent U_{eff} barrier calculated from the maxima of the $\chi''_M(T)$ plot (HF region) is very different from the diluted sample and the analysis of the relaxation times from the fit of the Argand plots shows similar barriers but a clear enlargement of the relaxation times.

SIM response is not expected for a fully isotropic Gd^{III} cation that must behave like a paramagnet but a weak D is induced in a strongly distorted environment. EPR measurements become crucial to determine the D parameter because D values in the 0.1–0.2 cm^{-1} range cannot be detected by susceptibility or magnetization experiments. Low D values are not able to generate conventional SIM/SMM systems because the barrier derived from the double-well takes values around 1 cm^{-1} which are orders of magnitude lower than the experimentally calculated barriers. Thus, QTM and over-barrier relaxation must be excluded meaning that the unusual SIM response for this cation can be related to its weak anisotropy that broke the degeneration of the $S = 7/2$ level mixing the m_s sublevels under moderate (∼0.5 T) external fields. This hypothesis for the origin of the slow relaxation of the magnetization was suggested by S. Gao *et al.*[30] stating that in the Gd^{III} systems, the D value of 0.1 cm^{-1} allows this separation that the

phonon needs to interact with the spin system, promoting a slow relaxation of the magnetization for a quasi-isotropic system. The occurrence of lower or higher values of D enables the apparition of spin–phonon relaxation, and this is what probably occurs in Gd systems which present field-induced slow relaxation of the magnetization.[31,32]

Conclusions

This paper presents the structure and magnetic characterization of a lanthanide series of complexes built from a Schiff base with a set of four N-donors. The characterization of three new induced SIMs with Dy^{III} and the unusual lanthanide cations Ce^{III} and Gd^{III} is remarkable. Single crystal and powder X-ray diffraction evidence isostructurality between the Dy^{III} and Gd^{III} complexes and with their magnetically diluted analogues. The comparison between the pure [Ln^{III}(L)(NO$_3$)$_3$] and the magnetically diluted (Ln^{III}/Eu^{III} ratio ∼0.2/0.8) shows the completely different behaviours of two isostructural systems and their dilutions, one derived from a highly anisotropic lanthanide and the other derived from the isotropic one. Even at the end, the result for both cases is the observation of the fingerprint of the SIM response in the ac measurements, the ultimate mechanism through this process is absolutely different for Dy^{III} and Gd^{III} due their opposite natures. This fact emphasizes the need for more detailed studies on Gd^{III} complexes to finally elucidate the ultimate origin of its relaxation, which is until today unexplained.

Conflicts of interest

There are no conflicts to declare.

Fig. 9 Top, Arrhenius plot (left) for the HF region from the $\chi''_M(T)$ data and ln(τ) vs. T^{-1} from the Argand plots (right) for the Dy^{III} compounds **3** (black) and **3d** (red). Down, the Arrhenius plot (left) for the HF region from the $\chi''_M(T)$ data and ln(t) vs. T^{-1} from the Argand plots (right) for the Gd^{III} compounds **2** (black) and **2d** (red).

Notes and references

1 J. Tang and P. Zhang, *Lanthanide Single Molecule Magnets*, Spriner Berlin Heidelberg, Berlin, Heidelberg, 2016.
2 D. Gatteschi, R. Sessoli and J. Villain, *Molecular nanomagnets*, Oxford University Press, 2006.
3 L. Sorace, C. Benelli and D. Gatteschi, *Chem. Soc. Rev.*, 2011, **40**, 3092.
4 N. Ishikawa, M. Sugita, T. Ishikawa, S. Koshihara and Y. Kaizu, *J. Am. Chem. Soc.*, 2003, **125**, 8694.
5 R. J. Blagg, L. Ungur, F. Tuna, J. Speak, P. Comar, D. Collison, W. Wernsdorfer, E. J. L. McInnes, L. F. Chibotaru and R. E. P. Winpenny, *Nat. Chem.*, 2013, **5**, 673.
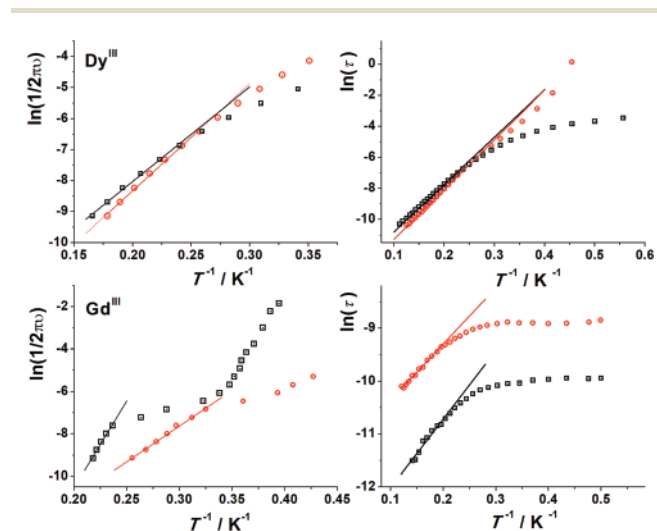
6 W. Wernsdorfer, N. Aliaga-Alcaide, R. Tiron, D. N. Hendrickson and G. Christou, *J. Magn. Magn. Mater.*, 2004, **272–276**, 1037.

7 D. Aravena, *J. Phys. Chem. Lett.*, 2018, **9**, 5327.

8 S. Hill, S. Datta, J. Liu, R. Inglis, C. J. Milios, P. L. Feng, J. J. Henderson, E. del Barco, E. K. Brechin and D. N. Hendrickson, *Dalton Trans.*, 2010, **39**, 4693.

9 P. Zhang, Y.-N. Guo and J. Tang, *Coord. Chem. Rev.*, 2013, **257**, 1728.

10 K. Zhang, V. Montigaud, O. Cador, G.-P. Li, B. Le Guennic, J.-K. Tang and Y.-Y. Wang, *Inorg. Chem.*, 2018, **57**, 8550.

11 C. A. P. Goodwin, F. Ortu, D. Reta, N. F. Chilton and D. P. Mills, *Nature*, 2017, **548**, 439.

12 Y.-N. Guo, G.-F. Xu, Y. Guo and J. Tang, *Dalton Trans.*, 2011, **40**, 9953.

13 F. Ortu, D. Reta, Y.-S. Ding, C. A. P. Goodwin, M. P. Gregson, E. J. K. McInnes, R. E. P. Winpenny, Y.-Z. Zheng, S. T. Liddle, D. P. Mills and N. F. Chilton, *Dalton Trans.*, 2019, **48**, 8541.

14 J. D. Rinehart and J. R. Long, *Chem. Sci.*, 2011, **2**, 2078.

15 F. Pointillart, O. Cador, B. Le Guennic and L. Ouahab, *Coord. Chem. Rev.*, 2017, **346**, 150.

16 J. Mayans, Q. Saéz, M. Font-Bardia and A. Escuer, *Dalton Trans.*, 2019, **48**, 641.

17 J. Mayans, L. Sorace, M. Font-Bardia and A. Escuer, *Polyhedron*, 2019, **270**, 264.

18 S. Gourbatsis, J. C. Plakatouras, V. Nastopoulos, C. J. Cardin and N. Hadjiliadis, *Inorg. Chem. Commun.*, 1999, **2**, 468.

19 J. Lisowski and J. Mazurek, *Polyhedron*, 2002, **21**, 811.

20 J. Mazurek and J. Lisowski, *Polyhedron*, 2003, **22**, 2877.

21 M. Tsiouri, N. Hadjiliadis, T. Arslan, B. M. Kariuki and J. C. Plakatouras, *Inorg. Chem. Commun.*, 2006, **9**, 429.

22 S. Kano, H. Nakano, M. Kojima, N. Baba and K. Nakajima, *Inorg. Chim. Acta*, 2003, **349**, 6.

23 S. Chen, R.-Q. Fan, S. Gao, X. Wang and Y.-L. Yang, *J. Lumin.*, 2013, **149**, 75.

24 F. Piccinelli, M. Leonzio, M. Bettinelli, M. Monari, C. Grazioli, A. Melchior and M. Tolazzi, *Dalton Trans.*, 2016, **45**, 3310.

25 M. Li, H. Wu, Q. Yang, H. Ke, B. Yin, Q. Shi, W. Wang, Q. Wei, G. Xie and S. Chen, *Chem. – Eur. J.*, 2017, **23**, 17775.

26 S. K. Singh, T. Gupta, L. Ungur and G. Rajaraman, *Chem. – Eur. J.*, 2015, **21**, 13812.

27 J. J. Le Roy, M. Jeleti, S. I. Gorelsky, I. Korovkov, L. Ungur, L. F. Chibotaru and M. Murugesu, *J. Am. Chem. Soc.*, 2013, **135**, 3502.

28 J. J. Le Roy, I. Korovkov, J. E. Kim, E. J. Schelter and M. Murugesu, *Dalton Trans.*, 2014, **43**, 2737.

29 R. J. Holmberg, L. T. A. Ho, L. Ungur, I. Korobkov, L. F. Chibotaru and M. Murugesu, *Dalton Trans.*, 2015, **44**, 20321.

30 M. Orendáč, L. Sedláková, E. Čižmár, A. Orendáčová, A. Feher, S. A. Zvyagin, J. Wosnitza, W. H. Zhu, Z. M. Wang and S. Gao, *Phys. Rev. B: Condens. Matter Mater. Phys.*, 2010, **81**, 214410.

31 A. Vráblová, M. Tomás, L. R. Falvello, L. Dlháň, J. Titiš, J. Černák and R. Boča, *Dalton Trans.*, 2019, **48**, 13943.

32 Y. Horii, K. Katoh, Y. Miyazaki, M. Damjanovic, T. Sato, L. Ungur, L. F. Chibotaru, B. K. Breedlove, M. Nakano, W. Wernsdorfer and M. Yamashita, *Chem. – Eur. J.*, 2020, **26**, 8076.

33 J. Mayans and A. Escuer, *Chem. Commun.*, 2021, DOI: 10.1039/D0CC07474H, WEB published.

34 T. Ghosh, S. Maity, J. Mayans and A. Ghosh, *Inorg. Chem.*, 2021, DOI: 10.1021/acs.inorgchem.0c03129, WEB published.

35 G. M. Sheldrick, *SHELXL-2014/7: Program for the Solution of Crystal Structures*, University of Göttingen, Göttingen, Germany, 2014.

36 C. M. Che, W. T. Tang and C. K. Li, *J. Chem. Soc., Dalton Trans.*, 1990, 3735.

37 M. Llunell, D. Casanova, J. Cirera, P. Alemany and S. Alvarez, *SHAPE version 2.0*, Barcelona, 2010. The program can be obtained by request to the authors.

38 J. Crassous, *Chem. Soc. Rev.*, 2009, **38**, 830.

39 H. Miyake, *Symmetry*, 2014, **6**, 880.

40 M. Liu, L. Zhang and T. Wang, *Chem. Rev.*, 2015, **115**, 7304.

Electronic Supplementary Material (ESI) for

Structural and magnetic studies of mononuclear lanthanide complexes derived from N-rich chiral Schiff bases.

E. Pilichos,[a] M. Font-Bardia,[b] A. Escuer,*[a] and J. Mayans*[c]

[a] Departament de Química Inorgànica i Orgànica, Secció Inorgànica and Institute of Nanoscience (IN²UB) and Nanotecnology, Universitat de Barcelona, Martí i Franquès 1-11, Barcelona-08028, Spain.

[b] Departament de Mineralogia, Cristal·lografia i Dipòsits Minerals and Unitat de Difracció de R-X. Centre Científic i Tecnològic de la Universitat de Barcelona (CCiTUB). Universitat de Barcelona. Solé i Sabarís 1-3. 08028 Barcelona.

[c] Instituto de Ciencia Molecular (ICMol), Universidad de Valencia, Catedrático José Beltran 2, 46980 Paterna (Valencia), Spain
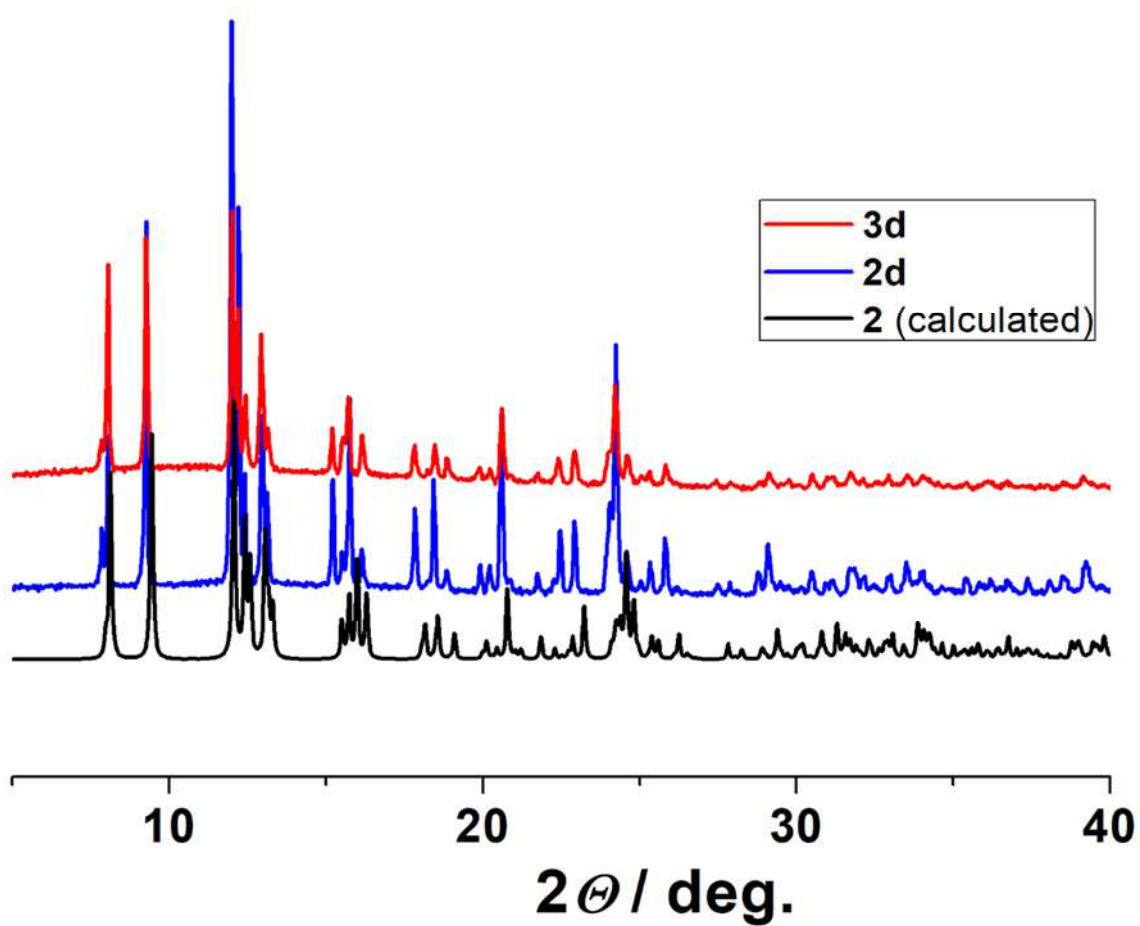
Fig. *S*1. Powder X-Ray spectra for the diluted complexes **2d** and **3d**. In black is represented the simulated powder spectra from the single crystal structure of the complex **2**.
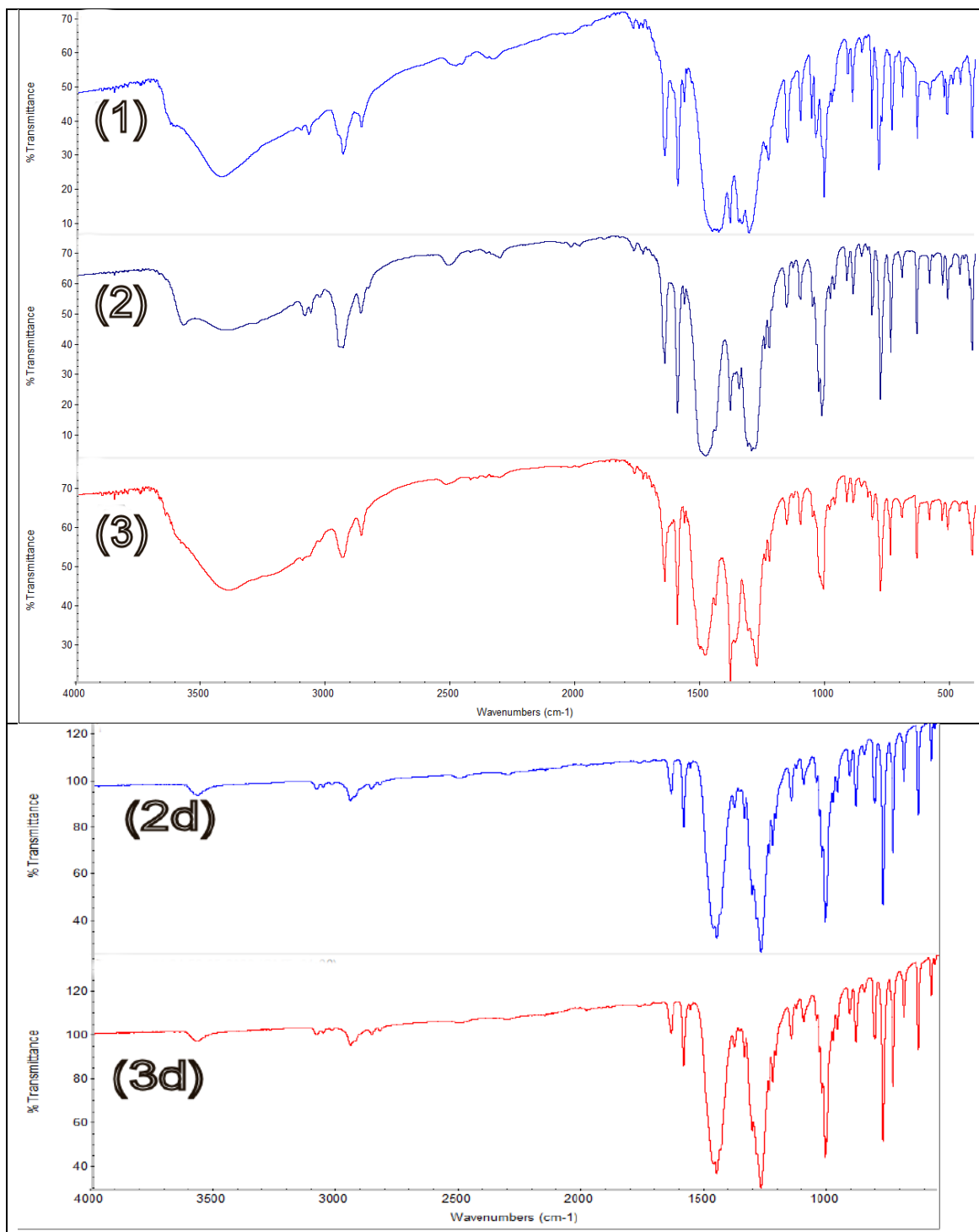
Fig. *S*2. IR spectra for complexes [Ce(L)(NO$_3$)$_3$(MeOH)] (**1**), [Gd(L)(NO$_3$)$_3$] (**2**) and [Dy(L)(NO$_3$)$_3$] (**3**) the diluted **2d** and **3d**.

Table S1. CShM values for the undecacoordinated environment of complex **1** and the decacoordinated complex **2**. The relatively high distortion with the ideal polyhedra are due to the low bite of the nitrato and *cis* N-donors of the Schiff base.

11-vertex Polyhedra	Ce[III] (**1**)	10-vertex Polyhedra	Gd[III] (**2**)
Capped pentagonal prism (C5v)	5.64	Bicapped cube (D4h)	9.77
Capped pentagonal antiprism (C5v)	5.99	Bicapped square antiprism (D4d)	4.67
Augmented sphenocorona (cs)	7.73	Metabidiminished icosahedron (C2v)	7.08
		Sphenocorona (C2v)	3.05
		Staggered Dodecahedron (D2)	4.66
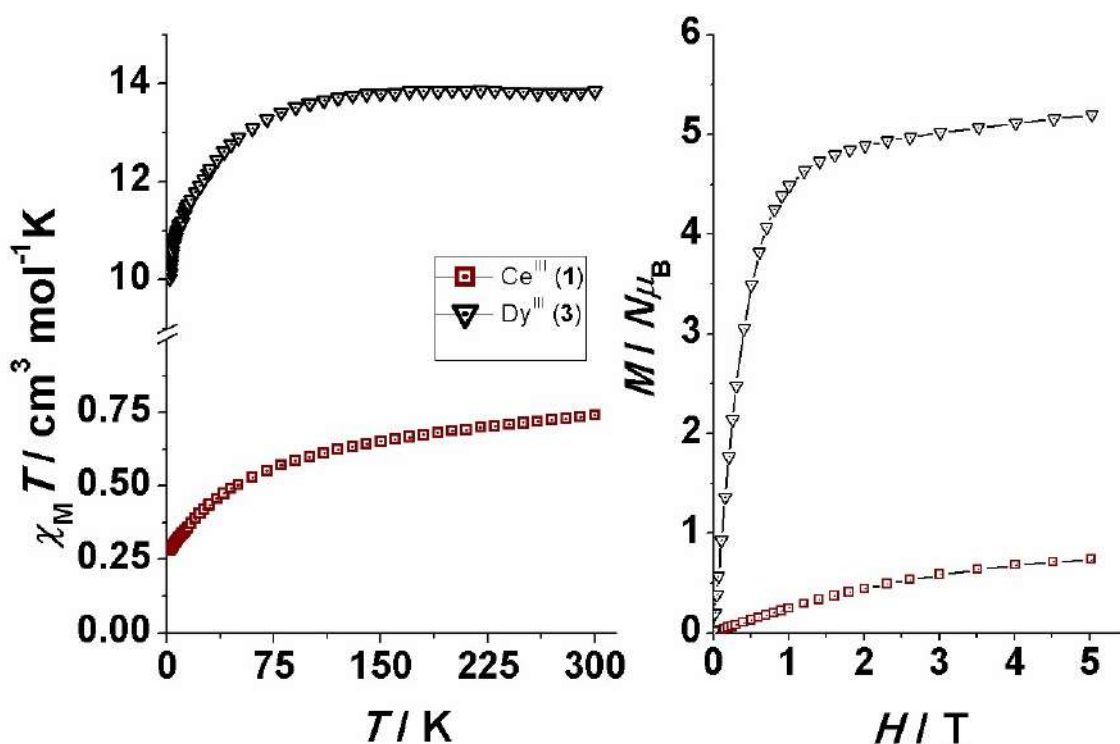
Fig. S3. $\chi_M T$ (left) and magnetization (right) plots for referred complexes. The $\chi_M T$ values at room temperature are very close to the expected values for a lonely isolated lanthanide ions (**expected**/experimental $cm^3 \cdot mol^{-1} \cdot K$): Ce[III], ($^2F_{5/2}$, g = 6/7, **0.80**/0.74 $cm^3 \cdot mol^{-1} \cdot K$), Dy[III] ($^6H_{15/2}$, g = 4/3, **14.2**/13.8 $cm^3 \cdot mol^{-1} \cdot K$).
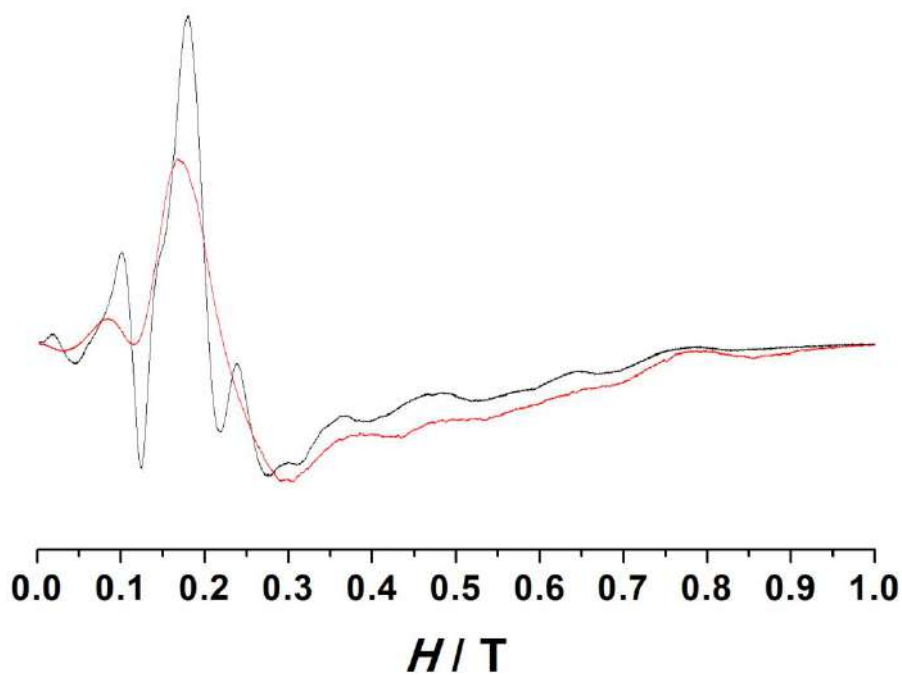
Fig. *S*4. *X*-band EPR spectra for the Gd^{III} compounds **2** (red) and **2d** (black). Reduction of dipolar interactions allows shaper lines for **2d**. The identical spectra confirm the same environment after dilution.
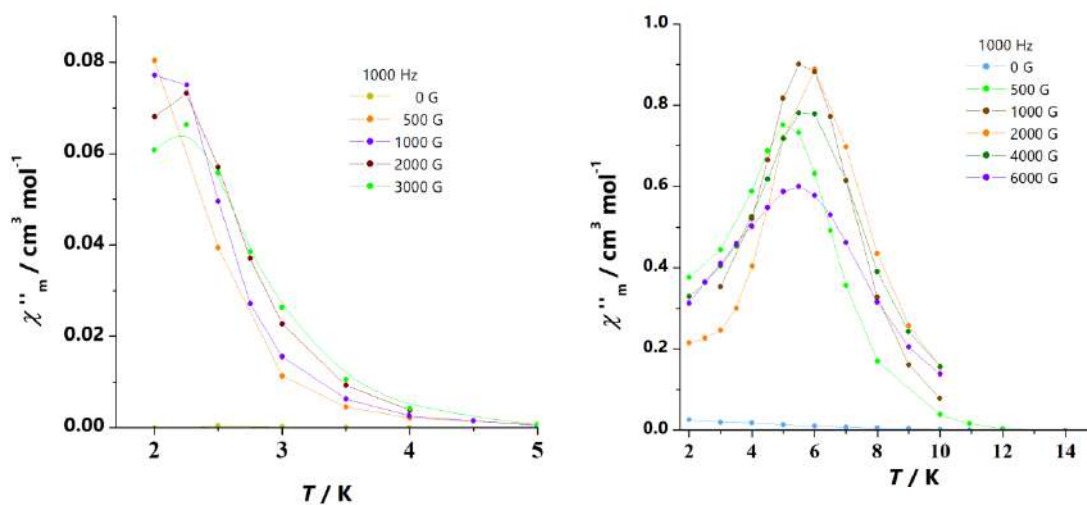
Fig. *S*5. χ_M'' dependence of the transverse field for complex **1** (left) and **3** (right). From this initial dependence the fields to perform the *ac* measurements were 2000 G for **1** and 1000 G for **3**.
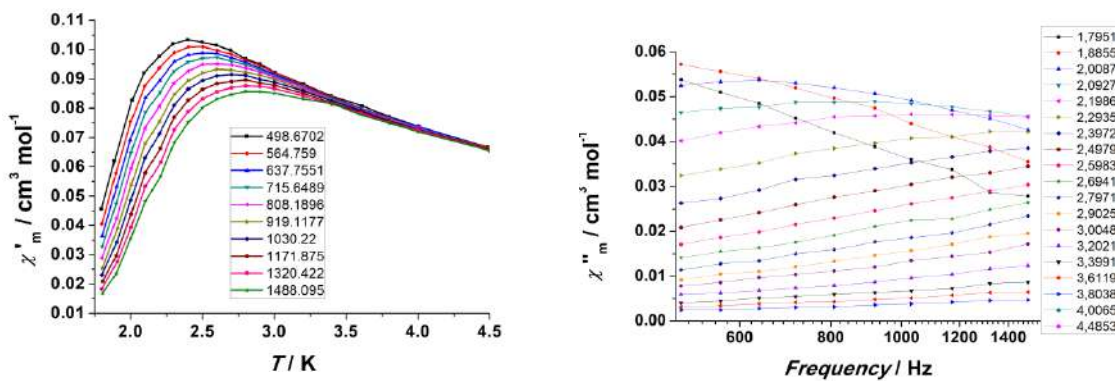
Fig. S6. χ'_M vs. T (left) and χ''_M vs. frequency (right) for complex **1**.
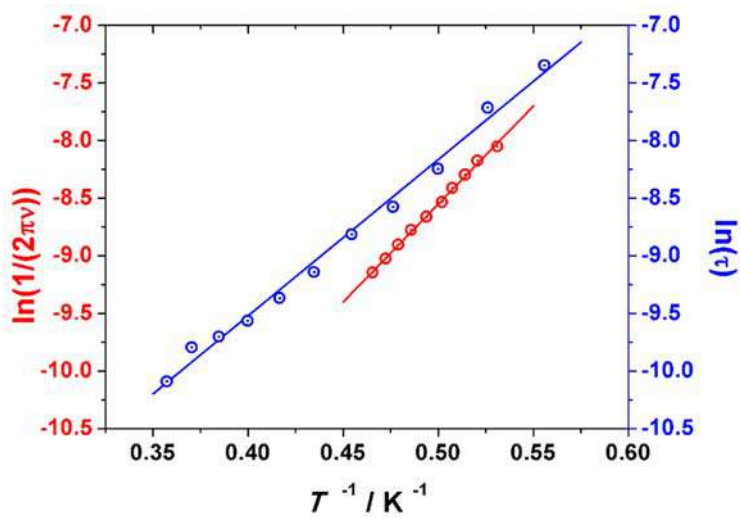
Fig. S7. Plot of $\ln(1/2\pi\nu)$ vs. T^{-1} from the $\chi''_M(T)$ data (red) and $\ln(\tau)$ vs. T^{-1} from the fit of the Argand plot (blue) for complex **1**.

PUBLICATION #2

"Magnetic and optical studies of a new family of multidimensional and multiproperty PO-lanthanide(III) derived systems"

PAPER
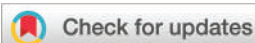
Magnetic and optical studies of a new family of multidimensional and multiproperty PO-lanthanide(III) derived systems†

Evangelos Pilichos,[a] Ànnia Tubau,[a] Saskia Speed,[a] Mercè Font-Bardia,[b] Albert Escuer, [ID][a,c] Arnald Grabulosa [ID] *[a,c] and Júlia Mayans [ID] *[a,c]

A new family of lanthanide compounds has been synthesized using 1,2-bis(diphenylphosphino)ethane dioxide (dppeO$_2$) as an O-donor ligand through the phosphoryl group to lanthanide(III) cations and structurally, magnetically and optically studied. Depending on the lanthanide, two different topologies appear: the two-dimensional structure [Ln^{III}(dppeO$_2$)$_{1.5}$(NO$_3$)$_3$(H$_2$O)$_{0.5}$]$_n$ (Ln = Ce (**1**), Sm (**2**) and Dy (**6**)) and the one-dimensional structure [Ln(dppeO$_2$)(NO$_3$)$_3$DMF]$_n$ (Ln = Eu (**3**), Gd (**4**) and Tb (**5**)). Some of the Ln-derived complexes have been used as structural probes, while others have been synthesized to use the specific characteristics of each cation to take advantage of their magnetic/luminescence properties. Complex **6** presents slow relaxation of the magnetization while **2**, **3** and **5** present emitting properties in the visible range.

Introduction

During the last few years, molecular lanthanide(III)-derived compounds climbed to the top of different new applications like luminescent sensors,[1,2] slow-relaxing magnetic systems[3,4] spintronics[5,6] or anticounterfeit technologies.[7,8] One of the most exploited applications of lanthanide molecular compounds is their use as potential Single Molecule Magnets (SMMs) or Single Ion Magnets (SIMs) due to their comparatively high single ion anisotropy arising from their Spin–Orbit Coupling (SOC) and from the crystal field splitting of the lowest *J* multiplet when they are forming a coordination complex.[4,9,10] Among this, lanthanide cations present extraordinary emitting properties originating from the electronic transitions within the partially filled 4f orbitals except for Ce^{III}, which presents 5d–4f electronic transitions. However, due to the very low sensitivity of lanthanide(III) to their surroundings, their hybridization is limited and, consequently, Ln^{III} exhibits very narrow emission lines, which can be considered as a fin-

gerprint of each cation. The main drawback of this approach to the luminescence of lanthanide-derived complexes is that transitions in-between 4f orbitals are partially Laporte-forbidden. Therefore, any strategy to increase the luminescence of lanthanide coordination compounds must consider the sensitization of lanthanide(III) cations.[11,12] To this end, a useful procedure is the coordination of lanthanide(III) ions to phosphine oxides, known to be excellent ligands.[13] Phosphine oxides are ideal for this purpose because they can be easily prepared by oxidation of the parent phosphines, a huge family of ligands extensively studied due to their application in organometallic homogeneous catalysis. Hence, this kind of ligand allows the fine-tuning of the system's properties.

Some extended systems derived from the diphosphine oxide bis(diphenylphosphino)ethane dioxide (dppeO$_2$), Scheme 1, were previously reported by other authors[14–19] but their magnetic properties remain practically unexplored.

Noteworthily, the stereochemistry or dimensionality of the dppO$_2$/Ln^{III} system can show a multifactorial dependence on

[a]Departament de Química Inorgànica i Orgànica, Secció de Química Inorgànica, Universitat de Barcelona, Martí i Franques 1-11, Barcelona-08028, Spain
[b]Departament de Mineralogia, Cristal·lografia i Dipòsits Minerals i Unitat de Difracció de R-X, Centre Científic i Tecnològic de la Universitat de Barcelona (CCiTUB), Universitat de Barcelona, Solé i Sabarís 1-3, 08028 Barcelona, Spain
[c]Institut de Nanociència i Nanotecnologia (IN2UB), Universitat de Barcelona, Barcelona-08028, Spain

Scheme 1 Structural formula of the ligand employed in this work, 1,2-bis(diphenylphosphino)ethane dioxide (dppeO$_2$).

factors such as the size of the cation, the counterions present in the reaction media, reaction conditions or the solvent employed.[20] In the present paper, we report a new family of Ln-derived systems using $dppeO_2$. Single crystal X-ray diffraction demonstrated that two different structures could be obtained with no changes in the reaction conditions: bidimensional networks with the general formula $[Ln^{III}(dppeO_2)_{1.5}(NO_3)_3(H_2O)_{0.5}]_n$ (Ln = Ce (**1**), Sm (**2**) and Dy (**6**)) and monodimensional compounds with the general formula $[Ln(dppeO_2)(NO_3)_3DMF]_n$ (Ln = Eu (**3**), Gd (**4**) and Tb (**5**)), which are apparently independent of the above-mentioned factors affecting the final structures. Complexes **1**, **3** and **4** were used as structural probes to test the isostructurality with other family members by X-ray powder diffraction. Noteworthily, the reported systems provide the first examples of 1-D arrangement for the $dppeO_2/Ln^{III}$ system. The anisotropic derivative **6** has been magnetically characterized (both statically and dynamically) while complexes **2**, **3** and **5**, the typical visible-range emitters, have been studied to check their emitting properties.

Experimental

X-ray crystallography

White (**1**, **3** and **4**) prism-like specimens were used for single crystal X-ray crystallographic analysis. The X-ray intensity data were measured on a D8 Venture system equipped with a multilayer monochromator and a Mo microfocus (Table 1).

The frames were integrated with the Bruker SAINT software package using a narrow-frame algorithm. The structures were solved and refined using the Bruker SHELXTL software.[21]

Powder X-ray diffraction was performed with a PANalytical X'Pert PRO MPD θ/θ powder diffractometer of 240 millimetre radius, in a configuration of the convergent beam with a foca-

lizing mirror and a transmission geometry with flat samples sandwiched between low absorbing films and Cu Kα radiation (λ = 1.5418 Å). Comparison between the calculated spectrum from the single crystal structures of **1** and **4** and the experimental powder X-ray spectrum for compounds **2**, **5** and **6** confirms the isostructurality among the two different groups, Fig. S1.†

Crystal data and refinement details for complexes **1**, **3** and **4** are summarized in Table 1. Further crystallographic details can be found in the corresponding CIF files provided in the ESI.†

Physical measurements

Magnetic susceptibility measurements were carried out on pressed polycrystalline samples with an MPMS5 Quantum Design susceptometer working in the range 30–300 K under magnetic fields of 0.3 T and under a field of 0.03 T in the 30–2 K range to avoid saturation effects at low temperature. Diamagnetic corrections were estimated from Pascal Tables. Infrared spectra (4000–400 cm^{-1}) were recorded from KBr pellets on a Bruker IFS-125 FT-IR spectrophotometer.

Solid-state fluorescence spectra of compounds **2**, **3** and **5** were recorded on a Horiba Jobin Yvon SPEX Nanolog fluorescence spectrophotometer (Fluorolog-3 v3.2, HORIBA Jovin Yvon, Cedex, France) equipped with a three-slit, double-grating excitation and emission monochromator with dispersions of 2.1 nm mm^{-1} (1200 grooves per mm) at room temperature. The steady-state luminescence was excited with unpolarized light from a 450 W xenon CW lamp and detected at an angle of 22.5° for solid-state measurement with a red-sensitive Hamamatsu R928 photomultiplier tube. The instrument was adjusted to obtain the highest background-to-noise ratio. The sample was mounted between two quartz plates. Spectra were corrected for both the excitation source light intensity variation (lamp and grating) and the emission spectral response (detector and grating). Lifetime decay curves were measured in the same instrument monitored in the phosphoresce mode using a 450 W xenon pulsed lamp (1.5 ns pulse). The measured decays were analysed using the OriginPro 8 software package. The decay curves of compounds **3** and **5** and the fit quality were determined by the χ^2 method of Pearson. A band pass of 0.5 nm was employed in order to not surpass 10^6 CPS to make sure that we are not measuring in the non-linear optical zone.

The ^1H and $^{31}P\{^1H\}$ NMR spectra of $dppeO_2$ were recorded at room temperature in a cryoprobe-equipped, 400 MHz Bruker Avance III spectrometer in dmso-d_6.

Syntheses

1,2-Bis(diphenylphosphino)ethane dioxide ($dppeO_2$). A 30% aqueous solution of H_2O_2 (1.0 mL, 9.8 mmol) was added dropwise to a THF solution (20 mL) of dppe (2.0 g, 5.0 mmol) with stirring and ice-cooling. When the exothermal process finished the solvent was concentrated under vacuum. A white powder was formed, which was filtered and washed with diethyl ether. Yield: 1.90 g, 88%. ^1H NMR (CDCl$_3$, δ ppm): 7.72–7.67 (m, 8H,

Table 1 Crystal data, collection and structure refinement details for the X-ray structure determination of complexes **1**, **3** and **4**

	1	**3**	**4**
Formula	$C_{78}H_{74}Ce_2N_6O_{25}P_6$	$C_{29}H_{31}EuN_4O_{12}P_2$	$C_{29}H_{31}GdN_4O_{12}P_2$
FW	1961.49	841.48	846.77
System	Trigonal	Monoclinic	Monoclinic
Space group	$R\bar{3}c$	$P2_1/c$	$P2_1/n$
a/Å	15.5252(3)	9.1723(5)	17.0768(7)
b/Å	15.5252(3)	17.776(1)	9.9525(5)
c/Å	60.112(2)	20.858(1)	20.509(1)
α/°	90	90	90
β/°	90	102.952(2)	104.076(2)
γ/°	120	90	90
V/Å^3	12 547.9(7)	3314.4(3)	3380.9(3)
Z	6	4	4
T, K	100(2)	100(2)	100(2)
λ(MoK$_\alpha$), Å	0.71073	0.71073	0.71073
p_{cal}, g cm^{-3}	1.557	1.686	1.664
μ(MoK$_\alpha$), mm^{-1}	1.269	2.057	2.123
R	0.0480	0.0316	0.0271
ωR^2	0.1138	0.0724	0.0530

C_6H_5), 7.54–7.42 (m, 12H, C_6H_5), 2.51 (d, J = 2.7 Hz, 4H, CH_2CH_2). $^{31}P\{^1H\}$ NMR (CDCl$_3$, δ ppm): 32.88 (s), which matched the published data.[22]

[Ln^{III}(dppeO$_2$)$_{1.5}$(NO$_3$)$_3$(H$_2$O)$_{0.5}$]$_n$ (Ln = Ce (1), Sm (2), Dy (6) and [Ln^{III}(dppeO$_2$)(NO$_3$)$_3$(DMF)]$_n$ (Ln = Eu (3), Gd (4) and Tb (5)). As a general procedure: In a mixture of 15 ml of MeOH/ 2 ml of DMF, the corresponding lanthanide nitrate salt (0.2 mmol) and dppeO$_2$ (0.2 mmol/0.086 g) were added. The reaction mixture was refluxed for 1 h and filtered. After one day, white crystals, suitable for X-ray diffraction, were formed by layering with diethyl ether. CHN for C$_{39}$H$_{36}$CeN$_3$O$_{12.5}$P$_3$: calc.: C, 47.81; H, 3.70; N, 4.29, found C, 47.66; H, 3.54; N, 4.38; C$_{39}$H$_{36}$SmN$_3$O$_{13}$P$_3$: calc.: C, 46.93; H, 3.64; N, 4.21, found C, 46.21; H, 3.71; N, 4.25; C$_{39}$H$_{36}$DyN$_3$O$_{13}$P$_3$: calc.: C, 46.37; H, 3.59; N, 4.16, found C, 45.97; H, 3.62; N, 4.08; C$_{29}$H$_{31}$EuN$_4$O$_{12}$P$_2$: calc.: C, 41.39; H, 3.71; N, 6.65, found C, 41.12; H, 3.53; N, 6.70; C$_{29}$H$_{31}$GdN$_4$O$_{12}$P$_2$: calc.: C, 41.13; H, 3.69; N, 6.61, found C, 41.42; H, 3.52; N, 6.52; C$_{29}$H$_{31}$TbN$_4$O$_{12}$P$_2$: calc.: C, 41.05; H, 3.68; N, 6.60, found C, 40.93; H, 3.47; N, 6.38. IR spectra for the two kinds of complexes are shown in Fig. S2.†

Results and discussion

Description of the structures

[Ce^{III}(dppeO$_2$)$_{1.5}$(NO$_3$)$_3$(H$_2$O)$_{0.5}$]$_n$ (1). The structure consists of a 2D layer of Ce^{III} cations linked by bis-monodentate dppeO$_2$ ligands. The Ce^{III} cation links three bidentate nitrato ligands, three O-donors from three dppeO$_2$ ligands and one water molecule along the C_3 symmetry axis with an occupancy of 50% and for the 50% of the molecules one of the nitrato anions is placed in a more axial position resulting ennea- and decacoordinated environments Fig. 1, top. The main bond parameters are reported in Table 2. The ligands show a *fac*-
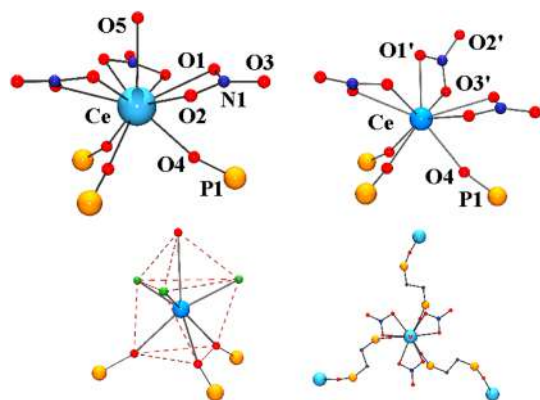

Fig. 1 Top, labelled plot of the Ce^{III} environment for complex **1**. Bottom, intermediate O$_h$/TP polyhedron around the decacoordinated Ce^{III} cation and in-plane arrangement of the dppeO$_2$ ligands. Color key for all figures, Ce^{III}, light blue; Gd^{III}, firebrick; P, orange; O, red; N, navy; and C, black. The positions indicated as green balls correspond to the mean position between the two O-donors of each bidentate nitrate ligand.

Table 2 Selected bond distances (Å) and angles (°) of complex **1**

Ce1–O1	2.641(4)	Ce1–O1′	2.35(1)
Ce1–O2	2.592(5)	Ce1–O3′	2.52(3)
Ce1–O5	2.74(1)	Ce1–O4	2.428(2)
P(1)–O(4)	1.503(2)		
O1–Ce1–O2	48.5(1)	O1–Ce1–O5	63.36(8)
O1–Ce1–O4	68.49(9)	O2–Ce1–O5	76.3(1)
O2–Ce1–O4	75.0(2)	P(1)–O(4)–Ce(1)	165.2(2)
O4–Ce1–O5	131.71(6)	O4–Ce1–O4′	80.55(9)

arrangement, symmetrically placed around the cation due to the C_3 symmetry axis along the O5–Ce bond. The dppeO$_2$ ligands act in its bis-monodentate coordination mode and the symmetrical in-plane arrangement, Fig. 1, allows for a 2D honeycomb network, Fig. 2. The short Ce–O distances correspond to the Ce–O$_{phosphine}$ (2.428 Å) bonds whereas the larger one is the Ce–O5 bond (2.74 Å). SHAPE[23] analysis of the coordination sphere around the Ce^{III} cation shows that it is far from any ideal polyhedron due to the low bite of the nitrato ligands, as indicated by a minimum CShM value of 3.49. The simplified environment referred to the seven ligands and assuming the position of the nitrate ligands as the mean position between the two O$_{nitrato}$ donors reveals an intermediate between a capped octahedron and one capped trigonal prismatic arrangement, Fig. 1, left.

[Ln^{III}(dppeO$_2$)(NO$_3$)$_3$(DMF)]$_n$, Ln = Eu^{III} (3) and Gd^{III} (4). Due to the similarity between the two structures and to avoid repetitive descriptions, only the structure of complex **4** will be described. The main bond parameters for the two compounds are summarized in Table 3.

The structure consists of a 1D arrangement of Gd^{III} cations bridged by bis-monodentate dppeO$_2$ ligands. The enneacoordinated environment around the Gd^{III} cation is formed by three bidentate nitrato ligands, two O-donors from two dppeO$_2$ ligands and one dimethylformamide molecule. The two dppO$_2$ ligands are coordinated in *trans* positions to the lantanoid cation (O–Gd–O bond angle of 149.3°) whereas the nitrato and DMF ligands are roughly linked in the equatorial plane, Fig. 3-top. The Gd–O bond distances are in the range of 2.313–2.506 Å, with the shorter ones being those involving the O$_{phosphine}$ bonds. The dppeO$_2$ ligands link the Gd^{III} cations resulting in a zig-zag chain along the *a*-axis of the cell, Fig. 3.
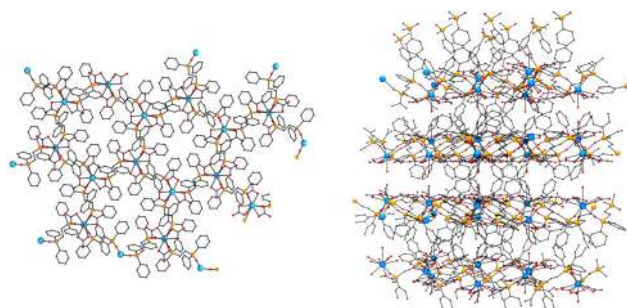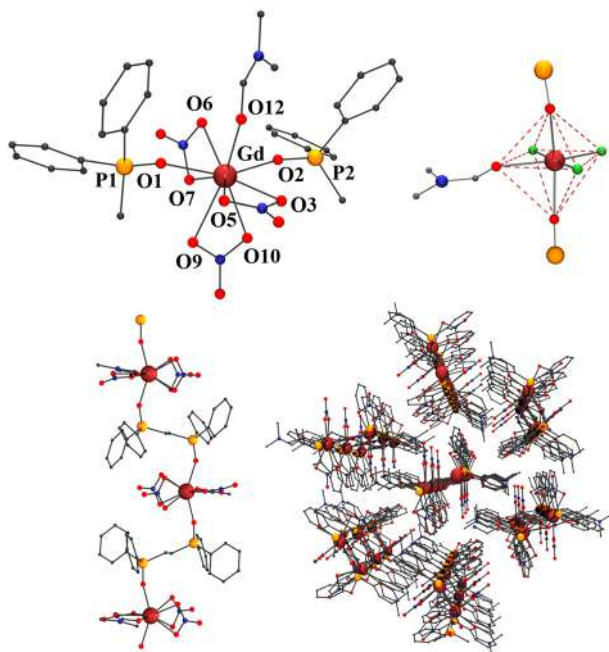

Fig. 2 Left, a view of the honeycomb layers of **1** along the *c*-axis; right, view of the network along the *a*-axis.

Table 3 Selected bond distances (Å) and angles (°) of complexes **3** and **4**
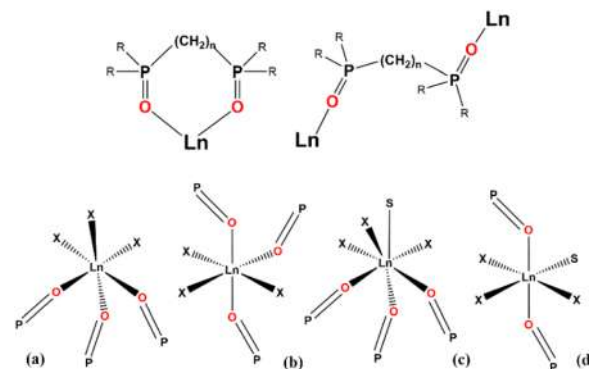
	(**3**) Ln = Eu	(**4**) Ln = Gd
Ln(1)–O(1)	2.315(2)	2.313(1)
Ln(1)–O(2)	2.323(2)	2.314(1)
Ln(1)–O(3)	2.531(3)	2.473(2)
Ln(1)–O(5)	2.503(3)	2.468(2)
Ln(1)–O(6)	2.498(3)	2.525(2)
Ln(1)–O(7)	2.538(3)	2.439(2)
Ln(1)–O(9)	2.474(3)	2.573(2)
Ln(1)–O(10)	2.523(3)	2.506(2)
Ln(1)–O(12)	2.386(3)	2.338(2)
P(1)–O(1)	1.508(2)	1.505(1)
P(2)–O(2)	1.506(3)	1.503(1)
O(1)–Ln(1)–O(2)	149.27(8)	149.26(5)
O(1)–Ln(1)–O(12)	84.13(9)	85.41(5)
O(2)–Ln(1)–O(12)	85.05(9)	83.97(5)
P(1)–O1–Ln(1)	166.4(2)	153.46(9)
P(2)–O(2)–Ln(1)	168.9(2)	166.43(9)

Scheme 2 Top, bidentate (left) and bis-monodentate (right) coordination modes of the dppeO$_2$ ligand. Bottom, previously reported *fac* (a) and *mer* (b) arrangement of the ligands around the lanthanide cations. Arrangement of the ligands for the 2D (c) and 1D (d) structures reported in this paper. X for (a) and (b): O,O′-NO$_3^-$ or Cl$^-$ allowing for coordination 9 or 6, respectively; X for (c) and (d): O,O′-NO$_3^-$; P=O represent one of the donors of the dppeO$_2$ ligand; S: solvent molecule.

Fig. 3 Top, partially labelled plot and polyhedral environment of complex **4**. Bottom, plot of the 1D chain of Gd^{III} cations (left) and network arrangement of the chains along the *a*-axis of the unit cell.

SHAPE[23] analysis of the coordination sphere around the Gd^{III} cation shows that, as for **1**, the minimum CShM value of 1.79 indicates a strong distortion from any ideal polyhedron whereas with regard to the six ligands, their arrangement is clearly octahedral, Fig. 3, right.

Structural and synthetic comments

The chemistry of bis(diphenylphosphine)-dioxide ligands with lanthanide cations is strongly dependent on several factors that can modify the denticity of the ligands and/or the dimensionality of the resulting complexes. This kind of ligand can

act as a bidentate or bis-monodentate donor Scheme 2-top, allowing for molecular or extended systems, respectively. The length of the flexible (CH$_2$)$_n$ spacer between the phosphor atoms is a determinant resulting in always a bidentate coordination for $n = 1$ and consequently exclusively molecular compounds have been reported whereas both modes have been characterized for $n = 2$–4. Interestingly, the bis-monodentate mode is preferred for the $n = 2$ case yielding 2D networks whereas the bidentate mode is preferred for the $n = 4$ case due to the flexibility of the butane spacer.

The simultaneous presence of both coordination modes has been found in dinuclear systems for the dppeO$_2$ ligand and Pr^{III}, Dy^{III} and Lu^{III} cations[18] but all the remainder complexes are 2D systems with exclusive presence of the bis-monodentate mode, Table 4. These 2D networks with the [Ln(dppeO$_2$)$_{1.5}$(X)$_3$]$_n$ formula are equally found for X = O,O′-NO$_3^-$ (resulting LnO$_9$ coordination), or for X = Cl$^-$, (resulting LnO$_3$Cl$_3$) hexacoordination. In the two cases the arrangement of the ligands can adopt a *fac*- or *mer*-arrangement around the lanthanide (Scheme 2a and b), which allows for different 2D network architectures (parquet-floor, brick-wall or honeycomb).

As can be extracted from Table 4, any relationship can be extracted from factors like the cation size or the size or denticity of the coordinated anions. In the same way, the syntheses

Table 4 Summary of the arrangement, coordination numbers (C. N.) and dimensionality (*n*-D) of the reported *n*-D systems derived from dppO$_2$ and Ln^{III} cations

Ln^{III} cation	Arrang.	Anion	C. N./*n*-D	Ref.
Dy	FAC	Cl$^-$	6 – 2D	18
Nd, Pr	FAC	NO$_3^-$	9 – 2D	15
La, Nd, Eu, Gd, Dy	MER	Cl$^-$	6 – 2D	14, 15, 17 and 18
Nd, Pr, Sm, Eu, Dy	MER	NO$_3^-$	9 – 2D	15–17
Dy	FAC/MER	Cl$^-$	6 – 3D	18
Ce, Sm, Dy	FAC	NO$_3^-$	9/10 – 2D	This work
Eu, Gd, Tb	MER	NO$_3^-$	9 – 1D	This work

under soft conditions (room temperature) or solvothermal conditions at high temperatures and large reaction times become also irrelevant.[18] In light of these data, the solvent employed as reaction medium becomes a determinant as was proposed by Spichal *et al.*[15] This assumption has been corroborated by means of the MeOH/DMF medium employed in the present work that allows for unprecedented coordination numbers or dimensionality of the reported systems, Table 4.

Magnetic properties

Static measurements. DC magnetic susceptibility (χ_M) data for **1**, **4**, **5** and **6** were measured on polycrystalline and pressed samples in the 2–300 K temperature range and plotted as $\chi_M T$ *vs. T* (Fig. 4).

Due to the topology of all the studied structures, the magnetic behaviour of the paramagnetic carriers in the compounds corresponds to single ion contributions. $\chi_M T$ values for complexes **1**, **5** and **6** are very close to the corresponding values for the isolated lanthanide cations $^2F_{5/2}$ (Ce^{III}, 0.80 cm^3 mol^{-1} K), $^7F_6$ (Tb^{III}, 11.82 cm^3 mol^{-1} K), and $^6H_{15/2}$ (Dy^{III}, 14.17 cm^3 mol^{-1} K), respectively. For these three compounds, $\chi_M T$ slowly decreases when lowering the temperature due to the progressive depopulation of the m_J levels, with a more pronounced decay below 50 K, probably due to antiferromagnetic intramolecular interactions in-between the extended structures. The isotropic compound **4** (Gd^{III}, $^8S_{7/2}$) shows a room temperature $\chi_M T$ value of 7.95 cm^3 mol^{-1} K close to the expected value of 7.875 cm^3 mol^{-1} K that follows a Curie law down to low temperature.

Experimental data from Fig. 4 was fitted using PHI software[24] and using a simple, but effective model reported by Lloret and co-workers for axial symmetry environments in lanthanide derived compounds, which has been previously used by us.[25,26] For compounds **1**, **5** and **6**, the used Hamiltonian (eqn (1)), in which $\hat{S}$ are the spin operators, L is the orbit operator, and λ is the spin–orbit coupling, while Δ describes the energy gap between m_L components. The value

for the orbital reduction parameter (κ) was assumed as **1** (lanthanide ions behave as purely ionic). The important point about this fitting is the different shapes of the $\chi_M T$ curves depending on the sign of Δ: if Δ is greater than 0, the smallest value of m_L corresponds to the ground states, so the lowest m_L will be the ground state. For Δ smaller than 0, occurs the opposite and the highest m_L corresponds to the ground state. The fact that only the shape of the curve is relevant here is because the low symmetry of the compounds tends to mix the ground state. The first term of the Hamiltonian describes the spin–orbit coupling, while the second term is related to the ligand field around the lanthanide cation while the third term describes the Zeeman effect.

$$H = (\lambda \hat{S}L) + \Delta[L_z^2 - L(L+1)/3] + [\beta H(-\kappa L + 2\hat{S})] \quad (1)$$

A very good fit of the experimental data was obtained (solid lines in Fig. 4) with Δ parameters of −8.3, −12.1 and −6.2 cm^{-1}, for **1**, **5** and **6**, respectively. Magnetization experiments performed at 2 K show quasi saturated plots with $N\mu_\beta$ values of 1.05 (**1**), 4.83 (**5**) and 5.31 (**6**) that confirm the negative Δ value for these cations and 7.09 for the isotropic gadolinium system (**4**).

Dynamic measurements. Preliminary alternate current measurements showed that no signals were found for any of the compounds at zero field. Measurements under static or increasing magnetic fields revealed weak tails of out-of-phase signals for **1** and **5** (Fig. S3†), but well defined $\chi''_M(T)$ peaks with a similar intensity in the 0.1–0.6 T range for complex **6** (Fig. 5-top). The absence of an ac response at zero field is

Fig. 5 Temperature (top) and frequency (bottom) dependence of χ''_M of complex **6** at an optimal applied external magnetic field of 0.1 T.
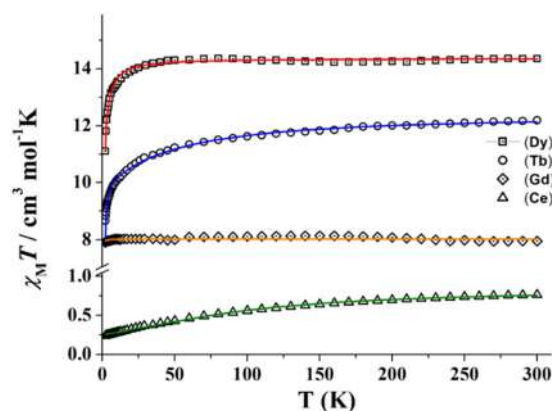

Fig. 4 $\chi_M T$ *vs.* temperature plots of complexes **1** (triangles), **3** (diamonds), **5** (circles) and **6** (squares). Solid lines show the best fit of the experimental data.
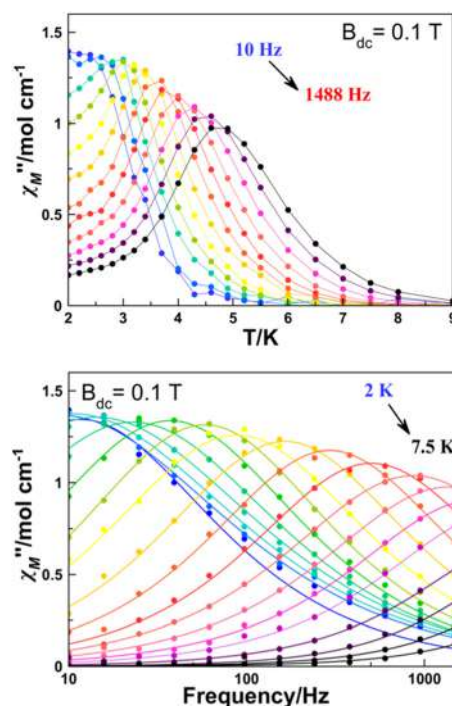
usually attributed to quantum tunnelling of the magnetization (QTM) which can be suppressed by removing the $\pm m_J$ degeneration when an external dc field is applied. As is shown in Fig. 5, complex **6** shows temperature and frequency-dependent behaviour both in χ'_M and χ''_M revealing slow magnetic relaxation behaviour, and it can be considered a Single Ion Magnet (SIM).

Plots of the maxima of χ''_M *vs.* inverse of the temperature, the so-called Arrhenius plot, evidence that their dependence is not linear and only a rough linearity can be found for higher temperatures, indicating the presence of more than one relaxation mechanism (Fig. S4†). Because for a Kramers ion the magnetic relaxation should occur through excited Kramers doublets with a sequential number of transitions induced by an emission of a quantum of energy lattice (a phonon), a preliminary fit of the high temperature region using the equation $\ln(1/(2\pi\omega)) = \ln(1/\tau_0) - U_{eff}/(k_BT)$ yields in the fitting parameters U_{eff} = 21.77 K and reasonable τ_0 = 2.00 10^{-7} s (Fig. S4†). However, on one hand, these values are poorly precise due to the low number of points in the linear region and on the other hand, the low U_{eff} values are probably much lower than the gap with the Dy^{III} first excited doublet.

A more precise analysis of the χ'_M and χ''_M behaviour was performed using the generalized Debye model,[27,28] where these two variables are analysed jointly with τ (the relaxation rate) and α (the parameter that defines the broadness of the spectra involving the distribution in the relaxation times) represented as Argand plots (Fig. 6, left).

The data extracted from the fitting (CCfit program), is represented in the form of $\ln(\tau)$ *vs.* $1/T$ (Fig. 6, right). Two different relaxations can be observed: the data were simulated following the combination of Orbach and Raman relaxations because the high temperature region clearly follows an Arrhenius-like behaviour while the low temperature region follows the two-phonon relaxation path (eqn (2)).

$$\tau^{-1} = \tau_0^{-1} e^{-Ea/KT} + CT^n \qquad (2)$$

The alpha parameter has a value of 0.06, indicating a narrow distribution of the relaxation times, while the Orbach parameters U_{eff} and τ_0 of 21.77 K and 2.0 × 10^{-7} s are in good agreement with those obtained from the $\chi''_M(T^{-1})$ fit. The

Raman relaxation path was fitted with C = 0.06 and n = 7.3. This value of the Raman coefficient is close to the ones expected for Kramers ions (typically 9–11). However, lower Raman coefficients have been reported commonly relating them to the participation of optical phonons in the spin–phonon interaction.[29,30]

To demonstrate the intervention of the lattice in the magnetic relaxation of complex **6**, ultra-low frequency Raman measurements have been performed (Fig. 7).[31,32] The spectrum evidences the presence of low frequency vibrations appearing at 27, 59 and 84 cm^{-1}, which are compatible with the energy required for a spin–phonon relaxation path.

Photoluminescence characterization

The emissive properties of compounds **2**, **3** and **5** have been studied in polycrystalline samples. As a previous step, the first absorption and emission of the free ligand, $dppeO_2$, was measured in a chloroform solution (Fig. S5†). The phosphine oxide ligand shows an absorption band at 265 nm. Additionally, the excitation and emission spectra of the free ligand have been recorded at an excitation wavelength (λ_{exc}) of 270 nm (an λ_{exc} of 260 nm cannot be used due to instrumental limitations) and at an emission wavelength (λ_{em}) of 320 nm, respectively.

Excitation of the lanthanide samples at 270 nm induces an emission response for the three measured compounds leading to the characteristic luminescence for each lanthanide cation. Nevertheless, the sensitization effect is not efficient since the emission intensity is rather low. Furthermore, in the excitation spectra recorded at λ_{em} values of 597 nm ($^4G_{5/2} \rightarrow {}^6H_{7/2}$) for **2**, 619 nm ($^5D_0 \rightarrow {}^7F_2$) for **3** and 545 nm ($^5D_4 \rightarrow {}^7F_5$) for **5** the signals arising from the excitation f–f transitions are more intense and can be well differentiated with respect to the bands corresponding to the π–π* and n–π* transitions from the benzene groups of the ligand moieties. Also, the free ligand absorption and emission wavelengths are found in the 270–300 nm UV range suggesting that the phosphine molecule in each Ln^{III} compound would also absorb light in this range. Then, the whole excitation of the ligand under 300 nm is difficult to observe in all the excitation spectra due to instrumental limitations.
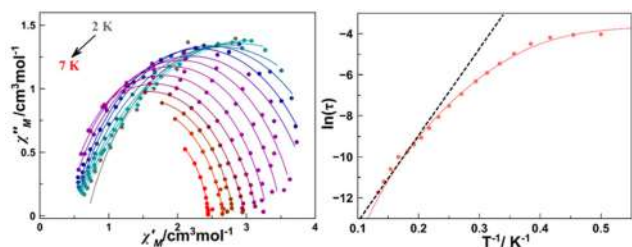
Fig. 6 Left, Argand plot of the magnetic susceptibility of **6**. Right, temperature dependence of the relaxation time as a function of the temperature plotted as $\ln(\tau)$ *vs.* inverse of T. Solid lines show the best fit of the experimental data (Orbach plus Raman fitting) and dotted lines show the slope of the Orbach high temperature regime.
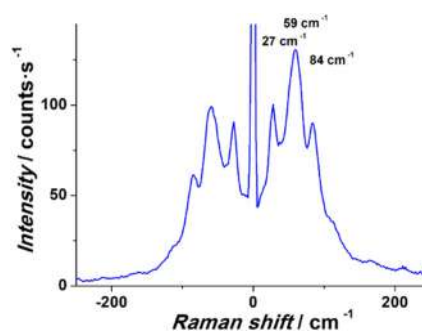

Fig. 7 Ultralow frequency Raman spectrum of complex **6** showing low energy vibrations.

Besides, the energy gaps between the excited singlet and triplet states of the ligand and the respective lanthanide emitting state ions ($^5D_0$ for Eu^{III}, $^4D_4$ for Tb^{III}, $^4G_{5/2}$ for Sm^{III}) are too large. Nevertheless, the distortion due to crystal field perturbation in these structures makes the f–f transitions less forbidden by Laporte's rule and excitation of each sample at their respective f–f excitation transitions, induced more intense emission signals than when exciting the sample in the ligand excitation wavelength, especially for the Eu^{III} and Tb^{III} compounds that the emission color could be seen in the naked eye (Fig. S6†).[33,34]

Compound 2 (Sm^{III}). The excitation spectrum recorded at the emission wavelength of 597 nm ($^4G_{5/2} \rightarrow {}^6H_{7/2}$) for compound **2** is presented in Fig. 8. The band in the 270–300 nm range is attributed to the excitation of the ligands present in the structure. Then, in the near UV range, a series of bands appear belonging to the excitation of Laporte forbidden transitions from the f orbitals of the Sm^{III} ion. The most intense band in the spectra appears at 403 nm and it is assigned to the $^6H_{5/2} \rightarrow {}^4F_{7/2}$ transition followed by the bands at 345, 363 and 375 nm that are assigned to $^6H_{5/2} \rightarrow {}^4H_{9/2}$, $^6H_{5/2} \rightarrow {}^4D_{3/2}$ and $^6H_{5/2} \rightarrow {}^4D_{1/2}$ transitions, respectively.[35,36] Moreover, the sharp band at 296 nm agrees with the residual $\frac{1}{2}$ harmonic signal from the lamp's instrument. By exciting the Sm^{III} sample at the ligand excitation wavelength of 275 nm, an emission spectrum with a poor signal is obtained.

Nevertheless, when **2** is excited at 403 nm, corresponding to the $^6H_{5/2} \rightarrow {}^4F_{7/2}$ excitation transition, a more intense spectrum with the expected Sm^{III} emission bands is acquired, Fig. 8. In this manner, there is a rapid non-radiative deactivation from the $^4F_{7/2}$ energy level to the emitting $^4G_{5/2}$ state due to the closely spaced energy levels of these spectroscopic terms. Then the $^4G_{5/2} \rightarrow {}^6H_{5/2-11/2}$ radiative transitions take place. The band at 564 nm is assigned to $^4G_{5/2} \rightarrow {}^6H_{5/2}$ which is a pure magnetic dipole transition ($\Delta J = 0$). The more intense signal at 597 nm corresponds to $^4G_{5/2} \rightarrow {}^6H_{7/2}$ ($\Delta J = \pm 1$) and along with the selection rule, the transition is partially magnetic and partially forced electric dipole allowed. Next the electric dipole transition ($\Delta J = \pm 2$) $^4G_{5/2} \rightarrow {}^6H_{9/2}$, more susceptible to the crystal field (hypersensitive transition), is discerned at 643 nm followed by $^4G_{5/2} \rightarrow {}^6H_{11/2}$ as a low intensity band. It is known that the intensity ratio between the magnetic dipole and electric dipole transitions can be an indicator of the symmetry site of the lanthanide cation inside the structure. For compound **2**, the integrated area of the $^4G_{5/2} \rightarrow {}^6H_{9/2}$ band is larger than that of the $^4G_{5/2} \rightarrow {}^6H_{5/2}$ band, indicating certain asymmetry in the Sm^{III} coordination environment[37–39] (the symmetry point group of the coordination polyhedron of **2** does not present an inversion symmetry).

Compound 3 (Eu^{III}). For compound **3**, the excitation spectra at 280 nm show an increase of the signal, suggesting the excitation of the ligand (Fig. 9). Measurements above 270 nm cannot be performed due to instrumental limitations. Then, the signals observed at a higher wavelength correspond to the f–f centred transitions from the Eu^{III} cation and are assigned to $^5D_4 \leftarrow {}^7F_0$ at 375 nm and the more intense band at 394 nm corresponds to $^5L_6 \leftarrow {}^7F_0$ and at 464 nm to $^5D_2 \leftarrow {}^7F_0$ transitions.
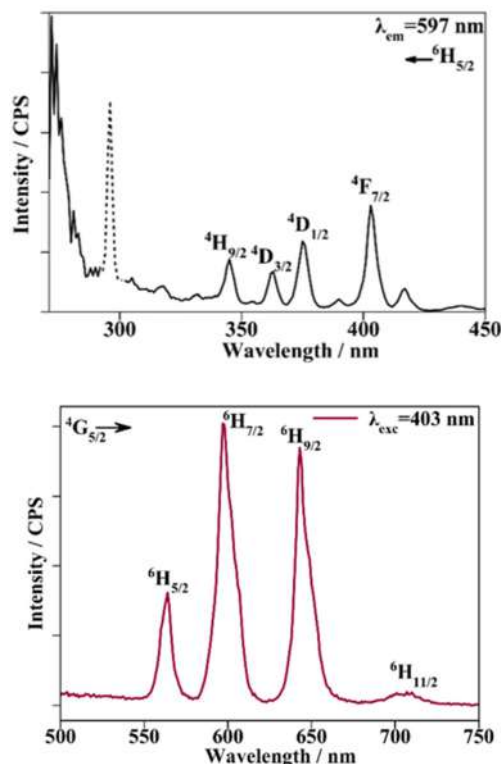

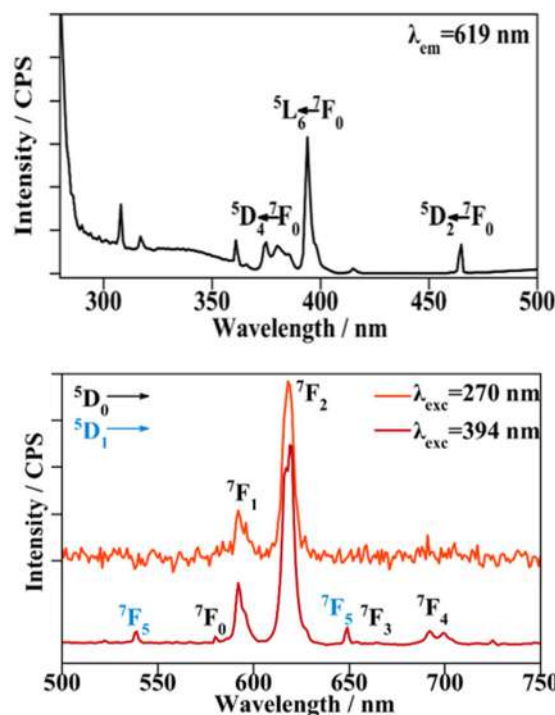Fig. 8 Excitation (top) and emission (bottom) spectra of compound **2**.

Fig. 9 Excitation (top) and emission (bottom) spectra of compound **3**.

When the sample is excited at the ligand excitation wavelength (270 nm) the emission spectrum (shown in Fig. 9, top) is recorded. The signal to noise ratio is high and only two bands are observed. Still, when the λ_{exc} employed is 394 nm, corresponding to the highest metal centred f–f excitation transition $^5L_6 \leftarrow {^7F_0}$, an emission spectrum with a higher resolution could be recorded (Fig. 9, bottom). The bands corresponding to the emission from the $^5D_0$ emitting energy level at 580, 592, 619, 654 and 696 nm are in good agreement with the $^5D_0 \rightarrow {^7F_{(0-4)}}$ transitions. The magnetic dipole $^5D_0 \rightarrow {^7F_1}$ transition, the intensity of which is independent of its environment, is split due to the crystal field in the spectrum recorded at λ_{exc} = 270 nm. This splitting is manifested as a shoulder for the λ_{exc} = 394 nm spectrum. Next, the most intense band corresponding to the electric dipole $^5D_0 \rightarrow {^7F_2}$ transition presents a small split due to the crystal field effect and the $^5D_0 \rightarrow {^7F_2}/^5D_0 \rightarrow {^7F_1}$ ratio is 4.7, suggesting that the Eu^{III} cation does not belong to a point group with inversion symmetry inside the structure. When exciting the sample at 394 nm, the $^5D_4$ excited level deactivates through radiationless transitions to the $^5D_0$ emitting level, leading to the above-mentioned transitions. In addition, radiative transitions take place from the $^5D_1$ energy level, higher in energy than the $^5D_0$ level. The bands corresponding to these transitions are located at 539 nm corresponding to $^5D_1 \rightarrow {^7F_1}$ and at 649 nm, they overlapped with the $^5D_0 \rightarrow {^7F_3}$ transition, assigned to $^5D_1 \rightarrow {^7F_5}$.[40]

$$I(t) = A_0 \exp\left(-\frac{t}{t_{obs}}\right) + I_0 \tag{3}$$

Luminescence lifetime decay was measured for the europium compound. The experiment was monitored at an emission wavelength of 614 nm and the sample was excited at 395 nm. The decay curve presented in the semi-log plot is shown in Fig. 10 and it could be fitted with a mono-exponential equation (eqn (3)) which is consistent with one de-activation mechanism. The luminescence lifetime (τ_{obs}) of **3** is 1.65 ms. Furthermore, the pure magnetic dipole character of
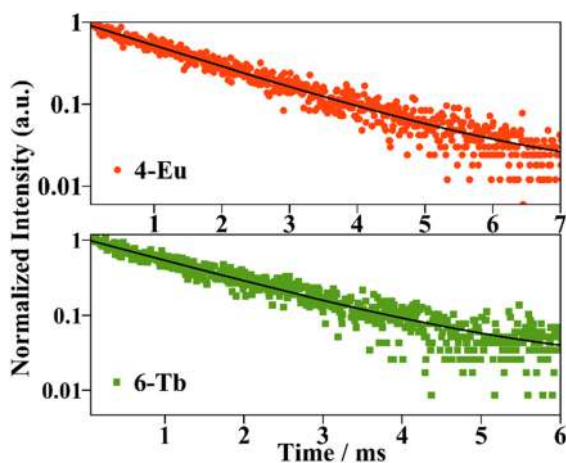
europium's $^5D_0 \rightarrow {^7F_1}$ transition allows the calculation of the radiative rate constant k_{rad} from the corrected emission spectrum, using a simplified equation presented by Werts *et al.* (eqn (4)).[41] The τ_{rad} ($k_{rad} = 1/\tau_{rad}$) parameter accounts for the lifetime of luminescence deactivation from the emitting level if all the deactivation transitions were of radiative nature and for **4** it was found to be 2.9 ms. The calculated τ_{rad} value is higher than the observed lifetime obtained from the measurement elucidating that faster non-radiative deactivation processes take place reducing the τ_{obs}. Additionally, the ratio between the radiative rate and the luminescence deactivation rate of the compound defines the intrinsic quantum yield (ϕ_{Ln}^{Ln}) which is the emission efficiency once the Eu^{III} emitting level is populated. For **3**, (ϕ_{Ln}^{Ln}) is 55%.

$$\phi_{Ln}^{Ln} = \frac{k_{rad}}{k_{rad} + k_{non-rad}} = \frac{\tau_{obs}}{\tau_{rad}} \tag{4}$$

Compound 5 (Tb^{III}). Finally, in the excitation spectra of compound **5**, excitation transitions from terbium's f^8 orbitals arise in the 300 to 400 nm range, Fig. 11. The bands corresponding to the excitation transitions from the $^7F_6$ ground state are assigned as follows: $^7F_6 \rightarrow {^5D_1}, {^5D_0}, {^5G_J}, {^5D_2}, {^5G_J}, {^5L_{10}}$, and $^5D_3$ at 318, 325, 340, 351, 359, 368 and 378 nm, respectively.[39] Furthermore, an increase of the signal intensity is perceived below 300 nm corresponding to ligand excitation that cannot be entirely seen since ligand absorption occurs at a lower wavelength in the UV range added to the poor sensitization effect in these systems. Nevertheless, f–f centred excitation tran-
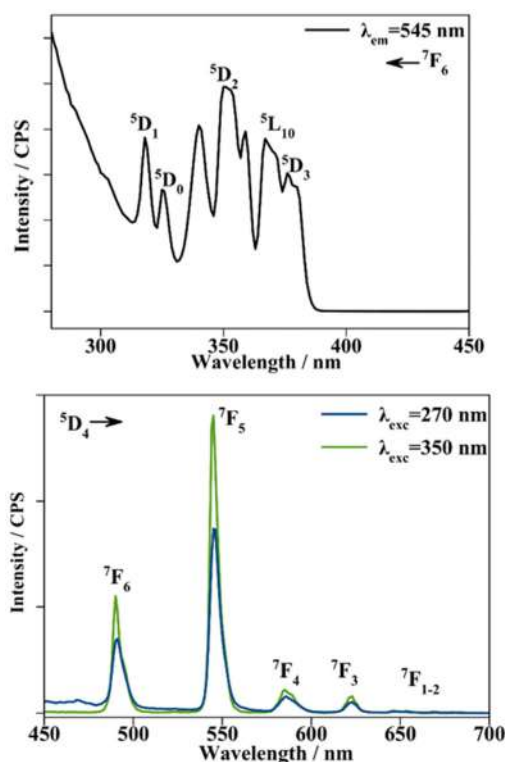

Fig. 10 Luminescence lifetimes curves of compounds **3** and **5**. Solid lines represent mono-exponential fittings using eqn (3).

Fig. 11 Excitation (top) and emission (bottom) spectra of compound **5**.

sitions from the lanthanide ion are well defined and intense enough to record the emission spectrum of compound **5** (Fig. 11). Exciting the sample at 270 nm (ligand excitation) induced the emission of **5** and the expected bands from f–f transitions are discerned at 490, 545, 586 and 623 nm, consistent with the radiative transitions from the $^5D_4$ emitting energy level to the $^7F_{6-3}$ ground state, respectively. Among this, very weak bands corresponding to $^5D_4 \rightarrow {}^7F_{2-1}$ transitions are perceived in the 650–700 nm range. Furthermore, when the emission measurement is monitored at an λ_{exc} of 350 nm, corresponding to the highest in intensity $^7F_6 \rightarrow {}^5D_2$ f–f excitation transition, the same terbium emission bands are recorded using the λ_{exc} that corresponds to the intraconfigurational 4f–4f transition of Tb^{III} leading to luminescence higher in intensity.[42–44]

The luminescence lifetime decay of **5**, monitored at an emission wavelength of 545 nm and at an excitation wavelength of 350 nm that agrees with the Tb^{III} centred $^7F_6 \rightarrow {}^5D_2$ transition, yielded 1.51 ms. For the terbium compound, the decay curve also followed a mono-exponentially function suggesting a single deactivation mechanism as the Eu^{III} compound.

Conclusions

A new family of phosphine oxide lanthanide-derived compounds has been synthesized and characterized by structural, magnetic and luminescence techniques. Two different structures can be achieved while using the same synthesis, and the final topology of the products seems independent of the previously proposed factors like lanthanide size or co-ligands but determined by the solvents. Moreover, the first monodimensional chain-like structure has been achieved for dppeO$_2$ lanthanide coordination compounds. All the family members have been magnetically characterized, but only Dy presents a field-induced SIM response following an Orbach-like plus Raman relaxation path. Among these, the visible emitters Sm^{III}, Eu^{III} and Tb^{III} systems have been studied in their specific emission range, and all of them present good emission properties.

Author contributions

E. P.: synthesis, magnetic measurements, and data analysis; A. T.: luminescence measurements, data analysis, and original draft writing; M. F.-B.: single crystal X-ray crystallography; S. S.: preliminary luminescence spectra; A. E.: structural analysis, conceptualization, writing and editing. A. G.: funding acquisition and project administration; and J. M.: supervision of the experimental work and measurements, final manuscript writing, and conceptualization.

Conflicts of interest

There are no conflicts to declare.

References

1 C. M. G. Dos Santos, A. J. Harte, S. J. Quinn and T. Gunnlaugsson, *Coord. Chem. Rev.*, 2008, **252**, 2512.

2 S. Shinoda and H. Tsukube, *Analyst*, 2011, **136**, 431.

3 A. Dey, P. Kalita and V. Chandrasekhar, *ACS Omega*, 2018, **3**, 9462.

4 R. A. Layfield and M. Murugesu, *Lanthanides and Actinides in Molecular Magnetism*, John Wiley & Sons, 2015.

5 R. Marin, G. Brunet and M. Murugesu, *Angew. Chem., Int. Ed.*, 2021, **60**, 1728.

6 L. Bogani and W. Wernsdorfer, *Nat. Mater.*, 2008, **7**, 179.

7 A. M. Kaczmaret, Y.-Y. Liu, C. Wang, B. Laforce, L. Vincze, P. Van Der Vort, K. Van Hecke and R. Van Deun, *Adv. Funct. Mater.*, 2017, **27**, 1700258.

8 W. Ren, G. Lin, C. Clarke, J. Zhou and D. Jin, *Adv. Mater.*, 2020, **32**, 1901430.

9 L. Sorace, C. Benelli and D. Gatteschi, *Chem. Soc. Rev.*, 2011, **40**, 3092.

10 J. Luzón and R. Sessoli, *Dalton Trans.*, 2012, **41**, 13556.

11 H. Zhang, Z.-H. Chen, X. Liu and F. Zhang, *Nano Res.*, 2020, **13**, 1795.

12 A. D'Aléo, F. Pointillart, L. Ouahab, C. Andraud and O. Maury, *Coord. Chem. Rev.*, 2012, **256**, 1604.

13 A. W. G. Platt, *Coord. Chem. Rev.*, 2017, **340**, 62.

14 R. D. Bannister, W. Levason, G. Reid and W. Zhang, *Polyhedron*, 2017, **133**, 264.

15 Z. Spichal, M. Necas and J. Pinkas, *Inorg. Chem.*, 2005, **44**, 2074.

16 Z. Spichal, M. Nekas, J. Pankas and J. Novosad, *Inorg. Chem.*, 2004, **43**, 2776.

17 P. Pekarkova, Z. Spichal, P. Taborsky and M. Nekas, *Luminescence*, 2011, **26**, 650.

18 W. Q. Lin, D. R. Wang, W. J. Long, L. S. Lin, Z. X. Tao, J. L. Liu, Z. Q. Liu and J. D. Leng, *Dalton Trans.*, 2022, **51**, 5159.

19 S. A. Cotton and P. R. Raithby, *Coord. Chem. Rev.*, 2017, **340**, 220.

20 A. M. J. Lees and A. W. G. Platt, *Inorg. Chem.*, 2003, **42**, 4673.

21 G. M. Sheldrick, *SHELXL-2014/7: Program for the Solution of Crystal Structures*, University of Göttingen, Göttingen, Germany, 2014.

22 F. Marchetti, C. Pettinari, A. Pizzabiocca, A. A. Drozdov, S. I. Troyanov, C. O. Zhuravlev, S. N. Semenov, Y. A. Belousov and I. G. Timokhin, *Inorg. Chim. Acta*, 2010, **363**, 4038.

23 M. Lunell, D. Casanova, J. Cirera, P. Alemany and S. Alvarez, *SHAPE v.2.0*, Barcelona, 2010. The program can be obtained by request to the authors.

24 N. F. Chilton, R. P. Anderson, L. D. Turner, A. Soncini and K. S. Murray, *J. Comput. Chem.*, 2013, **34**, 1164.

25 M. V. Marinho, D. O. Reis, W. X. C. Oliveira, L. F. Marques, H. O. Stumpf, M. Déniz, J. Pasán, C. Ruíz-Pérez, J. Cano, F. Lloret and M. Julve, *Inorg. Chem.*, 2017, **56**, 2108.

26 A. Worrell, D. Sun, J. Mayans, C. Lampropoulos, A. Escuer and T. C. Stamatatos, *Inorg. Chem.*, 2018, **57**, 13944.

27 K. S. Cole and R. H. Cole, *J. Chem. Phys.*, 1941, **9**, 341.

28 P. Debye, *Phys. Z.*, 1938, **39**, 616.

29 L. Gu and R. Wu, *Phys. Rev. B*, 2021, **103**, 01441.

30 K. N. Shivatava, *Phys. Status Solidi B*, 1983, **117**, 437.

31 M. Atzori, S. Benci, E. Morra, L. Tesi, M. Chiesa, R. Torre, L. Sorace and R. Sessoli, *Inorg. Chem.*, 2018, **57**, 731.

32 M. Briganti, F. Santanni, L. Tesi, F. Totti, R. Sessoli and A. Lunghi, *J. Am. Chem. Soc.*, 2021, **143**, 13633.

33 Y.-S. Meng, Y.-S. Qiao, Y.-Q. Zhang, S.-D. Jiang, Z.-S. Meng, B.-W. Wang, Z.-M. Wang and S. Gao, *Chem. – Eur. J.*, 2016, **22**, 4704.

34 M. Latva, H. Takalo, V. M. Mukkala, C. Matachescu, U. J. C. Rodríguez-Ubis and J. Kankare, *J. Lumin.*, 1997, **75**, 149.

35 F. A. Mautner, F. Bierbaumer, R. Vicente, S. Speed, A. Tubau, R. C. Fischer and S. S. Massoud, *Magnetochemistry*, 2022, **8**, 72.

36 C. K. Jayasankar and E. Rukmini, *Opt. Mater.*, 1997, **8**, 193.

37 R. Yu, N. Xue, T. Wang, Z. Zhao, J. Wang, Z. Hei, M. Li, H.-M. Noh and J.-H. Jeong, *Ceram. Int.*, 2015, **41**, 6030.

38 J. Bolton, *J. Lumin.*, 2021, **231**, 117717.

39 I. J. Al-Busaidi, R. Ilmi, D. Zhang, J. D. L. Dutra, W. F. Oliveira, N. K. Al Rasbi, L. Zhou, W.-Y. Wong, P. R. Raithby and M. S. Kahn, *Dyes Pigm.*, 2022, **197**, 109879.

40 K. Binnemans, *Coord. Chem. Rev.*, 2015, **295**, 1.

41 M. H. V. Werts, R. T. F. Jukes and J. W. Verhoeven, *Phys. Chem. Chem. Phys.*, 2002, **4**, 1542.

42 Y.-C. Li, Y.-H. Chang, Y.-J. Lin and C.-H. Laing, *J. Phys. Chem. C*, 2007, **111**, 210682.

43 A. J. Kanimozdhi and V. Alexander, *Dalton Trans.*, 2017, **46**, 8562.

44 X. Zhou, X. Zhao, Y. Wang, B. Wu, J. Shen, L. Li and Q. Li, *Inorg. Chem.*, 2014, **53**, 12275.

"Magnetic and optical study in a new family of multidimensional and multiproperty PO-lanthanide(III) derived systems."

Evangelos Pilichos,[a] Annia Tubau,[a] Mercè Font-Bardia,[b] Saskia Speed,[a] Albert Escuer[a,c] Arnald Grabulosa*[a,c] and Júlia Mayans *[a],c

[a] Departament de Química Inorgànica i Orgànica, Secció Inorgànica and Institute of Nanoscience (IN²UB) and Nanotecnology, Universitat de Barcelona, Martí i Franquès 1-11, Barcelona-08028, Spain.

[b] Departament de Mineralogia, Cristal·lografia i Dipòsits Minerals, Universitat de Barcelona, Martí Franqués s/n, 08028 Barcelona (Spain) and Unitat de Difracció de R-X. Centre Científic i Tecnològic de la Universitat de Barcelona (CCiTUB), Solé i Sabarís 1-3. 08028 Barcelona.

[c] Institute of Nanoscience and Nanotecnology (IN²UB). Universitat de Barcelona, Martí i Franquès 1-11, Barcelona-08028, Spain.

Fig. S1. Powder diffraction spectra

Fig. S2. Infrared spectra for complexes **1** and **3.**

Fig. S3. AC susceptibility measurements for complexes **1** and **5** under different dc applied fields

Fig. S4. Arrhenius-like fit for the high temperature region of complex **6**

Fig. S5. Absorption and emission spectra of the free ligand $DppO_2$

Fig. S6. Emission color under irradiation of a UV lamp of compounds **4** and **5**.
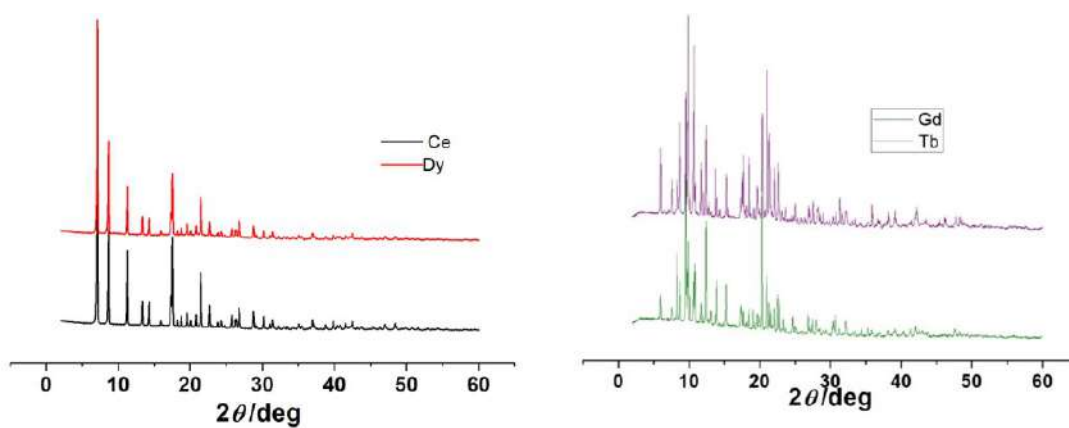
Fig. S1. Left, powder diffraction spectra for compounds **1** and **6**. Right, powder diffraction spectra for compounds **4** and **5.**
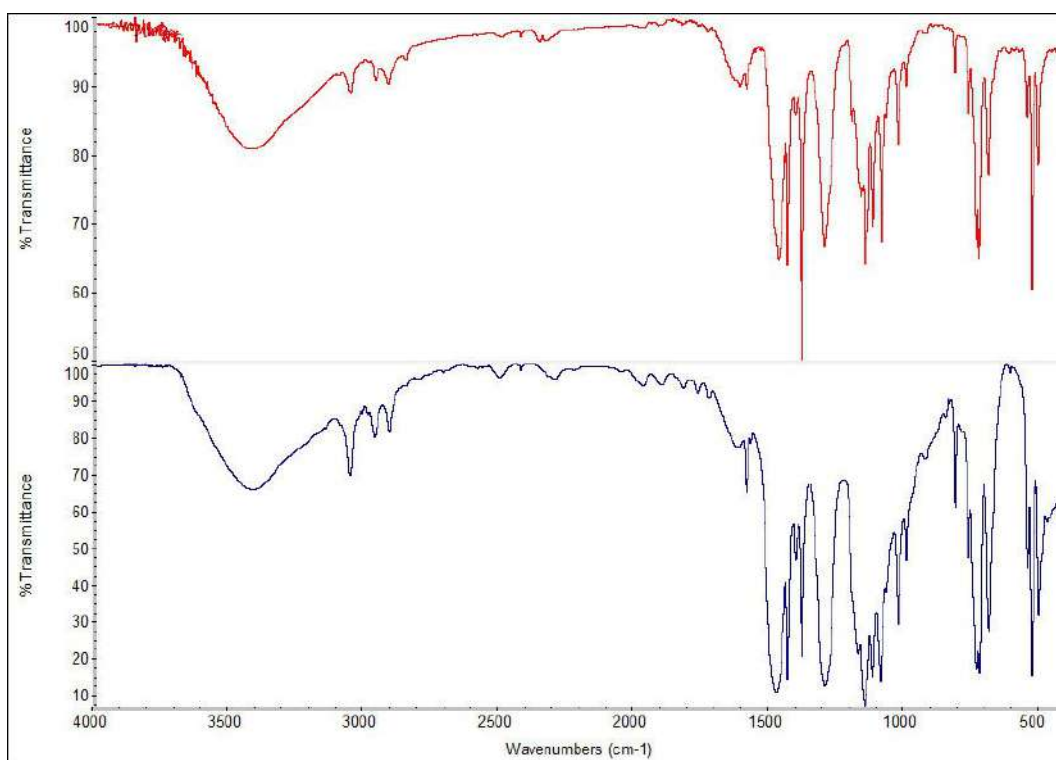
Fig. S2. Infrared spectra for the representative 2D Ce^{III} complex **1** (top) and the Eu^{III} 1D system **3.**
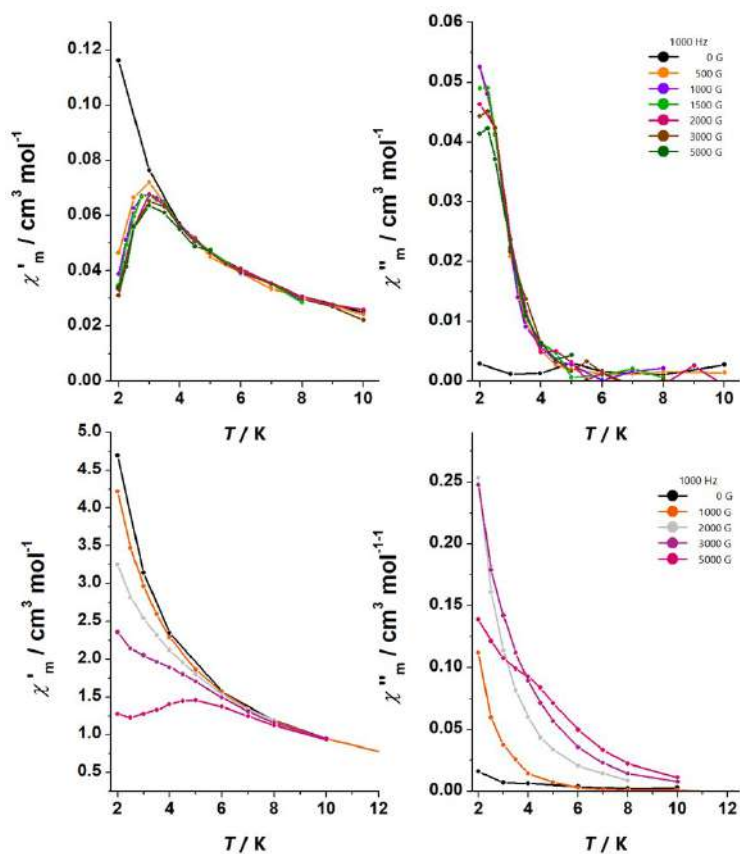
Fig. S3. AC susceptibility measurements for complexes **1** (top) and **5** (bottom) under different dc applied fields, swowing the tails of out-of-phase signals at low temperature.
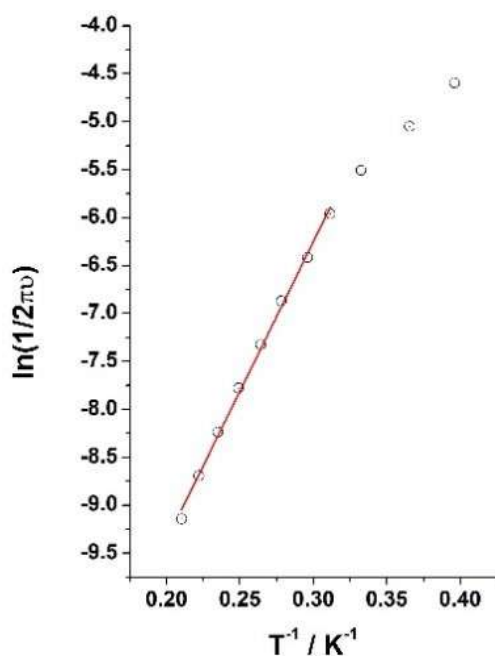
Fig. S4. Arrhenius-like fit for the high temperature region of complex **6**.
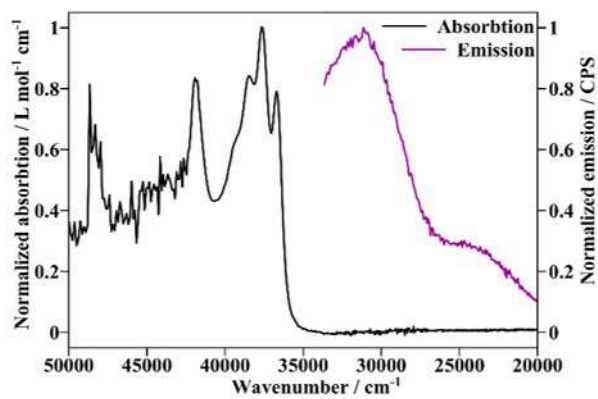
Fig. S5. Absorption and emission spectra of the free ligand DppO$_2$ measured in a 3.4·10^{-6} M CHCl$_3$ solution.
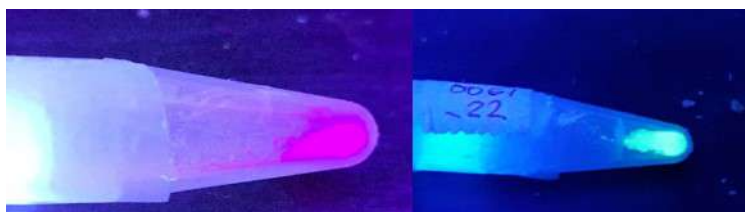
Fig. S6. Emission color under irradiation of a UV lamp of compounds **4** (left) and **5** (right).

PUBLICATION #3

"Field-Induced Slow Magnetic Relaxation in a New Family of Tetranuclear Double-Stranded Cu_2^{II}-Ln_2^{III} Metallohelicates"

Article

Field-Induced Slow Magnetic Relaxation in a New Family of Tetranuclear Double-Stranded $Cu_2^{II}-Ln_2^{III}$ Metallohelicates

Sergio Caballero, Evangelos Pilichos, Mercè Font-Bardia, Júlia Mayans, and Albert Escuer*

Read Online

ACCESS | Metrics & More | Article Recommendations | Supporting Information

ABSTRACT: A series of tetranuclear $Cu_2^{II}Ln_2^{III}$ (Ln^{III} from La^{III} to Yb^{III}), double-stranded metallohelicates have been synthesized using a bis-bidentate flexible ligand obtained by condensing *o*-vanillin with 4,4′-oxydianiline. The complexes exhibit a variety of $Ln^{III}$ environments and decreasing coordination number along the series and several nitrato coordination modes proved by the structural determination of the La^{III} (**1La**), Sm^{III} (**4Sm**), Gd^{III} (**5Gd**), Er^{III} (**9Er**), and Yb^{III} (**10Yb**) derivatives. The other members of the family (**2Ce**, **3Pr**, **6Tb**, **7Dy**, and **8Ho**) have been characterized by powder X-ray diffraction to verify their isostructurality. Susceptibility measurements show field-induced slow relaxation of the magnetization for the anisotropic Tb^{III} and Dy^{III} complexes and for the isotropic Gd^{III} system.
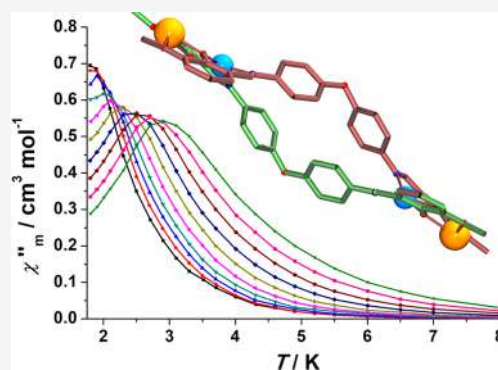
INTRODUCTION

The construction of helical arrays has been a playground for synthetic supramolecular chemists since the apparition of the first one reported in the mid-1950s.[1] Helical structures are achieved by wrapping molecular strands around a central axis, where this wrapping can be controlled by the coordination to a metallic center or by supramolecular interactions.[2−4] Despite this early example, the term helicate was first introduced by Lehn in 1987.[5] Metallohelicates are structures that contain metallic centers surrounded by an organic ligand that should fulfill some criteria to properly wrap around the cation: it should have several sets of donor atoms to be able to coordinate to one or more cations and it should have a flexible enough spacer between the coordination sites. The most common case consists of two sets of donor atoms connected by a more or less long but flexible spacer that can yield double-, triple-, or even quadruple-stranded helicates, benefiting the coordination number of the involved cations.

Many supramolecular structures have been used to build systems exhibiting slow relaxation of magnetization (single-molecule magnets, SMMs), which are, today, one of the main research areas in magnetochemistry because they have been proposed as functional molecules with possible applications in different fields like information storage,[6] molecular spintronics,[7] or quantum information processing (QIP).[8,9] Their characteristic slow relaxation of magnetization arises, in principle, from a high ground spin state (S) and a negative axial magnetic anisotropy (D), giving rise to a potential energy barrier that the spin has to overcome in order to demagnetize.[10,11] However, recently, many exceptions to these paradigms have appeared with the rise of slow-relaxing

molecules with $S = 1/2$, which slowly relax without the possibility of the potential barrier to overcome,[12,13] the apparition of slow-relaxing molecules with a positive value of D,[14−16] and, more recently, the discovery of this magnetic response for isotropic cations.[17−21] Among the wide diversity in slow-relaxing molecules, one of the most abundant types is the one using the highly anisotropic lanthanoid cations as paramagnetic centers, a property arising from their large and unquenched orbital angular momentum.[22,23] Almost any paramagnetic lanthanoid(III) cation can present slow magnetic relaxation under appropriate conditions,[24,25] but Dy^{III} is today the most used one in molecular magnetism, and, until today, it has given rise to some groundbreaking results.[26−28]

On the above basis, we chose the Schiff base 2-(((4-(4-((2-(oxido)-3-methoxybenzylidene)amino)phenoxy)phenyl)-imino)methyl)-6-methoxyphenolato (H_2L), which contains two sets of three donor atoms separated by a flexible spacer, Chart 1. This ligand provides two cavities at each end, which are able to coordinate two cations (or two groups of cations) bridged by phenolato bridges.

The cascade reaction of H_2L with Cu^{II} and further reaction with lanthanoid nitrates allows one to characterize a series of tetranuclear complexes with the common $\{Ln_2^{III}Cu_2^{II}L_2\}$ helical skeleton ($Ln^{III} = La^{III}$ (**1La**), Ce^{III} (**2Ce**), Pr^{III} (**3Pr**),

Chart 1. (top) Structural Formula of the H$_2$L Ligand Employed in This Work to Generate Helical Tetrameric {Ln$_2^{III}$Cu$_2^{II}$L$_2$} Complexes; (bottom) Schematic Plot of the Coordination of Two L^{2-} Ligands to Two Cations at Each End of the Helicate
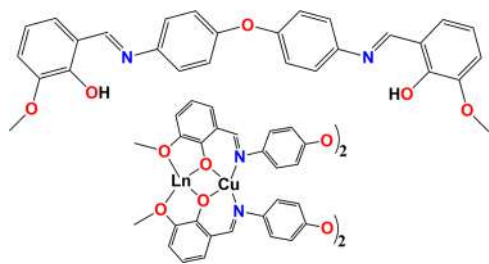
Sm^{III} (**4Sm**), Gd^{III} (**5Gd**), Tb^{III} (**6Tb**), Dy^{III} (**7Dy**), Ho^{III} (**8Ho**), Er^{III} (**9Er**), and Yb^{III} (**10Yb**)) and nitrato counteranions linked to the Ln^{III} and Cu^{II} cations in a variety of modes that fulfill their coordination spheres.

The single-crystal structures of complexes **1La**, **4Sm**, **5Gd**, **9Er**, and **10Yb** were determined, showing the influence of the radii and coordination number of the Ln^{III} cation on the local coordination of the counteranions. The static magnetic properties show weak intramolecular Cu^{II}···Ln^{III} interactions mediated by the phenoxo bridges, and alternating current susceptibility measurements reveal slow relaxation of magnetization for the anisotropic Tb^{III} (**6Tb**) and Dy^{III} (**7Dy**) complexes and also for the less common isotropic case of Gd^{III} (**5Gd**).

EXPERIMENTAL SECTION

Materials and Methods. All manipulations were performed under aerobic conditions. All reagents and solvents were used as received. The infrared spectra (4000−400 cm^{-1}) were recorded on a Thermo Scientific Nicolet IS5 spectrophotometer. The magnetic susceptibility and magnetization measurements were performed with a Quantum Design MPMS-XL SQUID magnetometer at the CCiT Magnetochemistry Unit of the University of Barcelona. Single crystals of compounds **1La**, **4Sm**, **5Gd**, **9Er**, and **10Yb** were set up on a Bruker D8-VENTURE diffractometer equipped with a multilayer monochromator and a Mo microfocus (λ = 0.71073 Å). The frames were integrated with the Bruker SAINT software package using a narrow-frame algorithm, and the structures were solved and refined using the Bruker SHELXTL software package.[29] The diffraction for the complex **5Gd** was not crystallographically satisfactory due to the poor quality of the crystals and the unsolved disorder of the nitrato ligands around one of the Gd^{III} cations; Figure S1. Several crystallizations were performed, but single crystals of better quality were not obtained; thus, the crystallographic data have been included only as Supporting Information for the readers. However, the core of the complex is well defined and the obtained data have been included in the general descriptions. Crystal and structure refinement data are summarized in Table S1. Powder X-ray diffraction analysis was performed with a PANanalytical X'Pert PRO MPD Θ/Θ powder diffractometer.

Synthesis. *H$_2$L Ligand.* The ligand was prepared by the condensation reaction of 2-hydroxy-3-methoxybenzaldehyde and 4,4′-oxydianiline following a slight modification of reported methods.[30] A total of 10 mmol (1.52 g) of the aldehyde was dissolved in 50 mL of ethanol and added to a 50 mL ethanolic suspension of 5 mmol (1.00 g) of the diamine. Upon addition, the mixture immediately took a deep-orange color and was refluxed until an orange precipitate appeared (around 30 min). The reaction mixture was left to cool at room temperature. It was vacuum-filtered, and the crude solid was washed several times with cold ethanol and ether. It was allowed to dry in a desiccator. IR (cm^{-1}): 3445 (br, m),

1615 (sh, s), 1485 (sh, s), 1467 (sh, s), 1286 (sh, s), 1197 (sh, s). ^{1}H NMR (500 MHz, CDCl$_3$) δ (ppm): 13.66 (s, ^{1}H), 8.64 (s, 1H), 7.34−7.28 (m, 2H), 7.12−7.06 (m, 2H), 7.01 (ddd, J = 15.4, 8.0, 1.5 Hz, 2H), 6.89 (t, J = 7.9 Hz, 1H), 3.94 (s, 3H).

Metallohelicates. All of the lanthanoid-derived complexes were prepared following the same procedure using the corresponding lanthanoid(III) nitrate salts. To a stirred suspension of H$_2$L (58.5 mg, 0.125 mmol) in a solvent mixture of MeOH/MeCN (10 mL, 1:1) was added 0.125 mmol (25.2 mg) of [Cu$_2$(CH$_3$COO)$_4$(H$_2$O)$_2$]. The resulting dark-brown solution was stirred until a brown precipitate of [Cu$_2$L$_2$] appeared. The corresponding equimolar amount (0.125 mmol) of Ln(NO$_3$)$_3$·xH$_2$O was dissolved in 10 mL of a MeOH/MeCN (1:1) mixture and added to the suspension of [Cu$_2$L$_2$]. The mixture was stirred for two hours until the solid dissolved and the solution took a dark-yellow-brown color. The resulting solution was filtered, and diethyl ether vapor was allowed to diffuse until dark-brown prism-like crystals suitable for X-ray diffraction appeared for compounds **4Sm** and **5Gd**. For complexes **1La**, **9Er**, and **10Yb**, dark-orange prism-like crystals (∼60% yield) were obtained after layering the corresponding solutions with diethyl ether. We were unable to obtain single crystals of compounds **2Ce**, **3Pr**, **6Tb**, **7Dy**, and **8Ho**, which give polycrystalline powders in all cases. Infrared spectra are provided in Figure S2, and analytical data are summarized in Table S2.

RESULTS AND DISCUSSION

Structural Description. *Powder X-ray Diffraction.* Despite the similar synthetic response and the practically
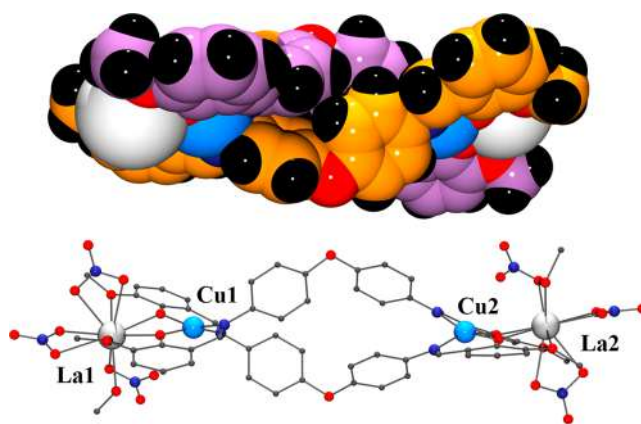

Figure 1. Space filling (top) and ball and stick (bottom) plots of the {Cu$_2$La$_2$(L)$_2$} helicate **1La**, showing the wrapping of the two L^{2-} ligands around the four cations.

superimposable IR spectra, XRPD spectra demonstrate that the structure of complexes **1−10** evolves along the series. The complexes derived from the larger cations **1La**, **2Ce**, and **3Pr** are isostructural, and also **5Gd** and **7Dy** show similar spectra, whereas complexes **4Sm**, **6Tb**, **8Ho**, **9Er**, and **10Yb** are different; Figure S3. From these preliminary data, the structures of five complexes along the series have been solved to check the origin of the structural differences.

Single-Crystal Diffraction. The structures of complexes **1La**, **4Sm**, **5Gd**, **9Er**, and **10Yb** were solved, and the five structures, as could be expected, show similarities in their general trends but show local differences in the coordination sphere around the lanthanoid and the Cu^{II} cations. To avoid repetitive descriptions, the structure of complex **1La** will be described in detail, and for the remaining complexes, only the main differences will be pointed out.
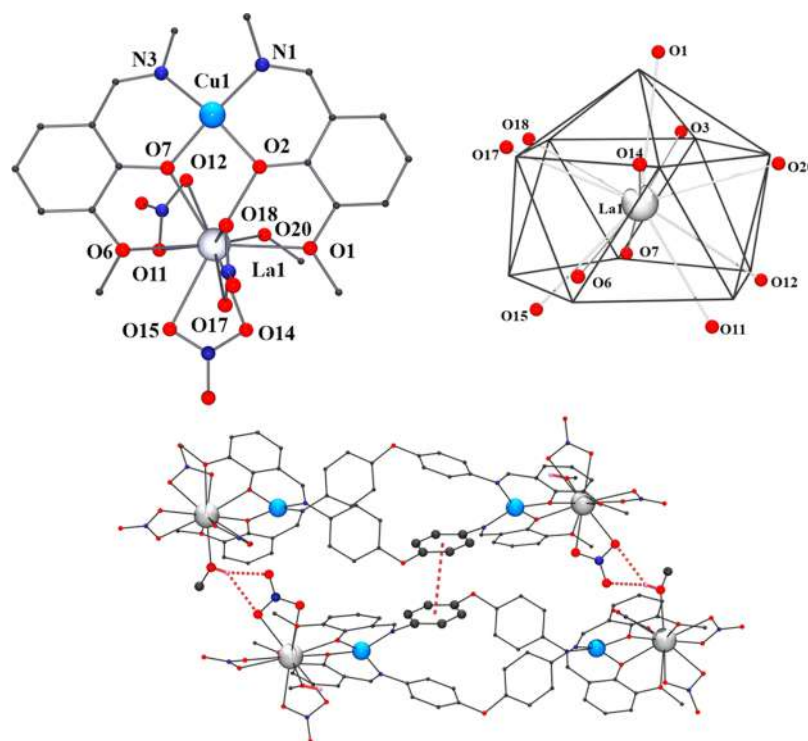
Figure 2. Top-left, labeled plot of the {La(1)Cu(1)} fragment of complex **1La**. For clarity, only this environment is shown because of the similarity to the {La(2)Cu(2)} fragment of the helicate. Top-right, plot of the closest ideal polyhedron around the La1 cation. Bottom, plot of the main intermolecular interactions present in the structure of complex **1La** (H-bonds and intercentroid distance are emphasized as dotted red bonds).

Table 1. Selected Bond Distances and Bond Angles for the {La(1)Cu(1)} Fragment of Complex 1La

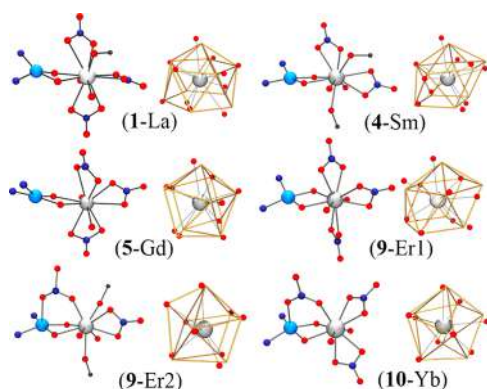| Bond Distances (Å)			
Cu1–O2	1.919(3)	Cu1–N1	1.964(3)
Cu1–O7	1.920(3)	Cu1–N3	1.965(3)
La1–O1	2.675(3)	La1–O6	2.719(3)
La1–O2	2.506(2)	La1–O7	2.527(2)
La1–O11	2.561(3)	La1–O12	2.855(4)
La1–O14	2.628(3)	La1–O15	2.647(3)
La1–O17	2.623(3)	La1–O18	2.675(3)
La1–O20	2.563(3)		
Bond Angles (deg)			
La1–O2–Cu1	107.0(1)	La1–O7–Cu1	106.2(1)

Figure 3. Coordination environment and ideal polyhedron of the lanthanoid cation for the Cu1/Ln1 fragments of complexes **1La**, **4Sm**, **5Gd**, and **10Yb**. The environments of Er1 and Er2 (complex **9Er**) are shown due their different coordination number.
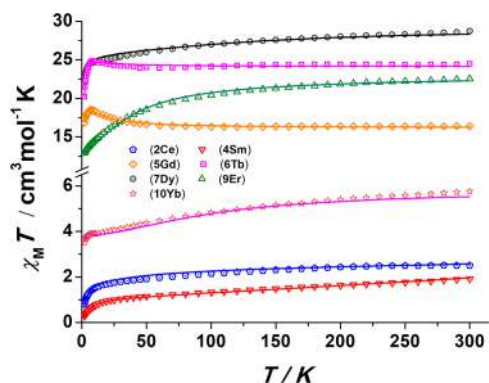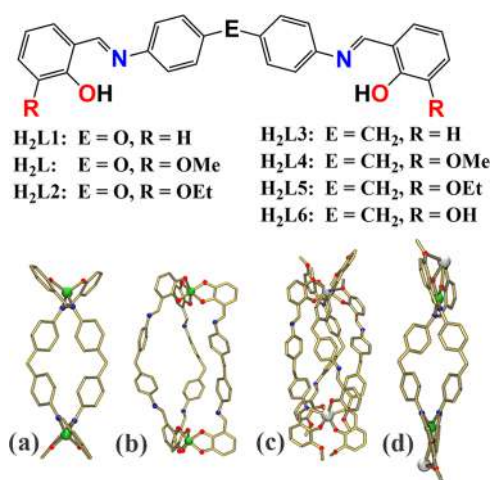
$[Cu_2La_2(L)_2(MeOH)_2(NO_3)_6]\cdot 1.5CH_3CN\cdot C_4H_{10}O$ (**1La**·$1.5CH_3CN\cdot C_4H_{10}O$). Complex **1La** consists of a {Cu_2La_2} tetranuclear double-stranded helicate in which the four cations are held together by the two deprotonated L^{2-} ligands; Figure 1. A labeled plot of **1La** is shown in Figure 2, and the main bond parameters are summarized in Table 1.

Each Cu^II cation is coordinated by one N-iminic atom and one O-phenoxo donor atom from each L^{2-} ligand, resulting in a N_2O_2 chromophore. The Cu^II cation is placed in a square planar environment with a significant tetrahedral distortion (the dihedral angle between the OCuO/NCuN mean planes is 30.5°). The Cu–N distances for both Cu^II cations vary between 1.957(3) and 1.965(3) Å, and the Cu–O distances are slightly shorter, comprising between 1.914(2) and 1.921(2) Å. The O_phenoxo donors act as bridges between the La^III and Cu^II cations, resulting in a bent four-membered Cu–(O)_2–La ring (Cu–O–O–La torsion angles of 19.5(1)° for the Cu1–O2–O7–La1 ring and 23.0(1)° for the Cu2–O4–O9–La2 ring). In addition to the two O_phenoxo donors, each La^III cation links two O_methoxo donors, three bidentate nitrate anions, and one methanol molecule, resulting in an undecacoordination (LaO_11). Intermolecular interactions between clusters comprise π···π stacking interactions established between neighboring phenyl rings from the diphenyl-ether moieties with a centroid ring distance of 3.576(2) Å and H-bonds between the coordinated methanol molecules and one oxygen of the nitrate from the neighbor clusters with O···O distances of 2.815(5)–2.920(5) Å; Figure 2, bottom.

Continuous shape measurements (CShMs) performed with the SHAPE[31] program for the La^III environment shows that the closest polyhedron is a capped pentagonal antiprism (JCPAPR-11), with an ideal C_{5v} symmetry (Figure 2, top-right). However, the CShM value of 3.82 implies a severe
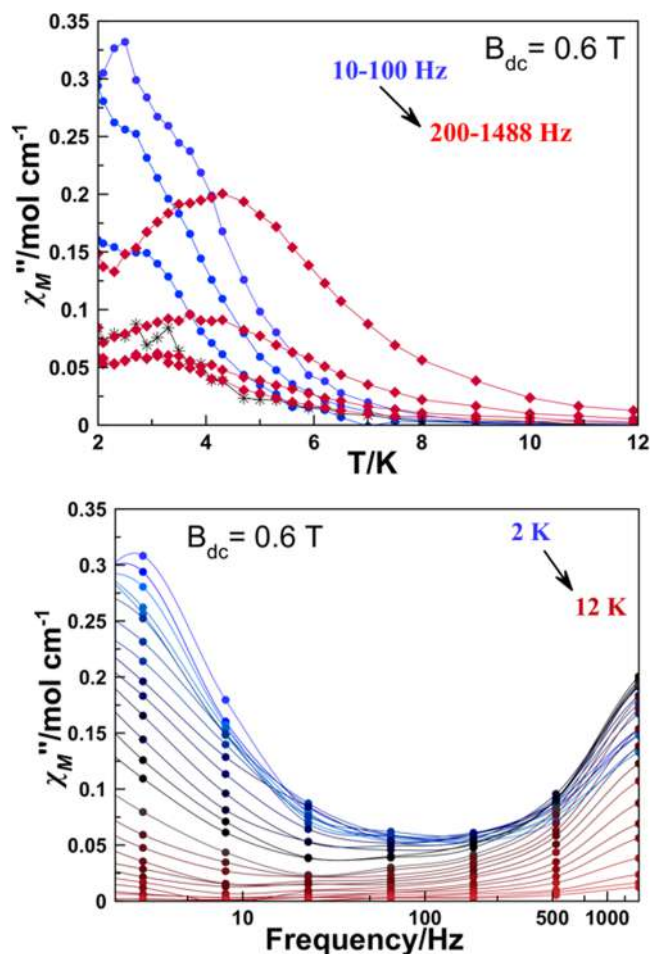
Table 2. Coordination Numbers and Evolution of the Main Bond Parameters (Mean Values) along the Series of Reported Complexes

	1La	4Sm	5Gd	9Er(1)	9Er(2)	10Yb
Cu^{II} coord. number	4	5	4	5	5	5
Ln^{III} coord. number	11	10	10	10	9	9
dCu⋯Ln (Å)	3.549(1)	3.508(1)	3.485(1)	3.465(1)	3.362(1)	3.349(1)
Ln−O$_{phenoxo}$ (Å)	2.507(3)	2.401(3)	2.378(6)	2.321(3)	2.306(3)	2.256(6)
Ln−O$_{methoxo}$ (Å)	2.726(3)	2.636(3)	2.579(6)	2.545(3)	2.565(3)	2.458(6)
torsion Cu−O−O−Ln (deg)	21.3(1)	10.6(1)	5.3(3)	2.0(1)	20.9(1)	18.02(3)
torsion O−O−N−N (deg)	28.3(1)	21.9(1)	22.30(3)	18.9(1)	11.2(1)	11.8(2)

Chart 2. (top) Reported Ligands Derived from Aromatic 4,4′-Diamines Employed to Generate Helical Structures; (bottom) Different Reported Cases of 3d (Tr) or Lanthanoid (Ln) Double Strand {Tr$_2$L$_2$} (a), Triple Strand {Tr$_2$L$_3$} (b), Quadruple Strand {Ln$_2$L$_4$} (c), or Double Strand {Tr$_2$Ln$_2$} (d) Helical Structures

H$_2$L1: E = O, R = H
H$_2$L: E = O, R = OMe
H$_2$L2: E = O, R = OEt

H$_2$L3: E = CH$_2$, R = H
H$_2$L4: E = CH$_2$, R = OMe
H$_2$L5: E = CH$_2$, R = OEt
H$_2$L6: E = CH$_2$, R = OH

(a)   (b)   (c)   (d)

Figure 4. $\chi_M T$ product vs temperature for complexes **2Ce**, **4Sm**, **5Gd**, **6Tb**, **7Dy**, **9Er**, and **10Yb**. The solid lines show the best fit of the data.

Figure 5. Temperature (top) and frequency (bottom) dependence of χ_M'' for the complex **5Gd** at the optimal applied external magnetic field of 0.6 T.

distortion from the ideal polyhedron due to the low O−Ln−O bond angles imposed by the bidentate nitrato ligands that take values lower than 50°. The intramolecular Cu(1)⋯Cu(2) and La(1)⋯La(2) distances are 11.863(1) and 18.930(1) Å, respectively.

{Cu$_2$Ln$_2$(L)$_2$} Complexes [Ln^{III} = Sm^{III} (4Sm), Gd^{III} (5Gd), Er^{III} (9Er), Yb^{III} (10Yb)]. The structures of complexes **4Sm**, **5Gd**, **9Er**, and **10Yb** are similar in general trends to the described La^{III} complex **1La**, with the same distribution of cations and helical shape. However, the flexibility of the L$^{2−}$ Schiff bases

and the radii contraction along the series induce significant differences that are mainly related to the coordination sphere of the Ln^{III} cation; Figure 3.

The decreasing radii of Ln^{III} along the series has, as a consequence, the regular variation of some bond parameters (Table 2) and the concomitant decrease of the coordination number, being 11 the larger one for complexes **1La** and the isostructural Ce^{III} (**2Ce**) and Pr^{III} (**3Pr**) compounds, with a set of four O-donors from the Schiff bases, three bidentate nitrato ligands, and one methanol molecule. For **4Sm** and **5Gd**, the coordination number 10 remains constant but with different nitrato coordination modes. For the complex **4Sm**, the coordination environment is formed by the four O-donors from the L$^{2−}$ ligands, two bidentate nitrato ligands, and two
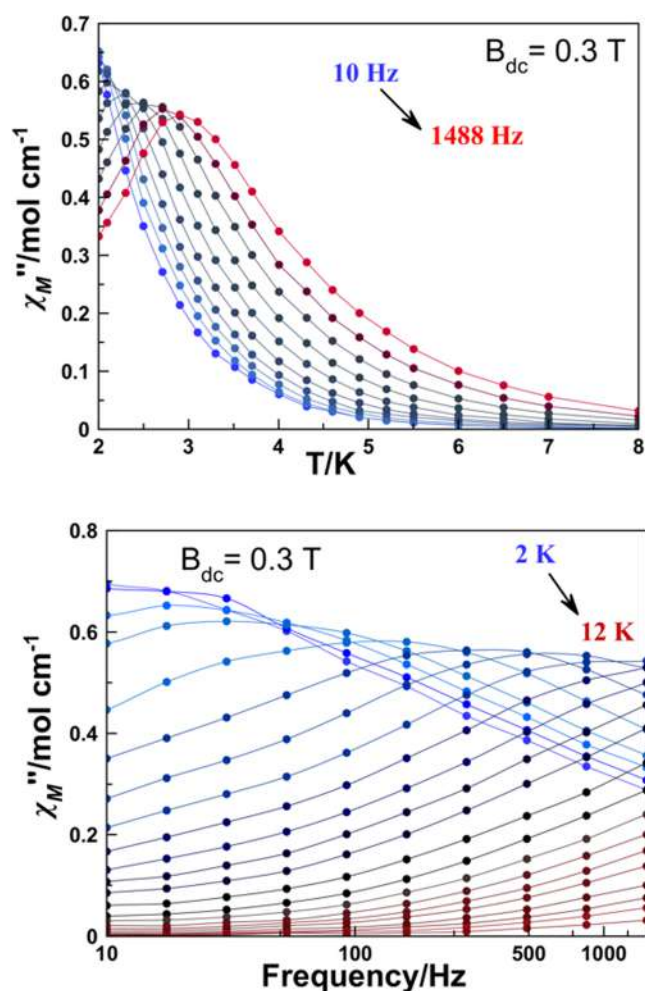
Figure 6. Temperature (top) and frequency (bottom) dependence of $\chi_M{}''$ for the complex **6Tb** at the optimal applied external magnetic field of 0.3 T.

Figure 7. Temperature (top) and frequency (bottom) dependence of $\chi_M{}''$ for the complex **7Dy** at the optimal applied external magnetic field of 0.5 T.

methanol molecules and one bridging nitrato ligand that links to the axial site of the distorted square pyramidal Cu^{II} cation, which shows a N_2O_3 environment.

The Gd^{III} derivative (**5Gd**) exhibits a decacoordination around the lanthanoid, formed by the four O-donor atoms from the L^{2-} ligands and three bidentate nitrato ligands and maintaining the pentacoordination around the Cu^{II} cation by coordination of a methanol molecule. The case of the Er^{III} complex (**9Er**) becomes interesting because Er1 and Er2 cations exhibit different environments, showing the transition to the enneacoordination. Er1 shows the same coordination number 10 and the same set of ligands as the Gd^{III} complex. However, Er2 shows a coordination number of 9, formed by the four O-donors from the L^{2-} ligands, one bidentate nitrato ligand, two methanol molecules, and one O-atom from a nitrato ligand that acts as a bridge with the Cu^{II} cation, which also becomes pentacoordinated. The resulting positive charge of the complex is fulfilled with an ionic nitrate counterion. This case has special interest in future applications because the search for asymmetric dilanthanoid coordination compounds is a hot topic today in the construction of potentially applicable quantum gates.[32] Finally, the Yb^{III} complex **10Yb** shows a similar enneacoordination as Er2 with the coordination sphere formed by the four O-donor atoms from the L^{2-} ligands, two
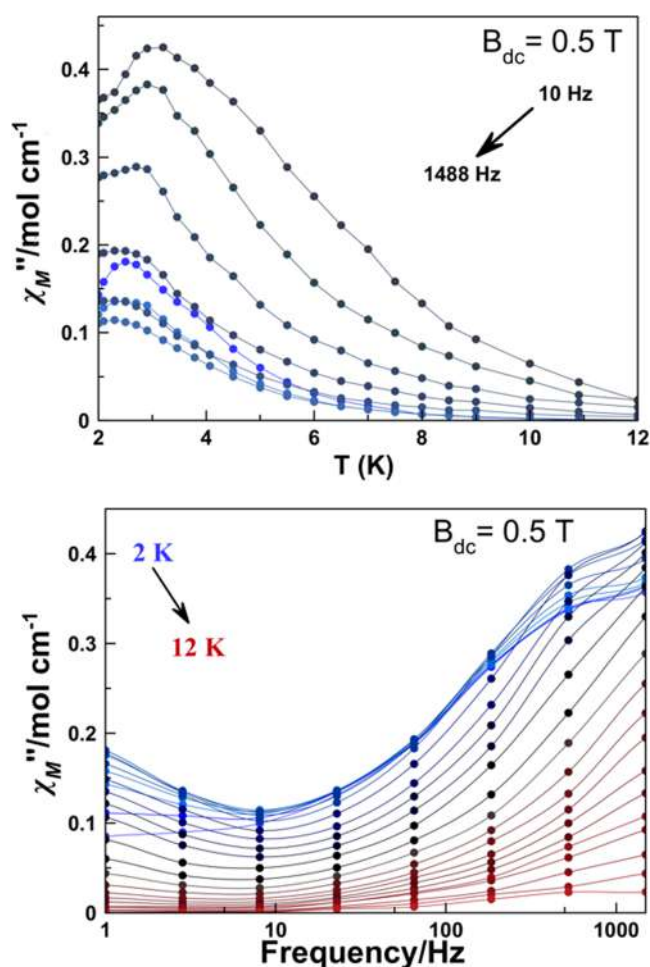

Figure 8. Left, Arrhenius dependence of the $\chi_M{}''(T)$ maxima plotted as $\ln(1/2\pi\nu)$ vs inverse of temperature. Right, fit of the relaxation times in front of inverse of temperature for complexes **6Tb** (green circles) and **7Dy** (blue diamonds) using data extracted from Cole–Cole plots.

bidentate nitrato ligands, and one O-atom from a nitrato ligand that acts as a bridge with the Cu^{II} cation.

In light of the structural data, the molecular formula for these complexes should be better described as $[Cu(L)La-(MeOH)(NO_3)_3]_2$ (**1La**), $[Cu(NO_3)(L)Sm-(MeOH)_2(NO_3)_2]_2$ (**4Sm**), $[Cu(L)Gd(NO_3)_3]_2$ (**5Gd**),

[{CuLEr(NO$_3$)$_3$}{(μ-NO$_3$)CuLEr(MeOH)$_2$(NO$_3$)}] (**9Er**), and [μ-(NO$_3$){Cu(L)Yb(NO$_3$)$_2$}]$_2$ (**10Yb**).

Ligand Overview. The combination of 4,4′-oxydianiline or 4,4′-diaminodiphenylmethane with aldehydes like salicylaldehyde, o-vanillin, 2-hydroxy-3-ethoxybenzaldehyde, or 2,3-dihydroxybenzaldehyde results in a family of highly tunable ligands closely related to H$_2$L. The ligands derived from salicylaldehyde exhibit two bidentate fragments, whereas the 2,3-substituted aldehydes generate ligands with two O,O,N-tridentate fragments with a clearly different coordination capability.

The bis-bidentate ligands derived from salicylaldehyde, H$_2$L1 and H$_2$L3, become adequate for the syntheses of neutral dinuclear helicates containing divalent cations with the general formula [M$_2^{II}$L$_2$]. Several complexes in which L = L1^{2-}, L3^{2-} and M = Co^{II}, Cu^{II}, Zn^{II} have been reported, with the cations usually placed in a N$_2$O$_2$ tetrahedral environment; Chart 2.[33−40] The ligands with an extra O-donor (−OMe, OEt, or −OH) generate bis-tridentate ligands with two sets of NO$_2$ donors that can increase the nuclearity of the helicates. However, their reaction with divalent 3d cations does not increase the nuclearity and tends to give helical dinuclear complexes with the [M$_2^{II}$L$_2$] general formula like those reported for the ligands H$_2$L5 with Cu^{II},[41] H$_2$L2 with Co^{II} and Zn^{II},[39] or H$_2$L with Cu^{II}, Zn^{II}, or Co^{II} [42,43] in which the extra O-methoxo or O-ethoxo donor atoms remain uncoordinated. Very unusual dinuclear triple and quadruple-stranded helicates or mesocates have been reported in two cases employing H$_2$L4 and Dy^{III} or H$_4$L6 and Ti^{IV}.[44,45]

Despite these ligands possessing two cavities with different donor properties able to place a divalent 3d cation in the inner N$_2$O$_2$ cavity and one trivalent 4f cation linked to the O$_4$ donor atoms, heterometallic 3d−4f systems with the {Tr$_2$Ln$_2$L$_2$} core (Tr, divalent 3d cation) have been poorly studied. The reaction of the ligands with the 3d cation acting as a guest generates the helicate topology that acts as a preformed template to bind the 4f cation in a cascade reaction. The scarce examples of this kind of system can be summarized as the {Cu$_2$Gd$_2$L5$_2$} complex that revealed the ferromagnetic Cu^{II}··· Gd^{III} interaction[46] or {Zn$_2$Ln$_2$L4$_2$} complexes in which Ln = Eu^{III}, Nd^{III}, and {Zn$_2$Ln$_2$L$_2$} Ln = Yb^{III}, Er^{III}, which exhibit luminescent response with potential sensor applications induced by the Zn^{II} cation.[47,48]

Magnetic Properties. Direct current (dc) magnetic susceptibility and magnetization measurements were performed for compounds **2Ce**, **4Sm**, **5Gd**, **6Tb**, **7Dy**, **9Er**, and **10Yb** on polycrystalline samples in the 2−300 K range of temperature; Figure 4. The room-temperature $\chi_M T$ values of 2.51, 0.80, 16.40, 24.47, 28.74, 22.53, and 5.75 cm^3 mol^{-1} K are in agreement with the expected values for two Cu^{II} and two Ln^{III} noninteracting cations of 2.35 (**2Ce**, Ce^{III}, ^{2}F$_{5/2}$), 1.36 (**4Sm**, Sm^{III}, ^{6}H$_{5/2}$), 16.50 (**5Gd**, Gd^{III}, ^{8}S$_{7/2}$), 24.39 (**6Tb**, Tb^{III}, ^{7}F$_6$), 29.09 (**7Dy**, Dy^{III}, ^{6}H$_{15/2}$), 23.72 (**9Er**, Er^{III}, ^{4}I$_{15/2}$), and 5.90 (**10Yb**, Yb^{III}, ^{2}F$_{7/2}$) cm^3 mol^{-1} K. On cooling, the $\chi_M T$ shows a roughly constant value for the **5Gd** and **6Tb** complexes, which show a $\chi_M T$ maximum at 7 K for **5Gd** and 10 K for **6Tb**, suggesting ferromagnetic interactions. For complexes **2Ce**, **4Sm**, **7Dy**, **9Er**, and **10Yb**, the $\chi_M T$ plot decreases from room temperature due to the depopulation of the corresponding Stark sublevels.

The Cu^{II}/Ln^{III} pairs are well isolated among them, and thus, the effective magnetic superexchange is mediated by the double diatomic phenoxo bridges between each Cu^{II}−Ln^{III}

independent dimeric fragment. On these bases, for the case of the complex **5Gd** (Cu−Gd pair), in which the Gd^{III} cation does not possess orbital momentum ($S = 7/2$, $L = 0$), the fit of the experimental data was performed with the PHI program[49] with the effective spin-only Hamiltonian

$$H = -2J(S_{Cu} \times S_{Gd}) \tag{1}$$

Best-fit values were $J = +1.72(4)$ cm^{-1}, $g = 1.977(1)$ (including a $z'J'$ intermolecular interaction of -0.01 cm^{-1} to simulate the low T decay).

The fit of the $\chi_M T$ plot for the remaining complexes in which there is orbital contribution was performed with the PHI program[49] applying the anisotropic spin Hamiltonian

$$H = -2J(S_{Cu} \times S) + \lambda LS + \Delta[L_z^2 - L(L+1)/3] + \beta H(-kL + 2S) \tag{2}$$

where S_{Cu} and S are the spin operators of the Cu^{II} and Ln^{III} cations, respectively; the J coupling constant describes the strength of the Cu^{II}−Ln^{III} interaction; λ is the spin−orbit coupling parameter; Δ represents the axial zero-field splitting parameter of the Ln^{III} cation; and κ is the orbital reduction parameter, which is related to the grade of covalence (1 for fully ionic compounds). This fitting method was previously used to approximate the sign of the axial zero-field splitting parameter, Δ.[50,51] Best-fit values for J and Δ (cm^{-1}) were $-0.80(2)$ and $-14.1(1)$ (**2Ce**), $-2.03(2)$ and $-23(1)$ (**4Sm**), 2.3(3) and $-14(2)$ (**6Tb**), 0.25(1) and $-21.6(7)$ (**7Dy**), 1.65 and 26.7(3) (**9Er**), and 3.9(2) and 58.1(8) (**10Yb**).

In light of the susceptibility data, alternate current (ac) measurements were performed for the reported complexes. Compounds **2Ce** and **10Yb** do not show any response, **8Ho** and **9Er** only exhibit very weak $\chi_M''(T)$ tails under the applied field (Figure S4), whereas for **5Gd**, **6Tb**, and **7Dy**, no signals were observed at zero field but well-defined out-of-phase $\chi_M''(T)$ peaks were found under external applied fields, suggesting the presence of strong tunneling of the magnetization that quenches the slow relaxation when no dc field is applied. Measurements under fields ranging between 0 and 0.6 T were performed to select the optimal field, and thus, ac measurements were performed under 0.6, 0.3, and 0.5 T for **5**, **6**, and **7**, respectively (Figure S4).

Despite the isotropic character of the half-filled 4f^7 shell of the Gd^{III} cation that excludes orbital contribution, the complex **5Gd** exhibits maxima in the $\chi_M''(T)$ plot below 4.5 K (Figure 5), suggesting slow magnetic relaxation. This behavior for a number of mononuclear systems derived from the Gd^{III} cation[17−21] has been reported during the past recent years, as well as some scarce examples of mononuclear Mn^{II} complexes[51−56] or even some Cu^{II}−Gd^{III} or Cu^{II}−Mn^{II} complexes with different nuclearities or spin ground states.[21] For these systems, where weak anisotropy (typically $D \leq 0.1$ cm^{-1}) is present, the conventional double-well potential takes very low DS^2 values, and it is thermally overcome even at 2 K; thus, the Orbach mechanism is not operative and the relaxation is attributed to other spin−lattice relaxation mechanisms. For **5Gd**, the $\chi_M''(T)$ plot shows frequency-dependent peaks for the larger frequencies with an apparent U_{eff} of 22(2) K and τ_0 of 6(1) × 10^{-7} s (Figure 5), a very weak response for intermediate frequencies, and intense frequency-independent peaks at low temperatures and frequencies below 60 Hz. $\chi_M''(\nu)$ has a long relaxation time at low frequencies and low temperature close to 0.1 s^{-1} from the $\chi_M''(\nu)$ peaks.

The Argand plot shows limited data, far from a semicircular plot, and the fit of χ_M'' vs χ_M' does not give reliable values; Figure S5.

The Tb^{III} and Dy^{III} derivatives (complexes **6Tb** and **7Dy**) show well-defined $\chi_M''(T)$ peaks between 2–4 K (**6Tb**) and 3–5 K (**7Dy**), Figures 6 and 7, respectively. Fit of the high-temperature data as $\ln(1/2\pi\nu)$ in front of $1/T$ yields in low barrier values of $U_{eff} = 21.1(6)$ K and $\tau_0 = 8(1) \times 10^{-8}$ s for **6** and $U_{eff} = 29(2)$ K and $\tau_0 = 8(3) \times 10^{-8}$ s for **7**; Figure 8, left.

A more precise analysis can be performed using the fit of the relaxation times extracted from the semicircular Argands plots (Figure S6), which reveal an Orbach relaxation mechanism for **6Tb** with $U_{eff} = 18.8(2)$ K and $\tau_0 = 1.2(1) \times 10^{-8}$ s and Orbach plus tunnel mechanisms for **7Dy**, using the equation $\tau^{-1} = QT + \tau_0^{-1} e^{-U_{eff}/KT}$, yielding the best fitting values of $U_{eff} = 10.9(2)$ K, $\tau_0 = 3.46(5) \times 10^{-7}$ s, and QT = 4400 s^{-1}. The order of magnitude of the effective energy barrier is fully comparable to the values extracted from the $\chi_M''(T)$ plot; Figure 8, right.

CONCLUSIONS

A new family of double-stranded metallohelicates has been synthesized following a cascade reaction with the Cu^{II} cation followed by the Ln^{III} cation and structurally and magnetically characterized. The structural data reveal a similar general {Cu$_2$Ln$_2$L$_2$} skeleton with important differences in coordination numbers and nitrato coordination modes along the lanthanoid series, while a structural comparison with similar compounds in the bibliography has been done. The static magnetic characterization shows ferromagnetic coupling from the Gd^{III} to Yb^{III} derivatives. Ac measurements show that the anisotropic **6Tb** and **7Dy** complexes show the usual field-induced slow magnetic relaxation and interestingly and following different relaxation mechanisms, slow relaxation was also observed for the isotropic **5Gd** complex. The structural and magnetic study of related systems with modified ligands and/or changing the 3d cation will be developed in future works in the search for improved magnetic properties.

ASSOCIATED CONTENT

Supporting Information

The Supporting Information is available free of charge at https://pubs.acs.org/doi/10.1021/acs.cgd.3c00121.

Synthetic, crystallographic, and complementary magnetic information (PDF)

Accession Codes

CCDC 2239235−2239238 (**1La**, **4Sm**, **9Er**, and **10Yb**, respectively) contain the supplementary crystallographic data for this paper. These data can be obtained free of charge via www.ccdc.cam.ac.uk/data_request/cif, or by emailing data_request@ccdc.cam.ac.uk, or by contacting The Cambridge Crystallographic Data Centre, 12 Union Road, Cambridge CB2 1EZ, UK; fax: +44 1223 336033.

AUTHOR INFORMATION

Corresponding Author

Albert Escuer − *Departament de Química Inorgànica i Orgànica, Secció Inorgànica and Institut de Nanociència i Nanotecnologia (IN^{2}UB), Universitat de Barcelona, 08028 Barcelona, Spain;* ● orcid.org/0000-0002-6274-6866; Email: albert.escuer@qi.ub.edu

Authors

Sergio Caballero − *Departament de Química Inorgànica i Orgànica, Secció Inorgànica and Institut de Nanociència i Nanotecnologia (IN^{2}UB), Universitat de Barcelona, 08028 Barcelona, Spain*

Evangelos Pilichos − *Departament de Química Inorgànica i Orgànica, Secció Inorgànica and Institut de Nanociència i Nanotecnologia (IN^{2}UB), Universitat de Barcelona, 08028 Barcelona, Spain*

Mercè Font-Bardia − *Departament de Mineralogia, Cristal·lografia i Dipòsits Minerals and Unitat de Difracció de R-X, Centre Científic i Tecnològic de la Universitat de Barcelona (CCiT-UB), Universitat de Barcelona, 08028 Barcelona, Spain*

Júlia Mayans − *Departament de Química Inorgànica i Orgànica, Secció Inorgànica and Institut de Nanociència i Nanotecnologia (IN^{2}UB), Universitat de Barcelona, 08028 Barcelona, Spain;* ● orcid.org/0000-0001-8875-8075

Complete contact information is available at: https://pubs.acs.org/10.1021/acs.cgd.3c00121

Author Contributions

The manuscript was written through contributions of all authors. All of the authors approved the final version of the manuscript. All of the authors contributed equally.

Notes

The authors declare no competing financial interest.

REFERENCES

(1) Stratton, W. J.; Busch, D. H. The Complexes of Pyridinaldazine with Iron(II) and Nickel(II). *J. Am. Chem. Soc.* **1958**, *80*, 1286−1289.

(2) Piguet, C.; Bernardinelli, G.; Hopfgartner, G. Helicates as Versatile Supramolecular Complexes. *Chem. Rev.* **1997**, *97*, 2005−2062.

(3) Albrecht, M. "Let's Twist Again". Double-Stranded, Triple-Stranded, and Circular Helicates. *Chem. Rev.* **2001**, *101*, 3457−3498.

(4) Hannon, M. J.; Childs, L. J. Helices and Helicates: Beautiful Supramolecular Motifs with Emerging Applications. *Supramol. Chem.* **2004**, *16*, 7−22.

(5) Lehn, J.-M.; Rigault, A.; Siegel, J.; Harrowfield, J.; Chevrier, B.; Moras, D. Spontaneous assembly of double-stranded helicates from oligobipyridine ligands and copper(I) cations: structure of an inorganic double helix. *Proc. Natl. Acad. Sci. U.S.A.* **1987**, *84*, 2565−2569.

(6) Rogez, G.; Donnio, B.; Terazzi, E.; Gallani, J. L.; Kappler, J. P.; Bucher, J. P.; Drillon, M. The quest for nanoscale magnets: The example of [Mn$_{12}$] Single Molecule Magnets. *Adv. Mater.* **2009**, *21*, 4323−4333.

(7) Bogani, L.; Wernsdorfer, W. Molecular spintronics using single-molecule magnets. *Nat. Mater.* **2008**, *7*, 179−186.

(8) Wasielewski, M. R.; Forbes, M. D. E.; Frank, N. L.; Kowalski, K.; Scholes, G. D.; Yen-Zhou, J.; Baldo, M. A.; Freedman, D. E.; Goldscmith, R. H.; Goodson, T.; Kirk, M. L.; McCusker, J. K.; Ojilvie, J. P.; Schultz, D. A.; Stoll, S.; Whaley, K. B. Exploiting chemistry and molecular systems for quantum information science. *Nat. Rev. Chem.* **2020**, *4*, 490−504.

(9) Troiani, F.; Affronte, M. Molecular spins for quantum information technologies. *Chem. Soc. Rev.* **2011**, *40*, 3119−3129.

(10) Sessoli, R.; Gatteschi, D.; Caneschi, A.; Novak, M. A. Magnetic bistability in a metal-ion cluster. *Nature* **1993**, *365*, 141−143.

(11) Sessoli, R.; Tsai, H. -L.; Schake, A. R.; Wang, S.; Vincent, J. B.; Folting, K.; Gatteschi, D.; Christou, G.; Hendrickson, D. N. High-spin

molecules: $[Mn_{12}O_{12}(O_2CR)_{16}(H_2O)_4]$. *J. Am. Chem. Soc.* **1993**, *115*, 1804−1816.

(12) Atzori, M.; Tesi, L.; Benci, S.; Lunghi, A.; Righini, R.; Taschin, A.; Torre, R.; Sorace, L.; Sessoli, R. Spin dynamics and low energy vibrations: insights from vanadyl based potential molecular qubits. *J. Am. Chem. Soc.* **2017**, *139*, 4338−4341.

(13) Atzori, M.; Benci, S.; Morra, E.; Tesi, L.; Chiesa, M.; Torre, R.; Sorace, L.; Sessoli, R. Structural effects on the spin dynamics of potential molecular qubits. *Inorg. Chem.* **2018**, *57*, 731−740.

(14) Yu, C.-J.; Krzyaniak, M. D.; Fataftah, M. S.; Wasielewski, M. R.; Freedman, D. E. A concentrated array of cooper porphyrin candidate qubits. *Chem. Sci.* **2019**, *10*, 1702−1708.

(15) Gómez-Coca, S.; Cremades, E.; Aliaga-Alcalde, N.; Ruiz, E. Mononuclear Single-Molecule Magnets: Tailoring the magnetic anisotropy of first row transition metal complexes. *J. Am. Chem. Soc.* **2013**, *135*, 7010−7018.

(16) Świtlicka, A.; Machura, B.; Kruszynski, R.; Moliner, N.; Carbonell, J. M.; Cano, J.; Lloret, F.; Julve, M. Magneto-structural diversity of Co(II) compounds with 1-benzylimidazole induced by linear pseudohalide coligands. *Inorg. Chem. Front.* **2020**, *7*, 4535−4552.

(17) Orendáč, M.; Sedláková, L.; Čižmár, E.; Orendáčová, A.; Feher, A.; Zvyagin, S. A.; Wosnitza, J.; Zhu, W. H.; Wang, Z. M.; Gao, S. Spin relaxation and resonant phonon trapping in $[Gd_2(fum)_3(H_2O)_4\cdot 3H_2O]$. *Phys. Rev. B* **2010**, *81*, No. 214410.

(18) Martínez-Pérez, M. J.; Cardona-Serra, S.; Schlegel, C.; Moro, F.; Alonso, P. J.; Prima-García, H.; Clemente-Juan, J. M.; Evangelisti, M.; Gaita-Ariño, A.; Sesé, J.; van Slageren, J.; Coronado, E.; Luis, F. Gd-based Single-Ion Magnets with tunable magnetic anisotropy: Molecular design of spin qubits. *Phys. Rev. Lett.* **2012**, *108*, No. 247213.

(19) Mayans, J.; Escuer, A. Correlating the axial zero field splitting with the slow magnetic relaxation in Gd^{III} SIMs. *Chem. Commun.* **2021**, *57*, 721−724.

(20) Pilichos, E.; Bhunia, P.; Font-Bardia, M.; Ghosh, A.; Mayans, J.; Escuer, A. Quasi-isotropic SMMs: Slow relaxation of the magnetization in polynuclear Cu^{II}/Mn^{II} complexes. *Dalton Trans.* **2022**, *51*, 1779−1783.

(21) Ghosh, T. K.; Maity, S.; Mayans, J.; Ghosh, A. Family of Isomeric Cu^{II}−Ln^{III} (Ln = Gd, Tb, and Dy) Complexes Presenting Field-Induced Slow Relaxation of Magnetization Only for the Members Containing Gd^{III}. *Inorg. Chem.* **2021**, *60*, 438−448.

(22) Sorace, L.; Benelli, C.; Gatteschi, D. Lanthanides in molecular magnetism: old tools in a new field. *Chem. Soc. Rev.* **2011**, *40*, 3092−3104.

(23) Liddle, S. T.; van Slageren, J. Improving *f*-element single molecule magnets. *Chem. Soc. Rev.* **2015**, *44*, 6655−6669.

(24) Pointillart, F.; Cador, O.; Le Guennic, B.; Ouahab, L. Uncommon lanthanide ions in purely 4f Single Molecule Magnets. *Coord. Chem. Rev.* **2017**, *346*, 150−175.

(25) Mayans, J.; Sáez, Q.; Font-Bardia, M.; Escuer, A. Enhancement of magnetic relaxation properties with 3d diamagnetic cations in $[Zn^{II}Ln^{III}]$ and $[Ni^{II}Ln^{III}]$, Ln^{III} = Kramers lanthanides. *Dalton Trans.* **2019**, *48*, 641−652.

(26) Zhang, P.; Guo, Y. -N.; Tang, J. Recent advances in dysprosium-based single molecule magnets: structural overview and synthetic strategies. *Coord. Chem. Rev.* **2013**, *257*, 1728−1763.

(27) Goodwin, C. A. P.; Ortu, F.; Reta, D.; Chilton, N. F.; Mills, D. P. Molecular magnetic hysteresis at 60 kelvin in dysprosocenium. *Nature* **2017**, *548*, 439−442.

(28) Guo, F. -S.; Day, B. M.; Chen, Y. C.; Tong, M. L.; Mansikkamäki, A.; Layfield, R. A. A dysprosium metallocene Single-Molecule Magnet functioning at the axial limit. *Angew. Chem., Int. Ed.* **2017**, *56*, 11445−11449.

(29) Sheldrick, G. M. *SHELXL-2014/7: Program for the Solution of Crystal Structures*; University of Göttingen: Göttingen, Germany, 2014.

(30) Chandra, R.; Manna, A. K.; Sahu, M.; Rout, K.; Patra, G. K. Simple salicylaldimine- functionalized dipodal bis Schiff base chromogenic and fluorogenic chemosensors for selective and sensitive detection of Al^{3+} and Cr^{3+}. *Inorg. Chim. Acta* **2020**, *499*, No. 119192.

(31) Lunell, M.; Casanova, D.; Cirera, J.; Alemany, P.; Alvarez, S. SHAPE v.2.0. Barcelona 2010. The Program Can be Obtained by Request to the Authors.

(32) Borilovic, I.; Roubeau, O.; Le Guennic, B.; van Slageren, J.; Lenz, S.; Teat, S. J.; Aromí, G. Three individually addressable spin qubits in a single molecule. *Chem. Commun.* **2022**, *58*, 7530−7533.

(33) Kruger, P. E.; Martin, N.; Nieuwenhuyzen, M. Dinuclear double helicates with a twist: synthesis, structure and supramolecular entanglement in $[M_2L_2]$ metallo-helices {M = Co(II), Cu(II), H$_2$L = bis(N-salicylidene-4,4′-diaminodiphenyl)methane}. *J. Chem. Soc., Dalton Trans.* **2001**, 1966−1970.

(34) Su, X.-C.; Zhou, Z.-F.; Zhu, S.-R.; Lin, H.-K.; Weng, L.-H.; Leng, X.-B.; Chen, Y.-T. Synthesis and structure of neutral double helicate. *Chin. J. Chem.* **2010**, *18*, 773−776.

(35) Yoshida, N.; Ichikawa, K.; Shiro, M. Supramolecular motifs in metal complexes of Schiff bases. Part 5. Zinc(II)-assisted self-assembly of some bis-N,N- and N,O-bidentate Schiff bases and chiral packing modes in solid state. *J. Chem. Soc., Perkin Trans.* **2000**, *2*, 17−26.

(36) Chu, Z.; Huang, W. Syntheses and structures of two new bis-N,O-bidentate Schiff base ligands and their respective copper(II) complexes with dinuclear double-helical configuration. *J. Mol. Struct.* **2007**, *837*, 15−22.

(37) Oshikawa, Y.; Yoneda, K.; Koikawa, M.; Yamada, Y. Syntheses, crystal structures, and solid-state spectroscopic properties of helical and non-helical dinuclear zinc(II) complexes derived from N$_2$O$_2$ ligands with different torsion-generating sources. *Inorg. Chim. Acta* **2019**, *495*, No. 118979.

(38) Yoshida, N.; Oshio, H.; Ito, T. Copper (II)-assisted self-assembly of bis-N, O-bidentate Schiff bases: new building blocks for a double-helical supramolecular motif. *J. Chem. Soc., Perkin Trans.* **1999**, *2*, 975−984.

(39) Mondal, A. K.; Parmar, V. S.; Biswas, S.; Konar, S. Tetrahedral M^{II} based binuclear double-stranded helicates: single-ion-magnet and fluorescence behaviour. *Dalton Trans.* **2016**, *45*, 4548−4557.

(40) Singh, V. K.; Kadu, R.; Roy, H.; Raghavaiah, P.; Mobin, S. M. Phenolate based metallomacrocyclic xanthate complexes of Co^{II}/Cu^{II} and their exclusive deployment in $[2:2]$ binuclear N,O-Schiff base macrocycle formation and in vitro anticancer studies. *Dalton Trans.* **2016**, *45*, 1443−1454.

(41) Kelly, N.; Schulz, J.; Gloe, K.; Doert, T.; Gloe, K.; Wenzel, M.; Acker, M.; Weigand, J. J. Self-assembly of dinuclear double-stranded copper(II) helicates with 3-ethoxy-2-hydroxyphenyl Substituted diimines. Synthesis, molecular structure, and host-guest recognition of H$_2$O. *Z. Anorg. Allg. Chem.* **2015**, *641*, 2215−2221.

(42) Cucos, P.; Tuna, F.; Sorace, L.; Matei, I.; Maxim, C.; Shova, S.; Gheorghe, R.; Caneschi, A.; Hillebrand, M.; Andruh, M. Magnetic and luminescent binuclear double-stranded helicates. *Inorg. Chem.* **2014**, *53*, 7738−7747.

(43) Hasi, Q.-M.; Fan, Y.; Yao, X.-Q.; Hu, D.-C.; Liu, J.-C. Synthesis, characterization, antioxidant and antimicrobial activities of a bidentate Schiff base ligand and its metal complexes. *Polyhedron* **2016**, *109*, 75−80.

(44) Habib, F.; Long, J.; Lin, P.-H.; Korobkov, I.; Ungur, L.; Wernsdorfer, W.; Chibotaru, L. F.; Murugesu, M. Supramolecular architectures for controlling slow magnetic relaxation in field-induced single-molecule magnets. *Chem. Sci.* **2012**, *3*, 2158−2164.

(45) Albrecht, M.; Janser, I.; Houjou, H.; Frohlich, R. Long-range stereocontrol in the self-assembly of two-nanometer-dimensioned triple-stranded dinuclear helicates. *Chem. - Eur. J.* **2004**, *10*, 2839−2850.

(46) Novitchi, G.; Costes, J. P.; Tuchagues, J. P.; Vendier, L.; Wernsdorfer, W. A single molecule magnet (SMM) with a helicate structure. *New J. Chem.* **2008**, *32*, 197−200.

(47) Jiang, D.; Yang, X.; Chen, H.; Wang, F.; Wang, S.; Zhu, T.; Zhang, L.; Huang, S. Cation sensing by luminescent high-nuclearity Zn−Eu Schiff base nanoscale complexes: high sensitivity to Ag$^+$ and Cd^{2+} ions at the ppm level. *Dalton Trans.* **2019**, *48*, 2206−2212.

(48) Chen, H.; Yang, X.; Jiang, D.; Shi, D.; Zhang, L. Construction of NIR luminescent polynuclear lanthanide-based nanoclusters with sensing properties towards metal ions. *Dalton Trans.* **2018**, *47*, 13880−13886.

(49) Chilton, N. F.; Anderson, R. P.; Turner, L. D.; Soncini, A.; Murray, K. S. PHI: A powerful new program for the analysis of anisotropic monomeric and exchange-coupled polynuclear *d*- and *f*-block complexes. *J. Comput. Chem.* **2013**, *34*, 1164−1175.

(50) Worrell, A.; Sun, D.; Mayans, J.; Lampropoulos, C.; Escuer, A.; Stamatatos, T. C. Oximato-based ligands in 3*d*-4*f* metal-cluster chemistry: A family of {Cu₃Ln} complexes with "propeller"-like topology and Single-Molecule Magnet behaviour. *Inorg. Chem.* **2018**, *57*, 13944−13952.

(51) Marinho, M. V.; Reis, D. O.; Oliveira, W. X. C.; Marques, L. F.; Stumpf, H. O.; Déniz, M.; Pasán, J.; Ruíz-Pérez, C.; Cano, J.; Lloret, F.; Julve, M. Photoluminescent and slow-magnetic relaxation studies on lanthanide(III)-2,5-pyrazinedinecarboxylate frameworks. *Inorg. Chem.* **2017**, *56*, 2108−2123.

(52) Benniston, A. C.; Melnic, S.; Turta, C.; Arauzo, A. B.; Bartolomé, J.; Bartolomé, E.; Harrington, R. W.; Probert, M. R. Preparation and properties of a calcium(II)-based molecular chain decorated with manganese(II) butterfly-like complexes. *Dalton Trans.* **2014**, *43*, 13349−13357.

(53) Rajnák, C.; Titis, J.; Moncol, J.; Micova, R.; Boca, R. Field-Induced Slow Magnetic relaxation in a mononuclear manganese(II) complex. *Inorg. Chem.* **2019**, *58*, 991−994.

(54) Da Cunha, T. T.; Barbosa, V. M. M.; Oliveira, W. X. C.; Pedroso, E. F.; Garcia, D. M. A.; Nunes, W. C.; Pereira, C. L. M. Field-induced slow magnetic relaxation of a six-coordinate mono-nuclear manganese(II) and cobalt(II) oxamate complexes. *Inorg. Chem.* **2020**, *59*, 12983−12987.

(55) Uchida, K.; Cosquer, G.; Sugisaki, K.; Matsuoka, H.; Sato, K.; Breedlove, B. K.; Yamashita, M. Isostructural M(II) complexes (M = Mn, Fe, Co) with field-induced slow magnetic relaxation for Mn and Co complexes. *Dalton Trans.* **2019**, *48*, 12023−12030.

(56) Pilichos, E.; Font-Bardia, M.; Escuer, A.; Mayans, J. Occurrence of slow relaxation of the magnetization in a family of copper(II)/manganese(II) quasi-isotropic complexes with different ground spin states. *Dalton Trans.* **2022**, *51*, 17653−17663.

🕮 Recommended by ACS

Tuning Quantum Tunneling in Isomorphic {Mᴵᴵ₂Dyᴵᴵᴵ₂} "Butterfly" System via 3d-4f Magnetic Interaction

Gao-Peng Li, Kun Zhang, *et al.*

FEBRUARY 13, 2023
CRYSTAL GROWTH & DESIGN

READ ☑

Slow Magnetic Relaxation of Linear Trinuclear M(II)–Gd(III)–M(II) Complexes with D_3 Point Group Symmetry (M(II) = Zn(II) and Mg(II))

Yuka Masuda, Takashi Kajiwara, *et al.*

FEBRUARY 06, 2023
THE JOURNAL OF PHYSICAL CHEMISTRY C

READ ☑

Family of Lanthanide–Manganese Heterometallic Metallacrowns: Syntheses, Structures, Magnetic Exchange, and Magnetocaloric Effects

Lan-Tao Cheng, Xiu-Ying Zheng, *et al.*

DECEMBER 20, 2022
CRYSTAL GROWTH & DESIGN

READ ☑

Synthesis, Structure, and Magnetic Properties of Homometallic Mono-, Penta-, and Hexanuclear Dysprosium Complexes

Wen-Qiang Li, Xiu-Jian Wang, *et al.*

APRIL 26, 2023
CRYSTAL GROWTH & DESIGN

READ ☑

Get More Suggestions >

Field-Induced Slow Magnetic Relaxation in a New Family of Tetranuclear Double-Stranded Cu$_2^{II}$-Ln$_2^{III}$ Metallo-Helicates.

Sergio Caballero,[¥] Evangelos Pilichos,[¥] Mercè Font-Bardia,[§], Júlia Mayans[¥] and Albert Escuer[¥]*

[¥] Departament de Química Inorgànica i Orgànica, sección Inorgànica and Institut de Nanociència i Nanotecnologia (IN^{2}UB). Universitat de Barcelona. Martí i Franqués 1-11, 08028-Barceloa, Spain.

[§] bDepartament de Mineralogia, Cristal·lografia i Dipòsits Minerals and Unitat de Difracció de R-X, Centre Científic i Tecnològic de la Universitat de Barcelona (CCiTUB), Universitat de Barcelona, Solé i Sabarís 1-3, 08028-Barcelona, Spain.

Figure S1. Ortep plot of the molecular structure of complex **5Gd**.

Figure S2. IR spectra for compounds **1-10**.

Figure S3. Powder X-Ray diffraction pattern for **1-3** (top) and **5-7** (bottom).

Figure S4. Ac preliminary measurements.

Figure S5. Argand plot for complex **5Gd**.

Figure S6. Argand plots for compounds **6Tb** (left) and **7Dy** (right).

Table S1. Crystal data, collection and structure refinement details for the X-ray structure determination of complexes **1La**, **4Sm**, **5Gd**, **9Er** and **10Yb**.

Table S2. Elemental analysis for **1-10** compounds.

Table S1. Crystal data, collection and structure refinement details for the X-ray structure determination of complexes **1La**, **4Sm**, **5Gd**, **9Er** and **10Yb**. Formula for **5Gd** is taken for the partially solved structure.

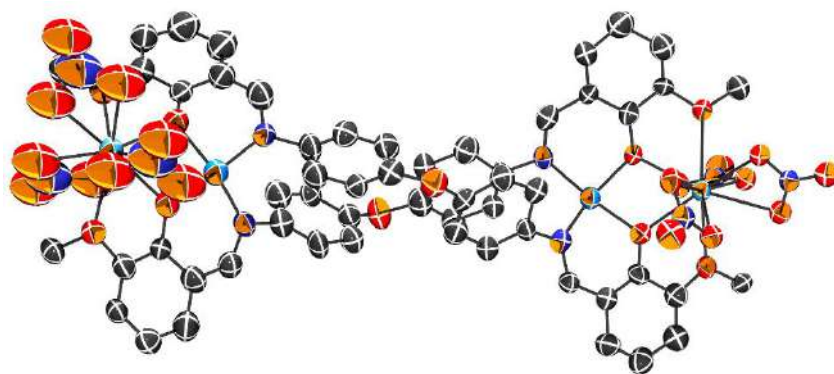|	1La	4Sm	5Gd*	9Er	10Yb
Formula	$C_{130}H_{131}Cu_4La_4$ $N_{23}O_{62}$	$C_{60}H_{60}Cu_2N_{10}$ $O_{32}Sm_2$	$C_{56}H_{44}Cu_2Gd_2$ $N_{10}O_{28}$	$C_{60}H_{60}Cu_2Er_2$ $N_{10}O_{32}$	$C_{122}H_{111}Cu_4$ $N_{21}O_{59}Yb_4$
FW	3817.37	1860.96	1746.59	1894.78	3761.63
System	Monoclinic	Monoclinic	Monoclinic	Orthorhombic	Monoclinic
Space group	$P2_1/c$	$P2_1/n$	$P2_1/n$	Pbca	$P2_1/n$
a/Å	15.5492(6)	15.2628(7)	16.060(1)	21.451(1)	14.2306(7)
b/Å	22.1056(9)	23.956(1)	23.437(1)	22.125(1)	28.741(2)
c/Å	22.677(1)	22.202(1)	19.282(1)	31.097(1)	19.011(1)
α/deg.	90	90	90	90	90
β/deg.	109.993(2)	104.474(2)	101.690(2)	90	91.626(2)
γ/deg.	90	90	90	90	90
V/ Å^3	7324.7(6)	7860.4(6)	7107.0(8)	14759(1)	7772.2(7)
Z	2	4	4	8	2
T, K	100(2)	100(2)	100(2)	100(2)	100(2)
Θ range/deg.·	1.671-30.582°	1.857-26.460°	---	1.841-30.574°	1.777-26.508°
Reflex. collected	233993	16140	---	22601	239352
Reflex. indep.	22459	16140	---	22601	16044
Parameters	990	952	---	979	949
λ(MoKα), Å	0.71073	0.71073	0.71073	0.71073	0.71073
ρ_{calc}, g·cm^{-3}	1.731	1.573	---	1.705	1.607
μ(MoK$_\alpha$), mm^{-1}	1.812	2.093	---	2.912	3.009
R	0.0461	0.0340	---	0.0456	0.0633
ωR^2	0.1071	0.0863	---	0.0991	0.1630

Figure S1. Ortep plot of the molecular structure of complex **5Gd**. Despite the resolution of the core, the large thermal agitation of the nitrato ligands around Gd(2) prevent a satisfactory resolution.
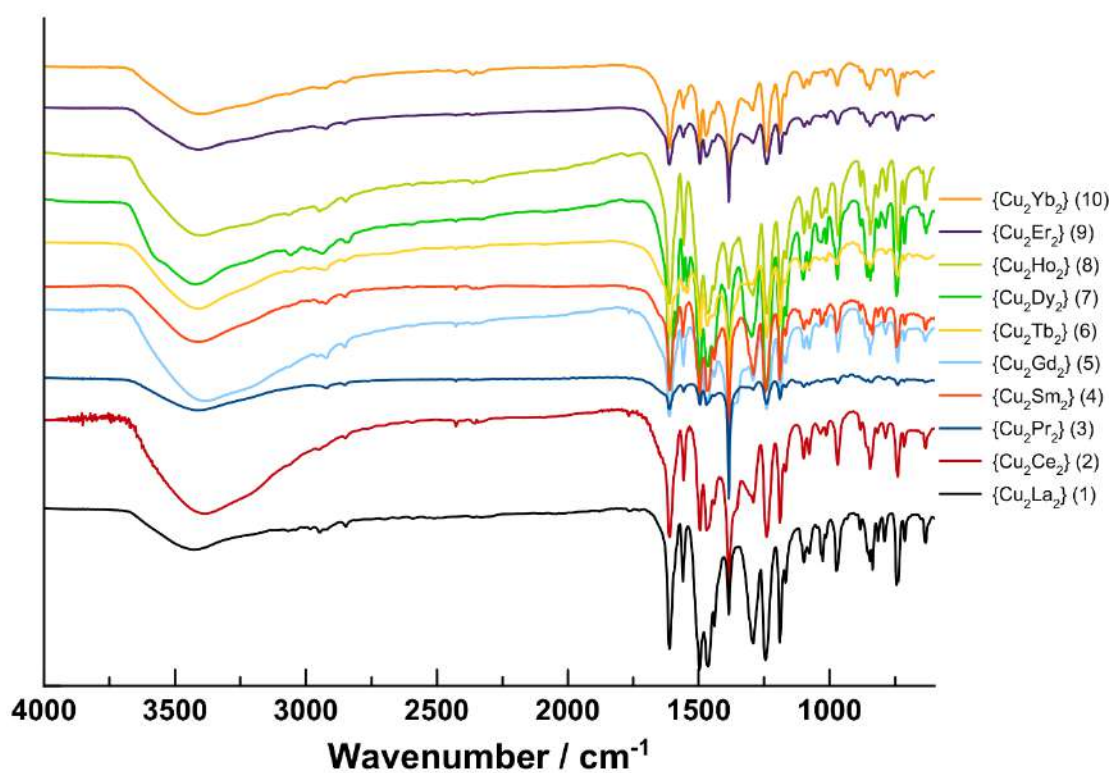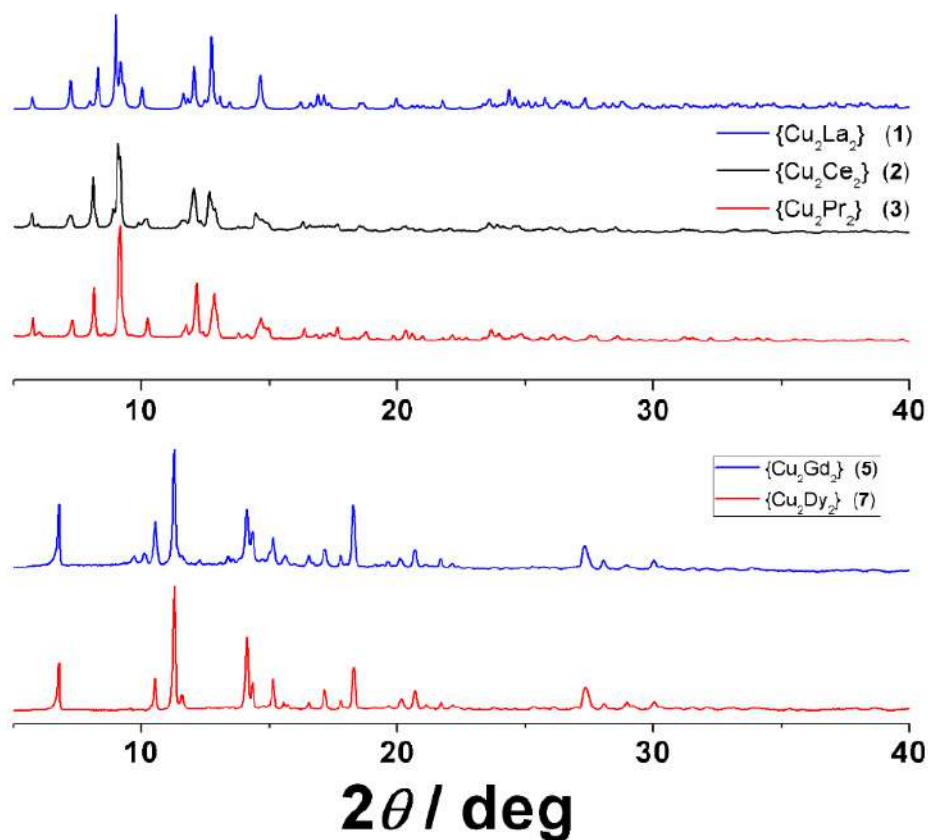

{Cu$_2$Yb$_2$} (10)
{Cu$_2$Er$_2$} (9)
{Cu$_2$Ho$_2$} (8)
{Cu$_2$Dy$_2$} (7)
{Cu$_2$Tb$_2$} (6)
{Cu$_2$Gd$_2$} (5)
{Cu$_2$Sm$_2$} (4)
{Cu$_2$Pr$_2$} (3)
{Cu$_2$Ce$_2$} (2)
{Cu$_2$La$_2$} (1)

Figure S2. IR spectra for compounds **1-10**.

Figure S3. Powder X-Ray diffraction pattern for **1-3** (top) and **5-7** (bottom).
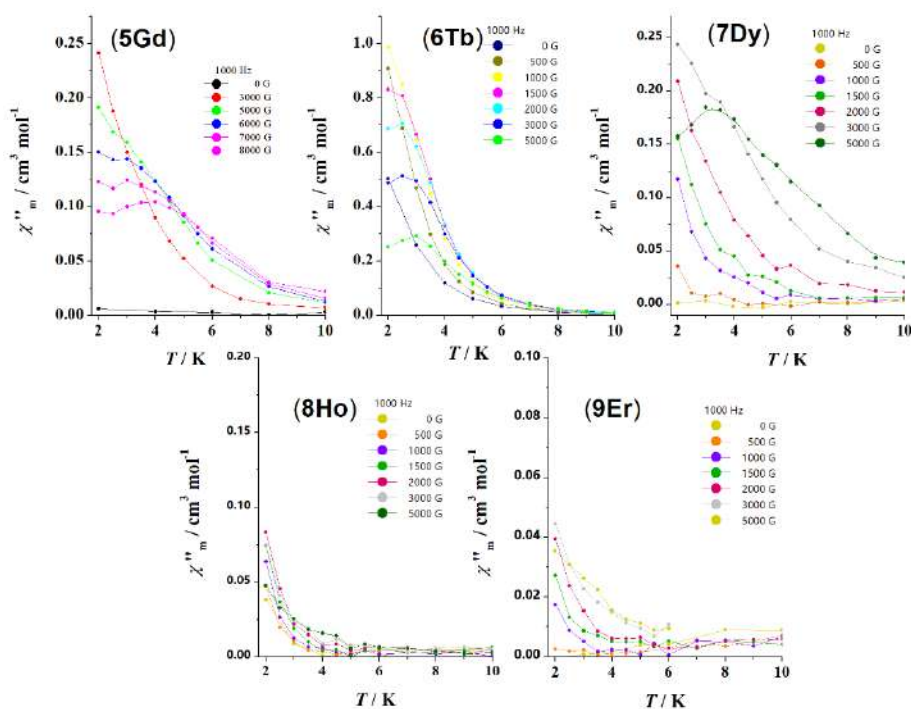
Figure S4. Ac preliminary measurements under different applied magnetic fields to check the best response. **2Ce** and **10Yb** do not give ac response either at zero or under external fields
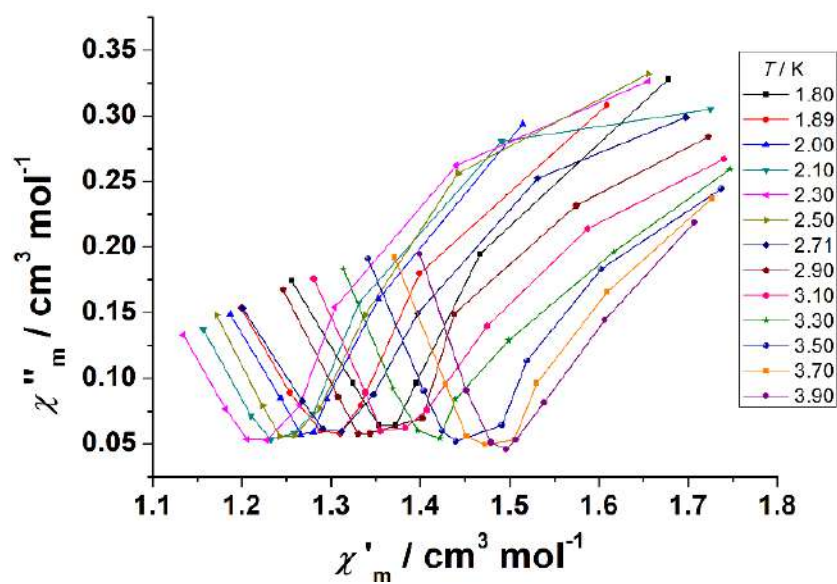
Figure S5. Argand plot for complex **5Gd** showing the limited data for the larger temperatures.
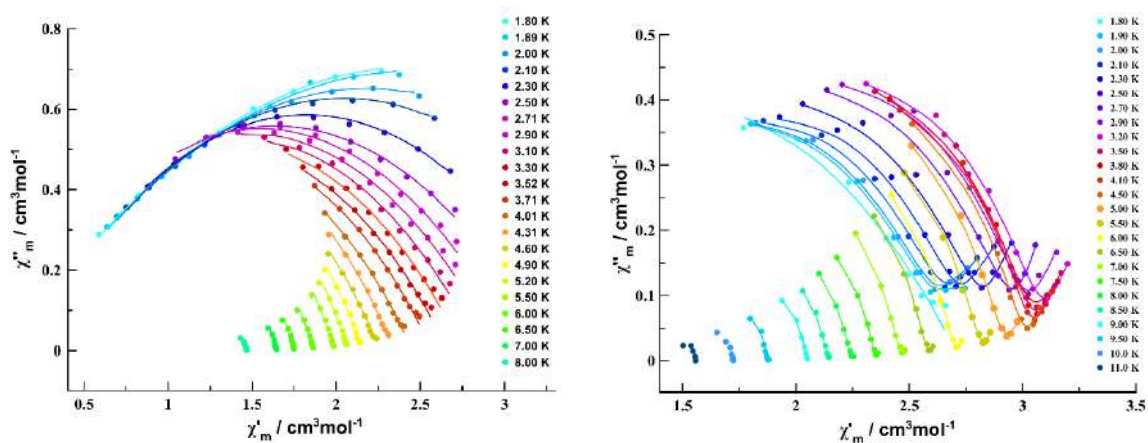
.

Figure S6. Argand plots for compounds **6Tb** (left) and **7Dy** (right).

Table S2. Elemental analysis for **1-10** compounds (vacuum dried samples).

	(1La)	(2Ce)	(3Pr)	(4Sm)	(5Gd)	(6Tb)	(7Dy)	(8Ho)	(9Er)	(10Yb)
%C_{calc}	39.27	39.22	39.19	38.72	38.51	38.44	38.28	38.15	38.04	37.83
%C_{exp}	38.92	39.76	39.30	38.21	3894	38.06	38.77	38.33	37.86	37.91
%N_{calc}	7.90	7.88	7.88	7.53	8.02	8.00	7.97	7.67	7.52	7.88
%N_{exp}	7.77	7.91	7.99	7.62	7.95	8.12	7.92	7.81	7.47	7.98
%H_{calc}	2.95	2.95	2.95	3.25	2.54	2.53	2.52	2.87	3.03	2.49
%H_{exp}	2.91	3.01	2.84	3.11	2.46	2.68	2.47	2.88	2.98	2.55

CHAPTER 3

SRM in Quasi-Isotropic Systems: The case of Cu^{II}-Mn^{II}

Chapter 3: SRM in Quasi-Isotropic Systems: The case of Cu^{II}-Mn^{II}

Chapter 3 comprises **Publication #4** and **Publication #5**.

Apart from Gd-Based SIMs, in the literature there are some examples of Mn(II)-based magnets. Mn(II) cation is a d^5 system, and thus its coordination environment is very plastic; with the use of appropriate ligands, magnetic relaxation phenomena could be observed. Thus, Mn(II) compounds could present intense interest in terms of magnetism, enriching the family of magnets with isotropic cations.

Publication #4 *"Quasi-isotropic SMMs: slow magnetic relaxation of the magnetization in polynuclear Cu^{II}/Mn^{II} complexes"* describes the synthesis and characterization of three complexes with formulas: $[\{Cu^{II}(L3)\}_2Mn^{II}(N_3)_2]\cdot 2H_2O$ (**20**$\cdot 2H_2O$), $[\{Cu^{II}(L4)Mn^{II}(H_2O)_2(MeOH)\}\{Cu^{II}(L4)\}_2](ClO_4)_2\cdot MeOH$ (**21**$\cdot MeOH$) and $[(\mu_{1,1}$-$N_3)_2\{Cu^{II}(L4)Mn^{II}\}\{Cu^{II}(L4)Na^I(MeOH)(N_3)\}_2](ClO_4)_2$ (**22**). The organic ligands, H_2L3 and H_2L4 (Fig. 34), were chosen by their ability to induce distorted environments around the Mn^{II} cation; distorted octahedral geometry for the salicylic base H_2L3 or pentagonal bipyramidal for the o-vanillin H_2L4 ligand. The three complexes were isolated by the reaction of the corresponding manganese(II) salt with the [Cu(L)] precursor. In all the cases, the Cu^{II} cation is placed in the N_2O_2 cavity of the ligand showing a square planar environment.
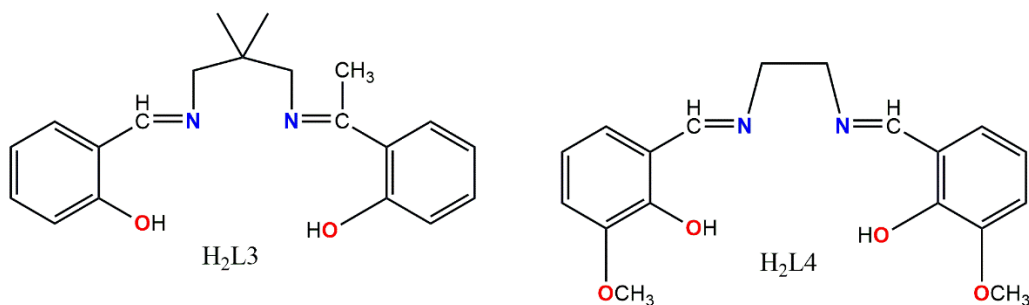

Figure 34: Structural formula of organic ligands H_2L3 and H_2L4 employed in **Publication #4**.

For complex **20** the Mn^{II} adopts an octahedral coordination environment. In complexes **21** and **22** Mn^{II} geometry could be described as trigonal bipyramidal or as pentagonal bipyramidal depending on counting or not the $O_{methoxide}$ donors from o-vanillin.

Additionally, in complex **22** the two fragments of $\{Cu^{II}Na^{I}(L2)(MeOH)\}$ are linked by a $\mu_{1,1}$-N_3 bridge between the Mn^{II} and Na^{I} cations.

Static magnetic measurements revealed that for complex **20** and complex **21** there is an antiferromagnetic interaction between the Cu^{II} and Mn^{II} cations; the exchange couplings are J = -13.9 cm^{-1} and J = -15.3 cm^{-1}, for complexes **20** and **21**, respectively. Complex **22** shows a ferrimagnetic magnetic interaction, where the two Mn^{II} are coupled ferromagnetically and the Cu-Mn interaction is antiferromagnetic. Thus, for the three complexes there are different ground states: S = 3/2 for **20**, S = 2 for **21** and S = 4 for **22**.

None of the complexes showed ac response without an application of external magnetic field, but clear peaks with strong dependency of the intensity and position of the maxima for increasing fields were observed. The relaxation mechanism that were present were Raman and QTM for **20**, while Raman and Direct process were dominating the relaxation for complexes **21** and **22**.

Publication #5 *"Occurrence of slow relaxation of magnetization in a family of copper(II)/manganese(II) quasi-isotropic complexes with different ground spin states"* is referred to the synthesis and magnetic characterization of five heterometallic complexes in which the nuclearity ranging from two to eight. The formulas of the complexes are: $[Cu^{II}Na^{I}(L6)(MeOH)(ClO_4)]$ (**23**), $[Cu^{II}_2Mn^{II}(SS\text{-}L5)(MeOH)](ClO_4)_2 \cdot 2CH_2Cl_2 \cdot 0.5H_2O$ (**24SS·2CH₂Cl₂·0.5H₂O**), $[\{Cu^{II}Mn^{II}(L4)(H_2O)_2(MeOH)\}\{Cu^{II}(L4)\}_2](ClO_4)_2 \cdot MeOH$ (**25·MeOH**), $[(\mu_{1,3}\text{-}N_3)\{Cu^{II}Mn^{II}(L6)(H_2O)\}_2\{Cu^{II}(L6)\}_2](ClO_4)_2 \cdot 2MeOH$ (**26·2MeOH**) and $[(\mu_{1,1}\text{-}N_3)_2\{Cu^{II}Mn^{II}(L4)(N_3)\}_2\{Cu^{II}Na^{I}(L4)(MeOH)\}_2](ClO_4)_2$ (**27**). The organic ligands that are used in this work are shown in Fig. 35. Different sources of azides were used, NaN_3 and $(Bu_4N)N_3$, in order to increase the nuclearities of the complexes and also to study their influence in the magnetic response. Because of the fact that complex **24** has a chiral ligand, ECD spectra of **24SS** and **24RR** were recorded in order to confirm the enantiomeric identity of this pair.
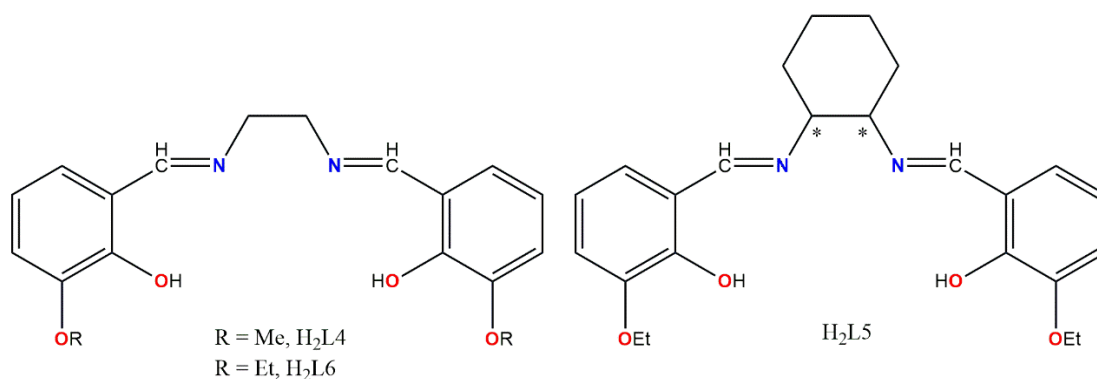
Figure 35: Structural formulas of the ligands employed in *Publication #5*. With asterisks are denoted the chiral centers.

The complexes **24**-**27** were studied magnetically; in Fig. 36 the coupling schemes for the complexes are presented. Complex **24** processes an $S = 3/2$ ground state with an antiferromagnetic exchange coupling of magnitude $J = -16.4$ cm^{-1}. For **25** the ground state is $S = 2$, while the interactions between the cations are $J_1 = -13.8$ cm^{-1} and $J_2 = -0.09$ cm^{-1}. For compound **26** the strong antiferromagnetic interactions are dominant and thus the $\chi_M T$ values at low temperatures corresponds to the two isolated Cu^{II} cations; the magnitudes of interactions are $J_1 = -26$ cm^{-1} and $J_2 = -2.6$ cm^{-1}. The weak interactions between the Mn^{II} and terminal Cu^{II} cations are were not taken into consideration. Finally, for **27** a ground state of $S = 4$ was confirmed, while the analysis of the data revealed a ferrimagnetic interaction with $J_1 = -12.5$ cm^{-1} and $J_2 = +2.03$ cm^{-1}.
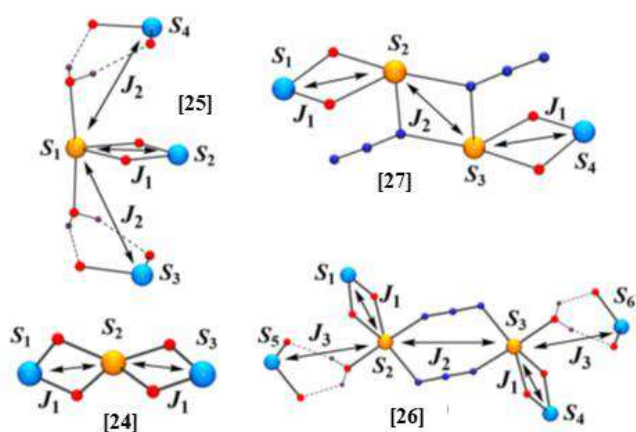

Figure 36: Coupling scheme for complexes **24**-**27**.

Dynamic magnetic measurements for the complexes showed slow relaxation of the magnetization in this family of quasi-isotropic complexes; Raman and Direct relaxation pathways are present and relatively large relaxation times were obtained. Furthermore, Raman spectroscopy in the terahertz region confirms that the relaxation cannot be attributed to an over-barrier process due to the lack of magnetic anisotropy. As a result, we can conclude that magnetic relaxation can happen not only in strongly anisotropic systems but also in any kind of clusters.

PUBLICATION #4

*"**Quasi-isotropic SMMs: slow magnetic relaxation of the magnetization in Cu^{II}/Mn^{II} complexes**"*
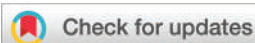
COMMUNICATION

Check for updates

Quasi-isotropic SMMs: slow relaxation of the magnetization in polynuclear CuII/MnII complexes†

Evangelos Pilichos,[a] Pradip Bhunia,[b] Mercè Font–Bardia,[c] Ashutosh Ghosh, [ID][b,d] Júlia Mayans [ID][a] and Albert Escuer [ID] *[a]

Three field induced SMMs built from quasi-isotropic cations like CuII and MnII have been characterized, showing that relatively large clusters with quasi-negligible D and different ground spin states, S = 3/2, 2 or 4, can also exhibit field-induced slow relaxation of magnetization.

Since the discovery of the single molecule magnet (SMM) response, anisotropy has played a central role in modulating the properties of these systems on the basis of the relationship between the barrier for the reversal of magnetization with the axial zero field splitting parameter (D), and the total spin state (S), parametrized as DS^2 or DS^2-1/4 for integer or half integer spins, respectively.[1] Despite the experimental limits of these barriers, due to the impossibility of increasing D while increasing S,[2] anisotropy has been crucial to reaching record barriers in single ion magnets (SIMs), generally derived from lanthanides that exhibit relatively low S values but possess an intrinsic strong single ion anisotropy.[3]

In contrast to the paradigmatic high anisotropy premise, some field-induced SIMs derived from isotropic cations like GdIII ($^8S_{7/2}$) have been recently reported.[4] A common feature of these compounds is the presence of a small D value that usually ranges around 0.1 cm^{-1}. Structurally, some of these compounds are dinuclear or 1D but, magnetically, they should be better assumed as SIMs instead SMMs because they exhibit $D > J_{Gd-Gd}$.[4h,i,p] The only GdIII derivative that can be assumed

as an SMM corresponds to one CuIIGdIII coupled dimer with a defined S = 3 ground state.[5] The high spin MnII cation, having a half-filled shell ($^6A_{1g}$ in an O_h environment), also has provided some examples of slow relaxation of the magnetization for an octahedral *cis*-complex[6a] that was earlier reported in 2014 and very recently, a similar response has been found for two mononuclear MnII complexes in *trans*-octahedral[6b,c] or pentagonal bipyramidal coordination environments.[6d] Due to the zero contribution of ligand field stabilization energy, the coordination sphere around the MnII ion is very plastic and thus, strongly distorted O_h, penta- or heptacoordinated environments are easily accessible employing adequate ligands. In contrast to the internal f orbitals of gadolinium, the 3d orbitals are highly sensitive to the ligand field and, for strong geometric distortions, the design of systems (initially isotropics such as MnII) with small D values can be tailored tuning its coordination environment. On this basis, the divalent manganese cation appears to be an attractive option, even better than GdIII, to explore the properties of this new class of field-induced SIMs or SMMs.

Following our previous work in this field,[4p,5] we have explored the response of new MnII derivatives of compartmental Schiff bases (Chart 1), selected by their ability to induce a strongly distorted coordination sphere around the manganese cation (distorted octahedron for the salicylic base H$_2$L1 or close to a pentagonal bipyramid employing the *o*-vanillin H$_2$L2 ligand).
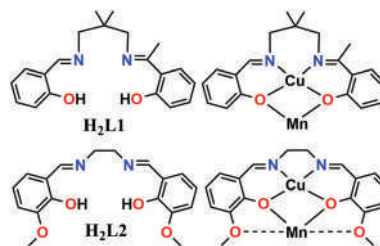
[a]*Departament de Química Inorgànica i Orgànica, Secció Inorgànica and Institute of Nanoscience and Nanotechnology (IN^{2}UB), Universitat de Barcelona, Martí i Franquès 1-11, Barcelona-08028, Spain. E-mail: albert.escuer@ub.edu*
[b]*Department of Chemistry, University College of Science, University of Calcutta, Kolkata 700009, India*
[c]*Departament de Mineralogia, Cristal·lografia i Dipòsits Minerals, Universitat de Barcelona, Martí Franqués s/n, 08028 Barcelona (Spain) and Unitat de Difracció de R-X. Centre Científic i Tecnològic de la Universitat de Barcelona (CCiTUB), Solé i Sabarís 1-3, 08028 Barcelona, Spain*
[d]*Rani Rashmoni Green University, Hooghly 712410, West Bengal, India*

Chart 1 Schematic drawing of the Schiff bases employed in this work and its coordination mode to generate bimetallic complexes.

This distortion promotes the required degree of small anisotropy and allowed the characterization of polynuclear systems that, for the very first time, are induced isotropic Mn^{II} SMMs.

Complexes $[\{Cu^{II}(L1)\}_2 Mn^{II}(N_3)_2]\cdot 2H_2O$ ($1\cdot 2H_2O$), $[\{Cu^{II}(L2)Mn^{II}(H_2O)_2(MeOH)\}\{Cu^{II}(L)\}_2](ClO_4)_2\cdot MeOH$ ($2\cdot MeOH$) and $[(\mu_{1,1}\text{-}N_3)_2\{Cu^{II}(L2)Mn^{II}\}\{Cu^{II}(L2)Na^{I}(MeOH)(N_3)\}_2](ClO_4)_2$ (3) were obtained by the reaction of the corresponding manganese salt with the neutral [Cu(L)] precursors in which the copper cation is placed in the inner N_2O_2 cavity of the deprotonated ligand (see ESI Fig. S1–S3 and Tables S1–S5† for synthetic details, structural determination, bond parameters and SHAPE[7] analysis of the Mn^{II} environments). The new compounds **1–3** afforded the first examples of slow relaxation of the magnetization for quasi-isotropic spins $S = 3/2$, 2 and 4, respectively, different from the previously reported SIMs with $S = 5/2$ (Mn^{II}) or $7/2$ (Gd^{III}), and also the first field-induced SMMs based on divalent manganese cations.

For complexes **1–3** the Cu^{II} cations are placed in the N_2O_2 cavity of the corresponding Schiff base showing a square planar environment with Cu–N and Cu–O bond distances of ~1.90 Å and no further comments will be given for the copper coordination.

Complex **1** consists of a trinuclear complex in which two $\{Cu(L1)\}$ fragments are linked to one manganese cation by means of the $O_{phenoxo}$ donors in a *cis*-arrangement, Fig. 1 – top. The coordination sphere of the Mn^{II} cation is completed with two azido ligands resulting in an octahedral N_2O_4 environment, Table S5 and Fig. S2.† The bond distances range between 2.058 Å for Mn–N(35) and 2.320 Å for Mn–O(11)
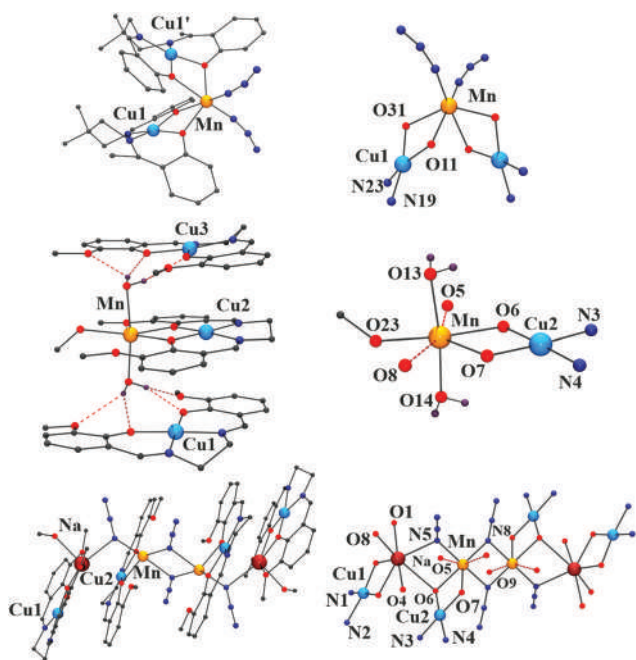

Fig. 1 View of the molecular units and labelled cores of **1** (top), **2** (middle) and **3** (bottom). Red dashed bonds show the H-bonds between the three fragments of complex **2**. Color code for all plots, O, red; N, navy blue; Cu^{II}, blue; Mn^{II}, orange; Na^{I}, firebrick; and C, black.
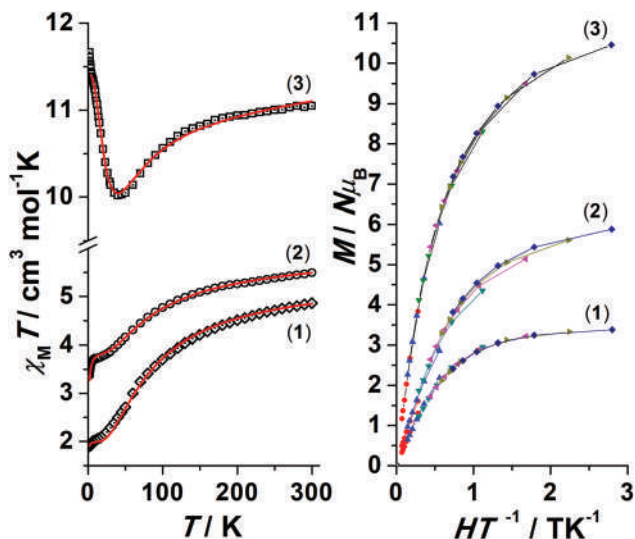
bonds and the bond angles between the donors placed in the *trans* position are 166.3° for N(35)–Mn–O(11) and 143.2° for O(31)–Mn–O(31′). The molecules of **1** are pillared forming chains of trimers along the c direction of the network, as shown in Fig. S4.†

Compound **2** consists of one $[Cu(L2)Mn(H_2O)_2(MeOH)]^{2+}$ dinuclear complex linked by means of H-bonds to two neutral [Cu(L2)] units and two perchlorate counteranions, as shown in Fig. 1 – middle. The heterodinuclear unit consists of one [Cu(L2)] unit linked to one Mn^{II} cation by means of the $O_{phenoxo}$ donors. The coordination of the manganese cations consists of two bridging $O_{phenoxo}$ donors, one methanol and two water molecules placed in a *trans* arrangement. In addition, the two O_{metoxo} donors O(5) and O(8) interact weakly with the Mn^{II} cation with Mn–O distances of ~2.60 Å. Thus, the environment around the Mn^{II} cation can be envisaged as MnO_5 or alternatively as MnO_7 if the large Mn–O(5) and Mn–O(8) contacts are taken into account. SHAPE[7] analysis of the coordination environment of the manganese cation shows a large deviation from any regular ML_5 polyhedron and is structurally better described as an ML_7 pentagonal bipyramid, as given in Table S5 and Fig. S2.†

The water molecules coordinated to the Mn^{II} cation link the neutral [Cu(L2)] fragments by means of bifurcated H-bonds with the O-donors of the Schiff bases resulting in a "sandwich" structure. The clusters of **2** are pillared forming chains that isolates the paramagnetic Mn^{II} cations with Mn⋯Mn distances along the chain of 11.904(1) Å and interchain distances of 11.611(1) Å, as shown in Fig. S3.†

Complex **3** consists of one $\{Cu(L2)Mn\text{-}(\mu_{1,1}\text{-}N_3)_2\text{-}Mn(L2)Cu\}$ tetranuclear unit capped by two $\{CuNa(L2)(MeOH)\}$ fragments that are linked by means of one $\mu_{1,1}\text{-}N_3$ bridge between the Mn^{II} and Na^{I} cations, Fig. 1 – bottom. The Mn^{II} cations are linked to two $O_{phenoxo}$ donors, two bridging $\mu_{1,1}\text{-}N_3$ and one $\mu_{1,1}\text{-}N_3$ ligand that links the Na^{I} cation. In addition, two large contacts with the two $O_{methoxide}$ donors determine a coordination environment that could be assumed as a MnN_3O_2 trigonal bipyramid, very distorted due to the low bite of the two $O_{phenoxo}$ donors or alternatively as also a distorted 5 + 2 pentagonal bipyramid with a MnN_3O_4 environment (SHAPE[7] analysis, Table S5 and Fig. S2†). The Mn–N–Mn bond angle takes a value of 104.55°. Clusters of **3** are pillared forming chains in the network in a similar manner to complex **2**, as shown in Fig. S3.†

Static susceptibility measurements were performed on powdered samples in the 300–2 K range. The room temperature $\chi_M T$ values for **1** and **2** are 4.86 and 5.49 cm³ mol⁻¹ K and decrease on cooling down to 1.92 and 3.38 cm³ mol⁻¹ K, respectively, at 2 K. The $\chi_M T$ plot for complex **3** shows a room temperature value of 11.05 cm³ mol⁻¹ K that decreases with temperature down to a minimum of 10.0 cm³ mol⁻¹ K at 40 K and below this temperature increases up to 11.65 cm³ mol⁻¹ K at 2 K, suggesting a ferrimagnetic response, as shown in Fig. 2, left.

Fit of the experimental data was performed with the PHI[8] program ($2J$ convention) and the best fit parameters were $J_{Cu–Mn} = -13.9(2)$ cm⁻¹ and $g = 2.068(3)$ for **1**, $J_{Cu–Mn} = -15.3(2)$

Fig. 2 Left, $\chi_M T$ product *vs.* temperature for complexes **1**–**3**. Right reduced magnetization plots.

Fig. 3 Temperature (left) and frequency dependence (right) of χ'' for complexes **1** (top), **2** (middle) and **3** under two 0.35 and 0.6 T fields (down).

cm^{-1} and $g = 2.035(1)$ for **2** and $J_{Cu–Mn} = −12.5(1)$ cm^{-1}, $J_{Mn–Mn} = +2.03(1)$ cm^{-1}, $g_{Cu} = 2.092(3)$ and $g_{Mn} = 2.050(1)$ for **3**.

These values indicate an antiferromagnetic interaction between the Cu^{II} and Mn^{II} cations with a magnitude similar to those of previously reported Cu^{II}/Mn^{II} dinuclear complexes with related Schiff bases,[9] and for complex **3**, ferromagnetic coupling mediated by the end-on azido bridges[10] between the Mn^{II} cations, resulted in well isolated ground spin states of $S = 3/2$ for **1**, $S = 2$ for **2** and $S = 4$ for **3** with a gap of 83, 91 and 22 cm^{-1}, respectively, to the first $S = 3$ excited state. In agreement with these data, the magnetization values under the maximum applied field are $3.37N\mu_\beta$ for **1** ($S = 3/2$), $5.88N\mu_\beta$ for **2** ($S = 2$ for the dimeric entity plus two isolated Cu^{II} cations) or $10.45N\mu_\beta$ for **3** ($S = 4$ for the tetranuclear entity plus two isolated Cu^{II} cations). Reduced magnetization measurements show quasi-superimposable plots revealing a quasi-negligible D effect, as shown in Fig. 2, right.

The out-of-phase field dependence of **1**–**3** (Fig. S4–S6†) shows that none of the three complexes show signals at zero dc field but clear peaks with strong dependence of the intensity and position of the maxima for increasing fields were observed. From these previous measurements, the ac in the 1–1488 frequency range were measured under the field that yielded the maximum χ''_m response.

Ac measurements show a similar response for the three complexes with two different high frequency (HF) and low frequency (LF) processes. The $\ln(1/2\pi\nu)$ *vs.* T plot shows nonlinear frequency-dependent peaks for the larger frequencies, whereas the LF peaks are found to be frequency-independent, Fig. S7.† These signals are centred at 2.1 K, and at 2.6 K for **1** and **3**, respectively, and are displaced below 2 K for **2**, as shown in Fig. 3 and S8.† Maxima in the $\chi''_m(\nu)$ plots were only found for lower temperatures for **2** in the LF region, centred at a constant value of around 2 Hz, implying LF with relatively large relaxation times of around 80 ms.
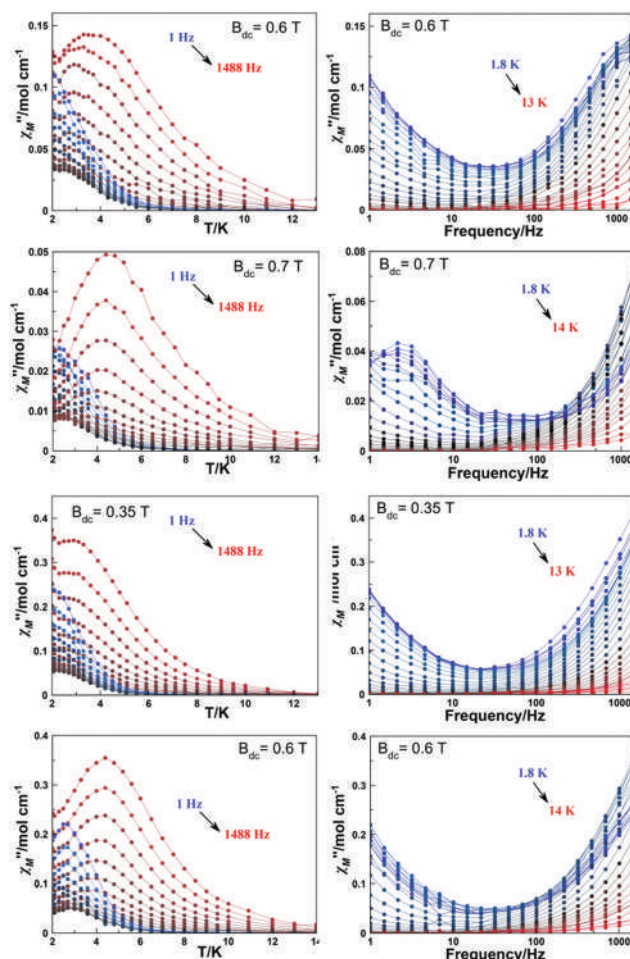
The two processes are also reflected in the corresponding Cole–Cole plots of the three compounds, as shown in Fig. S9.† The fit of the Argand plots shows relatively large τ values between 0.2 and 0.08 s for the LF process in agreement with the $1/2\pi\nu$ position of the χ''_m maxima that appear at 2.5 Hz for **2** and below 1 Hz for **1** and **3** and values of the order of 10^{-5} s for the HF process.

It is noticeable that the $\tau(T)$ values show low temperature clear maxima for compounds **2** and **3**, as shown in Fig. 4 and thus, the decreasing region of the $\ln(\tau)$ *vs.* T^{-1} plot cannot be fitted with the usual Orbach, Raman or Direct processes. The $\ln(\tau)$ *vs.* T^{-1} plot was fitted with Raman + QTM processes for **1** and the increasing region of the plots for **2** and **3** was simulated with the usual Raman + Direct processes (Fig. S10 and Table S6†).

The origin of the reversal of the magnetization in the case of quasi-isotropic systems, where there is no option of a potential barrier depending on the anisotropy separating the two magnetic bistable states, has been attributed to the crossing of the m_s levels that becomes accessible under low external
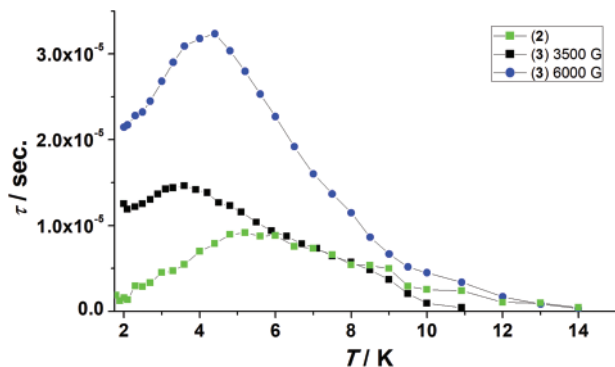
Fig. 4 Plot of $\tau(T)$ showing the maxima of τ for complexes **2** and **3**.

fields.[4o,p,11] The decrease at low temperatures of $\tau(T)$ has been parametrized with the so called "*strange term*"[4k,6b,12] but its physical meaning has not been rationalized. The LF signals have been attributed to intermolecular interactions but in contrast, they can be observed in well isolated or magnetically diluted complexes.[4p] These LF signals are not always present and they are usually (but not always) temperature and frequency independent and new examples to systematize these properties are still needed.

In conclusion, the Cu^{II}/Mn^{II} complexes **1–3**, based on compartmental Schiff bases with a predetermined distorted coordination polyhedron around the Mn^{II} cations, show some unprecedented features in slow relaxing zero-dimensional compounds: (i) irrespective of the system (isolated isotropic cations or polynuclear clusters), their ac magnetic responses are similar; (ii) the systems reveal field induced SMM responses despite the fact that they have been built from apparently unsuitable cations such as Cu^{II} and Mn^{II} for which a quasi-negligible D is expected; (iii) due to the moderately strong superexchange coupling, the ground states are clearly defined, one of them being an $S = 4$ that has become the highest spin reported until now exhibiting these kinds of properties and, (iv) the SMM response shows HF (temperature and frequency dependent) that follows the usual Raman plus direct relaxation and LF processes (temperature and frequency independent) with relatively large relaxation times for which the origin is still unclear.

Conflicts of interest

There are no conflicts to declare.

Acknowledgements

Notes and references

1 D. Gatteschi, R. Sessoli and J. Villain, *Molecular Nanomagnets*, Oxford University Press, Oxford, 2006.

2 (*a*) K. S. Pedersen, J. Dreiser, H. Weihe, R. Sibille, H. V. Johannesen, M. A. Sorensen, B. E. Nielsen, M. Siguist, H. Mutka, S. Rols, J. Bendix and S. Piligkos, *Inorg. Chem.*, 2015, **54**, 7600; (*b*) E. Ruiz, J. Cirera, J. Cano, S. Alvarez, C. Loose and J. Kortus, *Chem. Commun.*, 2008, 52.

3 J. Tang and P. Zhang, *Lanthanide Single Molecule Magnets*, Springer-Verlag Berlin Heidelberg, 2015.

4 (*a*) M. Orendáč, L. Sedláková, E. Čižmár, A. Orendáčová, A. Feher, S. A. Zvyagin, J. Wosnitza, W. H. Zhu, Z. M. Wang and S. Gao, *Phys. Rev. B: Condens. Matter Mater. Phys.*, 2010, **81**, 214410; (*b*) M. J. Martınez-Perez, S. Cardona-Serra, C. Schlegel, F. Moro, P. J. Alonso, H. Prima-Garcıa, J. M. Clemente-Juan, M. Evangelisti, A. Gaita-Ariño, J. Sese, J. van Slageren, E. Coronado and F. Luis, *Phys. Rev. Lett.*, 2012, **108**, 247213; (*c*) V. Tkac, A. Orendacova, R. Tarasenko, E. Cizmar, M. Orendac, K. Tibenska, A. G. Anders, S. Gao, V. Pavlık and A. Feher, *J. Phys.: Condens. Matter*, 2013, **25**, 506001; (*d*) P. I. Girginova, L. C. J. Pereira, J. T. Coutinho, I. C. Santos and M. Almeida, *Dalton Trans.*, 2014, **43**, 1897; (*e*) A. Arauzo, A. Lazarescu, S. Shova, E. Bartolome, R. Cases, J. Luzón, J. Bartolomé and C. Turta, *Dalton Trans.*, 2014, **43**, 12342; (*f*) R. J. Holmberg, L. T.-A. Ho, L. Ungur, I. Korobkov, L. F. Chibotaru and M. Murugesu, *Dalton Trans.*, 2015, **44**, 20321; (*g*) A. J. Calahorro, I. Oyarzabal, B. Fernandez, J. M. Seco, T. Tian, D. Fairen-Jimenez, E. Colacio and A. Rodrıiguez-Diéguez, *Dalton Trans.*, 2016, **45**, 591; (*h*) T. Yoshida, G. Cosquer, D. C. Izuogu, H. Ohtsu, M. Kawano, Y. Lan, W. Wernsdorfer, H. Nojiri, B. K. Breedlove and M. Yamashita, *Chem. – Eur. J.*, 2017, **23**, 4551; (*i*) D. C. Izuogu, T. Yoshida, H. Zhang, G. Cosquer, K. Katoh, S. Ogata, M. Hasegawa, H. Nojiri, M. Damjanovic, W. Wernsdorfer, T. Uruga, T. Ina, B. K. Breedlove and M. Yamashita, *Chem. – Eur. J.*, 2018, **24**, 9285; (*j*) L. Escalera-Moreno, J. J. Baldovi, A. Gaita-Ariño and E. Coronado, *Chem. Sci.*, 2018, **9**, 3265; (*k*) A. Vráblová, M. Tomás, L. R. Falvello, L. Dlhán, J. Titis, J. Cernák and R. Boca, *Dalton Trans.*, 2019, **48**, 13943; (*l*) M. Dolai, M. Ali, C. Rajnak, J. Titis and R. Boca, *New J. Chem.*, 2019, **43**, 12698; (*m*) Y.-C. Chen, Y.-Y. Peng, J.-L. Liu and M.-L. Tong, *Inorg. Chem. Commun.*, 2019, **107**, 107449; (*n*) Y. H. Pham, V. A. Trush, A. N. Carneiro Neto, M. Korabik, J. Sokolnicki, M. Weselski, O. L. Malta, V. M. Amirkhanov and P. Gawryszewska, *J. Mater. Chem. C*, 2020, **8**, 9993; (*o*) Y. Horii, K. Katoh, Y. Miyazaki, M. Damjanovic, T. Sato, L. Ungur, L. F. Chibotaru, B. K. Breedlove, M. Nakano, W. Wernsdorfer and M. Yamashita, *Chem. – Eur. J.*, 2020, **26**, 8076; (*p*) J. Mayans and A. Escuer, *Chem. Commun.*, 2021, **57**, 721.

5 T. K. Ghosh, S. Maity, J. Mayans and A. Ghosh, *Inorg. Chem.*, 2021, **60**, 438.

6 (*a*) A. C. Benniston, S. Melnic, C. Turta, A. B. Arauzo, J. Bartolomé, E. Bartolomé, R. W. Harrington and

M. R. Probert, *Dalton Trans.*, 2014, **43**, 13349; (*b*) C. Rajnak, J. Titis, J. Moncol, R. Micova and R. Boca, *Inorg. Chem.*, 2019, **58**(2), 991; (*c*) T. T. da Cunha, V. M. M. Barbosa, W. X. C. Oliveira, E. F. Pedroso, D. M. A. Garcia, W. C. Nunes and C. L. M. Pereira, *Inorg. Chem.*, 2020, **59**(18), 12983; (*d*) K. Uchida, G. Cosquer, K. Sugisaki, H. Matsuoka, K. Sato, B. K. Breedlove and M. Yamashita, *Dalton Trans.*, 2019, **48**, 12023.

7 M. Llunell, D. Casanova, J. Cirera, P. Alemany and S. Alvarez, *SHAPE, version 2.0*, Barcelona, 2010. The program can be obtained by request to the authors.

8 N. F. Chilton, R. P. Anderson, L. D. Turner, A. Soncini and K. S. Murray, *J. Comput. Chem.*, 2013, **34**, 1164.

9 S. Dutta, P. Bhunia, J. Mayans, M. Drew and A. Ghosh, *Dalton Trans.*, 2020, **49**, 11268.

10 A. Escuer, J. Esteban, S. P. Perlepes and Th. C. Stamatatos, *Coord. Chem. Rev.*, 2014, **275**, 87.

11 M. Orendáč, L. Sedláková, E. Čižmár, A. Orendáčová, A. Feher, S. A. Zvyagin, J. Wosnitza, W. H. Zhu, Z. M. Wang and S. Gao, *Phys. Rev. B: Condens. Matter Mater. Phys.*, 2010, **81**, 214410.

12 J. Titiš, C. Rajnák, D. Valigura and R. Boča, *Dalton Trans.*, 2018, **47**, 7879.

Electronic Supplementary Material (ESI) for Dalton Trans.

"Quasi-isotropic SMMs: slow relaxation of the magnetization in polynuclear Cu^{II}/Mn^{II} complexes"

Evangelos Pilichos,[a] Pradip Bhunia,[b] Mercè Font-Bardia,[c] Ashutosh Ghosh,[b,d] Júlia Mayans, [a] Albert Escuer *,[a]

[a] Departament de Química Inorgànica i Orgànica, Secció Inorgànica and Institute of Nanoscience (IN^{2}UB) and Nanotecnology, Universitat de Barcelona, Martí i Franquès 1-11, Barcelona-08028, Spain.

[b] Department of Chemistry, University College of Science, University of Calcutta, Kolkata 700009, India.

[c] Departament de Mineralogia, Cristal·lografia i Dipòsits Minerals, Universitat de Barcelona, Martí Franqués s/n, 08028 Barcelona (Spain) and Unitat de Difracció de R-X. Centre Científic i Tecnològic de la Universitat de Barcelona (CCiTUB), Solé i Sabarís 1-3. 08028 Barcelona

[d] Rani Rashmoni Green University, Hooghly 712410, West Bengal, India

1-Instrumental measurements

2-Syntheses and characterization.

3-Structural aspects.

4-Magnetic data.

1-Instrumental measurements

Physical measurements: Magnetic susceptibility measurements were carried out on powdered fresh crystals samples with a MPMS5 Quantum Design susceptometer working in the range 30-300 K under magnetic fields of 0.3 T and under a field of 0.03T in the 30 – 2 K range to avoid saturation effects at low temperature. Diamagnetic corrections were estimated from Pascal Tables. Samples for analysis were vacuum dried to remove crystallization solvents. Infrared spectra (4000-400 cm–1) were recorded from KBr pellets on a Bruker IFS-125 FT-IR spectrophotometer.

2-Syntheses and characterization.

[CuL1] metalloligand: the Cu^{II} complex [CuL1] derived from the unsymmetrical di-Schiff base ligand (H_2L = N-(α-methylsalicylidene)-N′-(salicylidene)-2,2-dimethyl-1,3-propanediamine) was synthesized following the reported method[1] by replacing the 1,3-propanediamine with 2,2-dimethyl-1,3-propanediamine.

N,N'-Ethylene-bis(3-ethoxysalicylaldiimine) (L2) The Schiff base was synthesized following reported methods[2] mixing an ethanolic solution (15 mL) of ethylenediamine (3 mmols/0.18 g)) and o-vanillin (6 mmol/0.91 g). The solution was stirred at room temperature during two hours and the formed yellow solid was collected by filtration and air dried. Yield 80%.

Synthesis of $[(Cu^{II}L1)_2Mn^{II}(N_3)_2]\cdot2H_2O$ ($1\cdot2H_2O$). $Mn(ClO_4)_2\cdot H_2O$ (0.361 g, 1 mmol) was dissolved in a 10 ml of MeOH and to it a 2 ml aqueous solution of NaN_3 (0.130 g, 2 mmol) and a 30 ml methanolic solution of the metalloligand [CuL1] (0.772 g, 2 mmol) were added to it with stirring. After ~ 30 min of stirring, the light green solution was filtered to remove any suspended particles. Brown coloured diffraction quality single crystals were formed within a few days on slow evaporation of solvent. The crystals were collected after 5 days. Yield: 61%. $C_{40}H_{44}Cu_2MnN_{10}O_4$. Calcd: C, 52.74; H, 4.87; N, 15.38. Found C, 52.61; H, 4.99; N, 15.50.

$[\{Cu^{II}(L2)Mn^{II}(H_2O)_2(MeOH)\}-\{Cu^{II}(L2)\}_2](ClO_4)_2\cdot MeOH$ ($2\cdot MeOH$) To a yellowish methanolic solution (10 ml) of the Schiff base L (0.8 mmol/0.3 g), an aqueous solution (5 ml) of $Cu(OAc)_2\cdot4H_2O$ (0.8 mmol/0.159 g) was added. The reaction mixture was placed into a microwaves furnace at 80˚C for 30 minutes. The precursor $[Cu^{II}(L)]$ was formed as a green precipitate that was filtered and air dried. The freshly formed powder of $[Cu^{II}(L)]$ was dissolved in 20 ml of CH_2Cl_2 and of MeOH (1:1) and $Mn(ClO_4)_2\cdot6H_2O$ (0.25 mmol/0.064 g) was added. The solution was heated in the microwaves furnace for 15 min. at 70˚C, resulting a clear dark solution. After 2 days brown crystals, suitable for X-ray diffraction, were formed by layering with diethylether. Yield: 70%. $C_{55}H_{61}Cl_2Cu_3MnN_6O_{23}$ Calcd: C, 44.32; H, 4.12; N, 5.64. Found C, 44.6; H, 4.4; N, 5.4.

$[(\mu_{1,1}-N_3)_2\{Cu^{II}(L2)Mn^{II}\}-\{Cu^{II}(L2)Na^I(MeOH)(N_3)\}_2](ClO_4)_2$ (3) The complex was prepared following the same procedure than complex **2** but adding NaN_3 (0.4 mmol/0.026 g) to the $[Cu^{II}(L)]$ / $Mn(ClO_4)_2\cdot6H_2O$ dissolution. The mixture was introduced to microwaves for 15 min. at 70˚C. After two days brown crystals, suitable for X-ray diffraction, were formed by vapor diffusion of diethylether. Yield: 40%. $C_{74}H_{80}Cl_2Cu_4Mn_2N_{20}Na_2O_{26}$. Calcd: C, 41.41; H, 3.75; N, 13.05. Found C, 41.0; H, 3.7; N, 13.1.
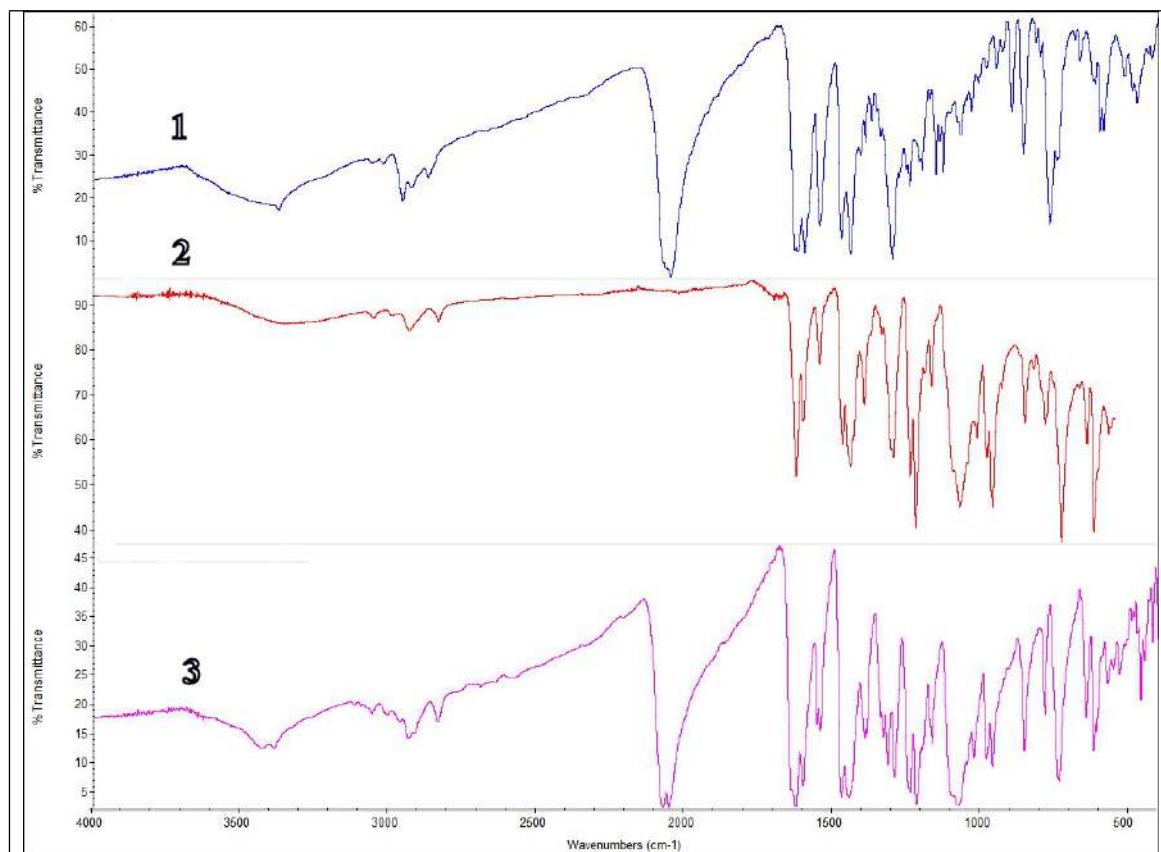
Figure S1. IR spectra for complexes **1** - **3**. Characteristic bands: st. C-H 3000-2800 cm^{-1}; N=C iminic ~1600 cm^{-1}; for **2** and **3**, st. ClO_4^- 1075 cm^{-1}; δ ClO_4^- 620 cm^{-1}. The stretching for the terminal and end-to-end azides for **3** appears differentiated at 2074 and 2055 cm^{-1} respectively.

3-Structural aspects.

Table S1. Crystal data and structure refinement for complexes **1**, **2** and **3**.

	1	2	3
Formula	$C_{40}H_{45}Cu_2MnN_{10}O_5$	$C_{56}H_{66}Cl_2Cu_3MnN_6O_{24}$	$C_{74}H_{80}Cl_2Cu_4Mn_2N_{20}Na_2O_{26}$
FW	927.88	1523.60	2146.5
System	Monoclinic	Monoclinic	Triclinic
Space group	C2/c	P21/c	P-1
a/Å	16.839(2)	15.4787(6)	12.3500(6)
b/Å	16.637(2)	22.7556(9)	13.0272(7)
c/Å	16.478(2)	17.7148(7)	13.9308(7)
α/deg.	90	90	107.897(2)
β/deg.	99.467(2)	97.002(1)	91.793(2)
γ/deg.	90	90	94.147(2)
V/ Å^3	4553.3(9)	6193.1(4)	2123.9(2)
Z	4	4	1
T, K	296(2)	100(2)	100(2)
λ(MoKα), Å	0.71073	0.71073	0.71073
ρ_{calc}, g·cm^{-3}	1.354	1.634	1.678
μ(MoK$_\alpha$), mm^{-1}	1.250	1.389	1.435
R	0.0609	0.0513	0.0334
ωR^2	0.1774	0.1188	0.0889

Table S2. Selected bond distances (Å) and angles (°) for compound **1**.

Bond lengths (Å)			
Cu1 – O11	1.880(3)	Mn(1) – O(11)	2.322(3)
Cu1 – O31	1.893(3)	Mn(1) – O(31)	2.138(3)
Cu1 – N19	1.912(4)	Mn(1) – N(35)	2.163(15)
Cu1 – N23	1.929(5)	Mn(1) – N(35) $^\#$	2.070(15)
O11 – Cu1 – O31	83.9(1)	O31 – Cu1 – N19	168.3(2)
O11 – Cu1 – N19	94.8(2)	O31 – Cu1 – N23	90.8(2)
O11 – Cu1 – N23	162.7(2)	N19 – Cu1 – N23	93.6(2)
O11 – Mn1 – O31	68.8(1)	O31 – Mn1 – N35	98.3(6)
O11 – Mn1 – N35	83.3(4)	O31 – Mn1 – O31$^\#$	142.5(2)
O11 – Mn1 – O11$^\#$	81.7(2)	O31 – Mn1 – N35^a	102.3(6)
O11 – Mn1 – O31$^\#$	82.9(1)	N35 – Mn1 – N35$^\#$	112.5(7)
O11 – Mn1 – N35$^\#$	163.3(4)		

Table S3. Selected bond distances (Å) and angles (°) for compound **2**.

d Å			
Cu2-O6	1.894(3)	Cu2-N3	1.919(3)
Cu2-O7	1.898(3)	Cu2-N4	1.908(3)
Mn-O6	2.192(2)	Mn-O13	2.153(3)
Mn-O7	2.191(3)	Mn-O14	2.141(3)
Mn-O23	2.164(3)		
Mn-O5	2.585(3)	Mn-O8	2.624(2)
Cu1-O2	1.905(3)	Cu1-N1	1.942(3)
Cu1-O3	1.916(3)	Cu1-N2	1.931(3)
Cu3-O10	1.908(3)	Cu3-N5	1.941(3)
Cu3-O11	1.904(3)	Cu3-N6	1.939(3)
Angles (º)			
O6-Mn-O7	69.71(9)	O7-Mn-O23	143.7(1)
O6-Mn-O23	145.1(1)	O13-Mn-O14	173.1(1)
O7-Mn-O8	63.78(8)	O8-Mn-O23	81.30(9)
O5-Mn-O23	81.77(9)	O5-Mn-O6	64.16(8)
Cu2-O6-Mn	103.9(1)	Cu2-O7-Mn	103.7(1)

Table S4. Selected bond distances (Å) and angles (°) for compound **3**.

d Å			
Cu2-O6	1.894(1)	Cu2-N3	1.921(1)
Cu2-O7	1.897 (1)	Cu2-N4	1.911(2)
Mn-O6	2.222(1)	Mn-N8	2.180(2)
Mn-O7	2.179(1)	Mn-N8'	2.269(2)
Mn-N5	2.146(2)		
Mn-O5	2.546(1)	Mn-O9	2.597(1)
Cu1-O2	1.898(1)	Cu1-N1	1.923(2)
Cu1-O3	1.892(1)	Cu1-N2	1.931(1)
Na-O1	2.680(1)	Na-O6	2.910(1)
Na-O2	2.326(1)	Na-O8	2.314(2)
Na-O3	2.344(1)	Na-N5	2.494(2)
Na-O4	2.681(1)		
Angles (º)			
O6-Mn-O7	69.69(4)	O6-Mn-N8	143.98(5)
O7-Mn-N8	138.48(6)	N5-Mn-N8'	171.89(6)
O5-Mn-O6	63.68(4)	O5-Mn-N8	84.81(5)
O7-Mn-O9	64.06(5)	O9-Mn-N8	82.96(5)
Cu2-O6-Mn	102.46(5)	Cu1-O7-Mn	103.96(5)
Mn-N8-Mn'	104.55(6)		

Table S5. SHAPE measures for the Mn^{II} cations of complexes **1-3** parametrized. $S(P) = 0$ corresponds to a structure fully coincident in shape with the reference polyhedron P, regardless of size and orientation. The closest polyhedron to the corresponding coordination sphere is highlighted in red.

	(1)	**(2)**	**(3)**
S(vOC-5)	--	7.00	5.89
S(TBPY-5)	--	6.88	6.98
S(SPY-5)	--	6.94	5.84
S(JTBPY-5)	--	8.86	8.50
S(OC-6)	**2.03**	--	--
S(TPR-6)	11.85	--	--
S(PBPY-7)	--	**1.85**	**2.84**
S(COC-7)	--	7.74	5.77
S(CTPR-7)	--	6.07	4.48
S(JPBPY-7)	--	4.00	5.59

Ideal ML$_5$ polyhedra: vOC-5 (C$_4$v) Vacant octahedron; TBPY-5 (D$_3$h) Trigonal bipyramid; SPY-5 (C$_4$v) Spherical square pyramid; JTBPY-5 (D$_3$h) Johnson trigonal bipyramid J12.
Ideal ML$_6$ polyhedra: OC-6 (Oh) octahedron; TPR-6 (D$_3$h) trigonal prism
Ideal ML$_7$ polyhedra: PBPY-7 (D5h) Pentagonal bipyramid; COC-7 (C3v) Capped octahedron; CTPR-7 (C2v) Capped trigonal prism; JPBPY-7 (D5h) Johnson pentagonal bipyramid J13; JETPY-7 (C3v) Johnson elongated triangular pyramid J7.
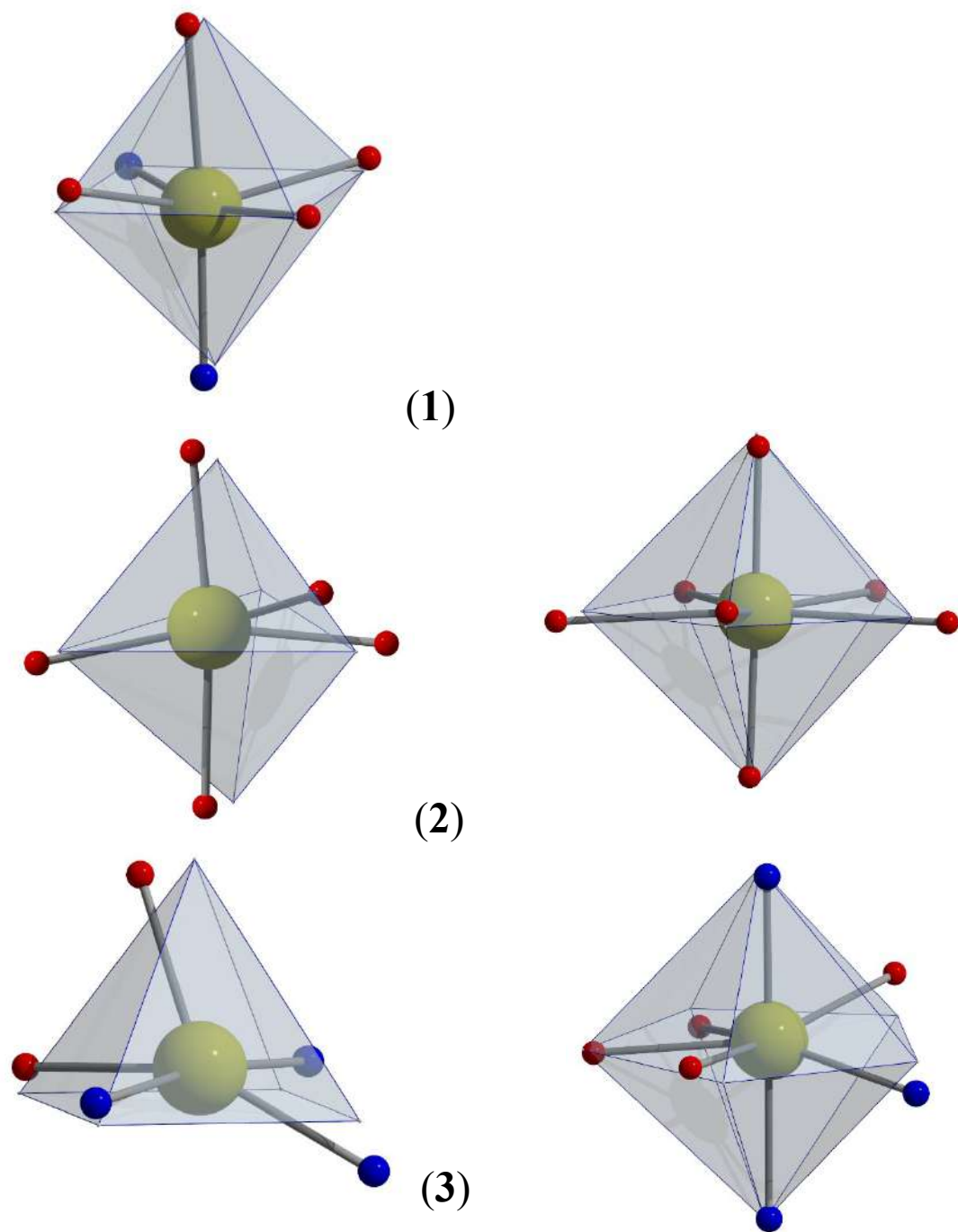
Figure S2. Plot of the coordination sphere for complexes **1-3**, referenced to the ideal polyhedron with lower *S*(*P*) value.

1

2

3
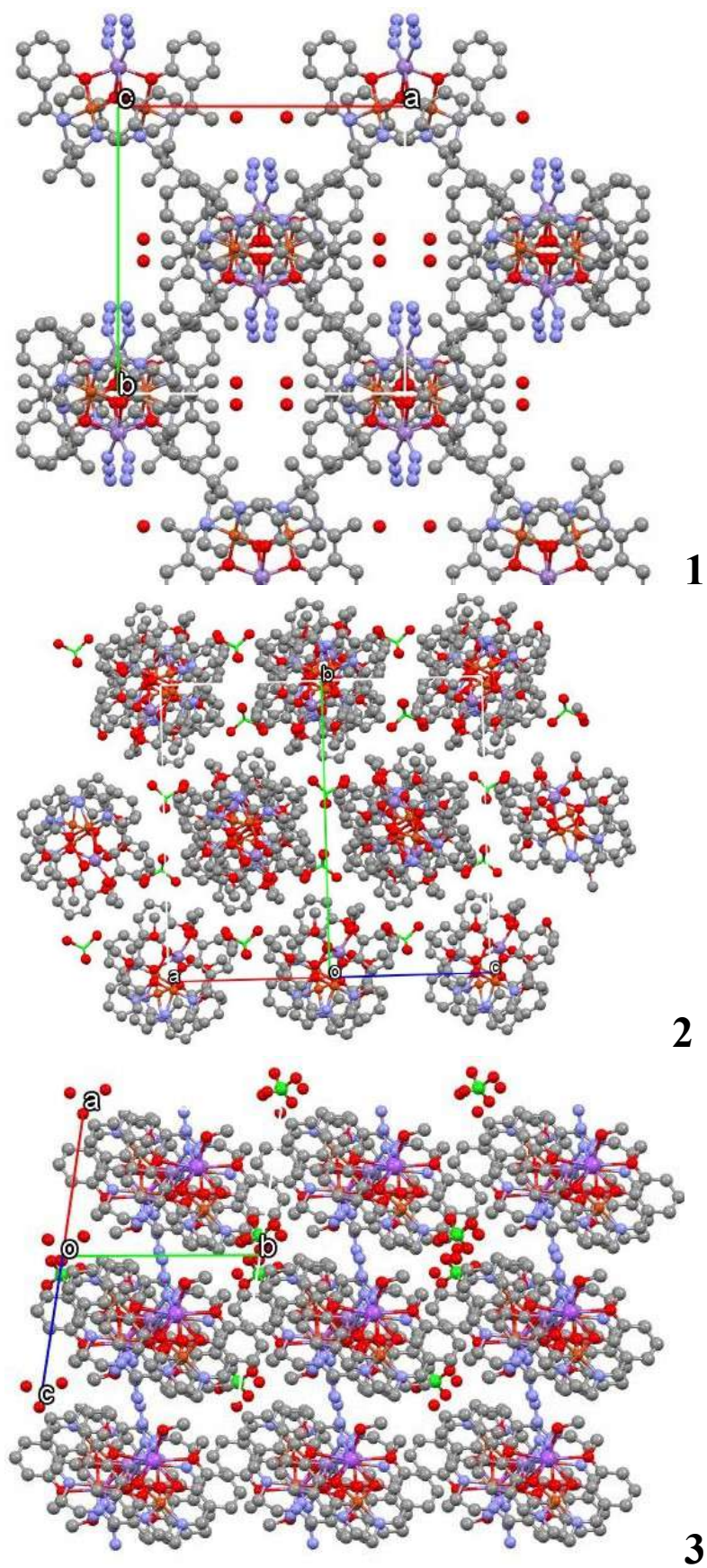
Figure S3. Plot of the network arrangement of complexes **1**-**3** viewed along the pillared clusters.

4-Magnetic data.
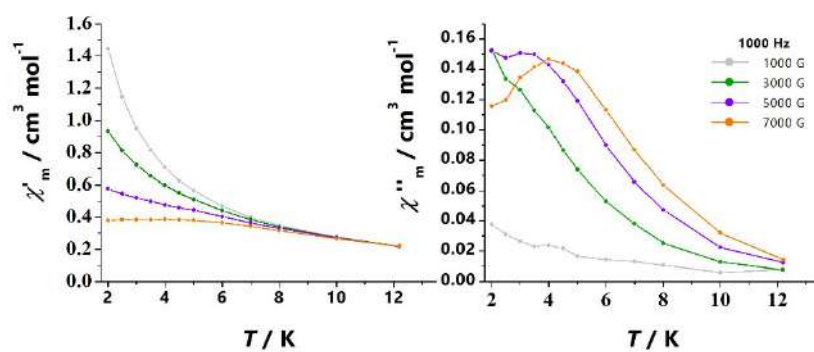
Figure S4. χ_M'' dependence of the transverse field for complex **1**.
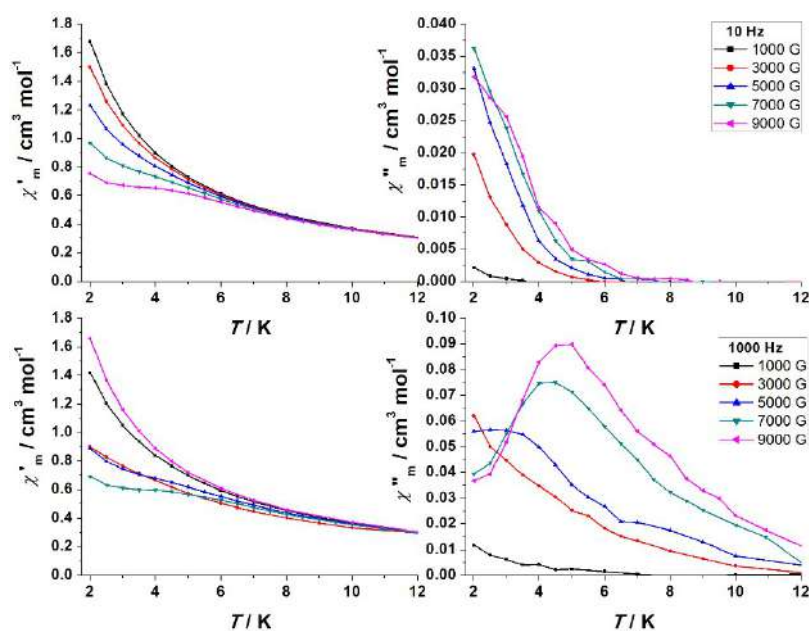
Figure S5. χ_M'' dependence of the transverse field for complex **2**.
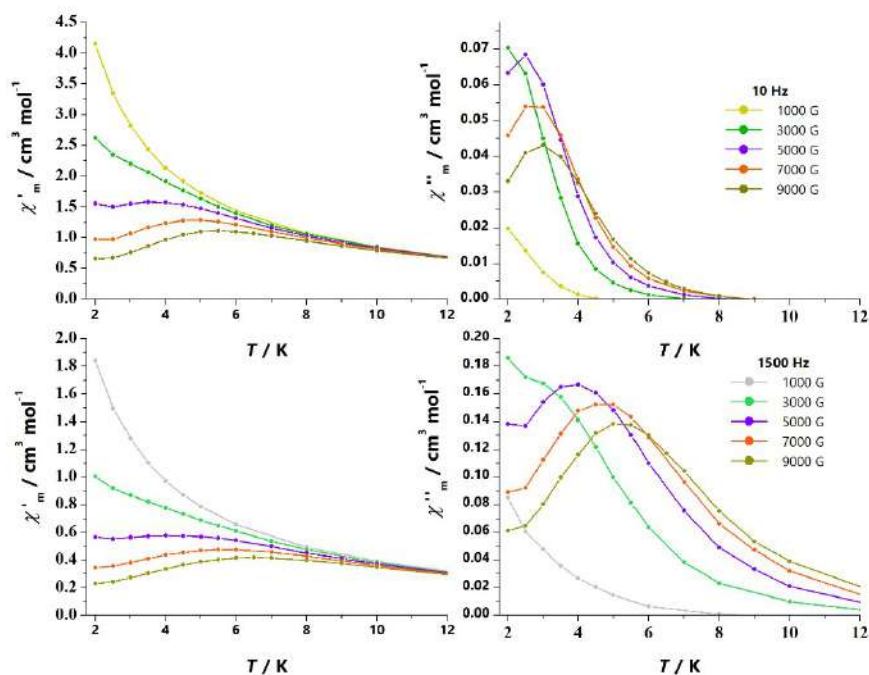
Figure S6. $\chi_M{}''$ dependence of the transverse field for complex **3**.
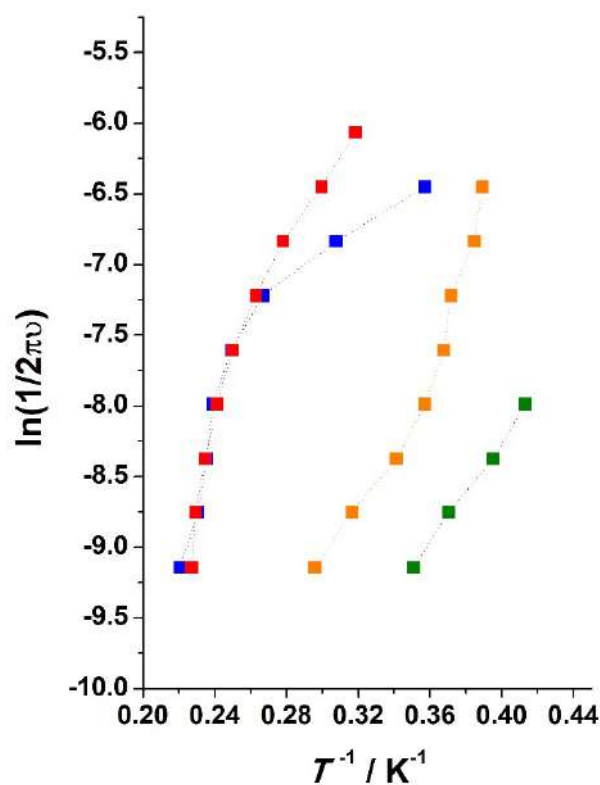
Figure S7. Plot of $\ln(1/2\pi\nu)$ vs. T^{-1} from the $\chi_M{}''(T)$ data for complexes **1** (orange) **2** (blue) and **3** (3500 G, green; 6000 G, red).The data is limited to the HF region for which the maxima of $\chi_M{}''$ can be observed.
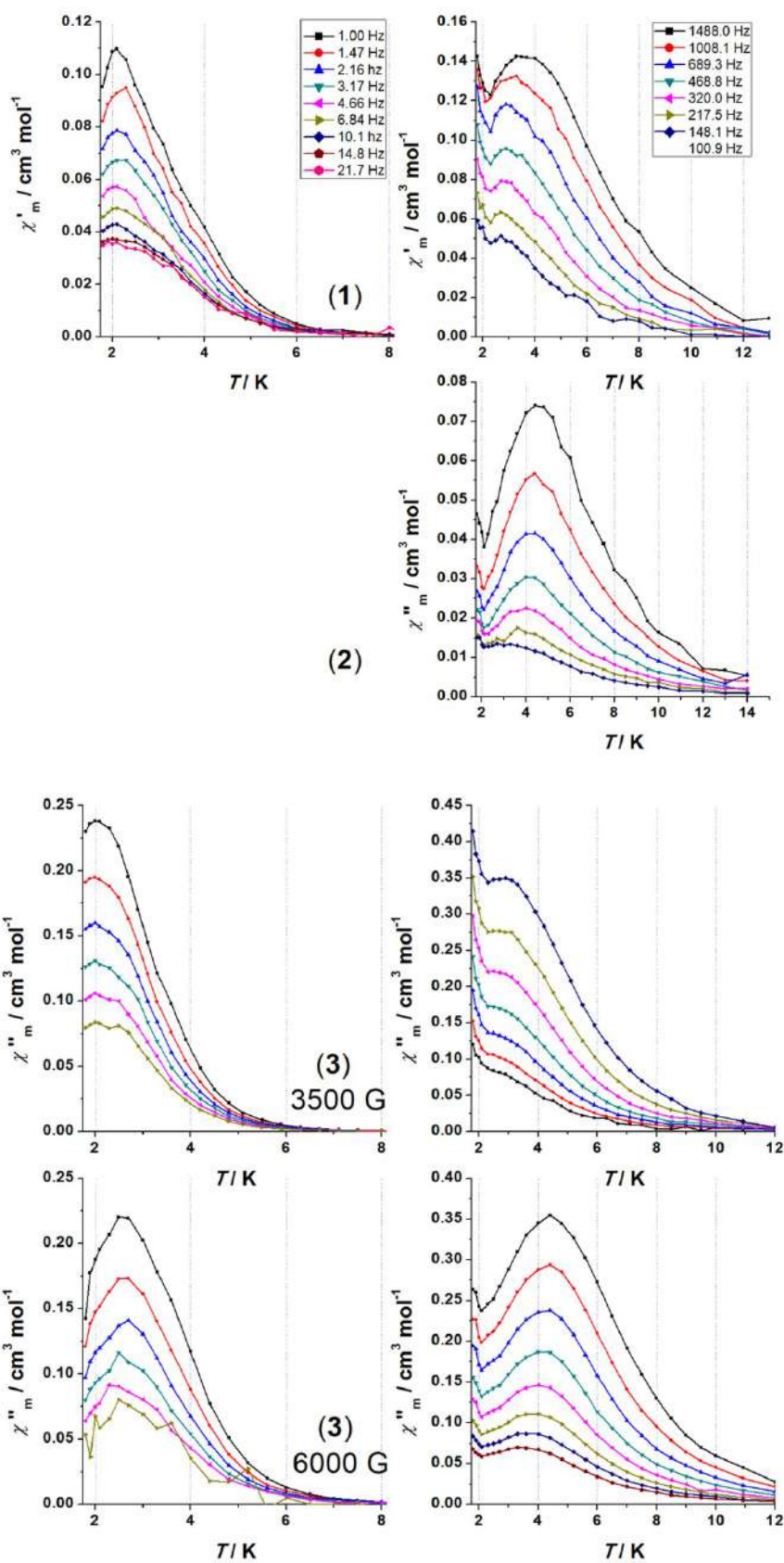
Figure S8. $\chi_M''(T)$ for complexes **1**, **2** amd **3** showing that the position of the maxima is temperature independent for the lower frequencies (left) and temperature dependent for the higher (right) frequencies. For the intermediate range of frequencies maxima are not defined.
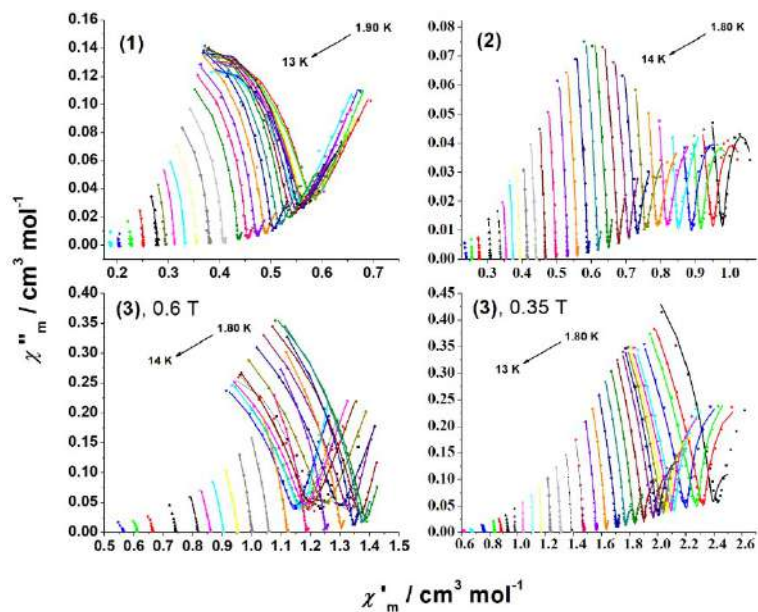
Figure S9. Cole-Cole plots for complexes **1**, **2** and **3.** Solid lines show the best fit of the experimental data.

$$\frac{1}{\tau} = CT^n + AT + QT$$

Table S6. Best fit values for the $\ln(\tau)$ *vs.* T^{-1} plot ( ) for complexes **1-3**.

	C	*n*	*QT*	*A*	E_a^*	τ_o^*
(**1**)	2.011	4.38	9745	--	13.5	$2.9 \cdot 10^{-6}$
(**2**)	0.001	8.4	--	20714	42.8	$4.9 \cdot 10^{-8}$
(**3**) - 3500 G	$2.9 \cdot 10^{-4}$	9.1	--	1847	32.5	$1.8 \cdot 10^{-8}$
(**3**) - 6000 G	0.95	5.23	--	6232	45.2	$6.7 \cdot 10^{-8}$

*Values extracted from the higher temperature data. Due to the limited number of points these values have a large degree of uncertain.
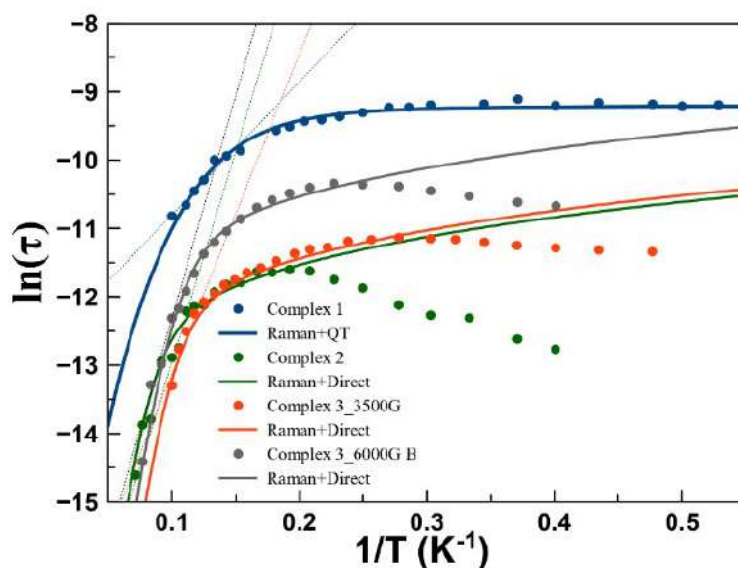
Figure S10. Plot of $\ln(\tau)$ *vs.* T^{-1} for complexes **1** – **3**. Solid lines show the best fit of the experimental data. For **2** and **3** the fit was performed for the increasing high temperature data. A after the maximum of the plot the decrease of $\ln(\tau)$ at lower temperatures. Straigh solid lines (gray), shows the slope of the linear region at higher temperatures.

References

1. P. Mahapatra, S. Ghosh, S. Giri, V. Rane, R. Kadam, M. G. B. Drew and A. Ghosh, *Inorg. Chem*., 2017, **56**, 5105.
2. I. Correia, J. C. Pessoa, M. T. Duarte, M. F. M.da Piedade, T. Jackush, T. Kiss, M. M. C. A. Castro, C. F. G. C. Geraldes and F. Avecilla, *Eur. J. Inorg. Chem*., 2005 , 732.

PUBLICATION #5

"Occurrence of slow relaxation of the magnetization in a family of copper(II)/manganese(II) quasi-isotropic complexes with different ground states"

Occurrence of slow relaxation of the magnetization in a family of copper(II)/manganese(II) quasi-isotropic complexes with different ground spin states†

Evangelos Pilichos,[a] Mercè Font-Bardia,[b,c] Albert Escuer ✶[a,d] and Júlia Mayans ✶[a,d]

A family of copper(II)/manganese(II) new clusters with the formulas [Cu^{II}Na^{I}(L2)(MeOH)(ClO$_4$)] (**1**), [Cu$_2^{II}$Mn^{II}(S,S-L3)$_2$(MeOH)](ClO$_4$)$_2$ (**2SS**), [{Cu^{II}Mn^{II}(L1)(H$_2$O)$_2$(MeOH)}{Cu^{II}(L1)}$_2$](ClO$_4$)$_2$ (**3**), [(μ$_{1,3}$-N$_3$)$_2${Cu^{II}Mn^{II}(L2)(H$_2$O)}$_2${Cu^{II}(L2)$_2$}](ClO$_4$)$_2$ (**4**) and [(μ$_{1,1}$-N$_3$)$_2${Cu^{II}Mn^{II}(L1)(N$_3$)}$_2${Cu^{II}Na^{I}(L1)(MeOH)}$_2$](ClO$_4$)$_2$ (**5**) with L1 = *N,N′*-ethylene-bis(3-methoxysalicylaldiimine), L2 = *N,N′*-ethylene-bis(3-ethoxysalicylaldiimine) and L3 = *N,N′*-cyclohexane-bis(3-ethoxysalicylaldiimine), has been synthesized, and structurally and magnetically characterized. Reduced magnetization studies demonstrate that the magnetic anisotropy of the systems is very small. However, dynamic magnetic studies and ultra-low-frequency Raman spectroscopy confirm the slow relaxation of these systems despite their quasi-isotropic nature, enlarging the range of non-anisotropic slow relaxing molecules.

Introduction

The single molecule/ion magnet (SMM/SIM) response has been traditionally associated with the magnitude of the barrier of the reversal of the magnetization (U_{eff}) as a function of the axial zero field splitting parameter (D), and the total spin state (S), parametrized for d cations as DS^2 or $DS^2 - 1/4$ for integer or half-integer spins respectively.[1] However, the control of D is challenging and researchers moved to the use of lanthanide cations which present a high ion anisotropy (thanks to their spin–orbit coupling) that allowed high blocking temperatures close to 80 K, or extremely large coercive magnetic fields of around 14 T to be reached.[2,3]

In contrast, in recent years, field-induced slow relaxation of the magnetization of isotropic cations, having a half-filled shell like Gd^{III} (^{8}S$_{7/2}$)[4–21] or high-spin Mn^{II} (^{6}A$_{1g}$ in an O$_h$

environment),[22–25] have been recently reported despite the fact that, *a priori*, this kind of magnetic response was not expected due to its low or negligible D value. A special case is the high-spin Fe^{III} cation that in spite of its ground ^{6}A$_{1g}$ term exhibits a sizable barrier for the reversal of the magnetization in mononuclear[26] or polynuclear[27] systems that has been justified by the presence of low-lying quartet or doublet states.[28]

All the Gd^{III} studied systems are mononuclear or extremely weak interacting 1D complexes with $D \gg J_{Gd–Gd}$ with the exception of one ferromagnetic coupled Cu^{II}Gd^{III} dimer reported by one of the authors with a defined $S = 3$ ground state.[20] For the Mn^{II} cation case, all the systems are mononuclear complexes in octahedral[22–24] or pentagonal bipyramid[25] coordination environments.

The Mn^{II} cation is more adequate than Gd^{III} to study this kind of system because the internal f orbitals of the lanthanides are poorly sensitive to the environment but the 3d orbitals of the Mn^{II} cation have some features that allow the control of its anisotropy in two ways: first, the ligand field of the ligands can be easily modified, employing donors that can induce different fields and, on the other hand, profiting from the zero contribution of the ligand field stabilization energy for the high-spin d^5 electronic configuration, the coordination sphere around the cation can be tuned (strongly distorted O$_h$, penta- or heptacoordination) by the adequate design of the topology of the ligands.

Hexadentate Schiff bases derived from the condensation of 1,2-diamines and *o*-vanillin are compartmental ligands that

[a]*Departament de Química Inorgànica i Orgànica, Secció Inorgànica, Martí i Franqués 1-11, Barcelona-08028, Spain. E-mail: albert.escuer@qi.ub.edu*
[b]*Departament de Mineralogia, Cristal·lografia i Dipòsits Minerals, Universitat de Barcelona, Martí Franqués s/n, 08028 Barcelona, Spain*
[c]*Unitat de Difracció de R-X. Centre Científic i Tecnològic de la Universitat de Barcelona (CCiTUB), Solé i Sabarís 1-3, 08028 Barcelona, Spain*
[d]*Institute of Nanoscience and Nanotecnology (IN²UB), Universitat de Barcelona, Spain*

can coordinate one cation in their inner N_2O_2 cavity and one second cation in the external cavity, which is usually placed in a strongly distorted environment. On this basis, we have chosen several Schiff bases like N,N'-ethylene-bis(3-methoxy-salicylaldiimine) (**L1**), N,N'-ethylene-bis(3-ethoxysalicylaldiimine) (**L2**) and the chiral N,N'-cyclohexane-bis(3-ethoxysalicylaldi-imine) (**L3**) (Scheme 1), with the aim of checking that the slow reversal of the magnetization is not restricted to mononuclear systems and that it can be observed in weak anisotropic poly-nuclear clusters with different nuclearities or S ground states. To try to increase the nuclearity and/or the spin ground state, some of the complexes have been obtained by reaction with azido ligands because of their high ability to coordinate tran-sition cations and their role as superexchange mediators that usually gives antiferromagnetic interactions for the end-to-end coordination mode and ferromagnetic coupling for the end-on case.[29]

Following our previous work on this topic,[19,20] we have characterized five heterometallic complexes with nuclearities ranging from two to eight and the molecular formulas $[Cu^{II}Na^I(L2)(MeOH)(ClO_4)]$ (**1**), $[Cu_2^{II}Mn^{II}(S,S\text{-}L3)_2(MeOH)]$ $(ClO_4)_2$ (**2SS**), $[\{Cu^{II}Mn^{II}(L1)(H_2O)_2(MeOH)\}\{Cu^{II}(L1)\}_2](ClO_4)_2$ (**3**), $[(\mu_{1,3}\text{-}N_3)_2\{Cu^{II}Mn^{II}(L2)(H_2O)\}_2\{Cu^{II}(L2)_2\}](ClO_4)_2$ (**4**) and $[(\mu_{1,1}\text{-}N_3)_2\{Cu^{II}Mn^{II}(L1)(N_3)\}_2\{Cu^{II}Na^I(L1)(MeOH)\}_2](ClO_4)_2$ (**5**). Magnetic susceptibility measurements show well isolated S ground states 3/2, 2, 0 and 4 for the core of complexes **2–5** respectively and ac measurements evidence field-induced slow relaxation of the magnetization for **2**, **3** and **5** following the expected Raman plus Direct relaxation mechanism. The spin-phonon relaxation is supported by ultra-low-frequency Raman spectroscopy to confirm the presence of low-energy vibrational modes that can participate in the relaxation mechanism. The reported complexes provide the first family of polynuclear systems exhibiting slow relaxation in quasi-isotropic systems and proving that they are not restricted to mononuclear systems. The properties of complexes **3** and **5** were partially advanced as a communication.[30]
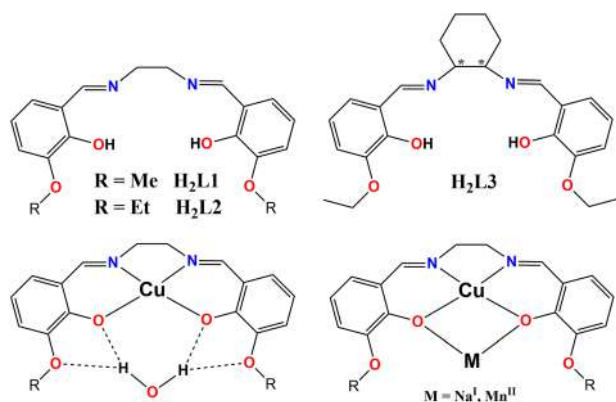
Scheme 1 Top, structural formula for the ligands described in the text. Bottom, H-bond linkage of [CuL] fragments found in compounds **3–5** (left) and compartmental cation coordination for **1–5** (right). The asterisk denotes chiral C-atoms.

Experimental

X-ray crystallography

Details of the crystal data, data collection and refinement for **1–5** are given in Table S1.† The X-ray intensity data for com-pounds **1–5** were measured on a D8 Venture system equipped with a multilayer monochromator and a Mo microfocus ($\lambda = 0.71073$ Å). All structures were solved using the Bruker SHELXTL software package, and refined using SHELXL.[31]

Physical measurements

Magnetic susceptibility measurements were carried out on polycrystalline samples with a MPMS-XL5 Quantum Design susceptometer working in the range 30–300 K under an exter-nal magnetic field of 0.3 T and under a field of 0.03 T in the 30–2 K range to avoid saturation effects. The fitting of suscepti-bility data was performed with the PHI program.[32] Diamagnetic corrections (269, 590, 730, 1103 and 1055 × 10^{-6} cm^3 mol^{-1} for **1–5** respectively) were estimated from Pascal tables.[33] The ECD spectra were recorded in methanolic solu-tions in a Jasco-815 spectropolarimeter. Infrared spectra (4000–400 cm^{-1}) were recorded from KBr pellets on a Bruker IFS-125 FT-IR spectrophotometer.

Syntheses

Caution: perchlorates and azides are potentially explosive. The samples must be handled with caution and in small amounts.

N,N'**-Ethylene-bis(3-methoxysalicylaldiimine)** **(H$_2$L1)**, N,N'**-ethylene-bis(3-ethoxysalicylaldiimine) (H$_2$L2) and N,N'-cyclo-hexane-bis(3-ethoxysalicylaldiimine) (H$_2$L3).** The Schiff bases H$_2$L1 and H$_2$L2 were synthesized following the reported methods[34] in high yields as yellow solids whereas H$_2$L3 was an oil. The neutral precursors [CuL(H$_2$O)] (L = L1^{2-} and L2^{2-}) were obtained as green solids with a 60–70% yield from a yel-lowish methanolic solution (10 mL) of the corresponding Schiff base H$_2$L (0.8 mmol) mixed with an aqueous solution (5 mL) of Cu(OAc)$_2$·4H$_2$O (0.8 mmol/0.145 g). The reaction mixture was placed into a microwave oven at 80 °C for 30 minutes and the solids were filtered and air dried.

The analogous [CuL3(H$_2$O)] precursor was obtained by direct heating in a microwave oven at 80 °C for 30 minutes of a mixture of ethyl-o-vanillin (0.8 mmol, 0.133 g) and (R,R) or (S,S)-cyclohexanediamine in 10 mL of methanol and Cu(OAc)$_2$·4H$_2$O (0.4 mmol/0.072 g) in 5 mL of water, and the solid was filtered and air dried. [CuL3(H$_2$O)] was prepared directly because the N,N'-cyclohexane-bis(3-ethoxysalicylaldii-mine) (**H$_2$L3**) ligand gives an oil instead of the solid ligand.

[Cu^{II}Na^I(L2)(MeOH)(ClO$_4$)] (1). The freshly formed powders of [Cu^{II}(L2)(H$_2$O)] (0.5 mmol/0210 g) and Mn(ClO$_4$)$_2$·6H$_2$O (0.5 mmol/0.125 g) were dissolved in 15 mL of MeOH and solid NaN$_3$ (0.032 g (0.5 mmol) was added. The mixture was maintained with stirring for 30 minutes and filtered. After 2 days brown crystals, suitable for X-ray diffraction, were formed by layering with diethylether. Yield: ~200 mg, 70%. C$_{21}$H$_{26}$ClCuN$_2$NaO$_9$. Calcd: C, 44.06; H, 4.58; N, 4.89. Found C, 44.4; H, 4.7; N, 4.8.

[Cu$_2^{II}$Mn^{II}(S,S-L3)$_2$(MeOH)](ClO$_4$)$_2$·2CH$_2$Cl$_2$·0.5MeOH (2SS·2CH$_2$Cl$_2$·0.5MeOH). The freshly formed powder of [Cu^{II}(S,S-L3)(H$_2$O)] (0.5 mmol/0.236 g) was dissolved in 20 mL of CH$_2$Cl$_2$ and MeOH (1 : 1) and Mn(ClO$_4$)$_2$·6H$_2$O (0.25 mmol/0.065 g) was added. The solution was heated in the microwave oven for 15 min at 70 °C, resulting in a clear dark solution. After 2 days brown crystals, suitable for X-ray diffraction, were formed by layering with diethylether. The (R,R)-complex was obtained following the same procedure starting from [Cu^{II}(R,R-L3)(H$_2$O)]. Yield: ~250 mg, 70%. C$_{50.5}$H$_{64}$Cl$_4$Cu$_2$MnN$_4$O$_{17.5}$. Calcd: C, 45.47; H, 4.85; N, 4.21. Found (SS) C, 45.1; H, 4.9; N, 4.4; Found (RR) C, 45.3; H, 4.7; N, 4.4.

[{Cu^{II}Mn^{II}(L1)(H$_2$O)$_2$(MeOH)}{Cu^{II}(L1)}$_2$](ClO$_4$)$_2$·MeOH (3·MeOH). The freshly formed powder of [Cu^{II}(L1)(H$_2$O)] (0.275 mmol/0.107 g) was dissolved in 20 mL of CH$_2$Cl$_2$ and MeOH (1 : 1) and Mn(ClO$_4$)$_2$·6H$_2$O (0.25 mmol/0.065 g) was added. The solution was heated in the microwave oven for 15 min at 70 °C, resulting a clear dark solution. After 2 days brown crystals, suitable for X-ray diffraction, were formed by layering with diethylether. Yield: ~300 mg, 70%. C$_{55}$H$_{61}$Cl$_2$Cu$_3$MnN$_6$O$_{23}$. Calcd: C, 44.32; H, 4.12; N, 5.64. Found C, 44.6; H, 4.4; N, 5.4.

[(μ$_{1,3}$-N$_3$)$_2${Cu^{II}Mn^{II}(L2)(H$_2$O)}$_2${Cu^{II}(L2)}$_2$](ClO$_4$)$_2$·2MeOH (4·2MeOH). The complex was prepared following the same procedure as complex **1** but adding (Bu$_4$N)N$_3$ (0.5 mmol/0.135 g) instead of sodium azide to the [Cu^{II}(L2)(H$_2$O)]/Mn(ClO$_4$)$_2$·6H$_2$O dissolution. The mixture was introduced to microwaves for 10 min at 60 °C. After two days brown crystals, suitable for X-ray diffraction, were formed by vapor diffusion of diethylether. Yield: 120 mg, 40%. C$_{82}$H$_{100}$Cl$_2$Cu$_4$Mn$_2$N$_{14}$O$_{28}$. Calcd: C, 45.50; H, 4.66; N, 9.06. Found C, 45.0; H, 4.9; N, 9.3.

[(μ$_{1,1}$-N$_3$)$_2${Cu^{II}Mn^{II}(L1)(N$_3$)}$_2${Cu^{II}Na^I(L1)(MeOH)}$_2$](ClO$_4$)$_2$ (5). The complex was prepared following the same procedure as complex **2** but adding NaN$_3$ (0.4 mmol/0.026 g) to the [Cu^{II}(L1)(H$_2$O)]/Mn(ClO$_4$)$_2$·6H$_2$O dissolution. The mixture was introduced into a microwave oven for 15 min at 70 °C. After two days brown crystals, suitable for X-ray diffraction, were formed by vapor diffusion of diethylether. Yield: 110 mg, 40%. C$_{74}$H$_{80}$Cl$_2$Cu$_4$Mn$_2$N$_{20}$Na$_2$O$_{26}$. Calcd: C, 41.41; H, 3.75; N, 13.05. Found C, 41.0; H, 3.7; N, 13.1.

IR spectra for **1–5** are shown in Fig. S1.†

Results and discussion

Comments on the syntheses

The synthesis of the reported complexes was revealed to be sensitive to several factors, such as the solvent, the Schiff base and the presence of Na^I cations in the reaction medium.

Complexes **2** and **3** were prepared following the same experimental procedure but two different topologies were obtained, being a trinuclear Cu–Mn–Cu complex for **2** and a sandwich Cu$_3$Mn system for **3** in spite of the fact that the only difference was the methyl or ethyl alcoxo arms. The trial to obtain azide derivatives starting from H$_2$L1 allowed complex **5** to be obtained, but in contrast when starting from H$_2$L2, also

employing sodium azide, crystals of the {CuNa} complex **1** and an unidentified powder containing a large amount of azido ligand was obtained. The strategy to avoid the sodium coordination and improve the crystallinity of the resulting product was the employment of (Bu$_4$N)N$_3$ instead of sodium azide, resulting in complex **4**. The different coordination modes for the azido bridges in complexes **4** (end-to-end) and **5** (end-on) provide a new example of the small difference in energy between the two coordination modes[29] that gives a completely different magnetic response, resulting in antiferromagnetic interactions and a zero spin ground state for the core of **4** and the largest S = 4 for the core of **5** as a consequence of the ferromagnetic interactions mediated by the end-on mode with Mn–N–Mn bond angles around 100°.[35]

Description of the structures

The environments of the copper cations are similar in the five complexes and thus the common trends are described as follows to avoid repetitive descriptions. The Cu^{II} cation is placed in the inner N$_2$O$_2$ cavity of the corresponding L^{2-} Schiff base in a square planar environment with N–Cu–N and O–Cu–O bond angles lower than 90° and N–Cu–O bond angles larger than 90°. The Cu–N and Cu–O bond distances are close to 1.9 Å in all cases. The Cu–O–Mn bond angles in the different dinuclear subunits are similar and range between 103 and 104°.

[Cu^{II}Na^I(L2)(MeOH)(ClO$_4$)] (1). A view of the molecular structure of complex **1** is shown in Fig. 1-top and selected intera-
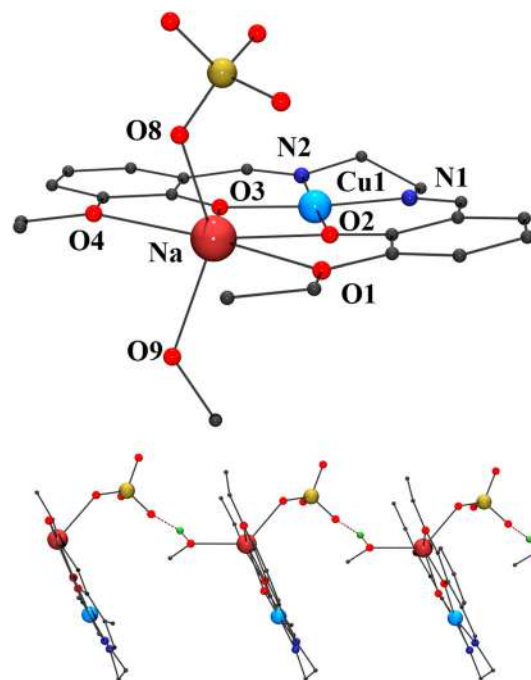

Fig. 1 Top, partially labeled view of the molecular structure of complex **1**. Bottom, one-dimensional H-bond arrangement along the a-axis of the network of monomers of complex **1**. Color key for all plots: Cu^{II}, light blue; Mn^{II}, orange; Na^I, firebrick; O, red; N, navy; C, black; Cl, bronze; H, green.
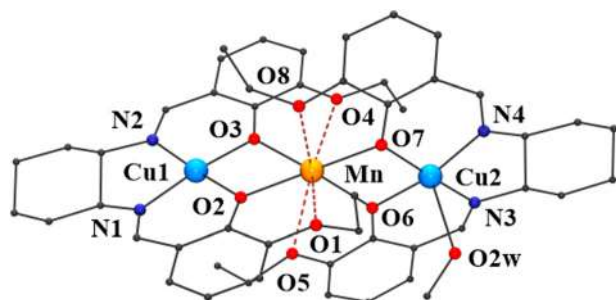
Paper

Table 1 Selected interatomic distances (Å) and angles (°) for compound **1**

Cu(1)–N(1)	1.924(2)	Cu(1)–N(2)	1.928(2)
Cu(1)–O(2)	1.888(1)	Cu(1)–O(3)	1.903 (1)
Na–O(1)	2.622(2)	Na–O(4)	2.661(2)
Na–O(2)	2.320(2)	Na–O(8)	2.360(2)
Na–O(3)	2.310(2)	Na–O(9)	2.306(2)
Cu(1)–O(2)–Na	102.95(6)	Cu(1)–O(3)–Na	102.82(6)

Table 2 Selected interatomic distances (Å) and angles (°) for compound **2SS**

Cu(1)–N(1)	1.917(5)	Cu(1)–N(2)	1.918(5)
Cu(1)–O(2)	1.892(4)	Cu(1)–O(3)	1.899(4)
Cu(2)–N(3)	1.925(6)	Cu(2)–N(4)	1.937(5)
Cu(2)–O(6)	1.918(4)	Cu(2)–O(7)	1.908(5)
Cu(2)–O(2w)	2.558(5)		
Mn–O(2)	2.148(4)	Mn–O(3)	2.166(4)
Mn–O(6)	2.169(4)	Mn–O(7)	2.133(4)
Mn–O(4)	2.682(4)	Mn–O(5)	2.748(5)
Mn–O(1)	2.579(4)	Mn–O(8)	2.452(5)
O2–Mn–O3	70.5(2)	O6–Mn–O7	70.7(2)
O2–Mn–O6	131.4(2)	O3–Mn–O6	119.9(2)
O2–Mn–O7	138.2(2)	O3–Mn–O7	135.8(2)
Cu(1)–O(2)–Mn	103.9(2)	Cu(1)–O(3)–Mn	103.0(2)
Cu(2)–O(6)–Mn	103.0(2)	Cu(2)–O(7)–Mn	104.7(2)

tomic distances and angles are listed in Table 1. The dinuclear complex consists of one Cu^{II} cation placed in the inner N_2O_2 cavity of one deprotonated $L2^{2-}$ Schiff base and one Na^{I} cation in the external O_4 cavity. The copper cation shows a square planar environment whereas the Na^{I} cation, linked to the four O-donors of the $L2^{2-}$ Schiff base, one methanol and one monodentate perchlorato ligand, exhibits strongly distorted octahedral coordination. The O1–Na–O4 bond angle takes a value of 167.58(5)° but the ethyl arms of the ligand prevent the coordination of a seventh ligand in the wide empty space between the O1 and O4 donors, and thus its polyhedron can be equally defined as a vacant pentagonal bipyramid. The perchlorate anion and the coordinated methanol molecule of the neighboring molecule are linked by one H-bond (distance O9···O5′ 2.831(2) Å, Table S2†) that promotes the one-dimensional arrangement of monomers in the network, Fig. 1, bottom.

$[Cu_2^{II}Mn^{II}(S,S\text{-}L3)_2(MeOH)](ClO_4)_2 \cdot CH_2Cl_2 \cdot 0.5MeOH$ (**2SS·CH_2Cl_2·0.5MeOH**). A view of complex **2SS** is illustrated in Fig. 2. Selected interatomic distances and angles are listed in Table 2. Complex **2SS** crystallizes in the chiral *P*1 space group and the unit cell contains two similar but crystallographically nonequivalent {CuMnCu} trinuclear molecules. To avoid repetitive data, the following descriptions will be referred to as the "A" labelled molecule. The trinuclear complex is formed by two neutral [CuL3] fragments that link one Mn^{II} cation by means of their deprotonated $O_{phenoxo}$ donors. The Cu^{II} cations are placed in the inner N_2O_2 cavity of the Schiff bases in a similar way to compound **1** but in this case, Cu1 shows the usual square planar environment whereas Cu2 links one methanol molecule in the axial site of its square pyramidal coordination sphere.

The manganese cation is surrounded by four $O_{phenoxo}$ donors in an elongated tetrahedral arrangement with Mn–O

bond distances around 2.15 Å and four O_{ethoxo} donors that form a "belt" around the tetrahedral MnO_4 polyhedron with large Mn–O bond distances, comprising between 2.452 and 2.747 Å, resulting in an unusual octacoordination.

SHAPE[36] analysis shows that the coordination environment of the Mn^{II} cation does not agree with any regular polyhedron, the closer ones being the biaugmented trigonal prism and the triangular dodecahedron but strongly distorted as indicated by the CShM values of 3.43 and 4.55, Fig. S2.† The trinuclear units are well isolated by the perchlorate counteranions and solvent molecules, the only intermolecular H-bond interactions being those established between one of the perchlorates and the coordinated methanol molecule.

$[\{Cu^{II}Mn^{II}(L1)(H_2O)_2(MeOH)\}\{Cu^{II}(L1)\}_2](ClO_4)_2 \cdot MeOH$ (**3**). Compound **3** exhibit a "sandwich" structure formed by one $[Cu(L1)Mn(H_2O)_2(MeOH)]^{2+}$ dinuclear fragment and two neutral [CuL1] units, which are linked by means of bifurcated H-bonds, Fig. 3-top and Table S2.† A labelled plot of the central unit is shown in Fig. 3-bottom, and the main bond parameters are summarized in Table 3. The Cu^{II} cations are placed in the inner N_2O_2 cavity of its Schiff base in a similar way to complex **1**, with a similar environment and bond parameters.

The coordination of the Mn^{II} cation is determined by two bridging $O_{phenoxo}$ donors, one methanol and two water molecules in a roughly MnO_5 trigonal bipyramid arrangement with the water molecules occupying the apical sites. The $O_{methoxo}$ donors O5 and O8 are placed at large distances (2.452 and 2.747 Å), inducing a weak interaction with the Mn^{II} cation and thus the environment around the Mn^{II} cation can be also envisaged as MnO_7. SHAPE analysis[36] of the coordination environment of the Mn^{II} cation shows a large deviation from any regular polyhedron, the pentagonal bipyramid being the closer one with a CShM value of 1.86, Fig. S2.†

The water molecules coordinated to the Mn^{II} cation link the neutral [CuL] fragments by means of bifurcated H-bonds with the O-atoms of the Schiff bases, being shorter those that involve the O-phenoxo atoms, resulting a "sandwich" structure. The clusters of **3** are pillared, forming an 1D arrangement that isolates the paramagnetic Mn^{II} cations with Mn···Mn distances
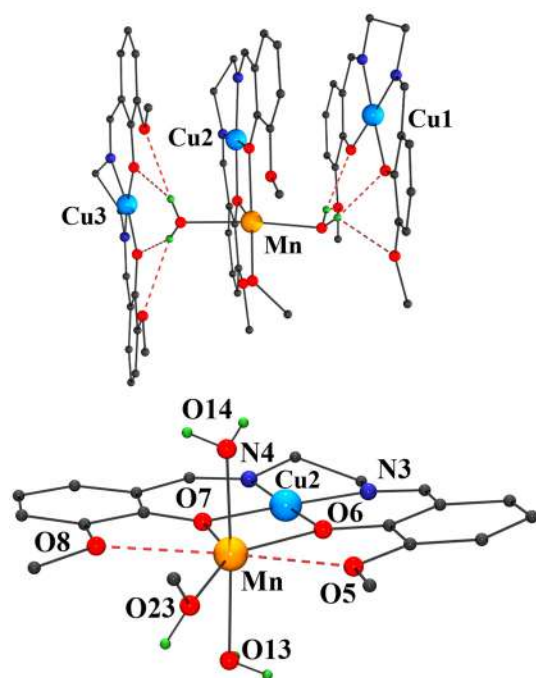

Fig. 2 Labelled plot of the molecular structure of complex **2SS**.

and 145.2(2)°. The Mn^{II}-($\mu_{1,3}$-N_3)$_2$–Mn^{II} fragment is not planar, with the dihedral angle between the plane defined by the azido ligands and the N3MnN5′ plane of 21.7(2)°, resulting in a Mn-(N_3)$_2$–Mn chair arrangement.

The two protons of the water molecule coordinated to the Mn^{II} cations form bifurcated H-bonds (Table S2†), with the four O-atoms of the capping neutral [Cu^{II}(L2)] fragments in a similar way to complex **3**, helping to stabilize the hexanuclear complex. The charge balance is fulfilled with two perchlorate counteranions and remarkable intermolecular interactions are not found in the network.

[($\mu_{1,1}$-N_3)$_2${$Cu^{II}Mn^{II}$(L1)(N_3)}$_2${$Cu^{II}Na^{I}$(L1)(MeOH)}$_2$](ClO$_4$)$_2$ (**5**). A view of the centrosymmetric complex **5** is shown in Fig. 5. Selected bond distances and angles are listed in Table 5. The octanuclear complex **5** combines several trends of compounds **1** and **4**: the complex consists of a central tetranuclear unit formed by two CuMn dimers linked by azido ligands that are capped by two CuNa fragments similar to those in complex **1**. The main differences compared with complex **4** lie in the coordination mode of the azido bridges, that in this case act in its end-on coordination mode, and in the linkage with the capping groups that in this case, instead of the previously described H-bonds, is formed by one single end-on azido bridge between the sodium and the manganese cations.

The Cu^{II} cations are placed in all fragments in the N_2O_2 inner cavity of the Schiff bases whereas the sodium and manganese cations are placed in the external O_4 cavities. The coordination sphere of the Na^{I} cation is formed by the O-donors from the L1^{2-} Schiff base, one azido ligand, one methanol solvent molecule and a large contact (Na–O6, 2.910

Table 5 Selected interatomic distances (Å) and angles (°) for compound **5**

Cu(2)–O(6)	1.894(1)	Cu(2)–N(3)	1.921(2)
Cu(2)–O(7)	1.897(1)	Cu(2)–N(4)	1.911(2)
Mn–O(6)	2.222(1)	Mn–N(8)	2.180(2)
Mn–O(7)	2.179(2)	Mn–N(8′)	2.269(2)
Mn–N(5)	2.146(2)		
Mn–O(5)	2.546(1)	Mn–O(9)	2.597(1)
Cu(1)–O(2)	1.898(1)	Cu(1)–N(1)	1.923(2)
Cu1–O(3)	1.892(1)	Cu1–N(2)	1.931(2)
Na–O(1)	2.679(2)	Na–O(6)	2.910(2)
Na–O(2)	2.326(2)	Na–O(8)	2.314(2)
Na–O(3)	2.344(2)	Na–N(5)	2.494(2)
Na–O(4)	2.681(2)		
O(6)–Mn–O(7)	69.69(5)	O(6)–Mn–N(8)	143.97(6)
O(7)–Mn–N(8)	138.49(6)	N(5)–Mn–N(8′)	171.89(7)
O(5)–Mn–O(6)	63.68(4)	O(5)–Mn–N(8)	84.81(5)
O(7)–Mn–O(9)	64.06(5)	O(9)–Mn–N(8)	82.96(5)
Cu(2)–O(6)–Mn	102.45(6)	Cu(1)–O(7)–Mn	103.97(6)
Mn–N(8)–Mn′	104.55(7)		

(2) Å) with one O$_{phenoxo}$ donor of the central Cu_2Mn_2 unit, determining a distorted pentagonal pyramidal polyhedron, in which the methanol molecule and the azido ligand are placed in the apical sites. The Mn^{II} cation is surrounded by the four O-donors from the Schiff base and three azido ligands in a very distorted pentagonal bipyramid environment due to the low N8–Mn–N8′ bond angle (CShM = 2.84, Fig. S2†), in which the apical coordination sites are occupied by azido ligands. As in the previous cases, the Mn–O bond distances to the O-donors from the alcoxo arms of the Schiff base, O5 and O9, are clearly larger than those for the Mn–O$_{phenoxo}$.

The clusters are linked by intramolecular H-bonds established between the methanol molecule and the azido ligand linked to the sodium cations, determining an 1D arrangement of clusters along c-axis of the unit cell, Fig. 5, right, Table S2.†

Electronic circular dichroism

Electronic circular dichroism confirms the enantiomeric identity of the pair of enantiomers of complex **2**. The spectrum of **2SS** collected in methanolic solution exhibits positive Cotton effects at λ_{max} = 390, 284, 243 and 207 nm and negative Cotton effects at 630, 490, 346 and 223 nm, whereas **2RR** shows a mirror image with the opposite sign at the same wavelengths, Fig. 6. The ECD spectrum for the S,S-H$_2$L3 ligand shows positive Cotton absorptions at λ_{max} = 416, 324, 271 and 232 nm and negative peaks at 248 and 217 nm, showing that the more energetic absorptions (below 300 nm) are due to the π–π^* transitions of the ligand and that the absorptions at larger wavelengths are related to the coordinated cations.

Magnetic properties

Static measurements

Static susceptibility measurements for the polynuclear complexes **2–5** were performed on powdered samples in the 300–2 K range. For **3–5** the term "*core*" will refer to the coupled Cu/Mn fragments, whereas the total susceptibility or magneti-

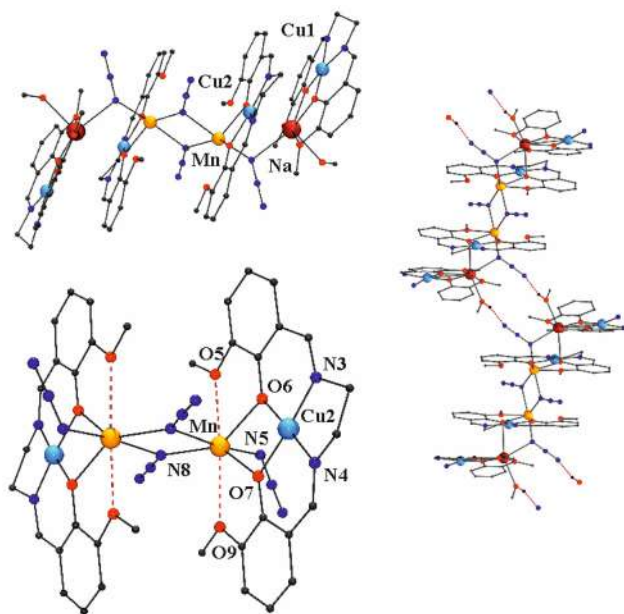**Fig. 5** Top, view of the molecular structure of complex **5**. Bottom, labeled plot of the core of complex **5**. Right, intermolecular H-bonds between clusters determining an 1D arrangement along c-axis.
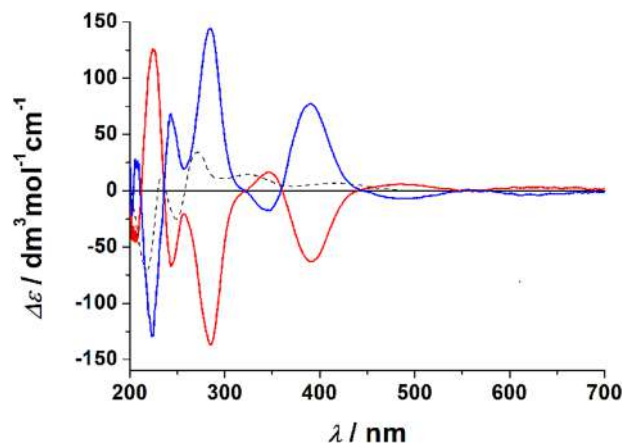
Fig. 6 Methanolic solution ECD spectra for the pair of **2RR/2SS** enantiomers (red line, **2RR**; blue line **2SS**). The dashed line shows the spectra of the ligand.

zation values are the value of the core plus the values of the non-interacting Cu^{II} cations. The room temperature $\chi_M T$ value for **2** is 4.80 cm³ mol⁻¹ K, slightly lower than the expected value for one $S = 5/2$ and two $S = 1/2$ isolated spins (5.125 cm³ mol⁻¹ K), which decreases continuously down to 20 K, reaching a value of 1.94 cm³ mol⁻¹ K at 2 K, evidencing an antiferromagnetic response, Fig. 7. Fitting of the experimental data was performed using the PHI[32] program on the basis of the coupling scheme shown in Scheme 2 and applying the Hamiltonian:

$$H = -2J(S_1 \cdot S_2 + S_2 \cdot S_3)$$

resulting in the best fit parameters $J = -16.4(1)$ cm⁻¹ and $g = 2.064(2)$. The low-temperature $\chi_M T$ value (1.94 cm³ mol⁻¹ K)
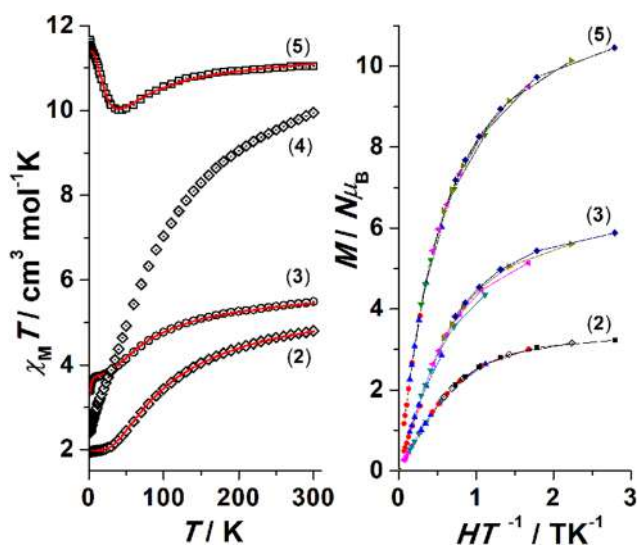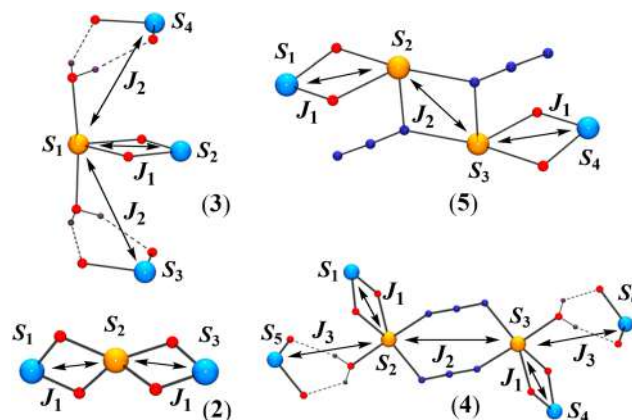

Fig. 7 Left, $\chi_M T$ plots for complexes **2–4**. Right, reduced magnetization for complexes **2**, **3** and **5**.

Scheme 2 Coupling schemes for complexes **2–5**.

agrees with the expected value for an $S = 3/2$ ground state (1.875 cm³ mol⁻¹ K), with a g value slightly larger than 2.00.

The $\chi_M T$ plot for complex **3** shows a 5.49 cm³ mol⁻¹ K value at room temperature, close to the expected value for one $S = 5/2$ and three non-interacting $S = 1/2$ spins (5.500 cm³ mol⁻¹ K). On cooling, the plot decreases continuously down to a plateau at 10 K followed by a weak decay below 4 K, reaching 3.38 cm³ mol⁻¹ K at 2 K, Fig. 7. This low-temperature step should be attributed to the weak intramolecular interaction mediated by the H-bond between the water molecule coordinated to the Mn^{II} cation and the $O_{phenoxo}$ donors linked to the Cu^{II} cation of the neighbouring molecule. Consequently, fitting of the experimental data was done according to the coupling scheme shown in Scheme 2 and applying the Hamiltonian:

$$H = -2J_1(S_1 \cdot S_2) - 2J_2(S_1 \cdot S_3 + S_1 \cdot S_4)$$

resulting in the best fit parameters $J_1 = -13.8(1)$ cm⁻¹, $J_2 = -0.09(1)$ cm⁻¹ and $g = 2.019(1)$. The $\chi_M T$ value for the plateau at low temperature (~3.8 cm³ mol⁻¹ K) agrees with the expected value for an $S = 2$ ground state (3.00 cm³ mol⁻¹ K) plus two isolated $S = \frac{1}{2}$ spins (0.75 cm³ mol⁻¹ K), with a g value slightly larger than 2.00.

Complex **4** shows a $\chi_M T$ room temperature value of 9.43 cm³ mol⁻¹ K, close to the expected value for two $S = 5/2$ and four non interacting $S = \frac{1}{2}$ spins of 10.250 cm³ mol⁻¹ K, which decreases continuously on cooling down to a 0.85 cm³ mol⁻¹ K value at 2 K, Fig. 7. The two interactions present in the core of compound **4** between the Cu^{II} and the Mn^{II} cations (J_1) and the Mn^{II} cations, mediated by the end-to-end azido bridges (J_2), were modeled according to the scheme shown in Scheme 2. Due to the dominant antiferromagnetic interaction in the central core of the complex, the weak contacts (modeled as J_3) between the Mn^{II} cations and the terminal Cu^{II} ions were discarded. Thus, fitting of the data was determined by applying the Hamiltonian:

$$H = -2J_1(S_1 \cdot S_2 + S_3 \cdot S_4) - 2J_2(S_2 \cdot S_3)$$

The best fit parameters were $J_1 = -26(1)$ cm⁻¹, $J_2 = -2.60(6)$ cm⁻¹ and $g = 2.10(1)$. The antiferromagnetic interactions

mediated by J_1 and J_2 cancel the spins of the central tetranuclear unit and thus the low-temperature $\chi_M T$ value corresponds to the two isolated $S = 1/2$ copper cations.

The $\chi_M T$ plot for complex **5** shows a room temperature value of 11.05 cm³ mol⁻¹ K, slightly larger than the expected value for two $S = 5/2$ and four non-interacting $S = \frac{1}{2}$ spins of 10.250 cm³ mol⁻¹ K, which decreases on cooling, reaching a minimum value of 10.0 cm³ mol⁻¹ K at 40 K. Below this temperature the $\chi_M T$ plot increases up to 11.65 cm³ mol⁻¹ K at 2 K, indicating a ferrimagnetic response, Fig. 7. The interaction scheme for the central Cu_2Mn_2 unit is the same as that for complex **4** but in this case the two peripheral Cu^{II} cations cannot interact with the Mn^{II} cations, and thus fitting of the experimental data was performed applying the Hamiltonian derived from the scheme shown in Scheme 2:

$$H = -2J_1(S_1 \cdot S_2 + S_3 \cdot S_4) - 2J_2(S_2 \cdot S_3)$$

plus two isolated $S = \frac{1}{2}$ with the same g value, resulting the best fit parameters $J_1 = -12.5(1)$ cm⁻¹, $J_2 = +2.03(1)$ cm⁻¹, $g_{Cu} = 2.092(3)$ and $g_{Mn} = 2.050(1)$. The $\chi_M T$ value at a low temperature (11.65 cm³ mol⁻¹ K) agrees with the expected value for an $S = 4$ ground state for the tetranuclear unit (10.00 cm³ mol⁻¹ K) plus two isolated $S = \frac{1}{2}$ spins (0.75 cm³ mol⁻¹ K), with a g value slightly larger than 2.00.

The interaction between the Cu^{II} and the Mn^{II} cations for **2–4**, mediated by a Cu^{II}–O–Mn^{II} double phenoxo bridge ~103°, shows a moderately strong antiferromagnetic coupling comparable with previously reported Cu^{II}/Mn^{II} dinuclear complexes with related Schiff bases and similar bond angles.[37] The coupling mediated by the azido bridges follows the usual rule of ferromagnetic interactions for the end-on coordination mode and antiferromagnetic coupling for the end-to-end coordination.[29]

Reduced magnetization experiments were performed for complexes **2SS**, **3** and **5**, showing quasi superimposable plots that evidence very low anisotropy. The $N\mu_\beta$ values under the maximum applied field of 5 T (3.23 $N\mu_\beta$ for **2SS**, 5.88 $N\mu_\beta$ for **3** or 10.45 $N\mu_\beta$ for **3**), taking into account the non-interacting Cu^{II} cations, confirm the well-defined ground spin states for the interacting fragments of $S = 3/2$ for **2**, $S = 2$ for **3** and $S = 4$ for **5**, Fig. 7, right.

Dynamic measurements

It has been proposed that the slow relaxation of the magnetization in quasi-isotropic systems is related to small D values that are able to mix the m_s levels under moderately low fields.[18,19] In our case, the origin of a moderate anisotropy for complexes **4** and **5** is a consequence of their penta- or heptacoordination[38] (including or not the weak methoxo interactions) whereas for complex **2SS** its strongly elongated MnO_4 tetrahedral environment is the source of axial anisotropy, Fig. 2, and the O–Mn–O bond angles are detailed in Table 2.

Alternating current (ac) susceptibility measurements were performed for complexes with a core ground state spin different from zero (**2SS**, **3** and **5**). Measurements at zero field do not show out of phase signals for all complexes but clearly

defined $\chi''_M(T)$ peaks were observed for all of them under applied fields, Fig. S3.† In light of these data, ac susceptibility measurements in the 1–1488 frequency range were performed under the fields that yielded the maximum χ''_m response. Well-defined slow relaxation of the magnetization has recently been characterized for some mononuclear Cu^{II} complexes in a variety of coordination environments[39–42] and thus, to discard the possibility that the origin of the out of phase response could be attributed to the [CuL] or [CuNaL] non-interacting fragments, ac experiments were also performed for the equivalent complex **1**. The absence of out-of-phase signals under a field up to 1 T confirms that the ac response in complexes **3** and **5** is only due to the interacting Cu^{II}/Mn^{II} system.

The $\chi''_M(T)$ plots show well-defined peaks below 5 K for complex **5**, Fig. 8, left column and Fig. S4,† with well-defined temperature-dependent high-frequency (HF) and temperature-independent low-frequency (LF) regions. The intensity of the signals was weaker for complex **3**, which was measured under an external field of 0.7 T, whereas the best defined out-of-phase responses of **2SS** and **5** were measured under two different fields to check if the relaxation times are field dependent.

The $\ln(1/2\pi\nu)$ vs. T plot for the observed maxima at the larger frequencies shows a nonlinear dependence due to the overlap of relaxation mechanisms, Fig. S5.†

The plot of $\chi''_m(\nu)$, Fig. 8, right column, reveals maxima in the studied range of frequencies for **2SS**, temperature dependent in the HF region and with a constant value around 2 Hz for the LF region, which from the expression $1/2\pi\nu$ implies relatively large relaxation times around 80 ms. For **3** and **5** the HF peaks are displaced at larger frequencies, out of the studied range, resulting in faster relaxation and similar characteristics for the LF range.

To continue the analysis of the magnetic dynamic properties, χ'_m and χ''_m were studied using the generalized Debye model,[43] with the CCfit program, where both susceptibilities are analysed together with the relaxation rate τ, and α, a parameter that defines the broadening of the Argand plot of χ'_m and χ''_m and is related to the distribution of the relaxation rates. The data extracted from the fit are represented in the so-called Cole–Cole plots (Fig. S6†) and represented in the form of $\ln(\tau)$ vs. $1/T$ (Fig. 8). The low-frequency process only gives some tails in the Cole–Cole plot and the data are not reliable, and thus the following analysis corresponds to the well-defined high-frequency process.

The occurrence of slow relaxation in transition metal compounds has usually been attributed to the over-barrier relaxation in the so-called Orbach process. However, compounds **2SS**, **3** and **5** belong to the family of the quasi-isotropic molecules, and this over-barrier relaxation is not allowed due to the intrinsic nature of a double-well potential derived from relatively low spins and very weak anisotropy, which is thermally overcome even at 4 K (Fig. 7, right). Tunnelling is also non-operative and for this reason Orbach and tunnel mechanisms were excluded and thus a combination of Raman plus Direct
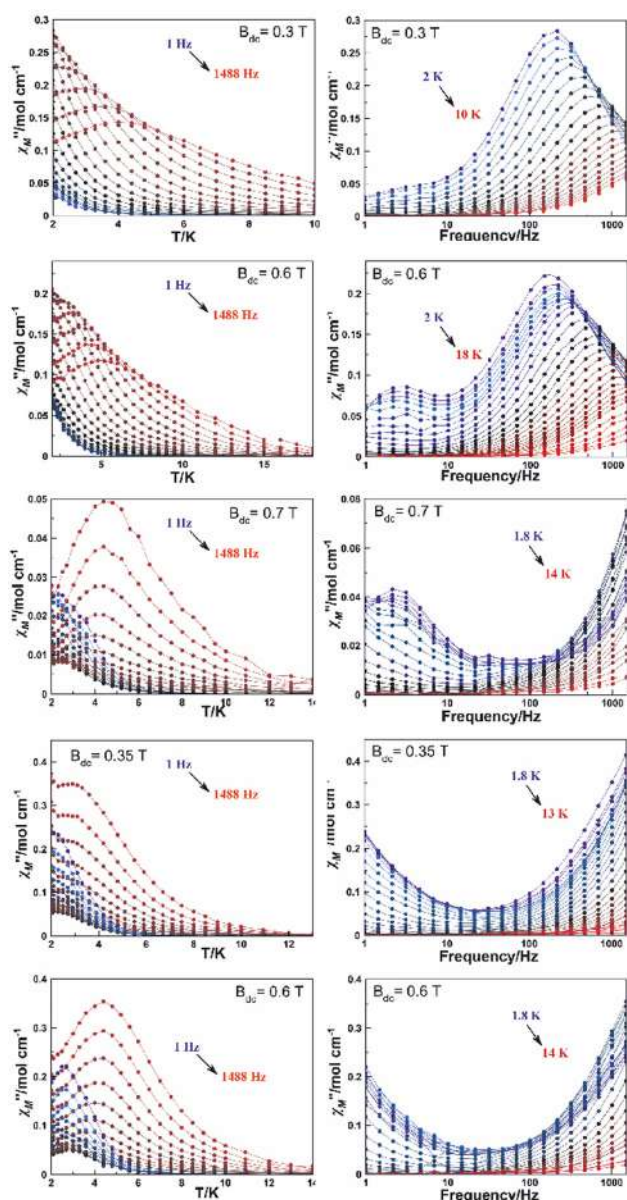
Fig. 8 Temperature (left) and frequency dependence (right) of χ'' for complexes **2SS** (top, 0.3 and 0.6 T), **3** (middle) and **5** under two 0.35 and 0.6 T fields (down, 0.35 and 0.6 T).

Fig. 9 Plot of ln(τ) vs. T^{-1} for complexes **2SS**, **3** and **5**. Solid lines show the best fit of the experimental data.

Table 6 Best fit C, n, A values for complexes **2**, **3** and **5**

	C	n	A
(**2SS**) 0.3 T	56.0	2.84	411
(**2SS**) 0.6 T	2.10	3.82	592
(**3**) 0.7 T	0.17	6.0	16 956
(**5**) 0.35 T	0.03	6.7	6558
(**5**) 0.6 T	0.95	5.2	6232

plexes **3** and **5** present a decay of the ln(τ) vs. $1/T$ curve at very low temperatures in a similar way to some Gd[III] systems. This behaviour of the curve has been parametrized by Boca *et al.* but for the moment there is no explanation of it and it has no physical meaning.[14,23,45]

For molecules where the relaxation cannot proceed through an energy barrier, the intervention of the lattice must have some important effects, so the energy of the vibration modes

relaxation is proposed (Fig. 9 and Table 6) following the equation:

$$\tau^{-1} = AT + CT^n$$

For all the compounds, the low-temperature region clearly follows the direct relaxation while the high-temperature region follows the two-phonon process Raman relaxation path. Among this, it can be observed in Table 6 that Raman coefficients (n) for some of the complexes present lower values than the expected ones for Kramer ions. This feature has been explained because the Raman relaxation can be attributed to the participation of optical phonons.[44] Fig. 9 shows that com-
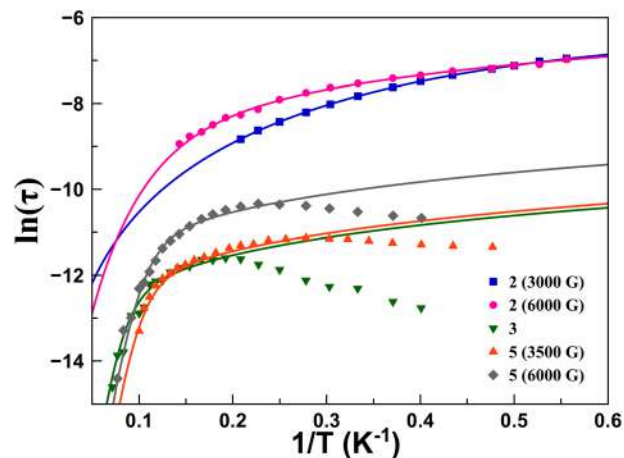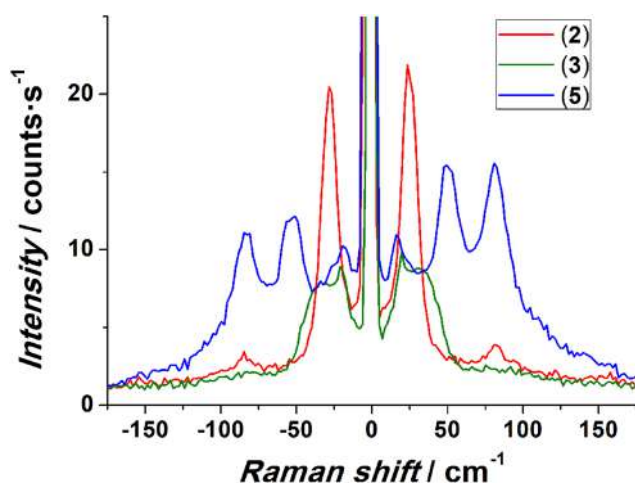

Fig. 10 Ultralow-frequency Raman spectrum for complexes **2SS**, **3** and **5** showing the low-energy vibrations.

in the terahertz region has been postulated as a relaxation mechanism.[46,47] For this reason the intervention of the lattice can be demonstrated by the measurement of the ultra-low-frequency Raman spectrum which is represented in Fig. 10. The analysis of the ultra-low-frequency Raman spectrum evidences the presence of very-low-frequency vibrations, appearing at 24 cm^{-1} for **2SS**, 20 and 30 cm^{-1} for **3** and 16.5 cm^{-1} for **5**, compatible with the energy required for a spin-phonon relaxation path.

Conclusions

A series of Cu^{II}/Mn^{II} complexes built from compartmental Schiff bases, with a variety of nuclearities ranging from tri- to octanuclear systems, have been characterized from structural and magnetic points of view. The preference for the inner N$_2$O$_2$ cavity of the Schiff bases for the Cu^{II} cation places the Mn^{II} cations in the external cavity, which favours a strongly distorted hepta- or octacoordinated environment around the Mn^{II} cations, inducing a predeterminated weak anisotropy. The additional employment of azido co-ligands increased the nuclearity of the systems and for the case of bridging azides in its end-on coordination mode, the ferromagnetic interactions allow an increase in the S ground state. A study of the magnetic properties of complexes **1–5** showed for the first time slow relaxation of the magnetization in a family of polynuclear systems derived from quasi isotropic cations with HF (temperature- and frequency-dependent relaxation) Raman plus Direct relaxation processes and LF (temperature- and frequency-independent relaxation) with relatively large relaxation times for which the origin is still unclear. Fitting of the experimental results and the measurement of Raman spectra in the terahertz region, showing low-energy vibrations, confirm that the relaxation of all the compounds cannot be attributed to an over-barrier process due to the lack of magnetic anisotropy. The main conclusion derived from this work is that slow relaxation of the magnetization is not restricted to strongly anisotropic systems and can be spread to any polynuclear cluster.

Author contributions

E. P. Synthesis, structural analysis, data curation; M. F.-B. X-Ray crystallography; J. M. supervision, writing – original draft, conceptualization; A. E. funding acquisition, project administration, supervision, conceptualization, writing – review and editing.

Conflicts of interest

There are no conflicts to declare.

Acknowledgements

References

1 D. Gatteschi, R. Sessoli and J. Villain, *Molecular Nanomagnets*, Oxford University Press, Oxford, 2006.

2 F.-S. Guo, B. M. Day, Y.-C. Chen, M.-L. Tong, A. Mansikkamäki and R. A. Layfield, *Science*, 2018, **362**, 1400.

3 C. A. Gould, Mc. K. Randall, D. Reta, J. G. C. Kragskow, D. A. Marchiori, D. E. Lachman, E.-S. Choi, J. G. Analytis, R. D. Britt, N. F. Chilton, B. G. Harvey and J. R. Long, *Science*, 2022, **375**, 198.

4 M. Orendáč, L. Sedláková, E. Čižmár, A. Orendáčová, A. Feher, S. A. Zvyagin, J. Wosnitza, W. H. Zhu, Z. M. Wang and S. Gao, *Phys. Rev. B: Condens. Matter Mater. Phys.*, 2010, **81**, 214410.

5 M. J. Martınez-Perez, S. Cardona-Serra, C. Schlegel, F. Moro, P. J. Alonso, H. Prima-Garcıa, J. M. Clemente-Juan, M. Evangelisti, A. Gaita-Ariño, J. Sese, J. van Slageren, E. Coronado and F. Luis, *Phys. Rev. Lett.*, 2012, **108**, 247213.

6 V. Tkac, A. Orendacova, R. Tarasenko, E. Cizmar, M. Orendac, K. Tibenska, A. G. Anders, S. Gao, V. Pavlık and A. Feher, *J. Phys.: Condens. Matter*, 2013, **25**, 506001.

7 P. I. Girginova, L. C. J. Pereira, J. T. Coutinho, I. C. Santos and M. Almeida, *Dalton Trans.*, 2014, **43**, 1897.

8 A. Arauzo, A. Lazarescu, S. Shova, E. Bartolome, R. Cases, J. Luzón, J. Bartolomé and C. Turta, *Dalton Trans.*, 2014, **43**, 12342.

9 R. J. Holmberg, L. T.-A. Ho, L. Ungur, I. Korobkov, L. F. Chibotaru and M. Murugesu, *Dalton Trans.*, 2015, **44**, 20321.

10 A. J. Calahorro, I. Oyarzabal, B. Fernandez, J. M. Seco, T. Tian, D. Fairen-Jimenez, E. Colacio and A. Rodrıiguez-Diéguez, *Dalton Trans.*, 2016, **45**, 591.

11 T. Yoshida, G. Cosquer, D. C. Izuogu, H. Ohtsu, M. Kawano, Y. Lan, W. Wernsdorfer, H. Nojiri, B. K. Breedlove and M. Yamashita, *Chem. – Eur. J.*, 2017, **23**, 4551.

12 D. C. Izuogu, T. Yoshida, H. Zhang, G. Cosquer, K. Katoh, S. Ogata, M. Hasegawa, H. Nojiri, M. Damjanovic, W. Wernsdorfer, T. Uruga, T. Ina, B. K. Breedlove and M. Yamashita, *Chem. – Eur. J.*, 2018, **24**, 9285.

13 L. Escalera-Moreno, J. J. Baldovı, A. Gaita-Ariño and E. Coronado, *Chem. Sci.*, 2018, **9**, 3265.

14 A. Vráblová, M. Tomás, L. R. Falvello, L. Dlhán, J. Titis, J. Cernák and R. Boca, *Dalton Trans.*, 2019, **48**, 13943.

15 M. Dolai, M. Ali, C. Rajnak, J. Titis and R. Boca, *New J. Chem.*, 2019, **43**, 12698.

16 Y.-C. Chen, Y.-Y. Peng, J.-L. Liu and M.-L. Tong, *Inorg. Chem. Commun.*, 2019, **107**, 107449.

17 Y. H. Pham, V. A. Trush, A. N. C. Neto, M. Korabik, J. Sokolnicki, M. Weselski, O. L. Malta, V. M. Amirkhanov and P. Gawryszewska, *J. Mater. Chem. C*, 2020, **8**, 9993.

18 Y. Horii, K. Katoh, Y. Miyazaki, M. Damjanovic, T. Sato, L. Ungur, L. F. Chibotaru, B. K. Breedlove, M. Nakano, W. Wernsdorfer and M. Yamashita, *Chem. – Eur. J.*, 2020, **26**, 8076.

19 J. Mayans and A. Escuer, *Chem. Commun.*, 2021, **57**, 721.

20 T. K. Ghosh, S. Maity, J. Mayans and A. Ghosh, *Inorg. Chem.*, 2021, **60**, 438.

21 M. Orts-Arroyo, A. Sanchis-Perucho, N. Moliner, I. Castro, F. Lloret and J. Martinez-Lillo, *Inorganics*, 2022, **10**, 32.

22 A. C. Benniston, S. Melnic, C. Turta, A. B. Arauzo, J. Bartolomé, E. Bartolomé, R. W. Harrington and M. R. Probert, *Dalton Trans.*, 2014, **43**, 13349.

23 C. Rajnak, J. Titis, J. Moncol, R. Micova and R. Boca, *Inorg. Chem.*, 2019, **58**(2), 991.

24 T. T. da Cunha, V. M. M. Barbosa, W. X. C. Oliveira, E. F. Pedroso, D. M. A. Garcia, W. C. Nunes and C. L. M. Pereira, *Inorg. Chem.*, 2020, **59**(18), 12983.

25 K. Uchida, G. Cosquer, K. Sugisaki, H. Matsuoka, K. Sato, B. K. Breedlove and M. Yamashita, *Dalton Trans.*, 2019, **48**, 12023.

26 R. Sato, K. Suzuki, T. Minato, M. Shinoe, K. Yamaguchi and N. Mizuno, *Chem. Commun.*, 2015, **51**, 4081.

27 J. Mayans, M. Font-Bardia and A. Escuer, *Dalton Trans.*, 2018, **47**, 8392.

28 D. Aravena, D. Venegas-Yazigi and E. Ruiz, *Inorg. Chem.*, 2016, **55**, 6405.

29 A. Escuer, J. Esteban, S. P. Perlepes and Th. C. Stamatatos, *Coord. Chem. Rev.*, 2014, **275**, 87.

30 E. Pilichos, P. Bhunia, M. Font-Bardia, A. Ghosh, J. Mayans and A. Escuer, *Dalton Trans.*, 2022, **51**, 1779.

31 G. M. Sheldrick, *SHELXL-2014/7: Program for the Solution of Crystal Structures*, University of Göttingen, Göttingen, Germany, 2014.

32 N. F. Chilton, R. P. Anderson, L. D. Turner, A. Soncini and K. S. Murray, *J. Comput. Chem.*, 2013, **34**, 1164.

33 G. A. Bain and J. F. Berry, *J. Chem. Educ.*, 2008, **85**, 532.

34 I. Correia, J. C. Pessoa, M. T. Duarte, M. F. M. da Piedade, T. Jackush, T. Kiss, M. M. C. A. Castro, C. F. G. C. Geraldes and F. Avecilla, *Eur. J. Inorg. Chem.*, 2005, 732.

35 E. Ruiz, J. Cano, S. Alvarez and P. Alemany, *J. Am. Chem. Soc.*, 1998, **120**, 11122.

36 M. Llunell, D. Casanova, J. Cirera, P. Alemany and S. Alvarez, *SHAPE, version 2.0*, Barcelona, 2010. The program can be obtained by request to the authors.

37 S. Dutta, P. Bhunia, J. Mayans, M. G. B. Drew and A. Ghosh, *Dalton Trans.*, 2020, **49**, 11268.

38 C. Duboc, *Chem. Soc. Rev.*, 2016, **45**, 5834.

39 R. Boca, C. Rajnak, J. Titis and D. Valigura, *Inorg. Chem.*, 2017, **56**, 1478.

40 H.-H. Cui, W. Lv, W. Tong, X.-T. Chen and Z.-L. Xue, *Eur. J. Inorg. Chem.*, 2019, 4653.

41 D. Valigura, C. Rajnak, J. Titis, J. Moncol, A. Bienko and R. Boca, *Dalton Trans.*, 2022, **51**, 5612.

42 D. Marcinkowski, A. Adamski, M. Kubicki, G. Consiglio, V. Patroniak, T. Ślusarski, M. Açıkgöz, D. Szeliga, N. Vadra, M. Karbowiak, I. Stefaniuk, C. Rudowicz, A. Gorczyński and M. Korabik, *Dalton Trans.*, 2022, **51**, 12041.

43 K. S. Cole and R. H. Cole, *J. Chem. Phys.*, 1941, **9**, 341.

44 L. Gu and R. Wu, *Phys. Rev. B*, 2021, **103**, 014401.

45 J. Titiš, C. Rajnák, D. Valigura and R. Boča, *Dalton Trans.*, 2018, **47**, 7879.

46 M. Atzori, S. Benci, E. Morra, L. Tesi, M. Chiesa, R. Torre, L. Sorace and R. Sessoli, *Inorg. Chem.*, 2018, **57**, 731.

47 M. Atzori, L. Tesi, E. Morra, M. Chiesa, L. Sorace and R. Sessoli, *J. Am. Chem. Soc.*, 2016, **138**, 2154.

Electronic Supplementary Material (ESI) for Dalton Trans.

 "*Occurrence of slow relaxation of the magnetization in a family of copper(II)/manganese(II) quasi-isotropic complexes with different ground spin states.*"

Evangelos Pilichos,[a] Mercè Font-Bardia,[b] Albert Escuer,[a,c*] Júlia Mayans, [a,c*]

[a] Departament de Química Inorgànica i Orgànica, Secció Inorgànica, Martí i Franquès 1-11, Barcelona-08028, Spain.
[b] Departament de Mineralogia, Cristal·lografia i Dipòsits Minerals, Universitat de Barcelona, Martí Franqués s/n, 08028 Barcelona (Spain) and Unitat de Difracció de R-X. Centre Científic i Tecnològic de la Universitat de Barcelona (CCiTUB), Solé i Sabarís 1-3. 08028 Barcelona.
[c] Institute of Nanoscience and Nanotecnology (IN^{2}UB), Universitat de Barcelona.

1- **IR spectra.**

    Fig, S1. IR spectra for **1-5**.

2- **Structural aspects.**

    Table S1. Crystal data and structure refinement for complexes **1 - 5.**

    Fig. S2. Coordination environment for the Mn^{II} cation in complexes **2–5**.

    Table S2. Relevant donor-acceptor distances (Å) and donor-H···acceptor angles for the H-bonds present in complexes **1**, **3**, **4** and **5**.

3- **Magnetic data.**

    Fig. S3. χ_M'' dependence of the transverse field for complexes **2** (top), **3** (middle) and **5** (bottom).

    Fig. S4. Plot of ln(1/2πν) vs. T^{-1} from the χ_M''(T) data for complexes **2**, **3** and **5.**

    Fig. S5. χ_M''(T) for complexes **2**, **3** amd **5** showing the lower frequencies and high frequencies out-of-phase response.

    Fig. S6. Cole-Cole plots for complexes **2**, **3** and **5.**
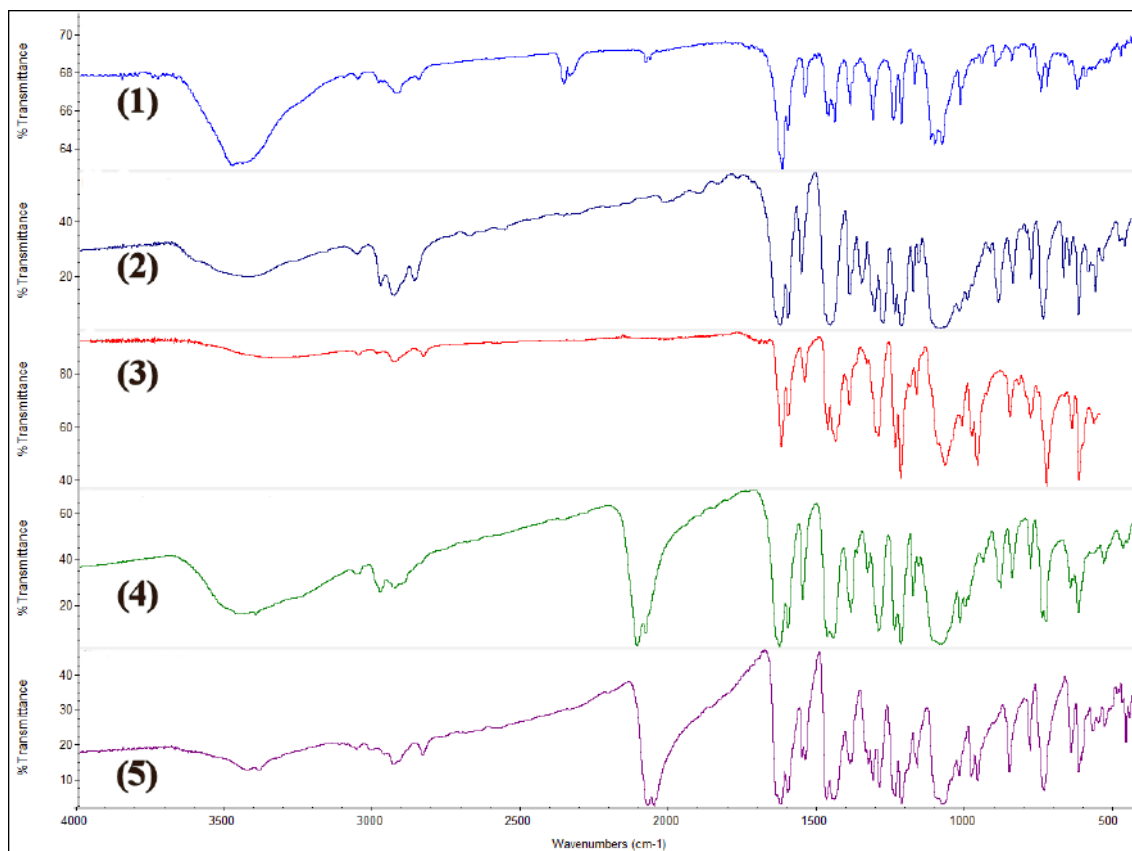
1- IR spectra.

Fig. S1. IR spectra for complexes **1 - 5**. Characteristic bands: st. C-H 3000-2800 cm⁻¹; N=C iminic ~1600 cm⁻¹; C-O st. ClO_4^- 1075 cm⁻¹; δ ClO_4^- 620 cm⁻¹. Stretching for the azido lignads for **4** and **5** appears between 2050-2100 cm⁻¹. **2RR** and **2SS** exhibit superimposable spectra and only one spectrum is shown.

2-Structural aspects.

Table S1. Crystal data and structure refinement for complexes **1** - **5**.

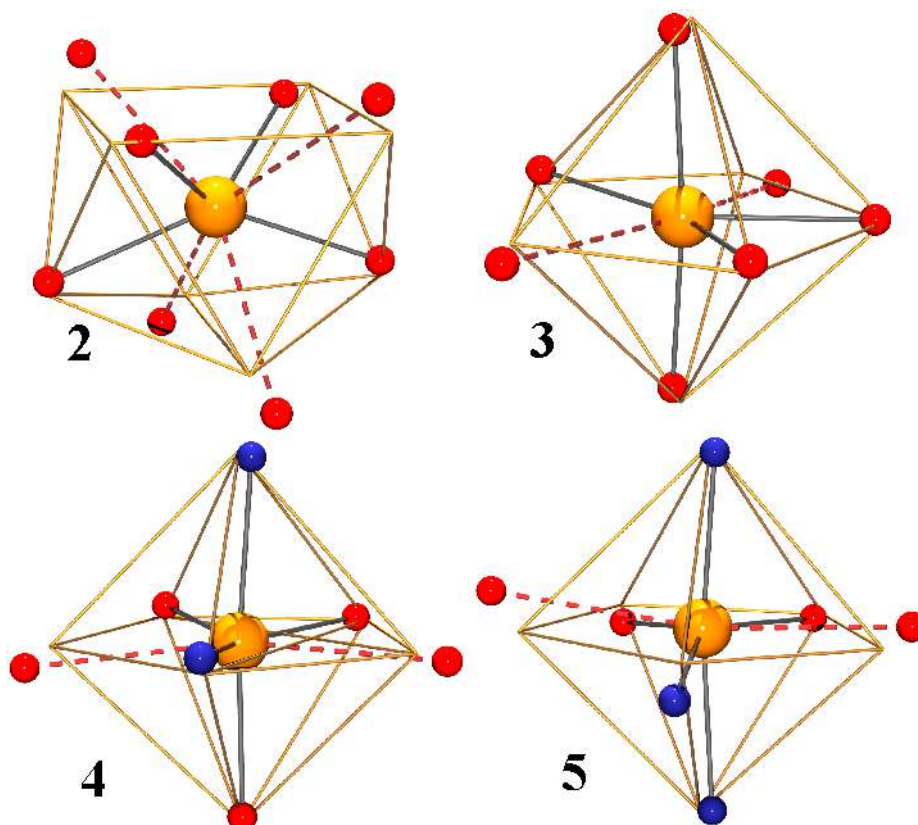|	**1**	**2SS·**2CH$_2$Cl$_2$·0.5MeOH	**3·MeOH**	**4·2MeOH**	**5**
Formula	C$_{21}$H$_{26}$ClCuN$_2$NaO$_9$	C$_{101}$H$_{128}$Cl$_8$Cu$_4$Mn$_2$N$_8$O$_{35}$	C$_{56}$H$_{66}$Cl$_2$Cu$_3$MnN$_6$O$_{24}$	C$_{82}$H$_{100}$Cl$_2$Cu$_4$Mn$_2$N$_{14}$O$_{28}$	C$_{74}$H$_{80}$Cl$_2$Cu$_4$Mn$_2$N$_{20}$Na$_2$O$_{26}$
FW	572.42	2661.75	1523.60	2164.69	2146.5
System	Monoclinic	Triclinic	Monoclinic	Triclinic	Triclinic
Space group	P21/c	P 1	P21/c	P-1	P-1
a/Å	8.0671(4)	12.2722(6)	15.4787(6)	9.876(1)	12.3500(6)
b/Å	21.2492(9)	14.5327(7)	22.7556(9)	14.787(2)	13.0272(7)
c/Å	14.0782(7)	17.2926(8)	17.7148(7)	16.663(2)	13.9308(7)
α/deg.	90	101.148(2)	90	73.292(5)	107.897(2)
β/deg.	103.285(2)	100.531(2)	97.002(1)	83.822(5)	91.793(2)
γ/deg.	90	111.062(2)	90	70.888(5)	94.147(2)
V/ Å^3	2348.7(2)	2714.5(2)	6193.1(4)	2201.8(5)	2123.9(2)
Z	4	1	4	1	1
T, K	100(2)	100(2)	100(2)	100(2)	100(2)
λ(MoKα), Å	0.71073	0.71073	0.71073	0.71073	0.71073
ρ_{calc}, g·cm^{-3}	1.619	1.628	1.634	1.633	1.678
μ(MoKα), mm^{-1}	1.118	1.279	1.389	1.376	1.435
Flack param.	----	0.02(1)	----	----	----
R	0.0340	0.0481	0.0479	0.0490	0.0334
ωR^2	0.0718	0.1328	0.1094	0.1328	0.0889

Fig. S2. Coordination environment for the Mn^{II} cation in complexes **2SS**–**5**. Dashed red bonds show the large contacts Mn-O$_{alcoxo}$. The ideal polyhedra (biapicated trigonal prism for **2SS** and pentagonal bipyramid for **3-5** are shown in orange.

Table S2. Relevant donor-acceptor distances (Å) and donor-H···acceptor angles for the H-bonds present in complexes **1**, **3**, **4** and **5**. For **1** and **5** correspond to the intermolecular H-bonds that determines the 1D arrangement in the network whereas for **3** and **4** correspond to the intramolecular H-bonds between the central and the capping [CuL] fragments.

|	D···A (Å)		D-H···A (deg.)		
Complex **1**	O9···O5'	2.831(2)	O9-H90···O5'	158.6(3)	Intermolecular
Complex **5**	O8···N7'	2.843(2)	O8-H8O···N7'	166(2)	
Complex **3**	O13···O9	2.955(4)	O13-H13B···O9	137(3)	Intramolecular
	O13···O10	2.806(3)	O13-H13B···O10	148(3)	
	O13···O11	2.752(3)	O13-H13A···O11	157(3)	
	O13···O12	2.975(4)	O13-H13A···O12	129(3)	
	O14···O1	3.024(4)	O14-H14A···O1	140(3)	
	O14···O2	2.762(4)	O14-H14A···O2	148(3)	
	O14···O3	2.809(3)	O14-H14B···O3	153(3)	
	O14···O4	3.059(4)	O14-H14B···O4	132(3)	
Complex **4**	O9···O5	2.963(3)	O9-H9B···O5	138(2)	
	O9···O6	2.820(2)	O9-H9B···O6	150(2)	
	O9···O7	2.872(3)	O9-H9A···O7	135(3)	
	O9···O8	2.971(3)	O9-H9A···O8	154(3)	

3-Magnetic data.
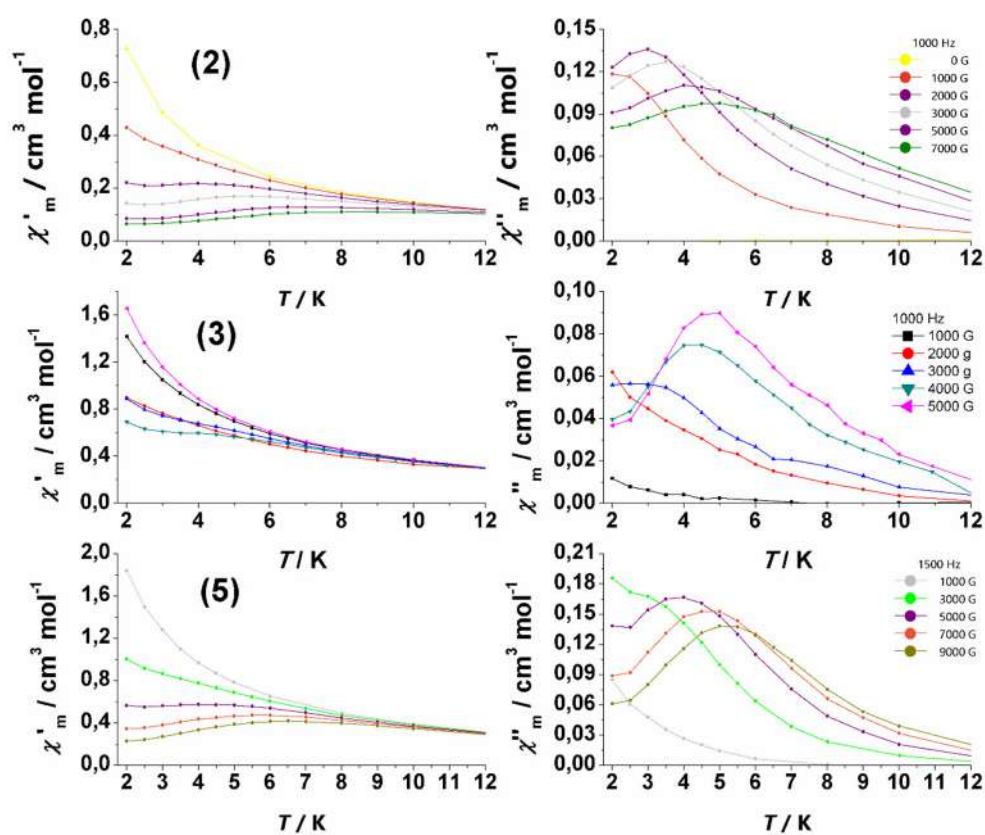
Fig. S3. χ_M'' dependence of the transverse field for complexes **2** (top), **3** (middle) and **5** (bottom).
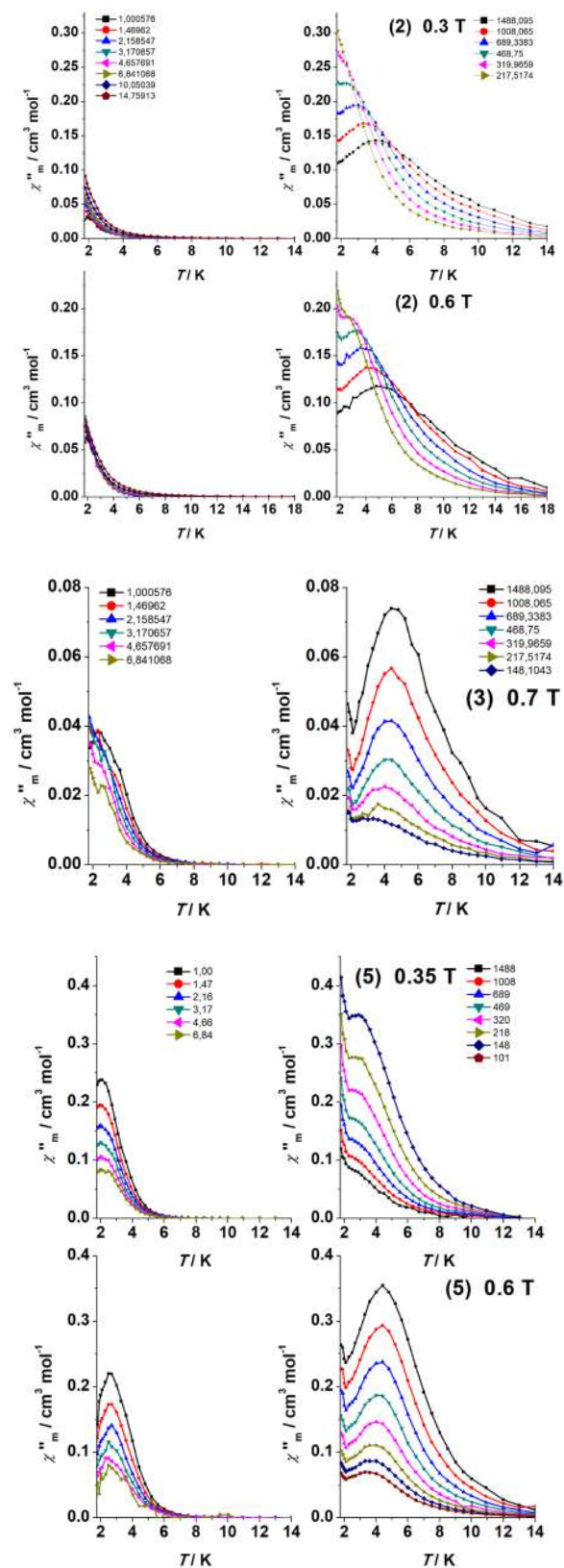
Fig. S4. $\chi_M''(T)$ for complexes **2**, **3** amd **5** showing the lower frequencies (left) and temperature dependent high frequencies (right) out-of-phase response. For the intermediate range of frequencies maxima are not defined.

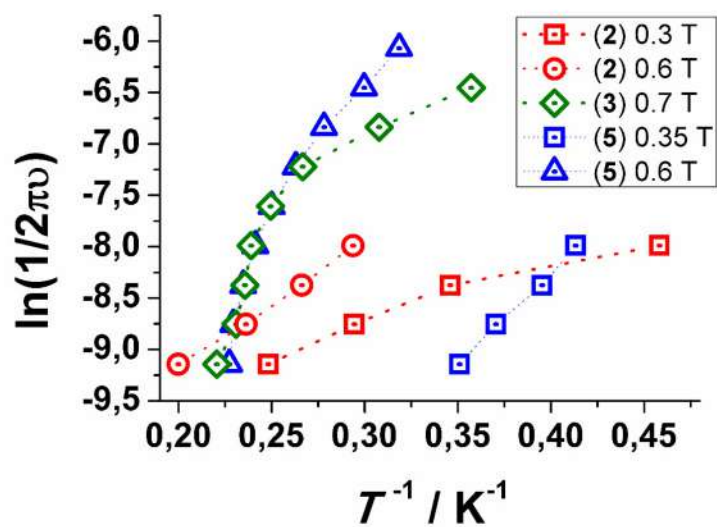**Fig. S5**. Plot of ln(1/2πν) vs. T^{-1} from the χ_M''(T) data for complexes **2** (red), **3** (green) and **5** (blue).The data is limited to the HF region for which the maxima of χ_M'' can be observed.
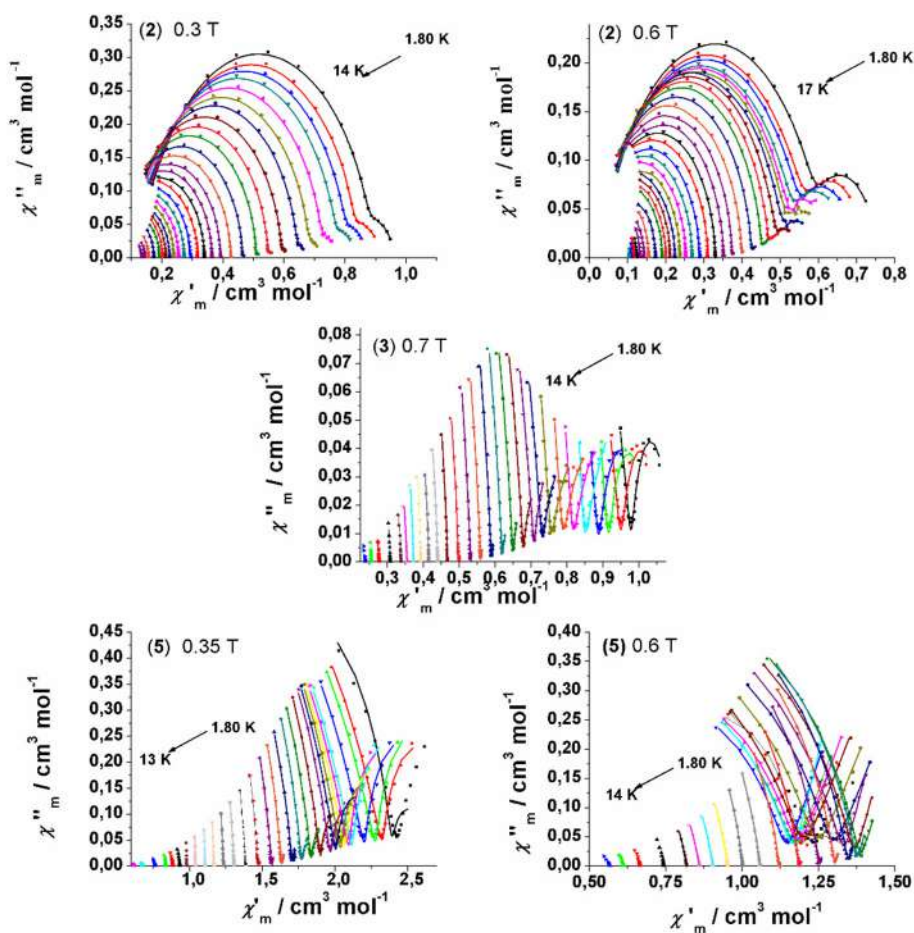

Fig. S6. Cole-Cole plots for complexes **2**, **3** and **5.** Solid lines show the best fit of the experimental data.

CHAPTER 4

SRM in Ni^{II}-Mn^{II} and mononuclear Mn^{II} complexes

Chapter 4: SRM in Ni^{II}-Mn^{II} and mononuclear Mn^{II} complexes

Introduction

Since the discovery of the first Single-Molecule Magnet, control of magnetic anisotropy has played a pivotal role in maximizing the energy barrier for the reversal of magnetization of these systems [7]. This is happening due to the direct relationship between the energy barrier U_{eff} and the axial zero field splitting parameter D; the energy barrier is calculated as DS^2 or as DS^2-1/4 for integer and half-integer spins, respectively, where S is the total spin state [7]. However, as has been postulated some years ago, increasing both D and S is impossible, and thus, magnetic anisotropy became the crucial factor in order to increase the energy barriers and achieving higher blocking temperatures (T_B). For this reason, lanthanides, are used extensively in the field of molecular magnetism, due to their high values of single-ion anisotropy [32,33]. Consequently, field-induced slow relaxation of magnetization of isotropic cations was discarded because following these rules their U_{eff} should be zero. However, in contrast with this paradigm, slow relaxation of magnetization has been recently reported for high spin Mn^{II} or Gd^{III} [59-68]. The main characteristic of these half-filled shell cations ($3d^5$ or $4f^7$), is the presence of low or quasi-negligible D value.

Regarding these two cations, Mn^{II} could be considered as more adequate than Gd^{III} for studying these kind of systems due to several reasons: on one hand, the internal f orbitals of lanthanides are poorly sensitive to the ligand field, but in contrast, the $3d$ orbitals of manganese are affected by the coordination of the metal with the ligands. On the other hand, the absence of crystal field stabilization energy (CFSE) for the high spin d^5 electronic configuration does not allow a preferred coordination polyhedron by electronic factors allowing the tuning of the coordination environment of the metal by the adequate design of the ligands. Thus, distorted exa-, penta- or heptacoordinated Mn^{II} environments could be designed and achieved in contrast with the poorly controllable coordination number and topology of the Gd^{III} environment. These facts, allows the control of the magnetic anisotropy by, firstly, modifying the ligands and secondly, modifying the coordination polyhedron of the metal.

When magnetic anisotropy has very low values, $D < 0.3$ cm^{-1}, susceptibility measurements are not able to give reliable values. Fit of the experimental data could be done either with

a small D or with intermolecular interactions (zj). In both cases, a good fit could be obtained but it is not clear if the drop of the susceptibility at lower temperatures is due to the presence of D or due to "zj", because these two parameters are correlated. Furthermore, reduced magnetization measurements could be sensitive to the presence of D, since the plots would not be superimposable. Determination of the D parameter from reduced magnetization experiments is a very useful tool for medium-large anisotropic systems but when the D is very low (< 0.5 cm^{-1}) then no reliable information can be extracted. Thus, EPR experiments become of paramount importance, because this technique is very sensitive and accurate values of the axial (D) or rombic (E) anisotropy can be extracted.

The magnitude of D in Mn^{II} coordination compounds is usually characterized by low values, normally lower than 1 cm^{-1}; an exception is a polyoxometalate complex displaying the highest value of D for Mn^{II} complexes ($D = +1.46$ cm^{-1}) [80a]. Especially, for mononuclear Mn^{II} complexes, investigated by EPR spectroscopy, there are two categories-classes of complexes: the complexes with N-, O- and S-donor atoms with $0.01 < D < 0.3$ cm^{-1} and the complexes with halides where $0.1 < D < 1.00$ cm^{-1} [80b, 81]. Mn^{II} is very sensitive to the nature of the ligands and the coordination number; for N- and O-donors the magnitude of D is larger for five-coordinated complexes compared to six- and to a lesser extend seven-coordinated ones. On the other hand, when Mn^{II} is coordinated with at least one halide, the D value is dictated by the nature of the halide with $D_{Cl} < D_{Br} < D_{I}$; this trend is associated with the SOC constant of the halide (ζ_X; X = Cl$^-$, Br$^-$ and I$^-$) [80c]. However, the number of halides that are coordinated to the cation does not affect the magnitude of D.

The study of the relaxation of the magnetization for the Mn^{II} cation has been done in three well defined families of complexes and thus, the organization of this Chapter is as follows:

- Section **4.1** The study of the first family of complexes, built with the same ligands employed in the Cu^{II}Mn^{II} systems (Chapter 3), describes the synthesis, structural and magnetic characterization of four heterometallic Ni^{II}-Mn^{II} compounds with formulas: [{Ni(L4)}$_2${NiMn(L4)(MeOH)(H$_2$O)$_2$}](ClO$_4$)$_2$(MeOH) (**28**·MeOH), [Ni$_2$Mn(L4)$_2$](ClO$_4$)$_2$(CH$_2$Cl$_2$)$_2$(MeOH) (**29**·2CH$_2$Cl$_2$·MeOH), [Ni$_2$Mn(L7)$_2$](ClO$_4$)$_2$ (**31SS**) and (**31RR**), [Ni$_2$Mn(L8)$_2$](ClO$_4$)$_2$(CH$_2$Cl$_2$)$_2$(MeOH)

($32 \cdot 2CH_2Cl_2 \cdot MeOH$), and one dinuclear Mn^{II} compound with formula ($\mu_{1,1}$-$N_3)_2[Ni_2Mn_2(L4)_2(N_3)_2]$ (30). The organic ligands that were employed for the synthesis of these complexes are shown in Fig. 37.

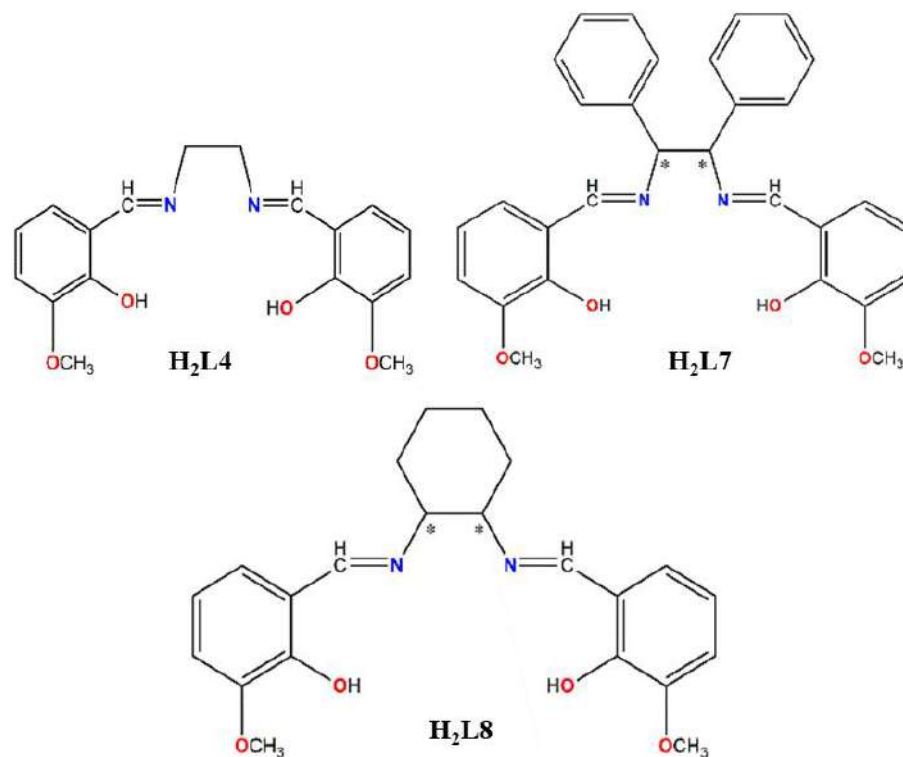Figure 37: Structural formula of ligands H_2L4 (top-left), H_2L7 (top-right) and H_2L8 (bottom). With asterisk the chiral centers are denoted.

These compartmental Schiff base ligands provide two coordination cavities. From the experiments and the results that were presented in the previous Chapter with the ligand H_2L4, Ni^{II} cation could "substitute" the Cu^{II} in the inner cavity and similar systems could be isolated. The interesting thing in this case is that the Ni^{II} cation adopts a square-planar environment (and thus diamagnetic) and the magnetic properties can be attributed only to the Mn^{II} cation. Complex 28 presents similar structure than 25 (sandwich-type $[Cu_3^{II}Mn^{II}]$ structure). Complex 29 was an unexpected trinuclear compound, which was co-crystallized with 28. Also, the ligands H_2L7 and H_2L8 were used in order to study if the use of diamines with different *R*-groups could affect the final products. Indeed, complexes 31 and 32 did

not present the sandwich-type structure that **28** does; instead their structure is similar to complex **24**, which is a trinuclear $[Cu_2^{II}Mn^{II}]$ complex.

- Section **4.2** The family of complexes described in this section are mononuclear Mn^{II} systems in all cases, comprising the synthesis and the characterization of seven Mn^{II} compounds with formulas: $[Mn^{II}L10^bCl_2]$ (**33**), $[Mn^{II}L10Br_2]$ (**34**), $[Mn^{II}L11Cl_2]$ (**35**), $[Mn^{II}L11Br_2]$ (**36**), $[Mn^{II}L11(N_3)_2]_n$ (**37**), $[Mn^{II}L12Cl_2]$ (**38**) and $[Mn^{II}L12Br_2]$ (**39**). The organic ligands that were used in this case are shown in Fig. 38. These ligands were selected because they can induce distorted geometries around the Mn^{II} cation and also they ensure predetermined coordination geometries. Thus, penta- and hexa-coordinated complexes were obtained.
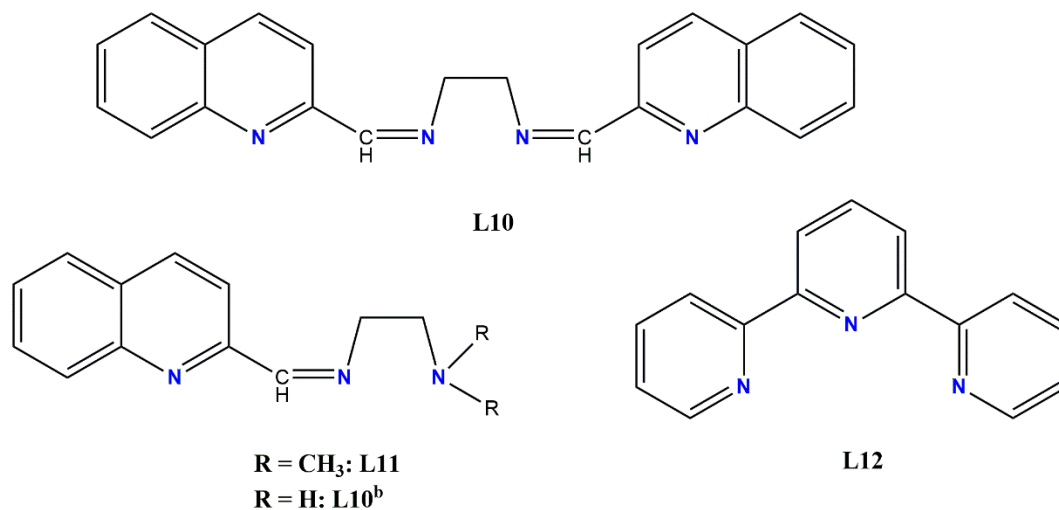
Figure 38: Structural formula of the organic ligands employed in Section **4.2**.

Complexes **33** and **34** were built from reactions employing as starting reagent ligand L10; interestingly in the case of **33** the ligand was partially hydrolyzed (ligand L10^b) while in **34** the ligand presented no changes. Complexes **35** and **36** presented the expected behavior and the complexes that were isolated are penta-coordinated with distorted geometries around the Mn^{II} cation. When N_3^- was employed in the reaction solution a 1D-polymer was isolated, complex **37**, where the two azido ligands are acting as terminal ligands and the other two as a bridge between the Mn^{II} cations adopting the end-to-end coordination mode.

Complexes **38** and **39** were already reported in the literature [82]. The magnetic studies revealed that from the pairs **35-36** and **38-39** only the complexes with chloro ligands showed magnetic relaxation behavior. This observation inspired us to investigate further details about these systems, and try to find an answer in the question, which is the main factor that governs this kind of behavior.

- Section **4.3** The family of complexes described in this section was specifically designed to have strong coordination distortion and a wide range of anisotropy. It comprises the synthesis and the characterization of four mononuclear Mn^{II} compounds with formulas: $[Mn^{II}(L13)(X)_2]$ where $X = Cl^-$ (**40RR** and **40SS**), Br^- (**41SS**), I^- (**42SS**) and NCS^- (**43SS**). The chiral organic ligand that used for the synthesis of these complexes is shown in Fig. 39.
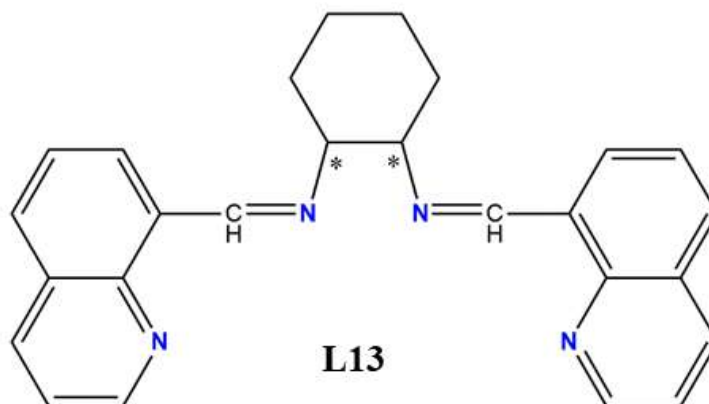
Figure 39: Structural formula of organic ligand L13; with asterisk the chiral carbons are depicted.

By employing the same ligand to this series of complexes, we ensured that the derived complexes will have predetermined geometries and also similar structures, in a try to provide a systematic study in order to prove experimentally which is the decisive factor for the presence of magnetic relaxation; these factors were: i) the crystal field promoted by the ligands, ii) the lattice vibration and iii) the presence of weak to relatively high anisotropy. The fact that the complexes are built by the same ligand, determines that they have similar lattice-vibrations, as was confirmed

by Raman spectroscopy, led to the conclusion that the parameter that is responsible for the presence of magnetic relaxation is the low D value.

Section 4.1

The Section **4.1** comprises the first family of complexes that used in order to study the magnetic relaxation of Mn^{II} cation. The compounds that are described in this Section are: [{Ni(L4)}$_2$[NiMn(L4)(MeOH)(H$_2$O)$_2$}](ClO$_4$)$_2$(MeOH) (**28**·MeOH), [Ni$_2$Mn(L4)$_2$](ClO$_4$)$_2$(CH$_2$Cl$_2$)$_2$(MeOH) (**29**·2CH$_2$Cl$_2$·MeOH), [Ni$_2$Mn(L7)$_2$](ClO$_4$)$_2$ (**31SS**) and (**31RR**), [Ni$_2$Mn(L8)$_2$](ClO$_4$)$_2$(CH$_2$Cl$_2$)$_2$(MeOH) (**32**·2CH$_2$Cl$_2$·MeOH), and one dinuclear Mn^{II} compound with formula ($\mu_{1,1}$-N$_3$)$_2$[Ni$_2$Mn$_2$(L4)$_2$(N$_3$)$_2$] (**30**). The organic ligand that employed are shown in Fig. 40. Additional information and details are given in Appendix.
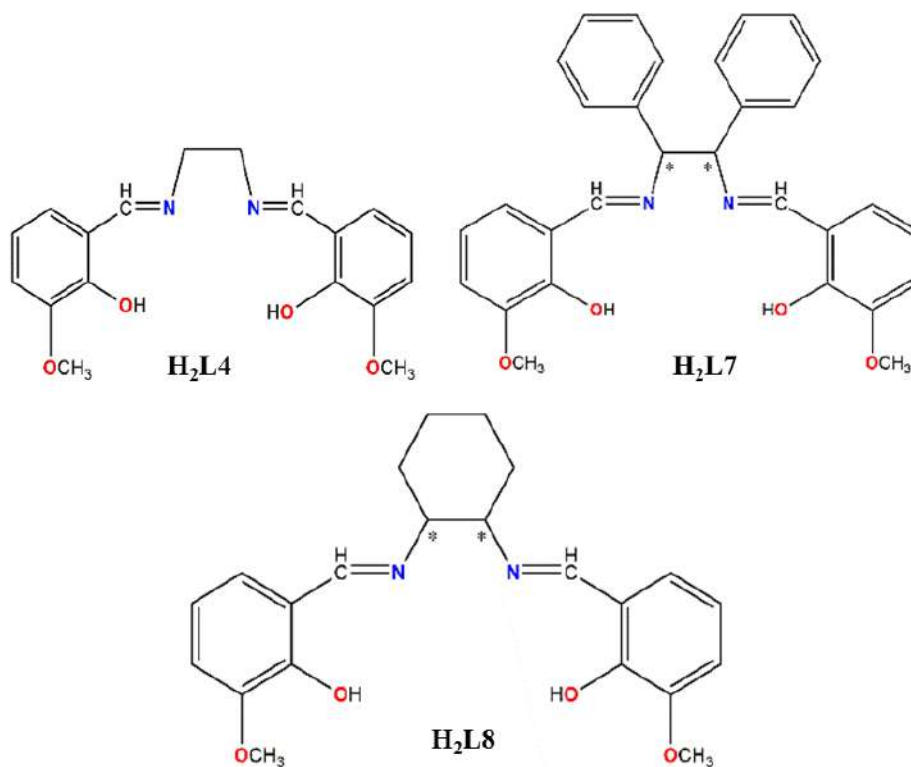

Figure 40: Structural formula of ligands H$_2$L4 (top-left), H$_2$L7 (top-right) and H$_2$L8 (bottom). With asterisk the chiral centers are denoted.

4.1.1 Synthesis

The organic ligand H$_2$L4 was synthesized following the procedure: in 20 ml of EtOH *o*-vanillin (12 mmol/1.83 g) and ethylenediamine (6 mmol/0.361 g) were added. The resulting yellow solution was left under magnetic stirring for 2 hours at room temperature and a yellow powder of product was formed. Then, the powder was filtered and washed with cold Et$_2$O (2x3 ml). Yield: 80%

The organic ligands H$_2$L7 and H$_2$L8 were not isolated as solids. Instead the neutral precursors [Ni(L)(H$_2$O)] were obtained as brown-dark red solids in very good yields from a methanolic solution (10 ml).

[Ni(*RR*-L7)(H$_2$O)] and [Ni(*SS*-L7)(H$_2$O)]: In a mixture of 5 ml of H$_2$O and 10 ml of MeOH, *o*-vanillin (0.8 mmol/0.121 g), (*1R,2R* or *1S,2S*)-1,2-diphenylethylenediamine (0.4 mmol/0.085 g) and nickel(II) acetate (0.4 mmol/0.098 g) were added. The reaction solution was placed in the microwaves for 30 minutes at 80 ˚C. A reddish precipitate of complex [Ni(L7)(H$_2$O)] was formed, collected and dried under vacuum.

[Ni(*RR*-L8)(H$_2$O)] and [Ni(*SS*-L8)(H$_2$O)]: In a mixture of 5 ml of H$_2$O and 10 ml of MeOH, *o*-vanillin (0.8 mmol/0.121 g), (1*R*,2*R* or 1*S*,2*S*)-1,2-diaminocyclohaxane (0.4 mmol/0.045 g) and nickel(II) acetate (0.4 mmol/0.098 g) were added. The reaction solution was placed in the microwaves for 30 minutes at 80 ˚C. A reddish precipitate of complex [Ni(L8)(H$_2$O)] was formed, collected and dried under vacuum.

[{Ni(L4)}$_2${NiMn(L4)(MeOH)(H$_2$O)$_2$}](ClO$_4$)$_2$(MeOH) (**28**·MeOH), and [Ni$_2$Mn(L4)$_2$](ClO$_4$)$_2$(CH$_2$Cl$_2$)$_2$(MeOH) (**29**·2CH$_2$Cl$_2$·MeOH): An aqueous solution (5 ml) of nickel(II) acetate tetrahydrate (0.8 mmol/0.197 g) was added to a suspension of H$_2$L4 (0.8 mmol/0.30 g) in MeOH (10 ml). The resulting solution was left in microwaves for 30 minutes at 80˚C and a reddish precipitate of complex [Ni^{II}L(H$_2$O)] was formed, collected and dried under vacuum. Then, the solution of the fresh prepared powder (~0.108 g) was dissolved in a mixture of CH$_2$Cl$_2$/MeOH (3:1, 15ml) and was added to a methanolic solution (5 ml) of Mn(ClO$_4$)$_2$·6H$_2$O (0.25 mmol/0.09 g). The reaction mixture was placed in microwaves for 15 min at 70˚C. An orange solution was obtained and left for crystallization by layer with Et$_2$O. After two days, two different kinds of well-shaped

orange crystals (needles for **28** and prisms for **29**), suitable for X-ray diffraction, were formed and separated manually. IR in KBr pellets, cm^{-1}: (**28**): 3413(sh), 2939(w), 2841(w), 1620(s), 1474(s), 1334(w), 1231(m), 997(m). (**29**): 3420(sh), 1618(m), 1474(m), 1456(m), 1303(w), 1088(s), 738(m).

($\mu_{1,1}$-N$_3$)$_2$[Ni$_2$Mn$_2$(L4)$_2$(N$_3$)$_2$] (**30**): The complex was synthesized by a modified method of the reported synthesis [78]. The complex was prepared following the same procedure as complexes **28** and **29** but adding NaN$_3$ (0.4 mmol/0.026 g) to the [Ni(L4)(H$_2$O)]/Mn(ClO$_4$)$_2$·6H$_2$O dissolution. After two days, well-shaped orange crystals suitable for X-ray diffraction were formed by layering with Et$_2$O. IR in KBr pellets, cm^{-1}: 3338(w), 2109(s), 1620(m), 1473(m), 1454(m), 1247(m), 741(w).

[Ni$_2$Mn(*RR*-L7)$_2$](ClO$_4$)$_2$ (**31*RR***) and [Ni$_2$Mn(*SS*-L7)$_2$](ClO$_4$)$_2$ (**31*SS***): A fresh prepared powder of [Ni(*RR*-L7)(H$_2$O)] or [Ni(*SS*-L7)(H$_2$O)] was dissolved in a mixture of CH$_2$Cl$_2$/MeOH (3:1, 15ml) and was added to a methanolic solution (5 ml) of Mn(ClO$_4$)$_2$·6H$_2$O (0.4 mmol/0.18 g). The reaction mixture was left in microwaves for 15 min at 70˚C. After two days, well-shaped orange crystals by layer with Et$_2$O, suitable for X-ray diffraction, were formed and collected. IR in KBr pellets, cm^{-1}: 3529(sh), 3065(w), 1606(s), 1562(w), 1470(s), 1299(m), 1227(s), 1073(w), 995(w).

[Ni$_2$Mn(*RR*-L8)$_2$](ClO$_4$)$_2$(CH$_2$Cl$_2$)$_2$(MeOH) (**32*SS*·**2CH$_2$Cl$_2$·MeOH) and [Ni$_2$Mn(*SS*-L8)$_2$](ClO$_4$)$_2$(CH$_2$Cl$_2$)$_2$(MeOH) (**32*RR*·**2CH$_2$Cl$_2$·MeOH): A fresh prepared powder of [Ni(*RR*-L8)(H$_2$O)] or [Ni(*SS*-L8)(H$_2$O)] (~0.1 g) was dissolved in a mixture of CH$_2$Cl$_2$/MeOH (3:1, 15ml) and was added to a methanolic solution (5 ml) of Mn(ClO$_4$)$_2$·6H$_2$O (0.25 mmol/0.09 g). The reaction mixture was left in microwaves for 15 minutes at 70˚C. After two days, well-shaped orange crystals by layer with Et$_2$O, suitable for X-ray diffraction, were formed and collected. The complex **32*RR*** was not prepared as single crystals. Instead, it was isolated as powder and was identified by IR spectroscopy. IR in KBr pellets, cm^{-1}: 3547(sh), 2939(w), 1628(w), 1608(w), 1290(w), 1268(w), 1076(m), 730(m).

93

4.1.2 Comments on Synthesis

The synthesis of complexes **28-32** was revealed to be sensitive to several factors, such as the solvents, the Schiff base used in each case, the presence of N_3^- and the crystallization procedures.

Complexes **28** and **29** were crystallized in the same tube, with the same conditions. Firstly, it was examined if the crystallization procedures were able to distinguish these two complexes. Different amounts of Et_2O or a mixture of Et_2O/Hexane was used in order to check the solubility of each product. With the mixture of crystallization solvents, no crystals or powder was isolated. Similarly, different ratio of Et_2O/solution did not lead to isolation of the any product. Also, different solvents were used in the reaction mixture but no results were obtained. As consequence, profiting the clearly different shape of the crystals, they were manually separated to dispose of pure samples for magnetic measurements. Furthermore, the use of NaN_3 in the reaction solution led to the complex **30** where the two Mn^{II} cations are bridged by two $\mu_{1,1}$-N_3 bridges showing weak ferromagnetic interaction.

The use of chiral Schiff base ligands H_2L7 and H_2L8 led to the similar complexes **31** and **32** selectively without co-crystallization of the equivalent complex **28**. Both ligands were coordinated on the same mode with the metal cations as H_2L4 in **29**.

4.1.3 Description of Structures

The environments of the nickel cations are similar in the six complexes. The Ni^{II} is placed in the inner N_2O_2 cavity of the corresponding L^{2-} ligand in a square planar environment with N-Ni-N and O-Ni-O bond angles lower than 90° and the bond distances close but lower than 1.9 Å as it is usual for Ni^{II} cations in square planar environment. Crystal data and structure refinement for compounds **28**, **29**, **31** and **32** are listed in Table A1, Appendix. The crystal structure of complex **30** was previously reported in the literature [78] with a CCDC code CIBPAF. Powder X-Ray diffraction spectra comparison of **30** and the simulated spectrum of the previous reported complex is shown in Fig. A1, Appendix, confirming the structure and purity of the complex.

[{Ni(L4)}$_2${NiMn(L4)(MeOH)(H$_2$O)$_2$}](ClO$_4$)$_2$(MeOH)　(**28**·MeOH):　A　view　of molecular structure of **28** is shown in Fig. 41 and selected interatomic distances and angle are listed in Table 2.
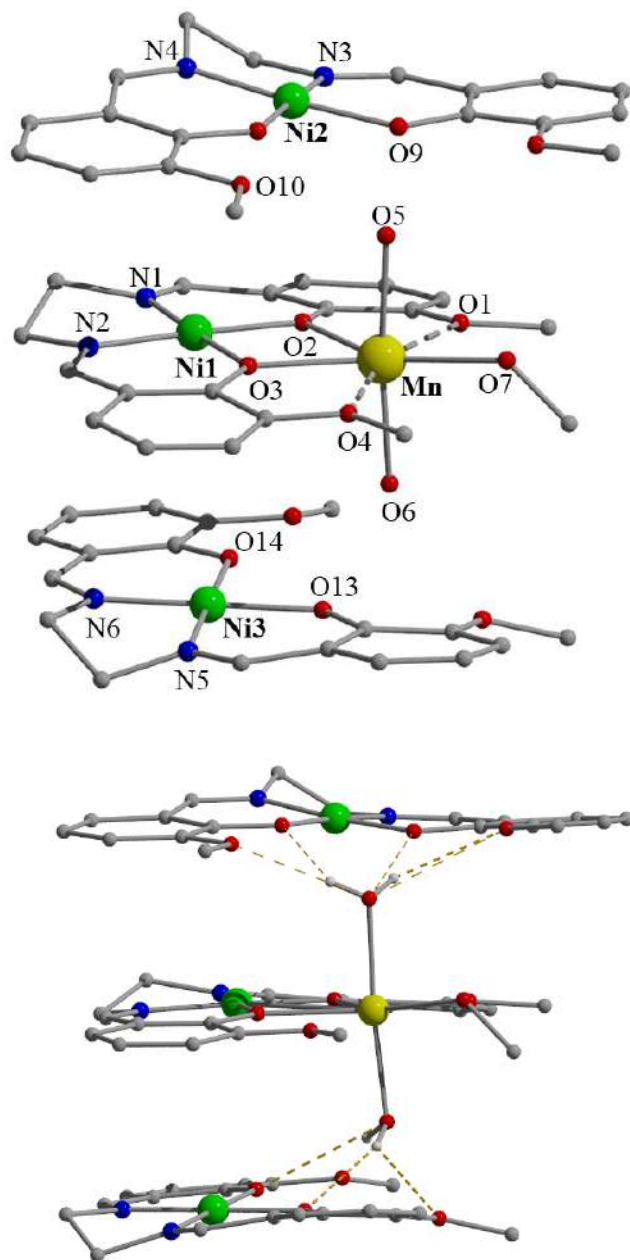

Figure 41: Partially labeled plot of the molecular structure of complex **28** (top) and intramolecular H-Bonds inside the cluster (bottom). Color key for all plots: Ni[II]: green, Mn[II]: yellow, O: red, N: blue, C: grey.

Compound **28** exhibits a "sandwich" structure formed by one $[NiMn(L4)(H_2O)_2(MeOH)]^{2+}$ fragment and two neutral [NiL4] units which are linked by means of bifurcated H-bonds. The coordination of Mn^{II} cation is determined by two $O_{phenoxo}$ donors, one methanol and two water molecules in a distorted MnO_5 vacant octahedron arrangement. The two $O_{methoxo}$, O4 and O1, are placed at larger distances (2.555 and 2.514 Å, respectively), inducing a weak interaction with the Mn^{II} cation and thus the environment around it can also be envisaged as MnO_7. SHAPE analysis of the coordination environment shows a large deviation from any regular polyhedron, where pentagonal bipyramidal (Fig. A2, Appendix) being the closer one with a CShM value of 1.58 (Table A2, Appendix).

Table 2: Selected interatomic distances (Å) and angels (°) for compound **28**.

Ni1-N2	1.8397(10)	Mn-O3	2.1963(9)
Ni1-N1	1.8398(10)	Mn-O2	2.2016(8)
Ni1-O2	1.8449(9)	N2-Ni1-N1	86.71(4)
Ni1-O3	1.8525(8)	N2-Ni1-O2	177.40(4)
Mn-O5	2.1411(9)	O6-Mn1-O5	174.22(3)
Mn-O6	2.1358(9)	O6-Mn1-O7	93.71(3)

[Ni₂Mn(L4)₂](ClO₄)₂(CH₂Cl₂)₂(MeOH) and (**29**·2CH₂Cl₂·MeOH): A view of complex **29** is shown on Fig. 42, while selected interatomic distances and angles are listed in Table 3.
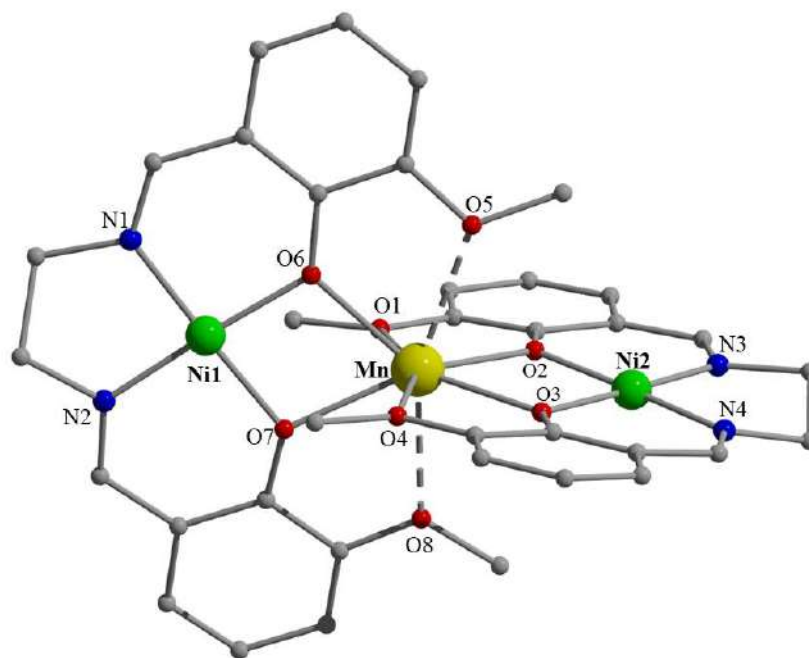

Figure 42: Partially labeled plot of complex **29**.

Complex **29** crystallizes in *P* 21/n space group and the unit cell contains a trinuclear $[Ni_2Mn(L4)_2]^{2+}$ molecule where the charge is stabilized by the presence two percholate anions in the lattice. The Ni^{II} cations are placed in the inner N_2O_2 cavity of the Schiff base ligand showing the square planar environment similar with **28**. Manganese cation is surrounded by four $O_{phenoxo}$ donors in a very distorted tetrahedral arrangement. However, the large distances with the $O_{methoxo}$ donors (Table 3) in the range of 2.42-2.55 Å induce a weak interaction and an unusual octacoordination. SHAPE analysis showed that the coordination environment does not agree with any regular polyhedron, and the closer one is the triangular dodecahedron (Fig. A2, Appendix) with a value of CShM=3.02 (Table A3, Appendix).

Table 3: Selected interatomic distances (Å) and angels (°) for compound **29**.

97

Ni1-N2	1.8366(10)	Mn1-O1	2.5198(10)
Ni1-N1	1.8383(10)	Mn1-O2	2.1732(8)
Ni1-O6	1.8468(8)	Mn1-O4	2.4790(9)
Ni1-O7	1.8481(8)	Mn1-O6	2.1780(8)
Mn1-O3	2.1731(8)	N2-Ni1-N1	87.11(5)
Mn1-O8	2.4238(8)	N2-Ni1-O6	95.97(4)

$(\mu_{1,1}\text{-}N_3)_2[Ni_2Mn_2(L4)_2(N_3)_2]$ (**30**): A view of the centrosymmetric complex **30** is shown in Figure 43. Selected bond distances and angles are listed in Table 4. The Ni^{II} cations, as usually, are placed in the N_2O_2 cavity adopting the usual square planar coordination geometry. Each Mn^{II} cation is coordinated with two $O_{phenoxo}$ donors from each Schiff base, one terminal azido ligand, and by two bridging end-on azides. At this case the Mn^{II} is pentacoordinated and adopts a spherical square pyramidal geometry. However, taking into consideration the larger distances and the weak interactions between Mn^{II} and $O_{methoxo}$ donors, the environment of manganese could be described as heptacoordinated and SHAPE measurements revealed that the ideal polyhedron is pentagonal bipyramid (Fig. A2, Appendix) with CShM= 2.66 (Table A2, Appendix).
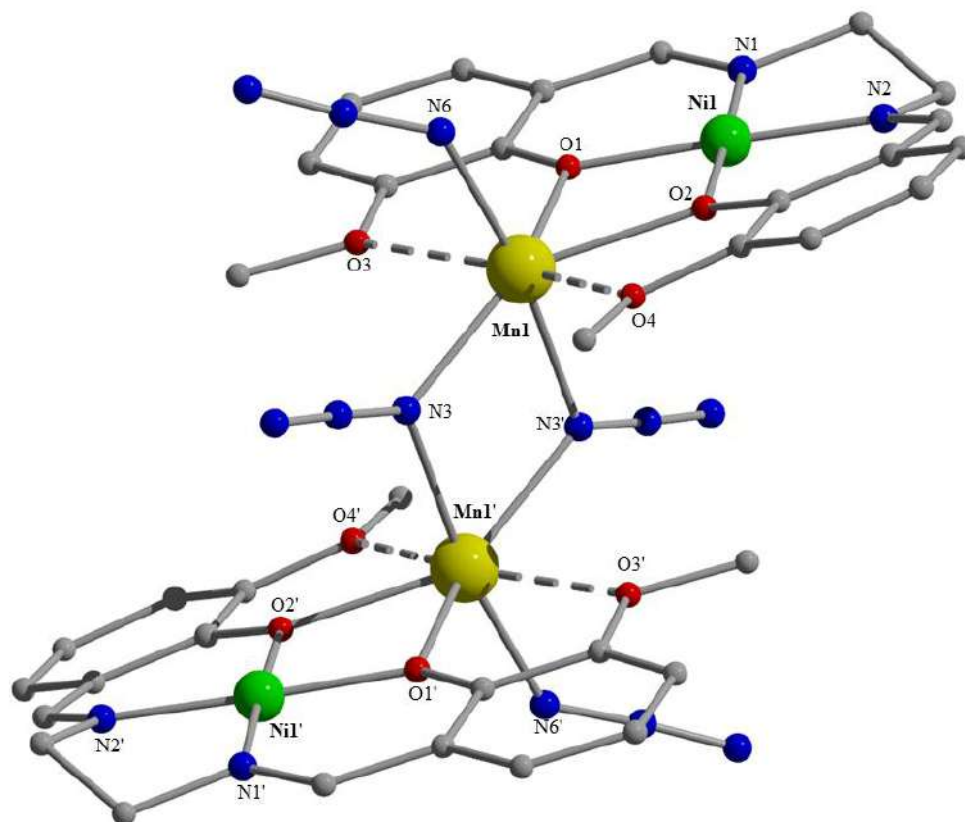
Figure 43: Partially labeled plot of complex **30**.

Table 4: Selected interatomic distances (Å) and angels (°) for compound **30**.

Ni1-O1	1.842	Mn1-O4	2.538
Ni1-O2	1.848	Mn1-O3	2.554
Ni1-N1	1.844	Mn1-N6	2.123
Ni1-N2	1.840	Mn1-N3	2.249
Mn1-O1	2.250	N2-Ni1-O1	177.53
Mn1-O2	2.221	O2-Ni1-N1	177.92

[Ni$_2$Mn(L7)$_2$](ClO$_4$)$_2$ (**31SS**)-(**31RR**): A partially labeled plot for the two complexes is shown in Figure 44, and selected bonds and angles are listed in Table 5. Due to the fact that the two structures are similar **31SS** is labeled as molecule A while **31RR** as molecule B. Thus, the description of the structure will be referred to molecule A. The unit cell of this compound contains two similar but crystallographically nonequivalent {NiMnNi} trinuclear molecules. As, a result the following description will be referred to the one the molecules.
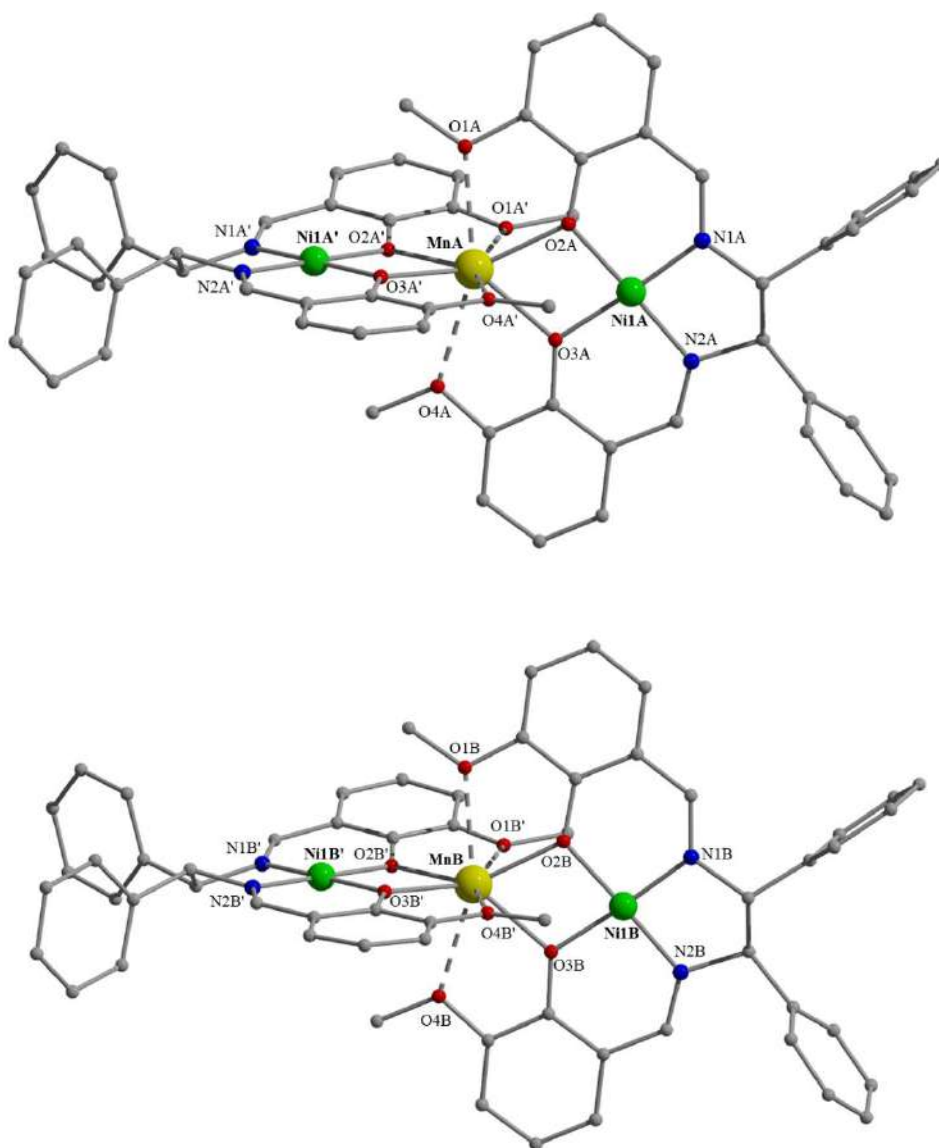

Figure 44: Partially labeled plot of **31SS** (top) and **31RR** (bottom).

The trinuclear complex is formed by two neutral [NiL7] fragments that link one Mn^{II} cation by means of their deprotonated $O_{phenoxo}$ donors. The Ni^{II} cations are in the inner N_2O_2 cavity of the $(L7)^{2-}$ Schiff base ligand showing the usual square planar coordination geometry. The manganese cation is coordinated by four $O_{phenoxo}$ donors in a very distorted tetrahedral arrangement, and four $O_{methoxo}$ donors that surround the MnO_4 polyhedron with large Mn-O distances, ranging from 2.456 to 2.580 Å. SHAPE measurements shows that the coordination environment of Mn^{II} does not agree with any regular polyhedron and the closer one is the triangular dodecahedron (Fig. A2, Appendix) with a value of CShM = 2.71 (Table A3, Appendix).

Table 5: Selected interatomic distances (Å) and angels (˚) for compound **31*SS*** and **31*RR***.

31*SS*		31*RR*	
Mn1A-O2A	2.149(5)	Mn1B-O2B	2.165(4)
Mn1A-O3A	2.166(4)	Mn1B-O3B	2.153(4)
Mn1A-O1A	2.437(5)	Mn1B-O1B	2.436(4)
Ni1A-N2A	1.826(5)	Ni1B-N2B	1.836(5)
Ni1A-N2A	1.832(5)	Ni1B-N2B	1.833(5)
O2A-Mn1A-O1A	67.35(16)	O2B-Mn1B-O1B	67.27(14)
O3A-Mn1A-O1A	134.49(17)	O3B-Mn1B-O1B	134.82(15)

$[Ni_2Mn(L8)_2](ClO_4)_2(CH_2Cl_2)_2(MeOH)$ (**32**·$2CH_2Cl_2$·MeOH): Partially labeled plot of complex **32** is shown in Fig. 45, while selected interatomic bond distances and angles are listed in Table 6. Complex **32** shows similar structure with complex **31**, where the main difference is that in this case two molecules of CH_2Cl_2 and one molecule of MeOH are cocrystallized in the lattice.

The trinuclear complex is formed by two neutral [NiL8] fragments that link one Mn^{II} cation by means of their deprotonated $O_{phenoxo}$ donors. The Ni^{II} cations are in the inner N_2O_2 cavity of the $(L8)^{2-}$ Schiff base ligand showing the usual square planar coordination geometry. The manganese cation is coordinated by four $O_{phenoxo}$ donors in a very distorted tetrahedral arrangement, and four $O_{methoxo}$ donors that surround the MnO_4 polyhedron with large Mn-O distances, ranging from 2.452 to 2.514 Å. SHAPE measurements shows that the coordination environment of Mn^{II} does not agree with any regular polyhedron and the closer one is the triangular dodecahedron (Fig. A2, Appendix) with a value of CShM = 2.85 (Table A3, Appendix).
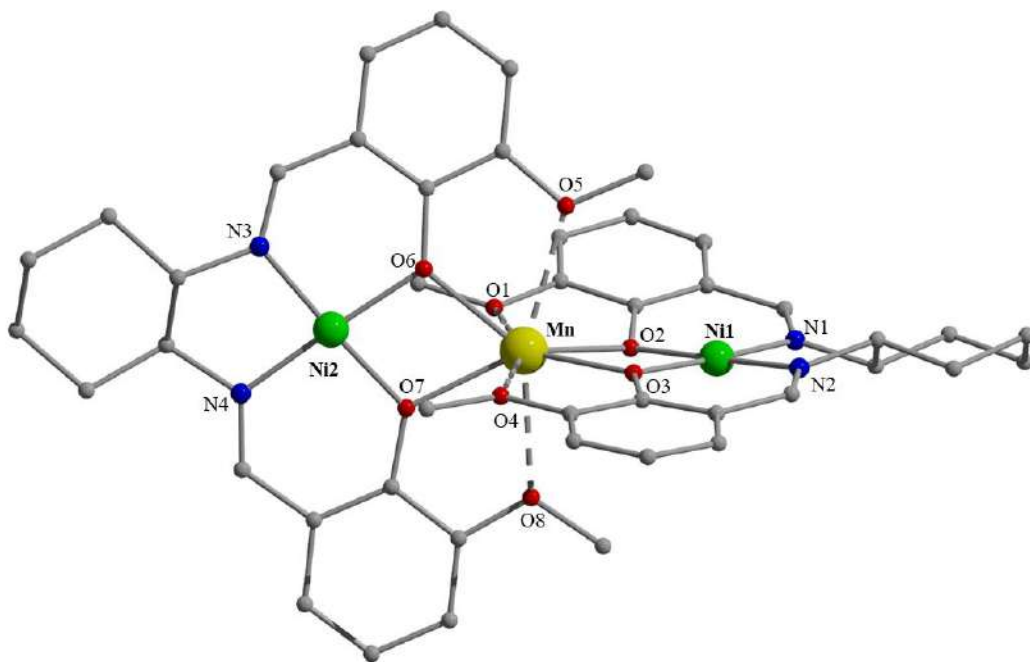

Figure 45: Labelled plot of complex **32**.

Table 6: Selected interatomic distances (Å) and angels (°) for compound **32**.

Ni1-N1	1.844(5)	Mn1-O8	2.470(4)
Ni1-O3	1.848(4)	Mn1-O5	2.503(4)
Ni1-N2	1.851(5)	Mn1-O4	2.514(5)
Ni1-O2	1.854(4)	N1-Ni1-O3	176.6(2)
Mn1-O3	2.159(4)	N1-Ni1-N2	87.1(2)
Mn1-O7	2.180(4)	O3-Ni1-N2	95.9(2)

4.1.4 Electronic Circular Dichroism

Transfer of chirality in coordination compounds is a common feature when enantiopure chiral ligands are employed. Complexes **31** and **32** were measured by means of Electronic Circular Dichroism (ECD). The transfer of chirality from the ligands to the metallic centers is not relevant for the Ni^{II} cation which present a square planar geometry or for the Mn^{II} cations appear in the structures. ECD spectra in methanolic solution were recorded for the enantiomeric pairs of complexes **31RR/31SS** and **32RR/32SS** (Fig. 46) and their mirror image confirms the enantiomeric nature of the reported complexes. The spectrum of **31RR** exhibits positive Cotton effect at λ_{max}= 409(w), 273, 223 and 217 nm, whereas **31SS** shows the same bands with opposite sign. **32SS** exhibits positive Cotton effect at λ_{max}= 394(w), 275, 247 and 203 nm, while **32RR** shows the same bands with opposite sign. The d-d transitions at larger wavelength are very weak and the intense absorptions below 400 nm are attributed to $\pi \rightarrow \pi^*$ transition of the ligands.
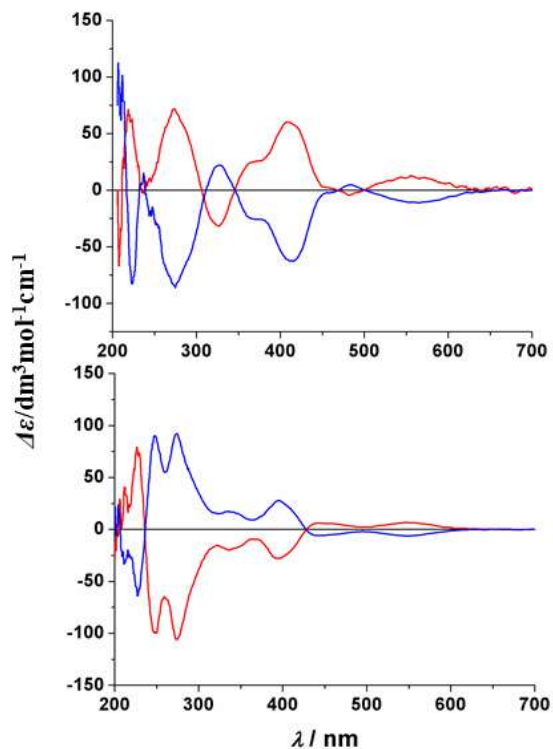
Figure 46: Top, methanolic solution ECD spectra for complex **31***RR* (red line) and **31***SS* (blue line). Bottom, ECD spectra of **32***RR* (red line) and **32***SS* (blue line).

4.1.5   Magnetic Susceptibility Measurements

Static susceptibility measurements for compounds **28-32** were performed on powdered samples in the 300-2 K range for **30** and **31**, 100-2 K for **28** and **29** and 120-2 K for complex **32**. The room temperature χ_MT values for complexes **28**, **29** and **32** are 4.35, 4.31 and 4.36 $cm^3mol^{-1}K$, respectively, which is in agreement with the expected value of one S = 5/2 (4.375 $cm^3mol^{-1}K$). For **30** the χ_MT value is 9.09 $cm^3mol^{-1}K$, which is slightly higher than the expected value for two non-interacting Mn^{II} cations (8.75 $cm^3mol^{-1}K$), whereas the mononuclear compound the **31** χ_MT plot shows a constant value of 4.1 $cm^3mol^{-1}K$. The susceptibility plots for **30** and **31** are shown in Fig. A3, Appendix.

Complex **28** shows a decrease of χ_MT value below 10 K arriving to a 3.9 $cm^3mol^{-1}K$ at 2 K (Fig. 47, top right), which is attributed to the presence of magnetic anisotropy and/or to intramolecular interactions. Reduced magnetization experiments (Fig. 47, top-left) showed quasi superimposable plots for **28** indicating the presence of very low anisotropy. For

complex **29**, the $\chi_M T$ plot (Fig. 47, bottom-right) shows a decrease upon cooling reaching the value of 3.81 $cm^3mol^{-1}K$ at 2K. This decrease should be attributed to intramolecular interactions due to the fact that reduced magnetization plots found to be superimposable, indicating that the magnetic anisotropy is negligible.
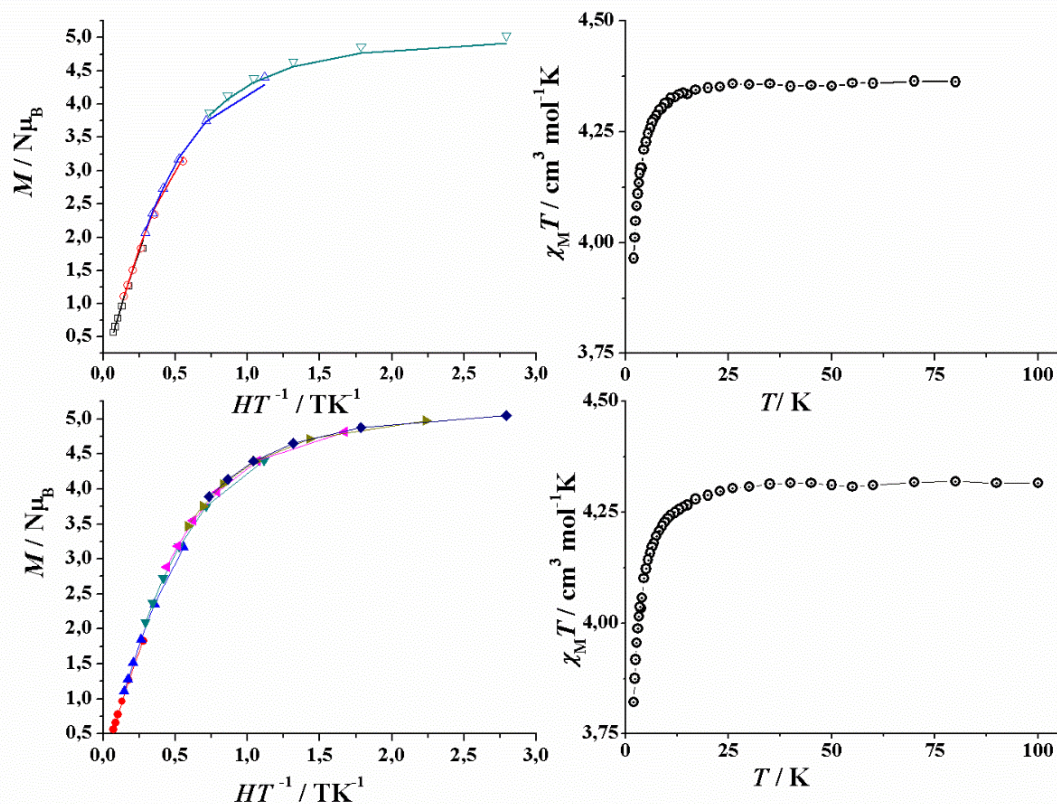
Figure 47: (Top-left) Fitted reduced magnetization for **28**. (Top-right) $\chi_M T$ plot for **28**. (Bottom-left) Reduced magnetization for **29**, and (Bottom-right) $\chi_M T$ plot for **29**.

For complex **30** the susceptibility value shows an increase upon cooling, reaching a maximum value of 14.24 $cm^3mol^{-1}K$ at 7 K, and below this temperature a slight decrease is observed (Fig. 48). Fitting of the susceptibility data, using program *PHI* [79], revealed a weak ferromagnetic interaction between the Mn^{II} cations, $J = +2.8$ cm^{-1}, mediated by the end-on azide bridging mode, and $g = 1.98$. The superimposable plots of reduced

magnetization indicate that the magnetic anisotropy of this system is negligible (Fig. 48, right).

Figure 48: (Left) Fitted χ_MT plot and (right) reduced magnetization plot for **30**.
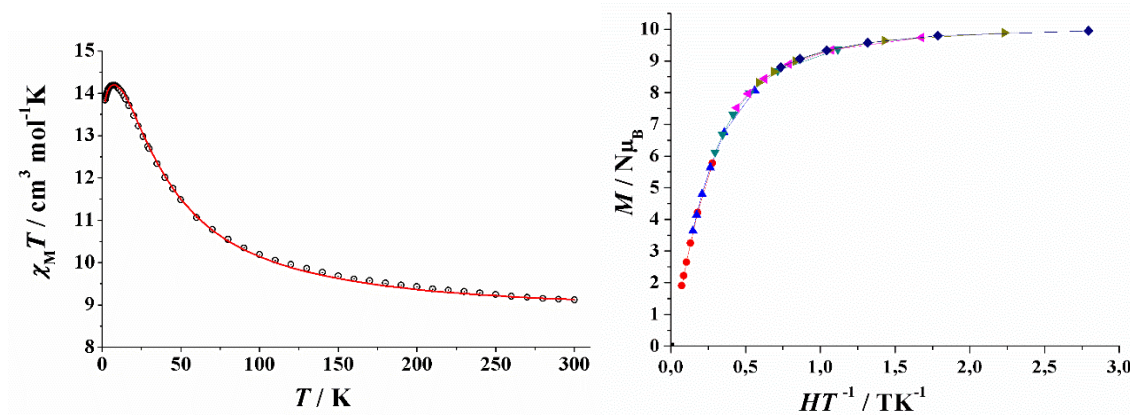
Alternating current (ac) susceptibility measurements were performed for complexes **28-32**. Due to fact that **30** was used for a more extended ac magnetic study and its dimeric nature, it will be described after the mononuclear systems. Measurements at zero field for the mononuclear systems do not show out of phase signals in any case, but peaks were observed for all of them under applied fields (Fig. 49 and Fig. 50). In light of these data, ac susceptibility measurements in the 1-1488 Hz frequency range were performed under the fields that yielded the maximum χ''_m response frequency region. Complex **28** shows signals below 2 K for frequencies below 2 Hz whereas for higher frequencies there is a weak signal around 3 K. For **29** there are weak signals in the lower frequency region and below 4 K; increasing the frequency the signal becomes more intense and is out of the studied range. Complexes **31** and **32** shows similar behavior with very weak response below 3 K for low frequencies, whereas for higher frequencies the signal becomes more intense and a well-defined maximum appears at 3.5 K. In all the cases there is one low-frequency (LF) and one high-frequency (HF) region that show ac response.

Figure 49: Temperature and frequency dependence of χ''_m for complexes **28** (left) and **29** (right) under an applied field of 0.5 and 0.7 T, respectively.

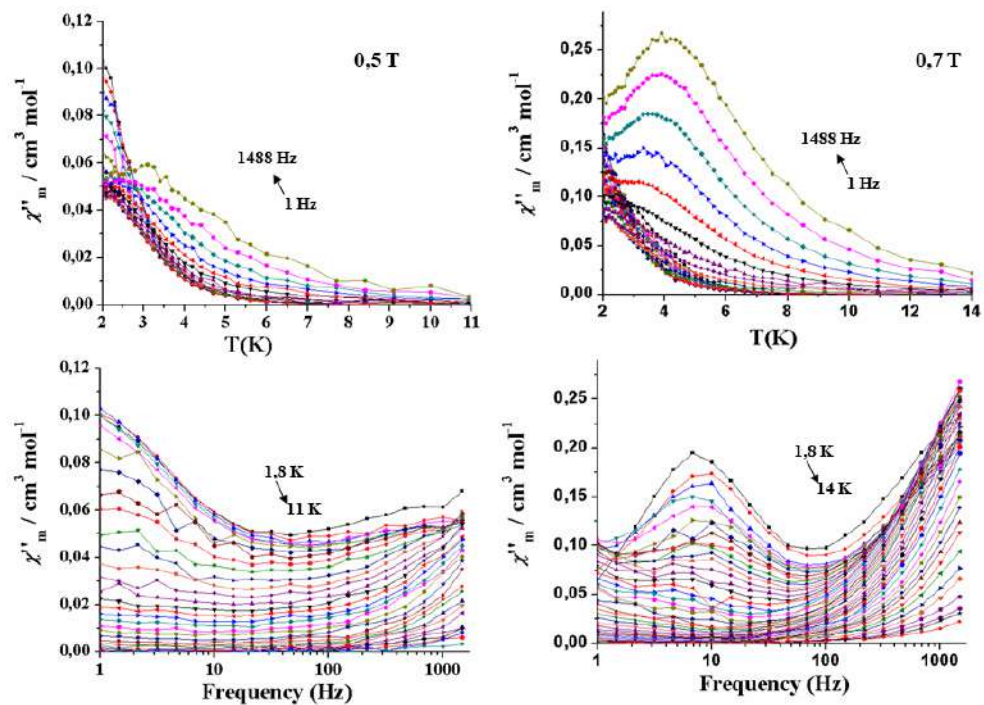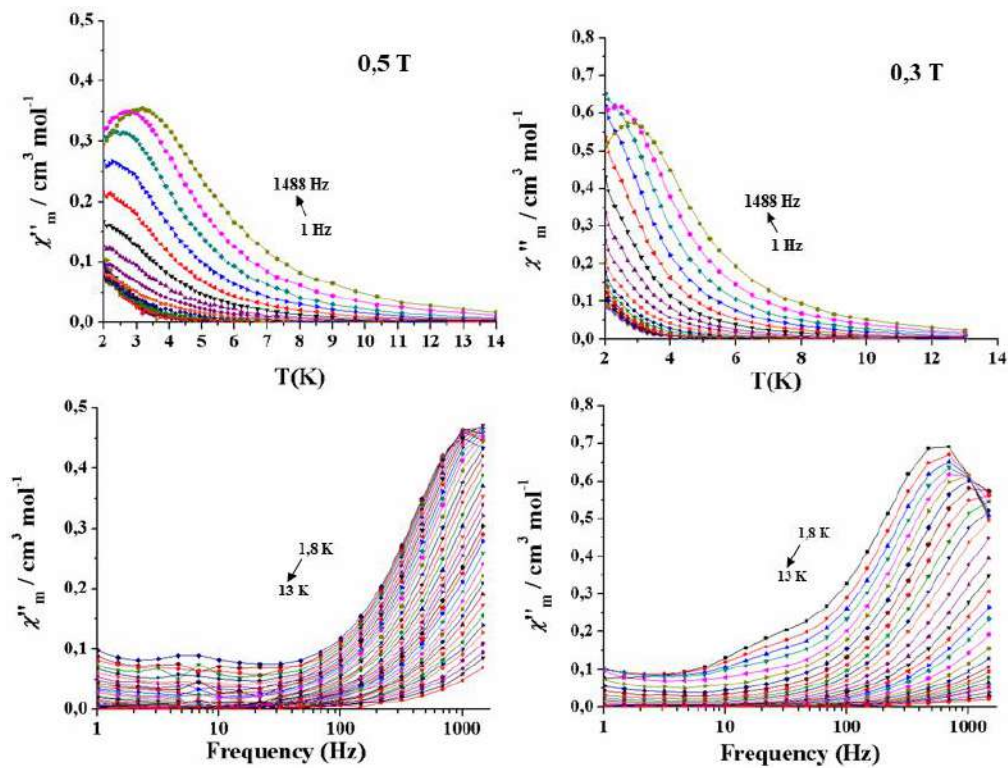Figure 50: Temperature and Frequency dependence of χ''_m for complexes **31** (left) and **32** (right) under an applied field of 0.5 and 0.3 T, respectively.

To continue the analysis of the magnetic data, dynamic properties χ''_m and χ'_m were studied using the generalized Debye model, with the CCfit program, where both susceptibilities are analyzed together with the relaxation rate τ and the α parameter; parameter α defines the broadening of the Argand plots and it is related to the distribution of relaxation times. The data extracted from the fit are represented in the so-called Cole-Cole plots (Fig. 51) and represented in the form of $\ln(\tau)$ vs. $1/T$ (Fig. 52, top). The four compounds show semi-circular plots, indicating the presence of two relaxation processes in accordance with the χ''_m vs. T measurements.

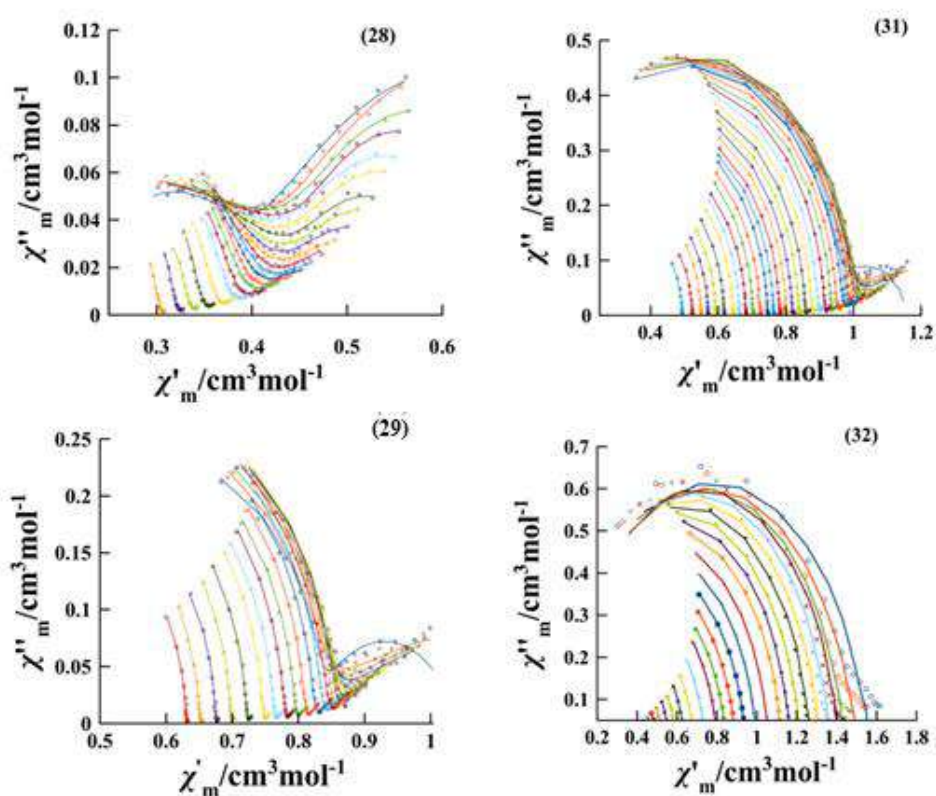Figure 51: Cole-Cole plots for complexes **28**, **29**, **31** and **32**. The solid lines show the best fit of the experimental data.

In general, the occurrence of slow relaxation in transition metal complexes compounds can be attributed to the over-barrier relaxation, the Orbach process. However, in these compounds, that belong to the family of isotropic molecules, this over-barrier process is

not allowed due to the intrinsic nature of a double-well derived from very weak anisotropy and can be thermally overcome even at low temperatures. Also, quantum tunneling is not allowed and thus a combination of Direct plus Raman is proposed following the equation:

$$\tau^{-1} = AT + CT^n$$

where A is an adjustable parameter, T is the temperature, C is a constant parameter; n is treated as an adjustable parameter and can strongly deviate from its theoretical temperature dependence ($n = 7$ and 9 for non-Kramers and Kramers systems, respectively). The presence of two relaxation mechanisms can be also observed in the plot of $\ln(\tau)$ vs $\ln(T)$ (Fig. 52, bottom), where two different slopes appear at low and high temperatures. For complex **32**, the data were not so clear and this tendency could not be observed.
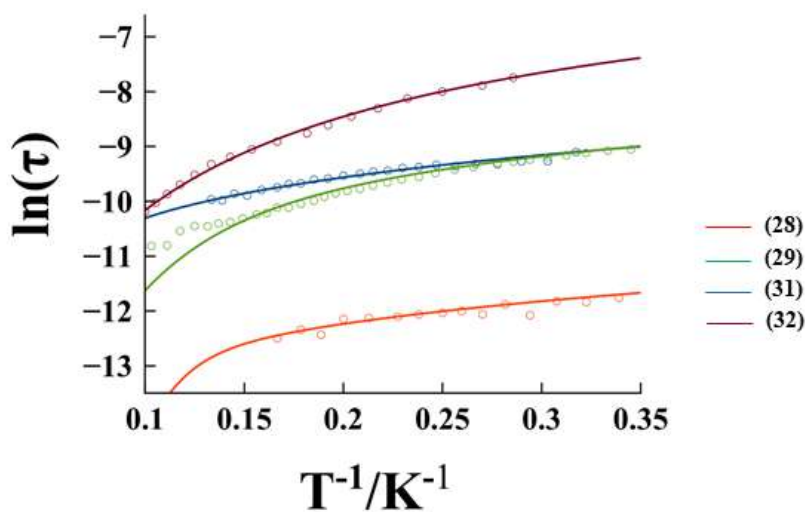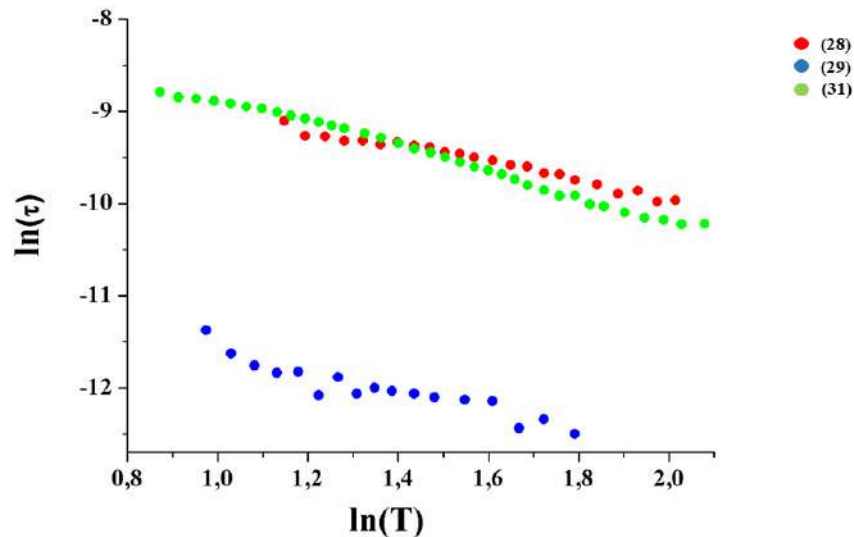
Figure 52: (Top) Plots of ln(τ) vs. 1/T for complexes **28**, **29**, **31** and **32** and (bottom) ln(τ) vs ln(T) for **28**, **29** and **31**.

Best fitting parameters are shown in Table 7. For all the compounds, the low-temperature region follows the direct relaxation while the high-temperature region follows the two phonon Raman process. Among this, from Table 7 it can be observed that Raman coefficient (*n*) for some of the complexes present lower values than the expected ones for Kramer ions; this can be explained because the Raman relaxation can be attributed to the participation of both optical and acoustic phonons.

Table 7: Best fit *C*, *n*, *A* values for complexes **28**, **29**, **31** and **32**.

	C	*n*	*A*
28 (0.5 T)	0.0004	9.38	40877
29 (0.7 T)	0.0032	5.70	2839
31 (0.5 T)	1.343	4.61	2489
32 (0.3 T)	30.363	2.78	560

As mentioned above, complex **30** was studied under three different magnetic fields: 0.15, 0.3 and 0.5 T. This happened because, until today, **30** possesses the highest ground spin state in the family of isotropic SMMs. Temperature and frequency dependence of χ''_m for

the three different fields is shown in Fig. 53. For the three fields there are two different signals; at 0.15 T clear peaks appear bolow 2 K for the lower frequencies, while in the high frequency region the peaks appear around 5 K. As it can be observed by Figure 53 the increase of the field lead to the displacement of the peaks at lower frequencies, where clear maxima can be seen at 0.5 T. Also at this field, there are two clear maxima, one located at 3 and the other at 6 K.
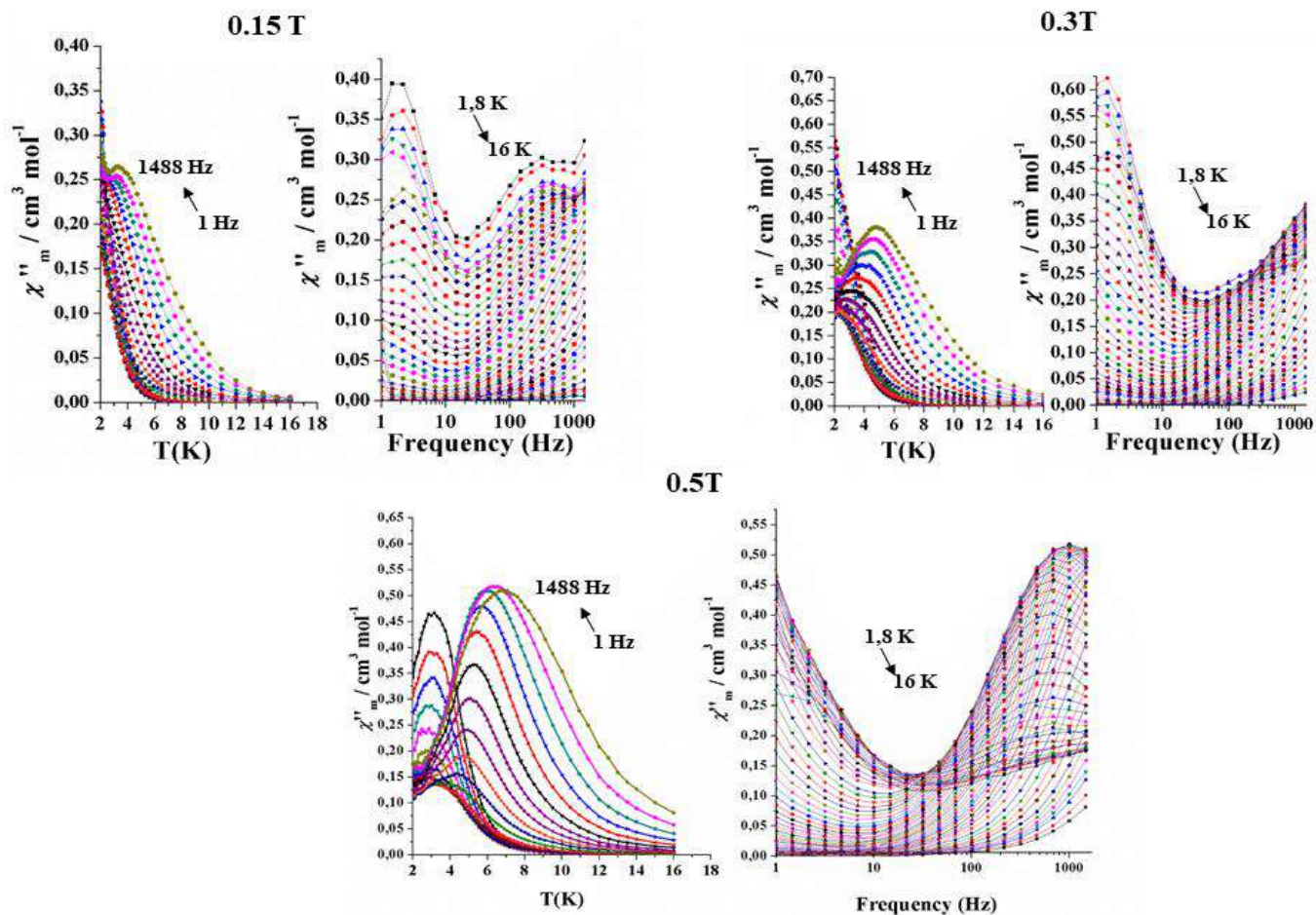
Figure 53: Temperature and frequency dependence of χ''_m for the three different fields for **30**.

To continue the analysis of the magnetic data, dynamic properties χ''_m and χ'_m were studied using the generalized Debye model, fitting with the CCfit program, where both susceptibilities are analyzed together with the relaxation rate τ and the α parameter, as happened with the others complexes of this family. The data extracted from the fit, for each

field, are represented in the Cole-Cole plots (Fig. 54) and represented in the form of $\ln(\tau)$ vs. $1/T$ (Fig. 55).
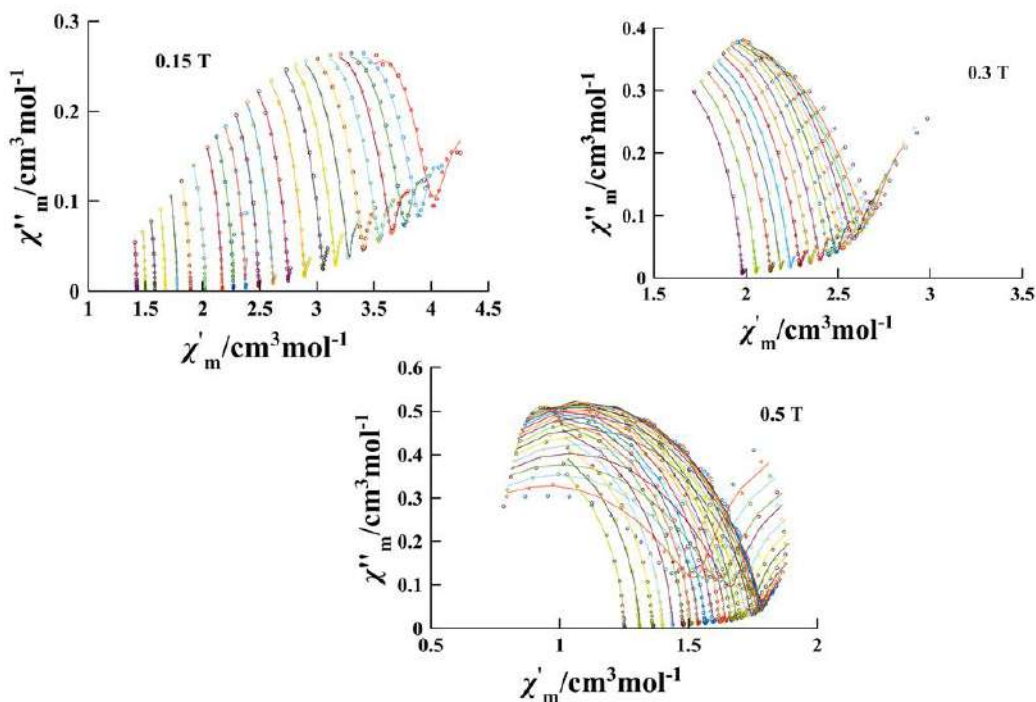
Figure 54: Cole-Cole plots for **30** at the three different magnetic fields.

Fitting of the magnetic data showed that compound **30** follows the Raman and Direct relaxation processes only under the field of 0.5 T. For the lower fields, quantum tunneling is also present as can be observed in Fig. 55 at the low temperature region. Best fitting parameters are shown in Table 8. The equation used in this case was:

$$\tau^{-1} = AT + CT^n + QT$$

In in the representation of $\ln(\tau)$ vs $\ln(T)$ (Fig. 55, bottom), two different slopes appear for the different fields at low and high temperatures, evidencing the presence of Direct and Raman relaxation mechanisms.
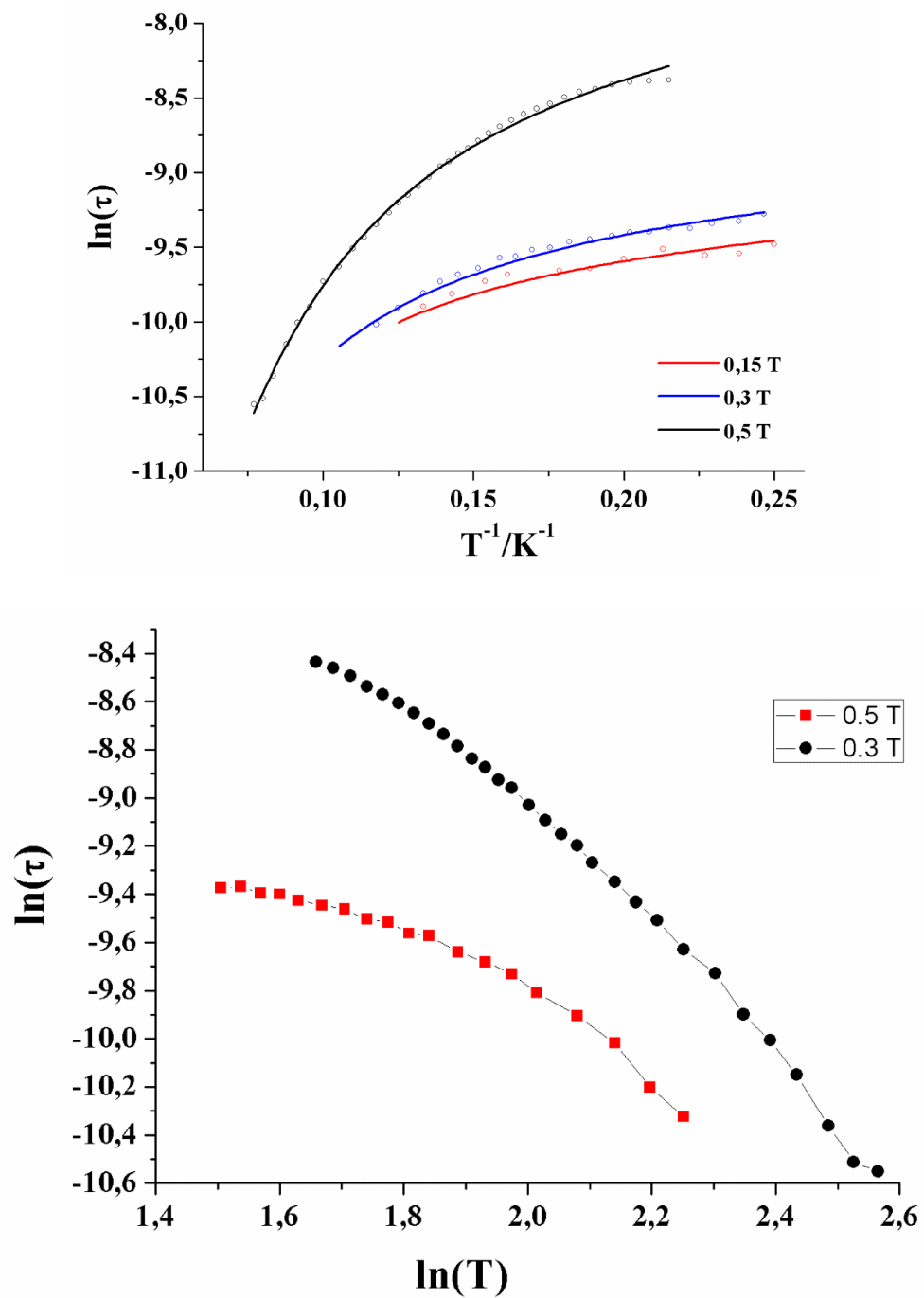
Figure 55: (Top) Plot of ln(τ) vs. 1/T for complex **30** and (bottom) plot of ln(τ) vs ln(T) for the three different fields.

Table 8: Best fit C, n, A and QT values for complex **30**.

	C	n	A	QT
0.15 T	0.134	4.57	$1.72 \cdot 10^3$	$5.83 \cdot 10^3$
0.3 T	1.321	3.72	$4.3 \cdot 10^3$	$4.57 \cdot 10^3$
0.5 T	0.3217	4.46	767	-

4.1.6 EPR Measurements

As mentioned in Introduction of this Chapter, when magnetic anisotropy is very low only EPR can give valuable information about its magnitude. In Fig. 56, there are the EPR spectra for the complexes **30** and **31**. For complex **30**, EPR measurements revealed a very low D value of 0.06 cm^{-1} and a rhombic anisotropy parameter E equal to 0.0189 cm^{-1}, (E/D ratio 0.31). For complex **31**, it was found that $D = 0.205$ cm^{-1} and $E = 0.0073$ cm^{-1}, (E/D ratio 0.035). These small values of D have as consequence the crossing of the m_s sublevels at fields lower than 1 T at which have been performed the ac measurements, Fig. 57, providing a relaxation path for the slow relaxation of the magnetization. It should be noted that the total gaps between the Kramer doublets at zero field take values lower than 2 cm^{-1}, excluding conventional double well approximation.

Also, as can be observed, *E/D* ratio is much higher in complex **30** than in **31**, for which is quasi negligible. From the structures of these two complexes it can be observed that the environment of Mn^{II} in **31** is very axial (Fig. 44), with the four short Mn-O bond distances arranged as an axially elongated MnO$_4$ tetrahedron. In contrast, the coordination sphere for the dimer **30** shows an important geometric distortion, intermediate between trigonal and pentagonal bipyramid in good agreement with the *E/D* ratios that show axial distortion for **31** and high rhombicity for **30**.
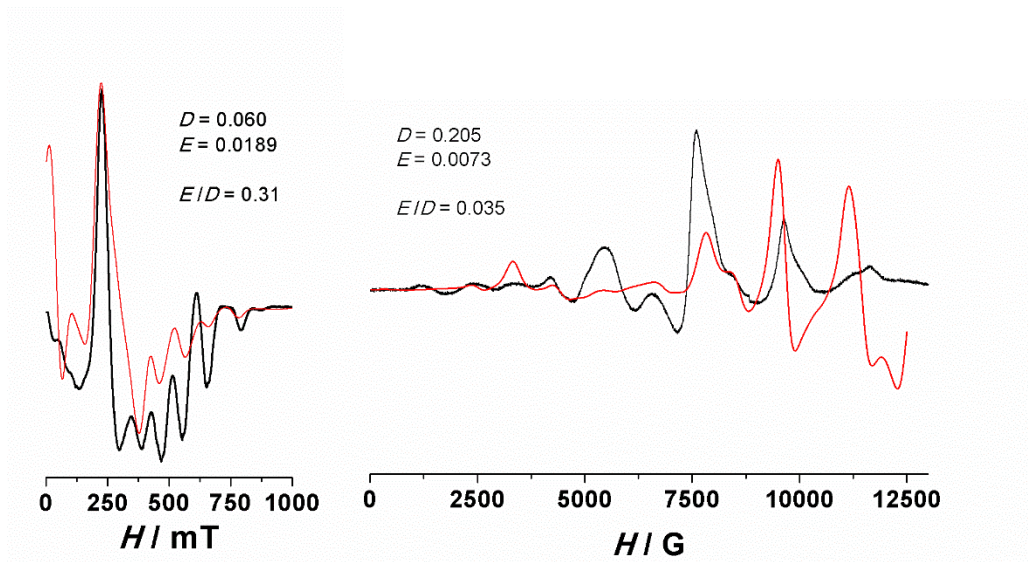
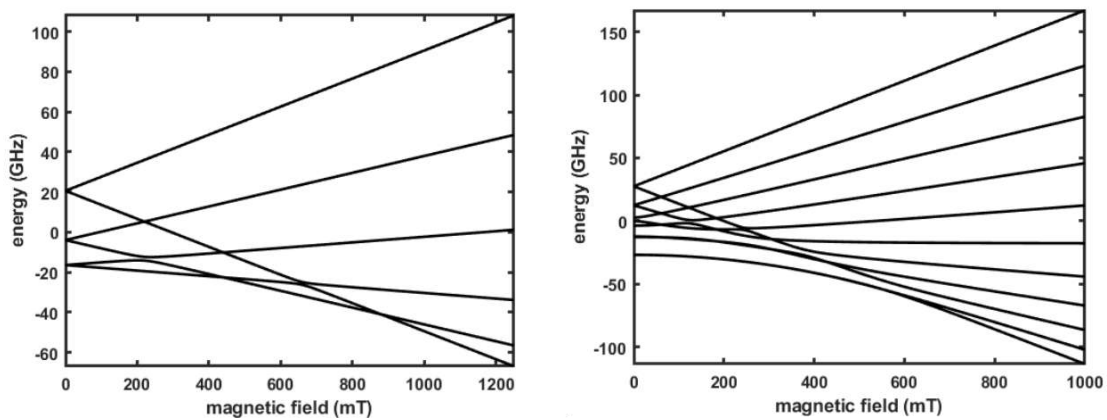Figure 56: EPR spectrum for **30** (left) and **31** (right).

Figure 57: Zeeman interaction for complexes **31** with $S = 5/2$ (left) and **30** with $S = 5$ along z-direction (right).

4.1.7 Conclusion

In this Section, the synthesis and magnetic characterization of six Ni^{II}-Mn^{II} complexes was described. In order to increase the nuclearity of the compounds, azides were used. Complex **30** is a dinuclear compound where the azido ligands bridge the two Mn^{II} cations *via* an end-on coordination mode yielding a ferromagnetic interaction. Thus, **30** has a ground spin state $S = 5$, which is the highest spin presented until now in the family of the isotropic SMMs. Magnetic measurements revealed slow relaxation of magnetization for all the compounds where for **28**-**29** and **31**-**32** Direct and Raman mechanisms are present. The dinuclear compound **30** was measured under three different applied fields; as observed the χ''_m response is clearly field dependent (Fig. 53). Also, the fitting for higher temperatures and frequencies showed increased relaxation times for the larger fields where the common relaxation pathways, Direct plus Raman, are dominating.

Also, compounds **30** and **31** were measured by EPR technique evidencing the presence of very low D values that can favor the slow relaxation of the magnetization *via* the crossing of m_s sublevels at the fields employed for the measurements. An interesting evidence derived from the structure of these compounds and the EPR measurements is that some degree of distortion in the coordination sphere is necessary to induce some anisotropy but the rhombicity plays a minor role in the final properties.

Section 4.2

This Section describes the synthesis, structural and magnetic characterization of seven Mn^{II} complexes with formulas: $[Mn^{II}L10^bCl_2]$ (**33**), $[Mn^{II}L10Br_2]$ (**34**), $[Mn^{II}L11Cl_2]$ (**35**), $[Mn^{II}L11Br_2]$ (**36**), $[Mn^{II}L11(N_3)_2]_n$ (**37**), $[Mn^{II}L12Cl_2]$ (**38**) and $[Mn^{II}L12Br_2]$ (**39**). The ligands that used in this Section are shown in Fig. 58. Additional information and structural details are given in Appendix.

L10

R = CH$_3$: L11
R = H: L10^b

L12
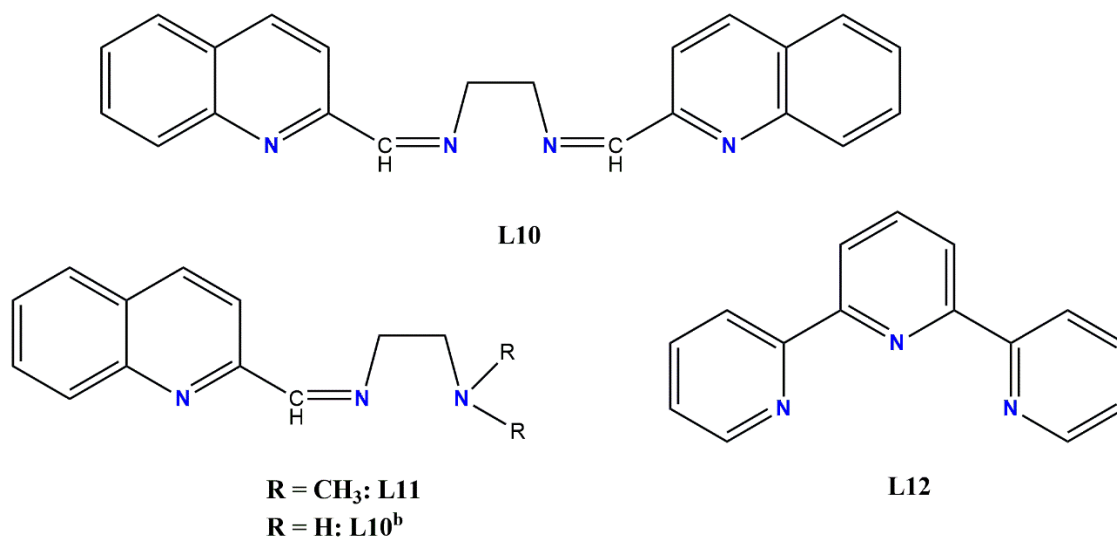
Figure 58: Structural formula of the organic ligands employed in Section **4.2**.

4.2.1 Synthesis

$[Mn^{II}L10^bCl_2]$ (**33**) and $[Mn^{II}L10Br_2]$ (**34**): The synthesis was accomplished by reaction of 2-quinolinecarboxaldehyde (0.8 mmol/0.126 g) and diethylenethylenediamine (0.4 mmol/0.024 g) in 10 ml of MeOH followed by addition of the corresponding manganese salt (0.4 mmol). The resulting mixture was heated in the microwaves furnace for 30 minutes at 80 ˚C, resulting an orange solution. Well-shaped crystals, suitable for X-ray diffraction, were formed by layering with diethylether.

$[Mn^{II}L11Cl_2]$ (**35**) and $[Mn^{II}L11Br_2]$ (**36**): The synthesis was accomplished by reaction of 2-quinolinecarboxaldehyde (0.8 mmol/0.126 g) and *N,N*-dimethylethylenediamine (0.8

mmol/0.071 g) in 10 ml of MeOH followed by addition of the corresponding manganese salt (0.8 mmol). The resulting mixture was heated in the microwaves furnace for 30 minutes at 80 ˚C, resulting a brownish solution. Well-shaped crystals, suitable for X-ray diffraction, were formed by vapor diffusion with Et_2O.

$[Mn^{II}L11(N_3)_3]_n$ (**37**): Complex **37** was synthesized following the same procedure that yielded complexes **35** and **36** but employing NaN_3 (0.6 mmol/0.039 g) and $Mn(ClO_4)_2 \cdot 6H_2O$ (0.4 mmol/0.102g) in the reaction mixture.

$[Mn^{II}L12Cl_2]$ (**38**) and $[Mn^{II}L12Br_2]$ (**39**): The organic L12 is a very common ligand in coordination chemistry; L12 is 2,2';6',2"-terpyridine and was used as received. Compounds **38** and **39** were synthesized following the previously reported methods [82]. To a stirred solution of L12 (0.214 mmol/0.05 g) in 3 mL of MeOH the corresponding manganese salt was added (0.214 mmol). The resulting yellow solution was stirred at room temperature for 10 minutes and filtered. Yellow crystals of the two complexes were grown by slow evaporation of the solvent.

4.2.2 Description of Structures

In this series of complexes three different ligands were used and similar compounds were isolated for each ligand. Thus, the description of structures will be separated in three different families: **33** and **34**, **35**-**47** and finally the complexes **38** and **39**.

Crystallographic data for compounds **33** and **34** are listed in Table A4, Appendix. A partially labeled plot for compound **33** is presented in Fig. 59 while representative angles and bond distances are listed in Table 9.
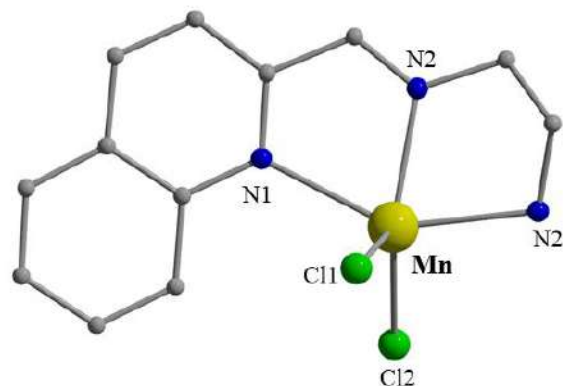
Figure 59: Partially labeled plot of **33**.

The structure of **33** consists of neutral [MnL10^{b}Cl$_2$] molecules without solvent molecules co-crystallized. The ligand is coordinated to the metal center via its N-donors while the two terminal chloro ligands complete the coordination sphere forming a MnCl$_2$N$_3$ chromophore. SHAPE continuous measurements revealed that the coordination environment shows a large deviation for any regular polyhedron and the closest polyhedron for the Mn^{II} cation is a distorted trigonal bipyramid (Fig. A4, Appendix) with CShM = 3.43 (Table A5, Appendix). Also the low bite angle N2-Mn-Cl2 is 136.19 ˚ indicating an axial distortion from the ideal geometry.

Table 9: Selected interatomic distances (Å) and angels (˚) for compound **33**.

Mn-N1	2.3295(11)	N2-Mn-N3	74.62(5)
Mn-N2	2.1938(12)	N2-Mn-N1	72.10(4)
Mn-N3	2.2946(12)	N2-Mn-Cl2	136.19(3)
Mn-Cl1	2.3943(4)	N3-Mn-N1	146.56(4)

An interesting fact in this case, is that the initial ligand used in this synthesis is a double Schiff base derived from the condensation of 2-quinolinecarboxaldehyde with ehtylenediamine in molar ratio 1:2. Surprisingly, when the metal coordinates to the ligand, the later becomes partially hydrolized and as a result the ligand that appears in the complex is a single Schiff base were the one of the two N of ethylenediamine are condensed with carbonyl group. The bond distance C-N2 is equal to 1.47 Å, indicating the presence of a

single bond. Several trials were made in order to obtain the complex containing the original L10 ligand, but the result was always the isolation of **33**.

For complex **34** a partially labeled plot is shown in Figure 60, while selected angles and bond distances are listed in Table 10. Complex **34** consists of neutral [MnL10Br$_2$] molecules. The organic ligand L10 is coordinated to the cation via the N-donors while the coordination sphere is completed by two bromo ligands. Thus, the chromophore that is formed is a MnN$_4$Br$_2$. In this case the ligand did not hydrolyzed and the Mn^{II} cation is located in the center of a distorted trigonal prism (Fig. A4, Appendix), as indicated by continuous SHAPE measurements (Table A6, Appendix). Regarding the calculation for the polyhedron from the value of CShM = 7.80 indicates a very big distortion from any ideal geometry.

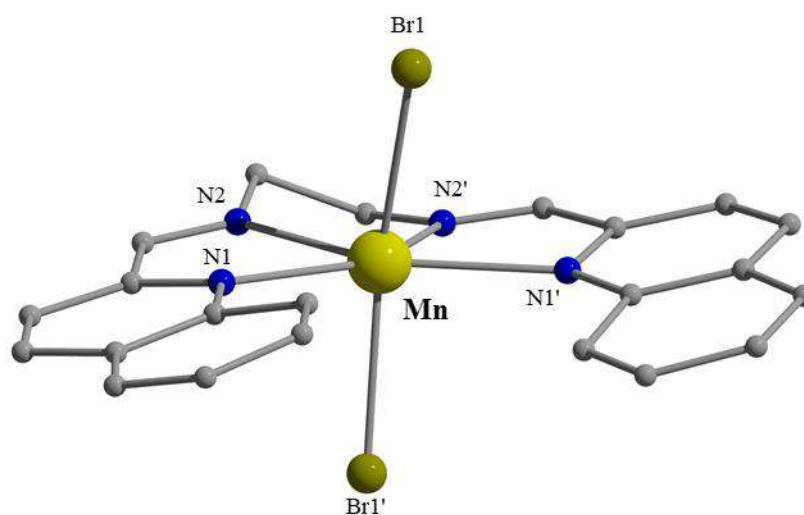Figure 60: Partially labeled plot for **34**.

As mentioned above, the coordination polyhedron for the Mn^{II} cation is a distorted trigonal prism. As can be seen from Table 10, the bite angle N1-Mn-Br1is larger and N2-Mn-N1' is lower than the expected ones; for an ideal trigonal prism this angles should be around 81.8˚ and 135.6˚, respectively. The deviation of these angles induce the distortion and this

is happening due to flexibility of the organic ligand L10 and the coordination requirements of the bromo ligands.

Table 10: Selected interatomic distances (Å) and angels (°) for compound **34**.

Mn-N1	2.3219(12)	N2-Mn-N1'	143.15(5)
Mn-N2	2.2432(13)	N2-Mn-Br1	96.81(3)
Mn-Br1	2.6264(2)	N1-Mn-Br1	83.50(3)

The second family of the series consist of complexes **35**, **36** and **37**. The two first complexes have similar structures with the only difference being the substitution of chloro with bromo ligands. Thus, the description of structure will be done for **35** and only some differences between them two will be mentioned. Compound **37** is a 1D polymer and will be described with details.

Partially labeled plots of **35** and **36** are shown in Fig. 61. Crystallographic data and refinement details are listed in Table A7, Appendix.
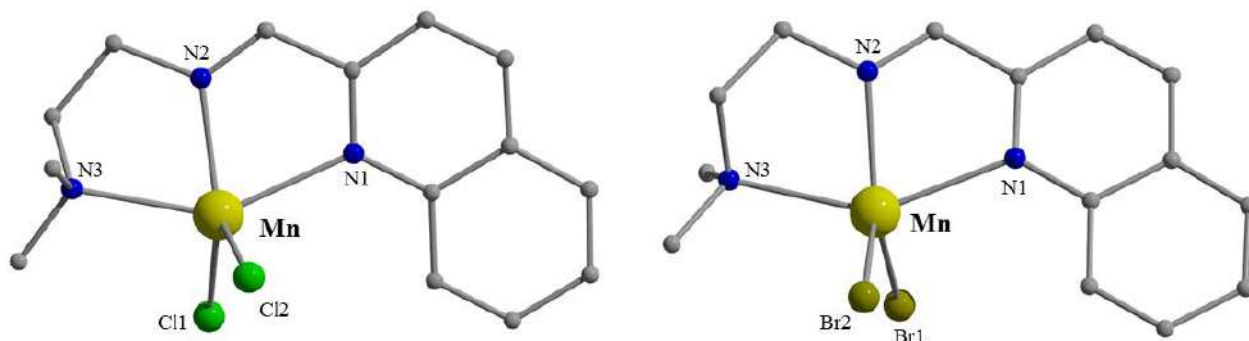
Figure 61: Partially labeled plots of **35** (left) and **36** (right).

Both complexes crystallize in the triclinic space group *P* -1. Compound **35** consists of neutral [MnL11Cl$_2$] molecules. Once more time, the coordination sphere of Mn^{II} cation is fulfilled by four N-donor atoms from the ligand and two terminal chloro ligands. In this case the coordination number is equal to five and thus the ideal polyhedron is a trigonal bipyramid (Fig. A5, Appendix), as indicated be continuous SHAPE measurements (Table

A8, Appendix). Selected interatomic angles and distances are shown in Tables 11 and 12 for compounds **35** and **36**, respectively.

Table 11: Selected interatomic distances (Å) and angels (˚) for compound **35**.

Mn-N1	2.3352(8)	N2-Mn-Cl1	127.25(2)
Mn-N2	2.1960(8)	N1-Mn-Cl2	121.18(2)
Mn-N3	2.3490(8)	Cl1-Mn-Cl2	111.573(10)
Mn-Cl1	2.3460(3)	N3-Mn-N1	145.03(3)

Table 12: Selected interatomic distances (Å) and angels (˚) for compound **36**.

Mn-N1	2.3292(10)	N2-Mn-Br1	126.67(3)
Mn-N2	2.1862(10)	N1-Mn-Br2	93.06(3)
Mn-N3	2.3530(10)	Br1-Mn-Br2	112.480(10)
Mn-Br1	2.4891(3)	N3-Mn-N1	145.32(4)

Molecular overlay structures of the two compounds are shown in Fig. 62. Due to the fact that both structures were measured in the same temperature, their structural deviation could be explained by the different halogen that act as terminal ligand. Compounds **35** and **36** present almost equal Mn-N bond distances. However, the larger N3-Mn-N1 angle in **36** by approximately 0.3˚ compared to **35** leads to a more bending structure for **35**. Also, the different size of the halogens generates larger X1-Mn-X2 angles for **36** due to steric hindrance.
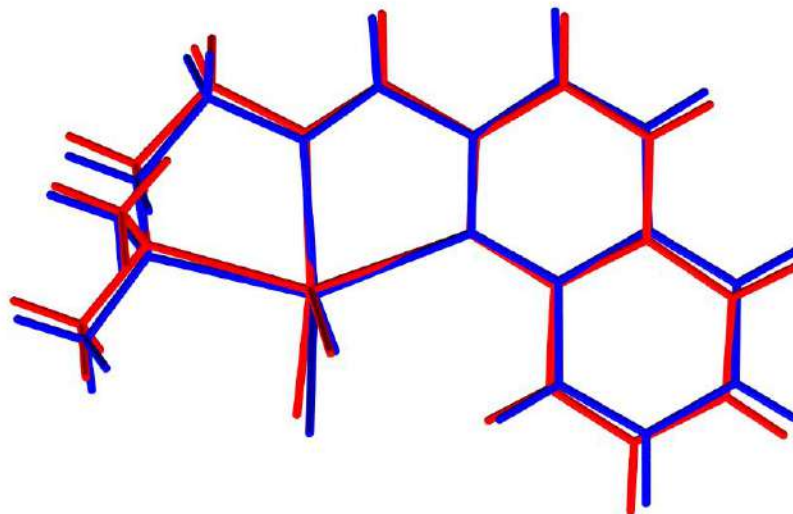
Figure 62: Molecular overlay structures of **35** (blue) and **36** (red). Both structures were measured at 100 K.

Wanting to increase the study of this family, several trials had been done in order to synthesize the iodide analogue. However, despite the plethora of solvents and reactants that used always the Mn cation was oxidized from +2 to +3 oxidation state and very dark solutions were obtained. Alternatively, azides were used in this case because, as pseudo-halides, they have similar chemistry, they prevented the oxidation of manganese in higher oxidation states and probably they could increase the nuclearity of the compounds. Finally, the use of sodium azides in the reaction mixture led to the isolation of a 1D polymer whose asymmetric unit structure is shown in Fig. 63.
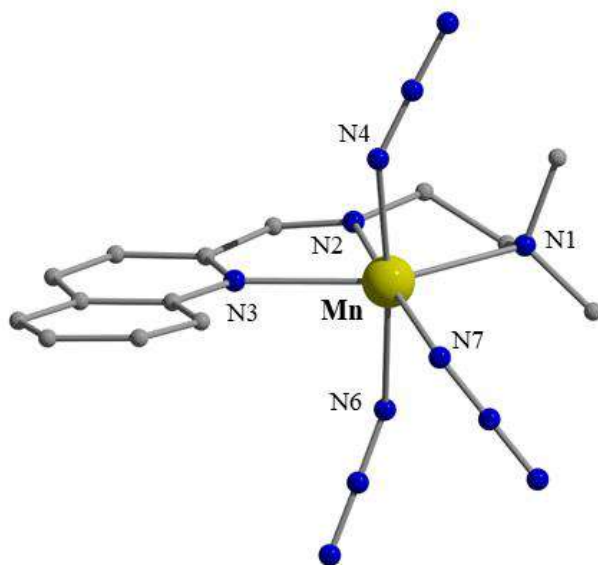
Figure 63: Partially labeled plot of asymmetric unit of **37**.

The asymmetric unit of **37** consists of mononuclear [MnL11(N_3)$_3$] units where the ligand binds the metal via its four N-donor atoms forming a MnN$_6$ chromophore. The two azides are presenting two different coordination modes; two azido ligands are terminal whereas the other acts as a bridge between the Mn^{II} cations in an end-to-end coordination mode leading to a zig-zag configuration (Fig. 64). Selected interatomic bond distances and angles are listed in Table 13.
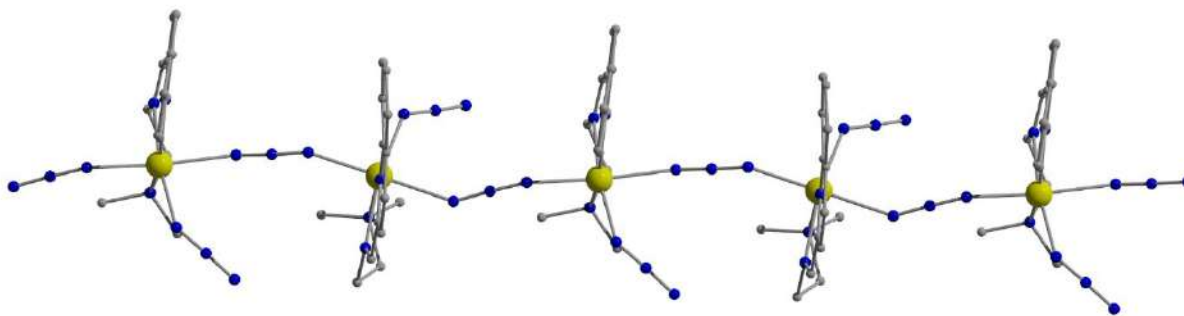
Figure 64: Zig-zag configuration of chain in **37**.

The Mn^{II} cation is located in the center of a distorted octahedron (Fig. A6, Appendix) as indicated by continuous SHAPE measurements (Table A9, Appendix). In this octahedron, the axial ligands are slightly bended since the angle N4-Mn-N6 is lower than 180° whereas

the two equatorial *cis* ligands are forming an angle equal to 167.2˚. The two *trans* N-atoms are forming angles of 98˚ and 88.9˚ yielding an overall distortion of the geometry.

Table 13: Selected interatomic distances (Å) and angels (˚) for compound **37**.

| Mn-N1	2.366	N4-Mn-N6	174.52
Mn-N2	2.217	N2-Mn-N7	167.27
Mn-N3	2.332	N6-Mn-N7	87.89
Mn-N7	2.119	N1-Mn-N7	98.05
Mn-N4	2.184	N1-Mn-N3	72.12

The last two complexes, **38** and **39**, are previously reported in the literature and their structure has been described elsewhere [82]. For these reason, the compounds were prepared as powders and XRDP spectra were used in order to clarify their identity. Comparison of the theoretical spectra of the two compounds and the experimental data led to the same spectra, proving the purity of the samples. In Fig. 65 appears the spectra comparison of the theoretical (black spectrum) and experimental data (red spectrum) for **38**. As can be observed the two spectra are similar and thus the reproduced powder corresponds to the absolute product. Also, the comparison of the spectra for **38** and **39** prove the isostructurality of the two compounds (Fig. 66).
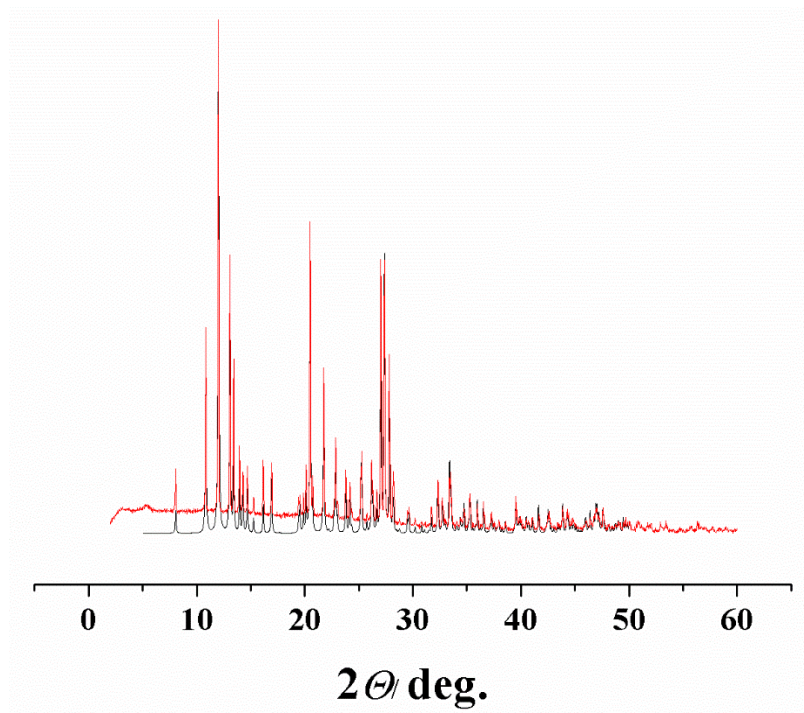
Figure 65: Comparison of the XRDP spectra of theoretical (black line) and experimental (red line) for **38**.
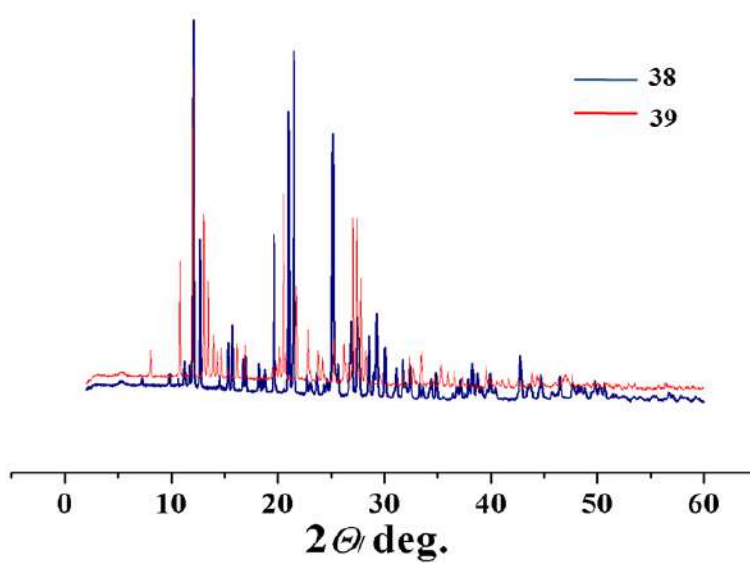
Figure 66: Comparison of the XRDP spectra or **38** and **39**.

4.2.3 Magnetic Susceptibility Measurements

The analysis of the dc magnetic measurements for the above mentioned compounds will follow the same order as in Section **4.2.2**; firstly, the magnetism of **35**-**37** will be mentioned and the magnetism of **38** and **39** will be mentioned next. Alternate current measurements will be discussed for the complexes that show ac response. For complexes **33** and **34** magnetic studies are still on-going.

Direct current measurements for **35**-**37** carried out. For **35** magnetic susceptibility measurements (Fig. 67) in the range of 300-2 K revealed that the room temperature value of $\chi_M T$ is 4.35 $cm^3 \cdot mol \cdot K^{-1}$ close to the expected one (4.375 $cm^3 \cdot mol^{-1} \cdot K$) and below 25 K $\chi_M T$ a decrease of the susceptibility is observed. Fit of the experimental data revealed a *g* = 1.97. Reduced magnetization measurements shown quasi-superimposable plots (Fig. A7, Appendix) indicating the presence of a weak anisotropy.
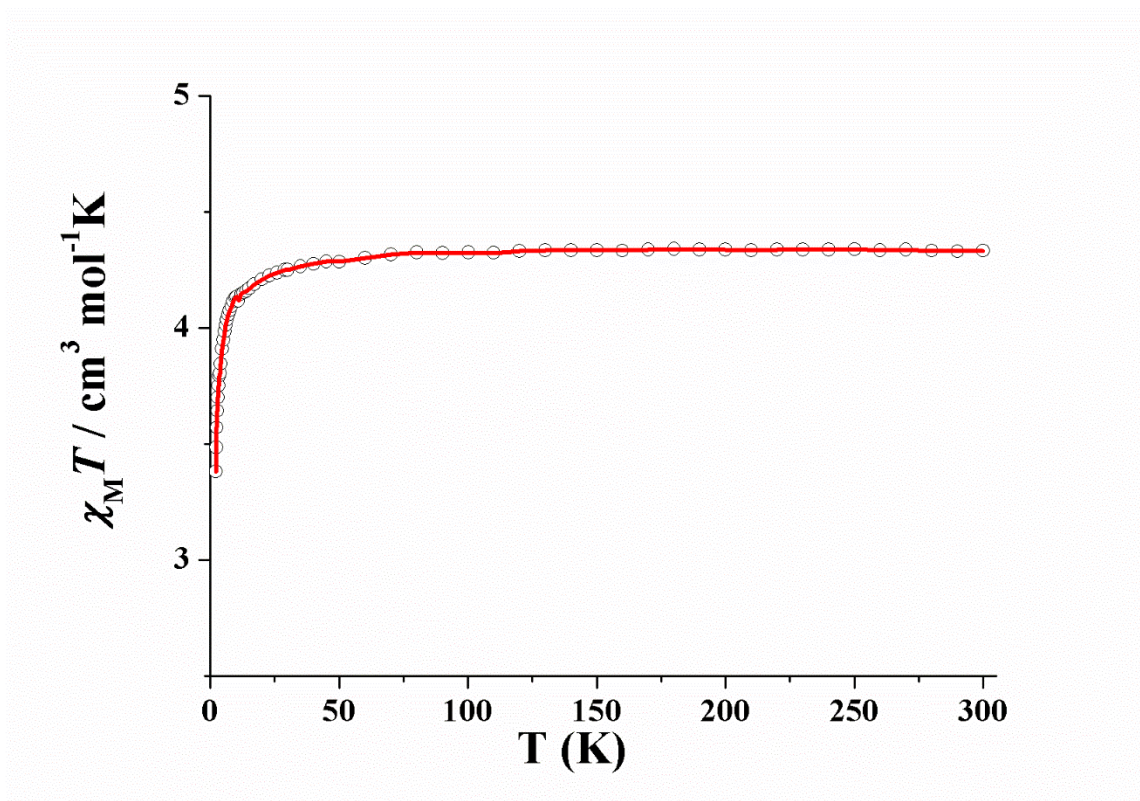
Figure 67: Plot of $\chi_M T$ for complex **35**.

Complex **36** shows similar behavior with **35**. In this case the $\chi_M T$ value is slightly lower than the expected one, having a value of 4.18 cm^3·mol^{-1}·K, while it shows a more intense decrease below 25 K. Fit of the magnetic data gave a g = 1.98. However, reduced magnetization plots revealed a different behavior for **36**. The non-superimposable plots (Fig. A7, Appendix) indicate the presence of D and higher in value than **35**.
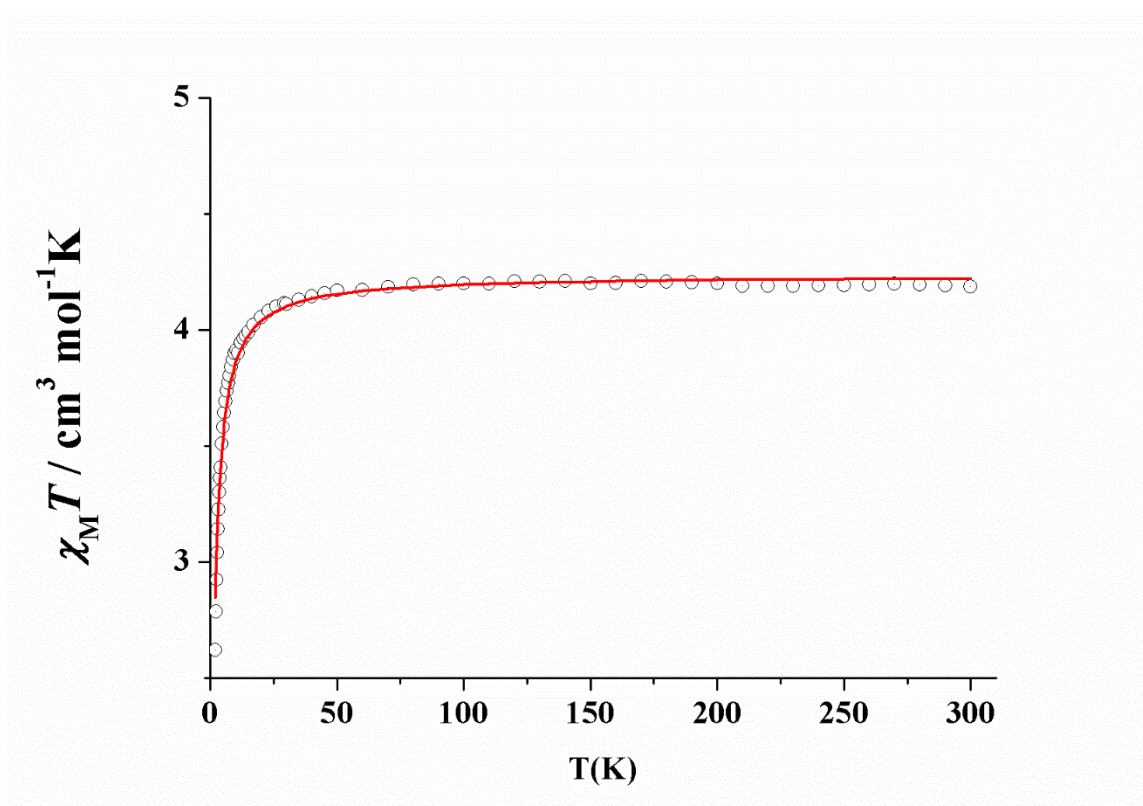
Figure 68: Plot of $\chi_M T$ for complex **36**.

In the case of **37** the $\chi_M T$ is lower than the expected value at room temperature, having a value of 3.9 cm^3·mol^{-1}·K. Lowering the temperature, the susceptibility decreases due to the antiferromagnetic exchange interaction between the Mn^{II} cations promoted by the end-to-end coordination mode of the azido ligands. The magnitude of the interaction J is equal to -2.01 cm^{-1} and g = 2.00. At temperature of 2 K, the susceptibility is zero, proving that the ground state of the complex is diamagnetic. This fact is confirmed by the magnetization plot in Fig. 69, left.
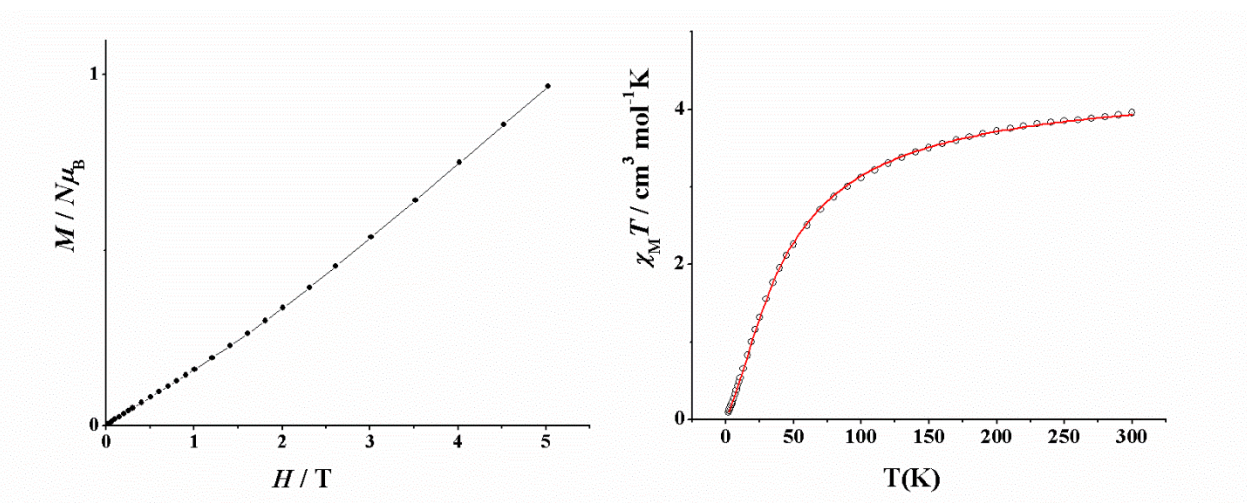
Figure 69: Magnetization (left) and χ_MT (right) plots for **37**.

Complex **38** shows similar magnetic behavior with complex **35**. The χ_MT value at room temperature is 4.35 cm³·mol⁻¹·K and remains constant until 25 K (Fig. 70). Below this temperature the susceptibility shows a slight decrease reaching a minimum value of 3.8 cm³·mol⁻¹·K. Fit of the data revealed a g = 1.98. Also, the superimposable plots in the reduced magnetization imply the presence of very low or negligible anisotropy (Fig. A8, Appendix). The χ_MT plot for **39** show similar behavior with **38** the values are quite lower (Fig. A9, Appendix); at room temperature the χ_MT product takes the value of 3.23 cm³·mol⁻¹·K and at lower temperatures reaches a minimum of 2.6 cm³·mol⁻¹·K.
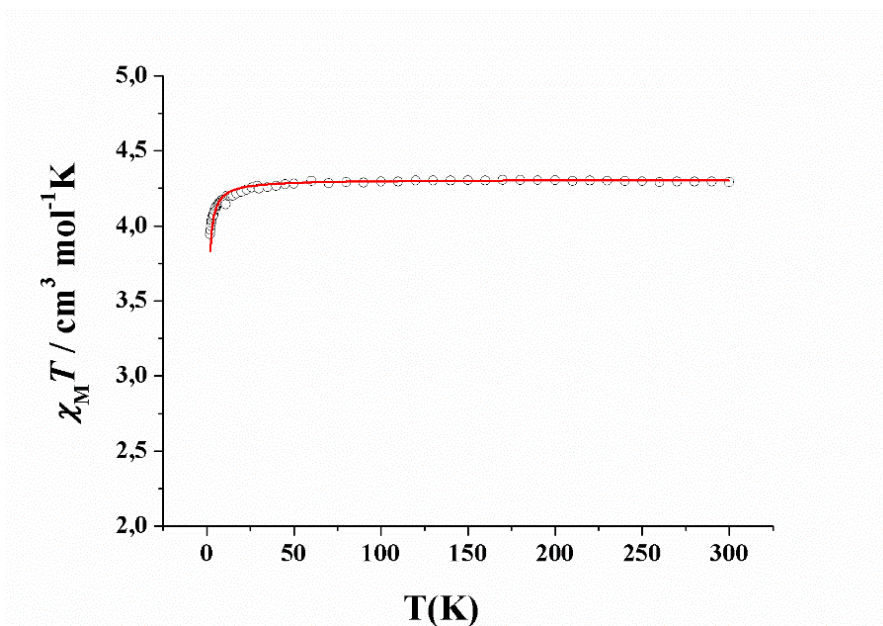
Figure 70: χ_MT plot for **38**.

Interestingly, the reduced magnetization plots (Fig. 71) show quasi-superimposable plots indicating the presence of low magnetic anisotropy. Comparing with the case of **38**, complex **39** shows higher magnetic anisotropy than the chloro derivative but still the magnitude of D remains low.
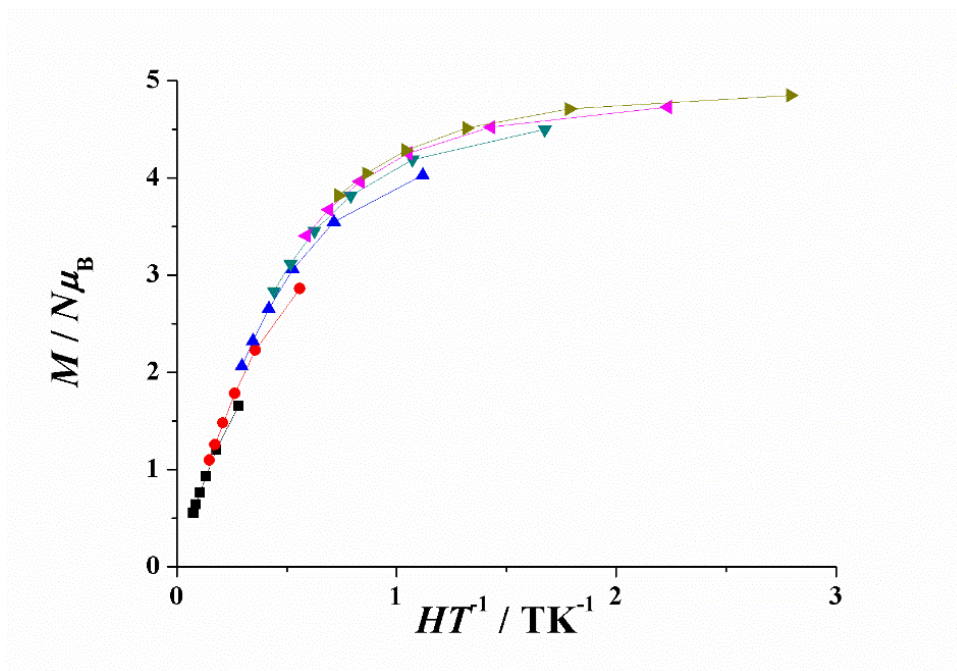
Figure 71: Reduced magnetization plot for **39**.

Dynamic magnetic measurements were carried out for all of the compounds. No ac signal were observed in the absence of an applied magnetic field, whereas for compounds **35** and **38** ac signals appeared under a field of 0.5 T.

Ac measurements were performed in the range of frewuency 1-1488 Hz, and at temperatures 1.8-16 K. For **35**, two clear peaks both frequency and temperature appeared. Thus, at least, two relaxation procceses are present; one low-frequency (LF) and one high frequency (HF). For the LF region maxima of χ''_m appear at temperatues below 4 K, while in the HF region maxima are observed at 6 K (Fig. 72).
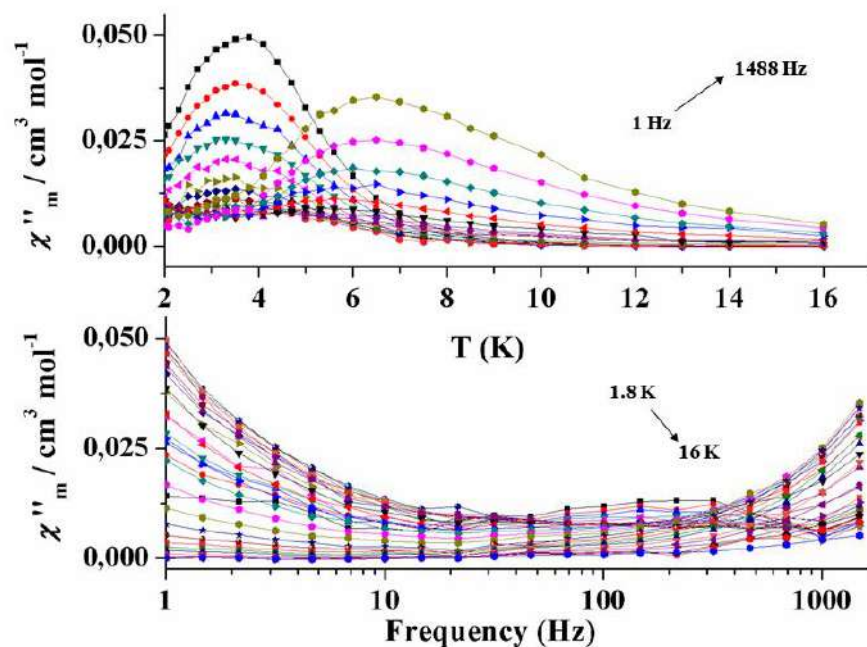
Figure 72: Temperature (top) and frequency (bottom) dependence of χ''_m for **35**.

Argand plots for the complex **35** were built in the range of 3-11 K (Fig. 73). Fitting of the experimental data was performed using the CCFit program. Relaxation times that extracted from the fit of Argand plots, using the generalized Debye model, are represented in the form of $\ln(\tau)$ vs T^{-1} (Fig. 74, top).
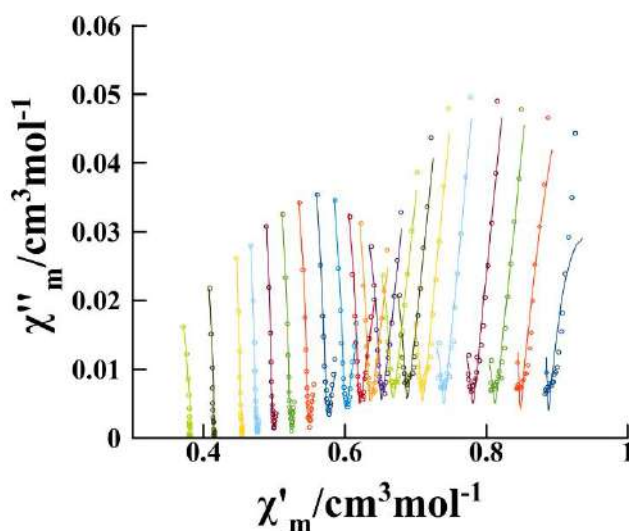
Figure 73: Fitted Argand plots for **35**.

The relaxation times for **35** were fitted with two relaxation procceses: Direct procces for low temperatures and Raman for higher temperatues. The presence of two relaxations is indicated by the presence of two different slopes in the plot of ln(τ) vs ln(T) (Fig. 74, bottom). The equation that used for the fit is:

$$\tau^{-1} = AT + CT^n$$

The first term of the equation correspond to Direct procces whereas the second correspond to Raman. The parameters that determined were: $A = 4126$, $C = 0.005$ and $n = 6.38$.
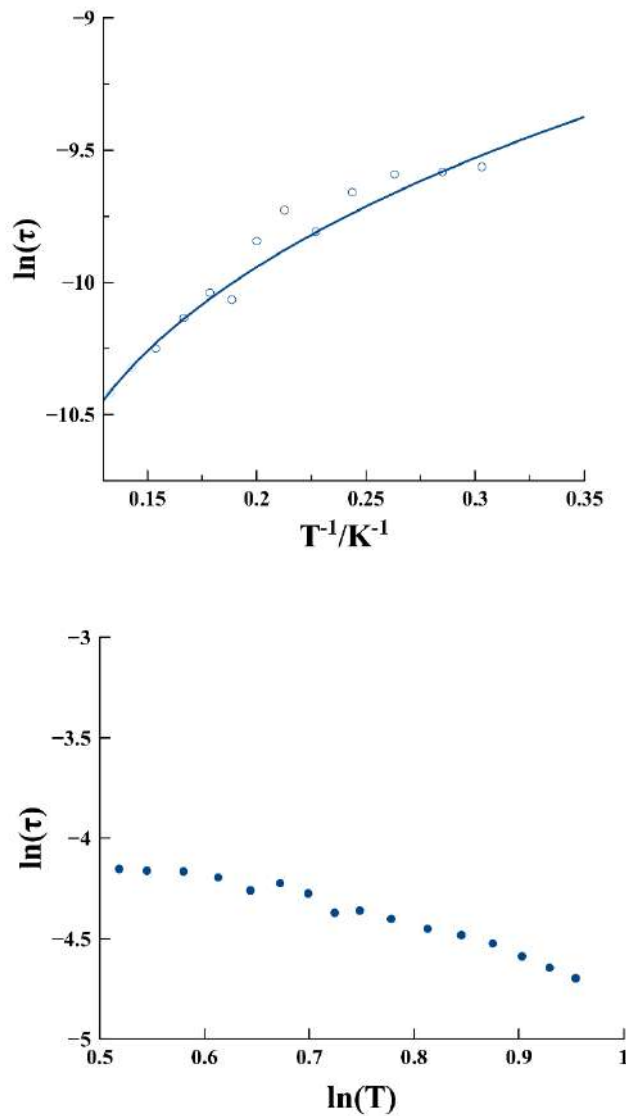
Figure 74: (Top) Plot of ln(τ) vs T^{-1} for **35** and (bottom) plot of ln(τ) vs ln(T).

Alternate current measurements were carried out for **38** in the range of frequencies 1-1488 Hz and between 2-20 K (Fig. 75). Also in this case, there two signals which show temperature and frequency dependence. There are clear maxima in low and high frequency region indicating the presence of two relaxation processes. The low frequency region shows peaks below 5 K whereas for higher frequencies the peak is positioned at 6 K.
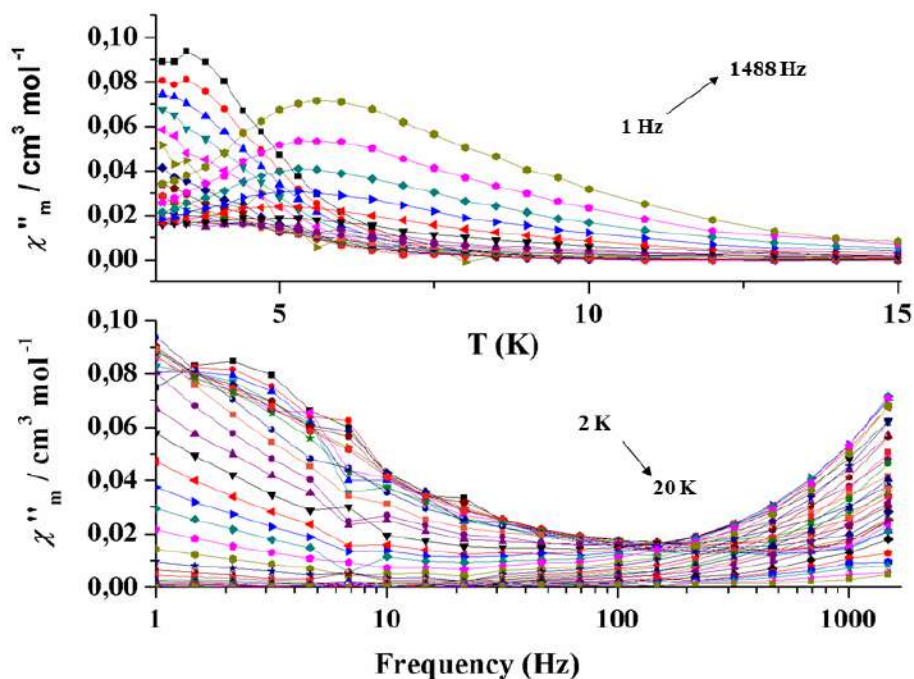
Figure 75: Temperature (top) and frequency (bottom) dependence of χ''_m for **38**.

As happened with complex **35**, complex **38** show quasi-semicircles and tails in the high frequency region. In Figure 76, appear the fitted Argand plots for compound **38** in the temperature range of 2.7-11 K. Fit of the data were performed using the CCFit program and the extracted relaxation times are represented in the form of $\ln(\tau)$ vs T^{-1} (Fig. 77). In this case, the plot $\ln(\tau)$ vs $\ln(T)$ is not indicative, as a clear tendency cannot be observed.
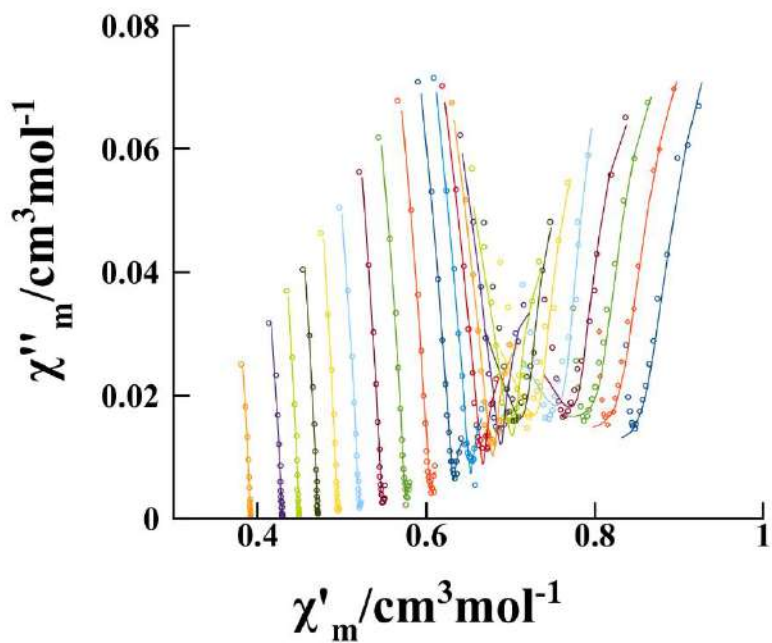
Figure 76: Argand plot for **38**.

Also in this case, the relaxation time was fitted with the same processes as **38** and at this time the parameters were: $C = 0.026$, $n = 2.87$ and $A = 2.163$.
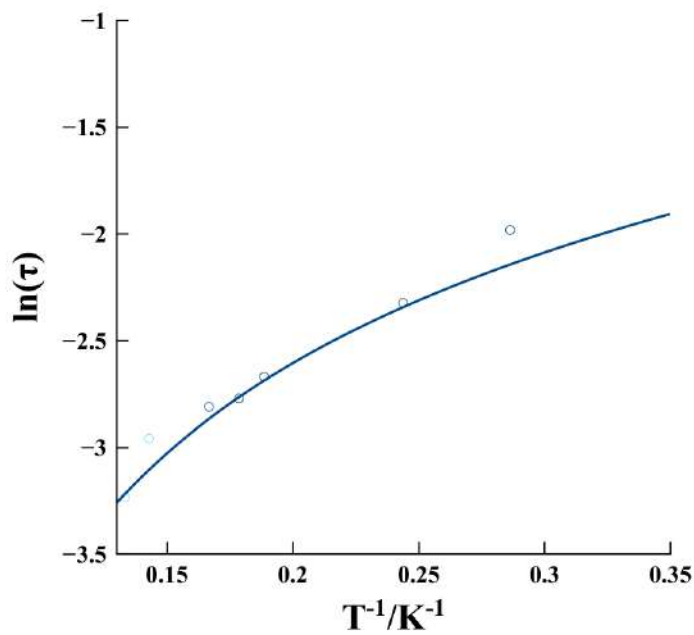
Figure 77: $\ln(\tau)$ vs T^{-1} plot for **38**.

Complexes **35** and **38** belong to the family of isotropic Single-Ion Magnets, where the over-barrier relaxation, the so-called Orbach relaxation, is not allowed due to the intrinsic nature of the double-well potential derived from relatively low spins and very low D values, which can be overcome even at 4 K. Most of the cases the relaxation is attributed to a combination of Direct + Raman or Raman + QTM relaxation mechanisms. In this case, the low-temperature region is governed by the Direct relaxation while the high-temperature region follows the two-phonon Raman process. As can be observed, the Raman coefficient (n) for the two complexes is lower than the expected for the Kramer ions. This feature can be explained as Raman relaxation can be attributed to the participation of optical phonons [83].

4.2.4 EPR Measurements

The two pair of complexes, **35**-**36** and **38**-**39** are mononuclear Mn^{II} complexes with strongly distorted environments and same ligands; L11 for the first pair and L12 for the second. The interesting observation is that the complexes with Cl^- ligands show relaxation of the magnetization and the complexes with Br^- do not.

In Figure 78 there are the EPR spectra of complexes **35** and **36**. For **35** EPR measurements revealed a relatively strong magnetic anisotropy parameter D equal to 0.305 cm^{-1} and an E parameter equal to 0.0937 ($E/D = 0.31$). For **36** the values were found to be $D = 0.539$ cm^{-1}, $E = 0.184$ ($E/D = 0.34$); as can be observed the D value for the bromo derivative is larger than the chloro, in agreement with the reduced magentization plots. In the case of **36** the spectrum consist of a broad line; thus in order to reproduce the main signal which is responsible for the spectrum, a simulation with a narrow linewidth were carried out (Fig. 78, blue line).

Due to the fact that these two complexes are built with the same ligand, the crystal field promoted by the ligands can be excluded as a decisive factor for magnetic relaxation, and instead it can be concluded that the low values of D are responsible for the slow relaxation of magnetization. These low D values can induce m_s crossing that provide relaxation, whereas while the D increases in value the m_s states ½, 3/2 and 5/2 are enough separated to avoid the m_s crossings and it is too low to create an effective double well.
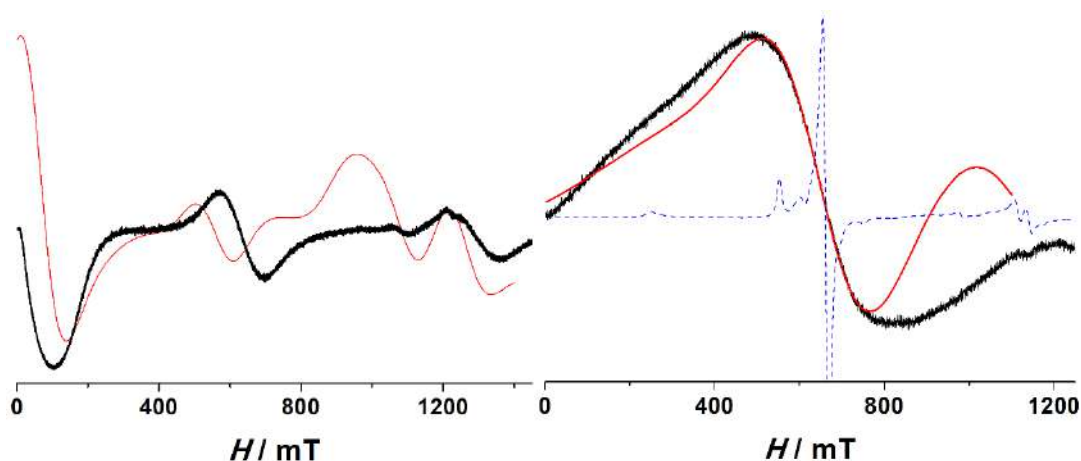
Figure 78: (Left) EPR spectrum for complex **35** and (right) EPR spectrum for complex **36**. Black lines correspond to experimental data; red lines correspond to the fitting and the blue line for spectrum of **36** correspond to the a spectrum that simulated with a narrow linewidth.

4.2.5 Conclusion

At this Section three different families of compounds were discussed. The first family, contains two Mn^{II} compounds, complexes **33** and **34**. The two complexes were synthesized with the same organic ligand, L10, but in the case of **33** the ligand has been hydrolyzed and appears as a single Schiff base resulting a penta-coordinated environment around the Mn^{II} cation. While in **34** the ligand was found to be a double Schiff base, yielding a coordination number equal to six. For these complexes the magnetic measurements are still on-going.

The second family, contains two isostructural complexes, **35** and **36**, and the complex **37** which is a 1D coordination polymer. In compound **37** the antiferromagnetic interaction promoted by the end-to-end azido bridges gives a diamagnetic ground state, whereas the other two complexes were studied by means of alternate current measurements. Complex **35** show clear out-of-phase maxima. In contrast, **36** despite the fact that the reduced magnetization plots are non-superimposable ac signals did not appear. Same behavior was noticed also for the two complexes built with ligand L12, **38** and **39**. As a result a clear tendency is observed: the compounds with chloro ligands show ac signals whereas the

compounds with bromo ligands do not. This fact suggests that low D values are relevant for the presence of magnetic relaxation.

Thus, this Section provide a first experimental evidence that the decisive factor that governs the relaxation in these kind of systems is the low value of magnetic anisotropy.

Section 4.3

In the final Section of this Chapter, the third family of Mn^{II} compounds is described. The mononuclear complexes are: $[Mn^{II}(L13)(X)_2]$ where X = Cl⁻ (**40RR** and **40SS**), Br⁻ (**41SS**), I⁻(**42SS**) and NCS⁻ (**43SS**), where the organic ligand that employed in this Section is depicted in Fig. 79. This ligand was chosen due to the fact that it can induce distorted environment around the Mn^{II} cation; the steric hindrance between the protons of carbon atoms C2-C2' lead to a non-planar arrangement (Fig. 79, bottom) of the ligand and thus a distorted geometry is ensured. Additional crystallographic and spectroscopic data are given in Appendix.
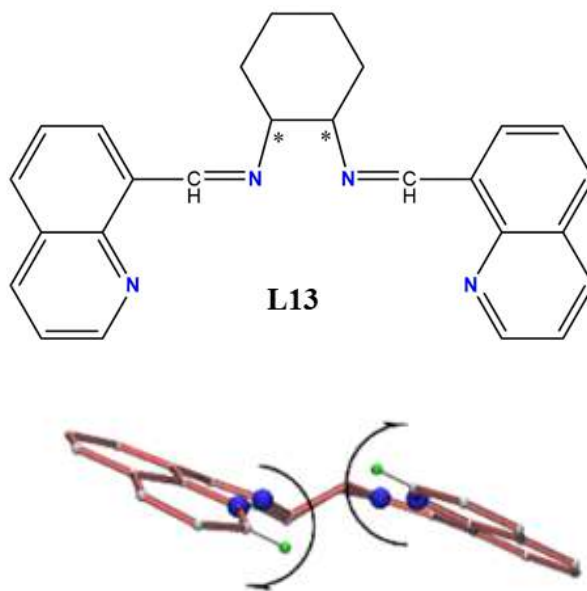
Figure 79: (Top) Schiff base L13 employed in this Chapter and (bottom) non-planar arrangement induced by the protons on C2-C2'.

4.3.1 Synthesis

$[Mn^{II}(L13)(X)_2]$, X = Cl⁻ (**40RR** and **40SS**), Br⁻ (**41SS**), I⁻(**42SS**): The four complexes were prepared following the same procedure: 0.4 mmol (0.062 g) of 8-quinolylaldehyde,

0.2 mmol (0.225 g) of (1*SS*)- or (1*RR*)-1,2-cyclohexanediamine and 0.2 mmol of the corresponding manganese halide (0.039 g for MnCl$_2$·4H$_2$O, 0.057 g for MnBr$_2$·4H$_2$O and 0.062 g for MnI$_2$) were dissolved in 10 mL of methanol and heated at 80ºC for 20 minutes in a microwaves furnace. The yellowish-orange solutions were layered with Et$_2$O to give well-formed crystals in three days.

[Mn^{II}(L13)(NCS)$_2$] (**43SS**): 0.4 mmol (0.062 g) of 8-quinolylaldehyde, 0.2 mmol (0.225 g) of (1*SS*)-1,2-cyclohexanediamine, 0.2 mmol (0.072 g) of Mn(ClO$_4$)$_2$·6H$_2$O and 0.2 mmols (0.016 g) of sodium thiocyanate were solved in 10 mL of methanol and heated for 30 minutes in a microwaves furnace at 80ºC. The resulting orange solution was layered with diethyl ether to produce crystals suitable for X-ray diffraction in a week.

4.3.2 Description of Structures

The complexes **40**, **42** and **43** were characterized by means of X-ray diffraction. Crystallographic data and refinement details are listed in Table A10, Appendix. Partially labeled plot of the structure of **40** is shown in Fig. 80, whereas representative interatomic bond distances and angles are listed in Table 14.
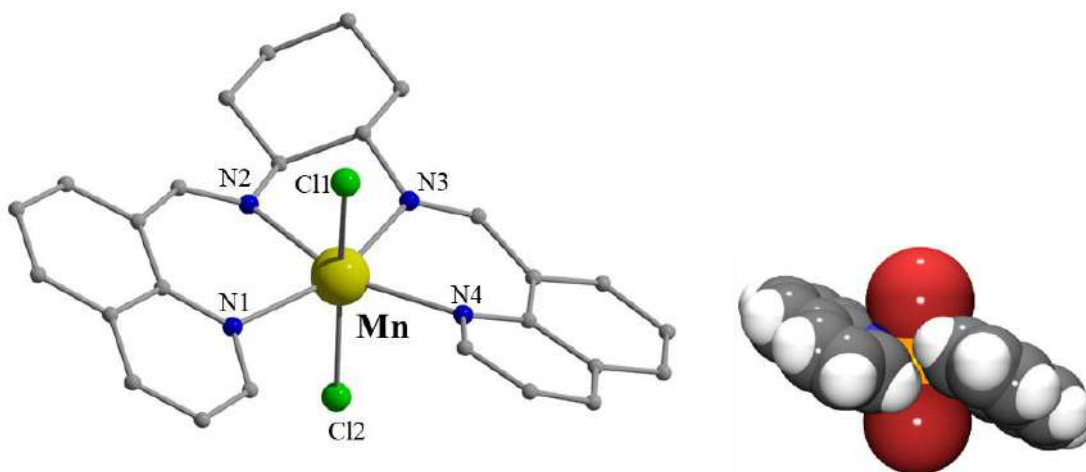
Figure 80: (Left) Partially labeled plot for **40** and (right) plot of the *Λ* helical arrangement of the ligand around the Mn^{II} cation.

The structure of complex **40** consist of neutral [Mn^{II}(L13)(Cl)$_2$] molecules and co-crystallized methanol molecules. The chloro ligands are placed in *trans* arrangement and

the ligand L13 links four coordination sites of the cation via the N-donor atoms resulting a MnN_4Cl_2 chromophore. The octahedral coordination is strongly distorted due to the low bite of the N-donors of the Schiff base (angles in *trans* N1-Mn-N3, 158.9(1); N2-Mn-N4, 157.8(1); Cl1-Mn-Cl2, 163.3(4)). The quinoline fragments are tilted 25º with respect to the mean MnN_4 plane (Fig. 80, right), resulting a Λ helical arrangement due to the steric hindrance between the H-atoms on the neighbor C2-C2' atoms, that also prevent the pentagonal bipyramid environment despite the available space between N1 and N4 donor atoms (N1-Mn-N4 bond angle is 118.7(1)º). SHAPE analysis revealed that the environment of the MnII cation is far from any regular polyhedron (Table A11, Appendix), and the closer one is the distorted octahedron (Fig. A10, Appendix) with CShM = 3.52.

Table 14: Selected interatomic bond distances (Å) and angles (˚) for **40**.

Mn-N1	2.275(3)	N1-Mn-N2	83.1(1)
Mn-N2	2.224(3)	N2-Mn-N3	75.8(1)
Mn-Cl1	2.569(1)	N3-Mn-N4	82.3(1)
Mn-N3	2.207(3)	Cl1-Mn-Cl2	163.34(4)
Mn-N4	2.265(3)	N1-Mn-N3	158.9(1)
Mn-Cl2	2.496(1)	N2-Mn-N4	157.8(1)

The molecular structures of **42** and **43** are very similar but interestingly, the unit cell contains two molecules with opposite Λ/Δ helicity, which show similar bond parameters for the Λ, in respect with **40Λ**, molecule and a larger distortion for the Δ one. This feature is rare because the transfer of chirality usually imposes different helicity for the *RR* or *SS* enantiomers. Partially labeled plots for **42** and **43** are shown in Figs. 81 and 82, respectively. Selected bond distances and angles are listed in Tables 15 and 16, for **42** and **43**, respectively. The environment of Mn^{II} cation in complexes **42** and **43** is far from any regular polyhedron (Table A11, Appendix) and the closest polyhedron is the distorted octahedron (Fig. A10, Appendix) with CShM = 4.72 and 4.32 for **42** and **43**, respectively.
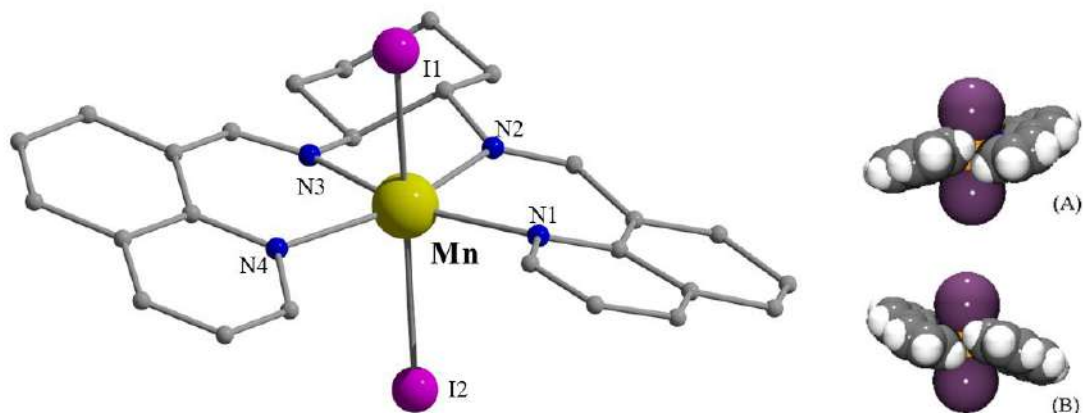
Figure 81: (Left) partially labelled plot for **42**. (Right) Space-filled plot showing the helical arrangement of the ligand around the Mn^{II} cation. The structure contains two opposite helicities, labelled as structures A and B.

Table 15: Selected interatomic bond distances (Å) and angles (˚) for **42**.

	42-A	**42**-B
Mn-N1	2.293(7)	2.255(6)
Mn-N2	2.215(6)	2.234(6)
Mn-N3	2.212(7)	2.208(7)
Mn-N4	2.268(7)	2.281(6)
Mn-I1	2.949(1)	2.924(1)
Mn-I2	2.935(1)	2.888(1)
N1-Mn-N2	84.1(2)	82.4(2)
N2-Mn-N3	76.4(2)	76.3(2)
N3-Mn-N4	84.7(2)	82.1(2)
N1-Mn-N4	117.6(2)	119.1(2)
N1-Mn-N3	155.5(2)	158.7(2)
N2-Mn-N4	156.1(2)	158.4(2)
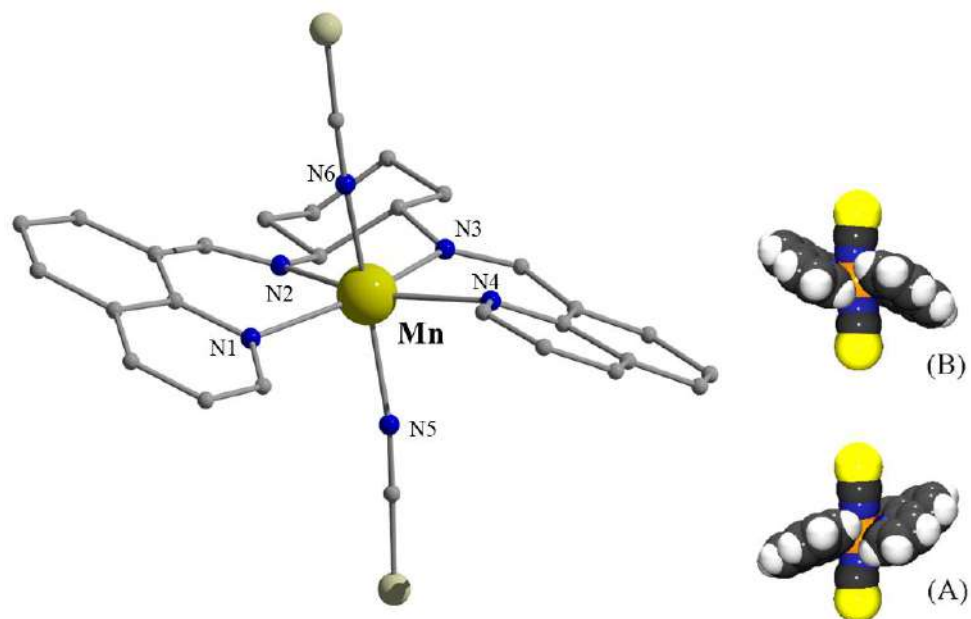
Figure 82: (Left) partially labelled plot for **43**. (Right) Space-filled plot showing the helical arrangement of the ligand around the Mn^{II} cation. The structure contains two opposite helicities, labelled as structures A and B.

Table 16: Selected interatomic bond distances (Å) and angles (°) for **43**.

	43-A	**43**-B
Mn-N1	2.295(6)	2.268(6)
Mn-N2	2.236(5)	2.216(6)
Mn-N3	2.204(5)	2.207(5)
Mn-N4	2.298(6)	2.292(6)
Mn-N5	2.171(6)	2.189(6)
Mn-N6	2.166(6)	2.196(8)
N1-Mn-N2	81.7(2)	83.3(2)
N2-Mn-N3	75.6(2)	76.0(2)
N3-Mn-N4	82.3(2)	83.5(2)
N1-Mn-N4	120.5(2)	121.4(2)
N1-Mn-N3	157.2(2)	151.6(2)
N2-Mn-N4	157.6(2)	153.2(2)
N5-Mn-N6	156.7(2)	155.2(3)

Regarding the complex **41**, its structure was not determined by means of X-ray diffraction. Instead, powder X-ray diffraction studies were performed and the obtained spectrum obtained was compared with the spectrum of **42**. As can be observed, the two spectra are similar (Fig. 83) and thus it can be assumed that **41** and **42** have similar structures.
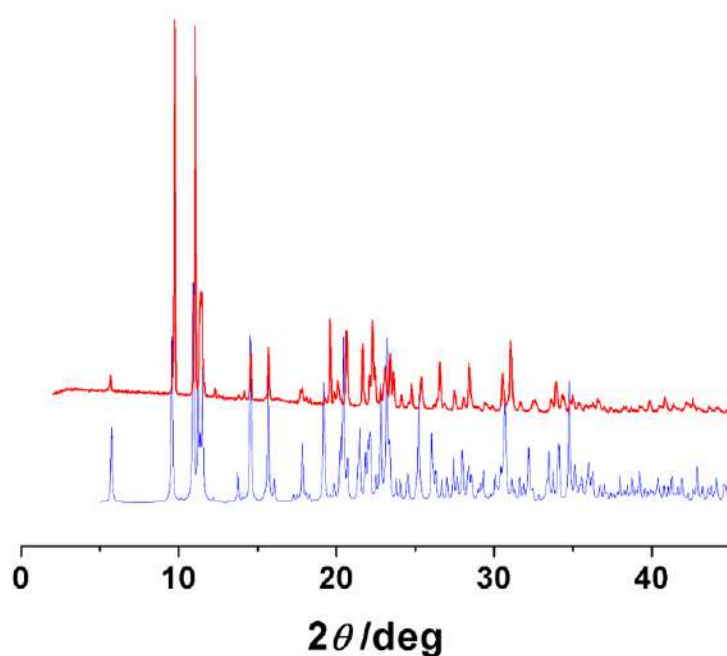
Figure 83: Powder X-ray diffraction spectrum for **41** (red) and the reference spectra of **42** (blue).

4.3.3 Magnetic Susceptibility Measurements

Static magnetic measurements were carried out for the compounds **40**-**43**, in the temperature range 100-2 K. The four compounds show similar behavior; at higher temperature the value of $\chi_M T$ is close to the expected one for one Mn^{II} cation (Fig. 84, left). Reduced magnetization measurements revealed quasi-superimposable plots for **40** and **43** suggesting a very low or negligible anisotropy (Fig. 84, right). On the other hand, fit of the reduced magnetization plots for **41** and **42** revealed D values of 0.65 cm^{-1} and 0.80 cm^{-1}, respectively. In the literature there are six-coordinated monuclear Mn^{II} complexes, containing different anions, that have been studied by means of HF-EPR and their magnetic anisotropy has been determined [81, 82]. The D values are in the range of 0.16-0.30 cm^{-1} for Cl$^-$, 0.5-0.7 cm^{-1} for Br$^-$ and 0.9-1.21 cm^{-1} for I$^-$. As can be observed the values of D that

has been determined in the complexes **40**, **41** and **42** follow the same tedency and are in the same range with the reported ones.
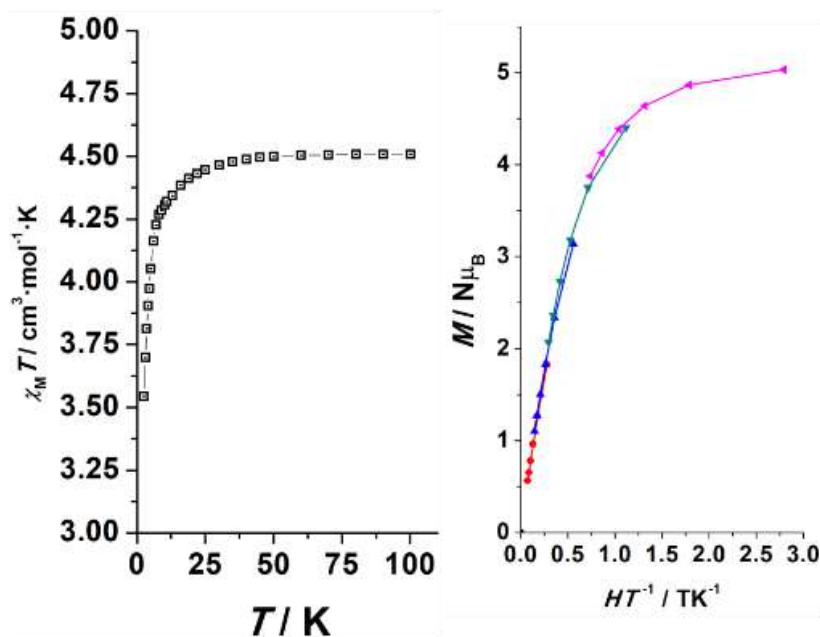
Figure 84: (Left) $\chi_M T$ product for the low temperature region for **40**. (Right) Reduced magnetization plot for **40**.

Alternate current measurements were carried out for all of the compounds. However, any of them give a response under zero field. Clear signals were observed only for compounds **40** (Fig. 85) and **43** (Fig. 86) under an external field of 0.6 T.
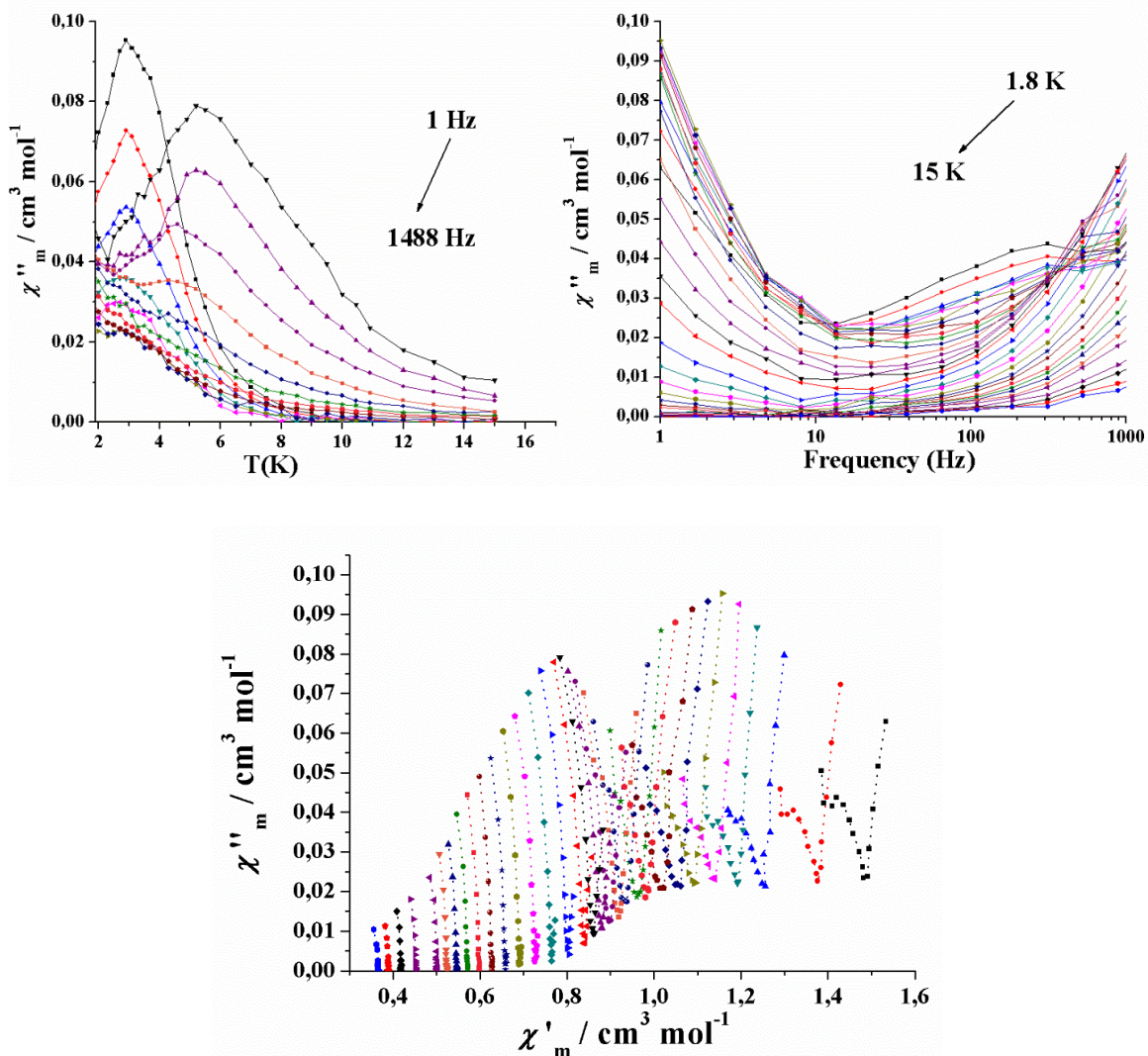
Figure 85: Ac plots vs. T / frequency and Argand plot for **40** (0.6 T).

The χ''_m *(T)* plots for **40** shows two different sets of signals; one for the lower frequencies and temperatures (LFT) and one for the higher frequencies and temperatures (HFT). The LFT signals are frequency independent and the strong overlap between the two sets of signals gives two partial semicircles in the Argand plots, and as a result reliable information about the relaxation could not be obtained.

In contrast, for complex **43**, better defined plots were obtained. Plot of $\ln(\tau)$ vs T^{-1} (Fig. 87, top) was fitted by the following equation:

$$\tau^{-1} = AT + CT^n$$

which corresponds to Direct and Raman relaxation processes. The presence of two relaxation processes can be identified by the plot $\ln(\tau)$ vs $\ln(T)$, where two different slopes are present. Fit of the data gave the values of $C = 0.036$, $n = 5.1$ and $A = 2380$.
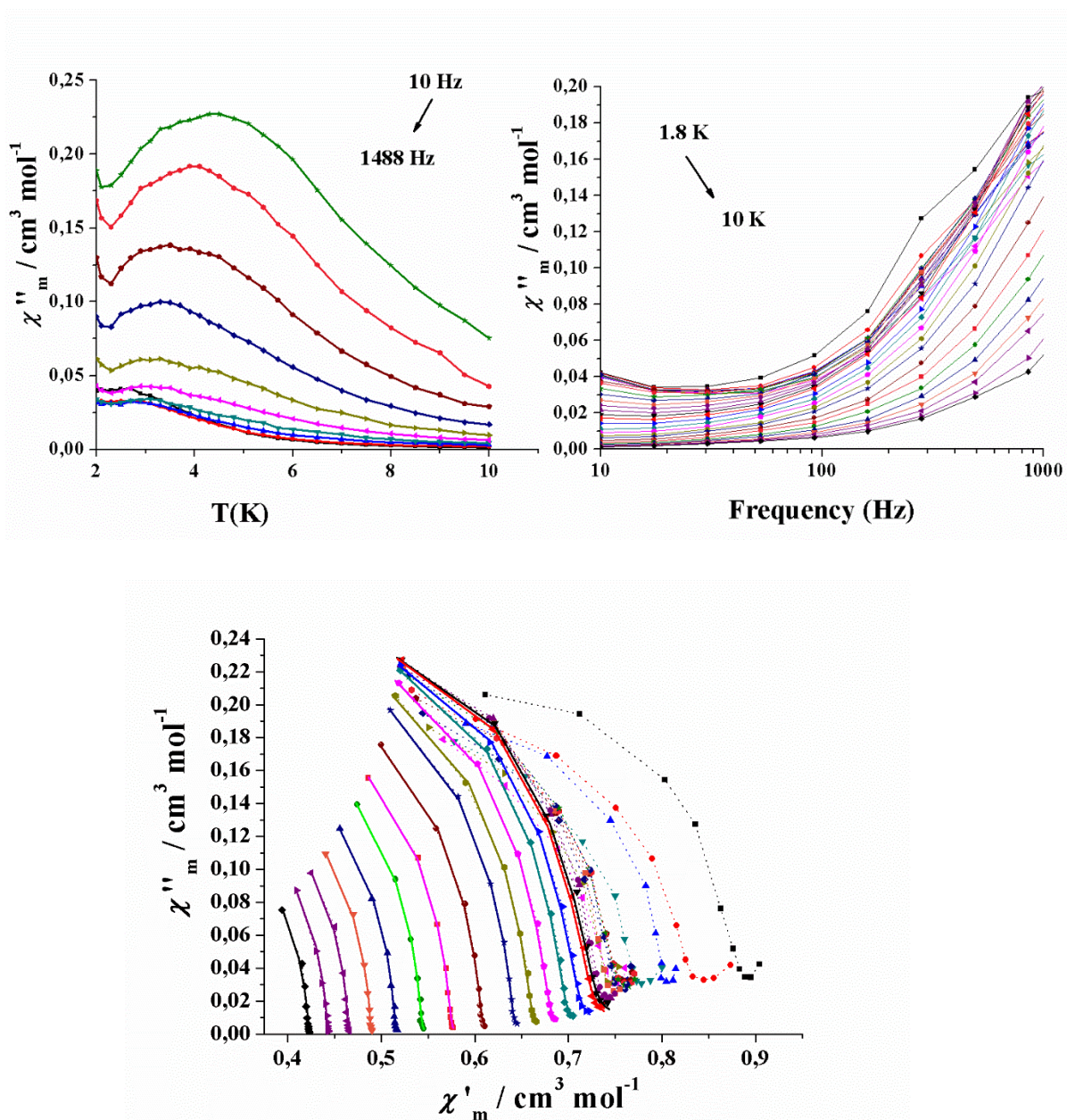
Figure 86: (Top)Ac plots vs. T / Frequency and (bottom) Argand plot for **43** (0.6 T). The solid lines represent the fitting of the experimental data, while the dashed lines are the temperatures excluded for the fiting.
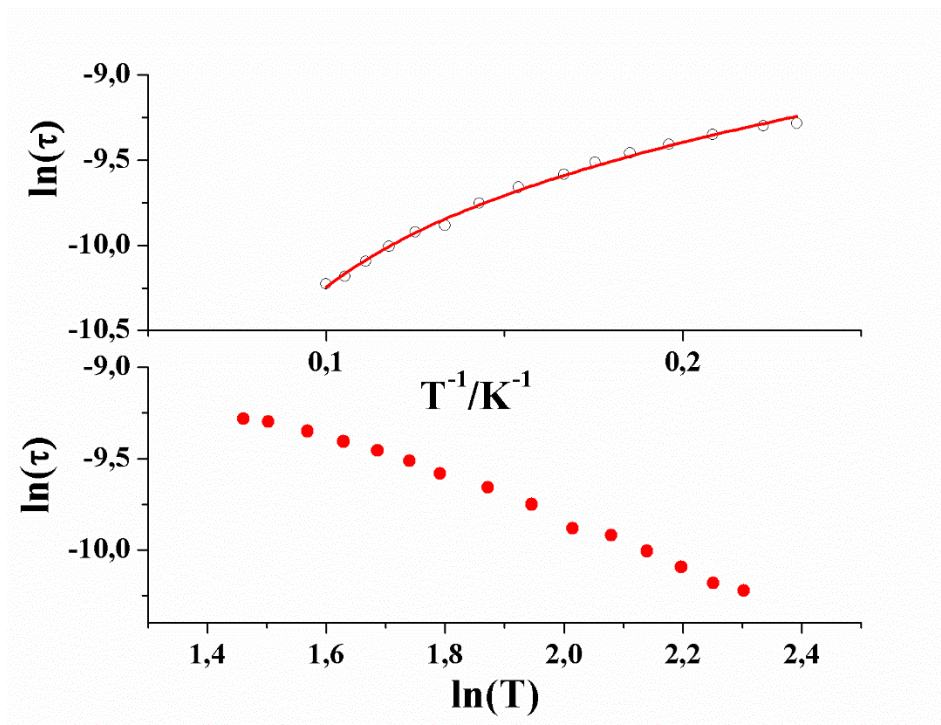
Figure 87: (Top) $\ln(\tau)$ vs T^{-1} plot for **43** and (bottom) plot of $\ln(\tau)$ vs $\ln(T)$.

As mentioned above, complexes **41** and **42**, did not show similar behaviour, and thus it is necessary to clarify the reasons behind this behaviour. The already reported Mn^{II} complexes that show magnetic relaxation, present different environments but the main feature is the presence of a very low *D* which is around 0.1 cm^{-1}. In this series the four complexes have strongly distorted geometries, but at molecular level they do not show relevant differences in their lattice vibrations that could provide different relaxation mechanisms, as was proved by Raman spectroscopy in the THz region (Fig. A1, Appendix).

4.3.4 EPR Measurements

In order to decide which factor is responsible for the presence of magnetic relaxation in these kind of molecules, some factors were taken into consideration. First of all, the above mentioned complexes were built by the same organic ligand. These complexes show strongly distorted environments without relevant structural differences between them in

their network vibrations as can be proved by ultra-low frequency Raman spectroscopy, where the four complexes present similar spectra (Fig. 88). Secondly, four different anions were used in order to study the affection of the crystal field. The three halides (Cl^-, Br^- and I^-) are π-basic ligands and have different field contribution with the thiocyanate. However, the observation of magnetic relaxation for **40** and **43** can lead to the deduction that the crystal field provided by the ligands can be excluded.
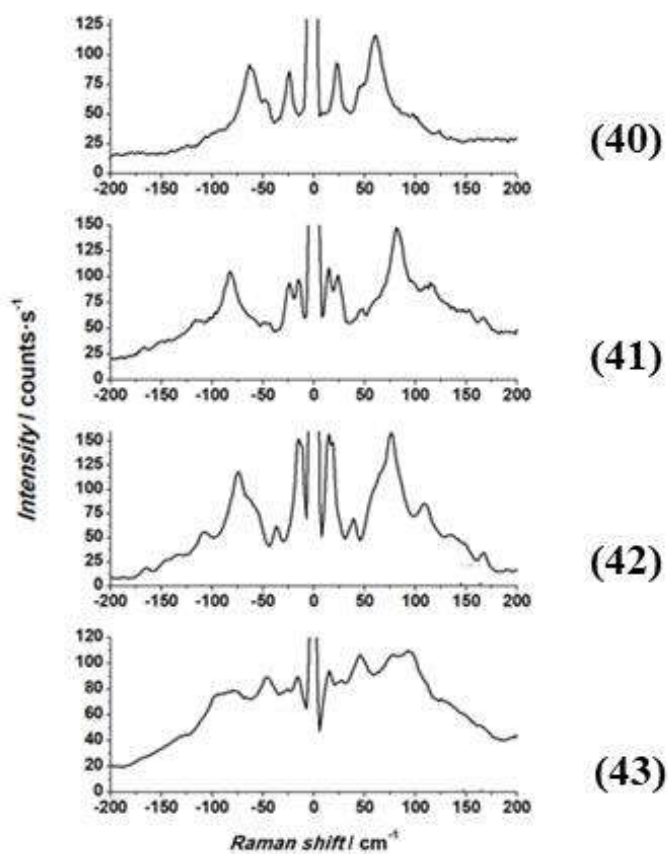
Figure 88: Ultra-low frequency Raman spectra for **40-43**.

Thus, the last factor that has to be taken into consideration is the presence of D. Until today, all the reported Mn^{II} complexes that show slow relaxation of magnetization have very low values of D (~0.1 cm^{-1} or even lower). Q-band EPR spectrum for **40** (Fig. 89) revealed a value of $D = 0.188$ cm^{-1}, $E = 0.0475$ ($E/D = 0.25$), where the value of D is in the expected range.

Figure 89: EPR spectrum for **40**.

Furthermore, EPR spectrum was recorder for compound **41** (Fig. 90). In this case the spectrum is more complicated than **40**. The black line corresponds to the experimental data while the red line corresponds to the simulated one. As mentioned to paragraph 4.3.2, complexes **41** and **42** present similar structures based on their pXRD spectra. Thus, also in this case there are two molecules in the cell with Λ and Δ helicity, where the molecule with the Δ configuration is more distorted than Λ. As a result, the EPR spectrum of complex **41** is the sum of the two different spectra; one that comes from the molecule with Λ helicity and the other that comes from the molecule with Δ. The orange line corresponds to the molecule with Λ helicity and reveals the values of $D = 0.397$ cm^{-1} with $E/D = 0.24$. The blue line corresponds to the molecule with Δ helicity and gives $D = 0.481$ cm^{-1} with $E/D = 0.24$.
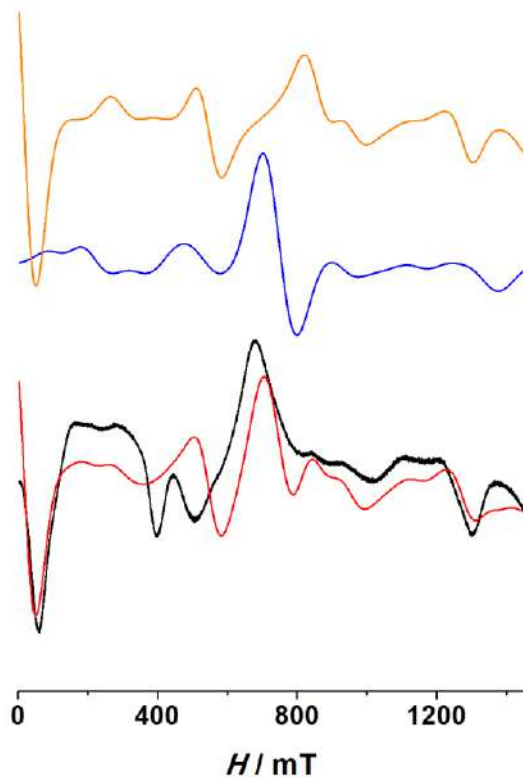
Figure 90: EPR spectrum for **41**.

The similar response of **40** and **43** can lead to the conclusion that relaxation of magnetization is irrelevant with the crystal field promoted by the ligands and the crucial factor that governs the magnetic relaxation is the presence of very low D values. When magnetic anisotropy is low, induces crossing of the m_s and thus relaxation can be observed. In contrast, when D is larger (such as the cases of Br$^-$ and I$^-$ complexes) the m_s doublets are enough separated to give a barrier with (DS^2-1/4) value of just few wavenumbers that can be overcome even at low temperature.

4.3.5 Conclusion

In conclusion, in this Section the synthesis and the magnetic characterization of four similar Mn^{II} compounds was described. All the complexes, were built with the neutral, flexible ligand L13, which can promote predetermined topologies around the cation. Also, two different crystal field ligands were used; halides (Cl$^-$, Br$^-$ and I$^-$) and thiocyanate. All the

complexes were studied by means of magnetism, where revealed that only complexes **40** and **43** show slow magnetic relaxation. Due to the fact that, all the complexes are built from the same ligand and they do not show enormous differences in their vibrational modes, as indicated by low frequency Raman spectroscopy, the presence of slow relaxation is attributed to the low values of magnetic anisotropy. When the D is low these kind of systems can behave as SMMs/SIMs, while when D takes larger values the ac response disappears. Thus, the decisive factor for the presence of slow magnetic relaxation is only the low D values promoted by the structural distortions.

APPENDIX

FOR CHAPTER 4

Table A1: Crystal data and structure refinement for complexes **28**, **29**, **31** and **32.**

	28	**29**	**31**	**32**
Formula	$C_{56}H_{66}Cl_2MnN_6Ni_3O_{24}$	$C_{78}H_{86}Cl_{14}Mn_2N_8Ni_4O_{33}$	$C_{60}H_{52}Cl_2MnN_4Ni_2O_{16}$	$C_{47}H_{56}Cl_6MnN_4Ni_2O_{17}$
FW	1509.11	2504.56	1328.31	1334.01
System	Monoclinic	Monoclinic	Orthorhombic	Monoclinic
Space group	P 21/c	P 21/n	P 222$_1$	P 21
a/Å	15.460(2)	15.4867(11)	14.4382(9)	8.4442(6)
b/Å	22.1183(3)	16.9740(11)	18.2949(8)	14.2499(10)
c/Å	17.992(3)	19.4904(14)	23.1532(12)	22.4771(18)
α/deg.	90	90	90	90
β/deg.	95.684(5)	93.893(3)	90	95.482(3)
γ/deg.	90	90	90	90
V/Å^3	6122.2(14)	5111.6(6)	6115.8(6)	2692.3(3)
Z	4	2	4	2
T, K	100(2)	100(2)	100(2)	100(2)
λ(MoKα), Å	0.71073	0.71073	0.71073	0.71073
ρ_{calc}, g·cm^{-3}	1.637	1.627	1.443	1.646
μ(MoKα), mm^{-1}	1.285	1.408	0.970	1.295
Flack param.	---	---	---	---
R	0.0372	0.0333	0.1058	0.0827
ωR^2	0.0685	0.0819	0.1262	0.2540
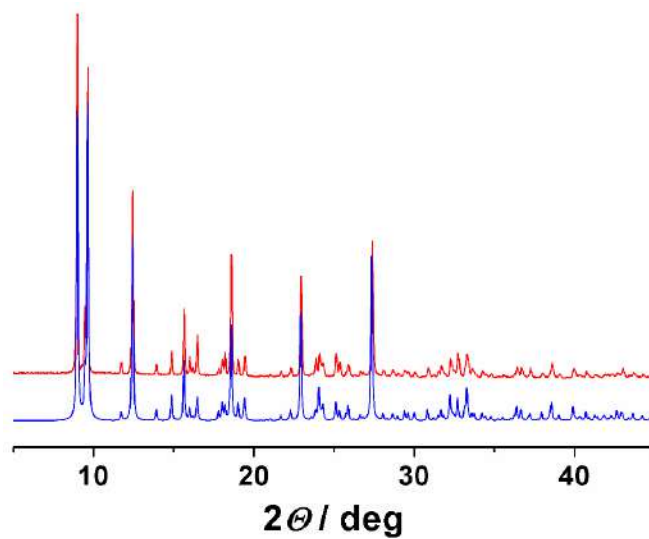
Figure A1: XRDP spectrum for **30** (red) vs. the simulated spectrum of the previously reported complex (CCDC: CIBPAF).
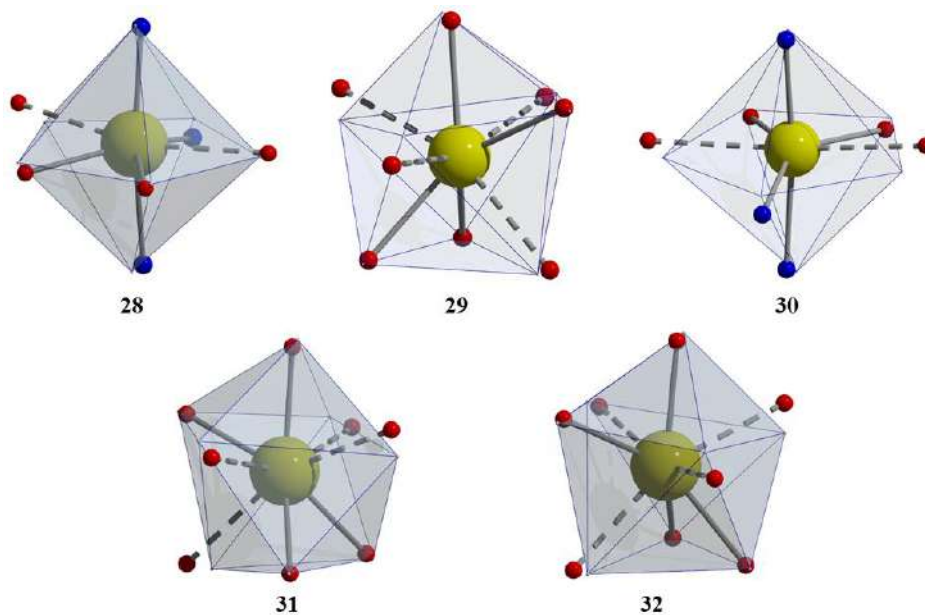
Figure A2: Coordination environment for the Mn^{II} cation in complexes **28**-**32**. Dashed bonds show the large contacts Mn-O_{alcoxo}. The ideal polyhedral are shown in blue lines.

Table A2: SHAPE measures for the Mn^{II} cations of complexes **28** and **30**. The ideal polyhedron for each complex has been highlighted in bold.

Ideal Geometry	CShM for **28**	CShM for **30**
HP-7 Heptagon	32.86041	32.55380
HPY-7 Hexagonal pyramid	21.94192	21.97262
PBPY-7 Pentagonal bipyramid	**1.58106**	**2.66560**
COC-7 Capped octahedron	7.64643	6.40116
CTPR-7 Capped trigonal prism	5.92484	4.92035
JPBPY-7 Johnson pentagonal bipyramid J13	3.82798	5.16592
JETPY-7 Johnson elongated triangular pyramid J7	20.32394	18.03524

Table A3: SHAPE measures for the Mn^{II} cations of complexes **29**, **31** and **32**. The ideal polyhedron for each complex has been highlighted in bold.

Ideal Geometry	CShM for **29**	CShM for **31**	CShM for **32**
OP-8 Octagon	30.79817	34.54721	31.27510
HPY-8 Heptagonal pyramid	24.28831	22.84599	24.64190
HBPY-8 Hexagonal bipyramid	13.75333	14.23820	13.53945
CU-8 Cube	10.02427	11.43582	9.91382
SAPR-8 Square antiprism	3.32107	4.44065	3.32148
TDD-8 Triangular dodecahedron	**3.02533**	**2.71964**	**2.85991**
JGBF-8 Johnson gyrobifastigium J26	13.58258	14.40507	13.53949
JETBPY-8 Johnson elongated triangular bipyramid J14	26.79846	27.91735	27.34751

JBTPR-8 Biaugmented trigonal prism J50	4.43019	5.56773	4.42887
BTPR-8 Biaugmented trigonal prism	2.82899	3.76677	2.87308
JSD-8 Snub diphenoid J84	6.28964	6.47223	6.07258
TT-8 Triakis tetrahedron	10.71925	12.26347	10.62739
ETBPY-8 Elongated trigonal bipyramid	23.14045	22.09068	23.46232
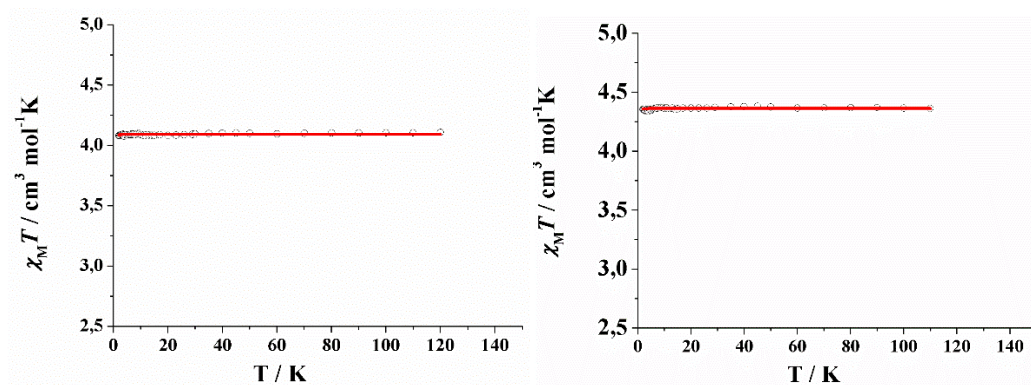
Figure A3: (Left) χ_MT plot for **31** and (right) χ_MT plot for **32**.

Table A4: Crystal data and structure refinement for complexes **33** and **34**.

	33	**34**
Formula	$C_{24} H_{26} Cl_4 Mn_2 N_6$	$C_{22} H_{18} Br_2 Mn N_4$
FW	650.19	553.16
System	Triclinic	Monoclinic
Space group	P -1	C 2/c
a/Å	7.1539(4)	13.1390(11)
b/Å	7.6612(4)	11.1113(8)
c/Å	12.4908(7)	14.3370(11)
α/deg.	84.610(2)	90
β/deg.	83.362(2)	101.419(3)
γ/deg.	82.457(2)	90
V/Å^3	672.29(6)	2051.6(3)
Z	1	4
T, K	100(2)	100(2)
λ(MoKα), Å	0.71073	0.71073
ρ_{calc}, g·cm^{-3}	1.606	1.791
μ(MoKα), mm^{-1}	1.363	4.555
Flack param.	---	---
R	0.0274	0.0269
ωR^2	0.0729	0.0470

Table A5: SHAPE measures for the Mn^{II} cations of complex **33** The ideal polyhedron for each complex has been highlighted in bold.

Ideal Geometry	CShM for **33**
PP-5 Pentagon	29.59743
vOC-5 Vacant Octahedron	5.87998
TBPY-5 Trigonal bipyramid	**3.42840**
SPY-5 Spherical square antiprism	3.96875
JTBPY-5 Johnson trigonal biryramid	6.8260

Table A6: SHAPE measures for the Mn^{II} cations of complex **34**. The ideal polyhedron for each complex has been highlighted in bold.

Ideal Geometry	CShM for **34**
HP-6 Haxagon	31.65935
PPY-6 Pentagonal pyramid	17.09676
OC-6 Octahedron	8.78511
TRP-6 Trigonal prism	**7.79824**
JPPY-6 Johnson pentagonal pyramid J2	22.25309
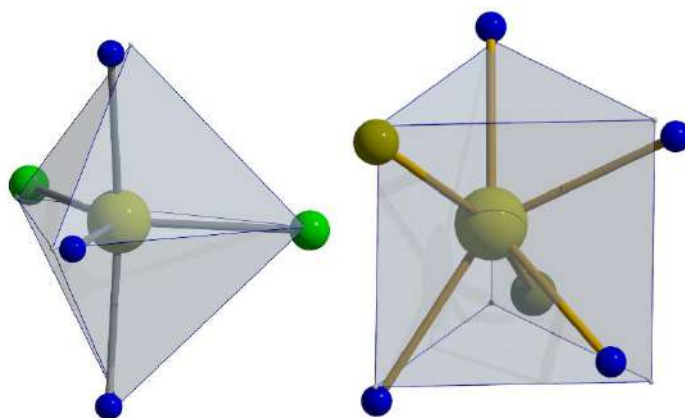
Figure A4: Coordination environment for the Mn^{II} cation in complexes **33** (left) and **34** (right). The ideal polyhedral are shown in blue lines.

Table A7: Crystal data and structure refinement for complexes **35** and **36**.

	35	**36**
Formula	$C_{14} H_{17} Cl_2 Mn N_3$	$C_{14} H_{17} Br_2 Mn N_3$
FW	353.14	442.06
System	Triclinic	Triclinic
Space group	P -1	P -1
a/Å	7.4659(4)	7.4816(7)
b/Å	7.8870(4)	8.1505(7)
c/Å	13.2290(7)	13.3712(11)
α/deg.	76.203(2)	73.602(3)
β/deg.	82.975(2)	85.395(3)
γ/deg.	83.785(2)	83.015(3)
V/Å^3	748.28(7)	775.48(12)
Z	2	2
T, K	100(2)	100(2)
λ(MoKα), Å	0.71073	0.71073
ρ_{calc}, g·cm^{-3}	1.567	1.893
μ(MoKα), mm^{-1}	1.231	5.996
Flack param.	---	---
R	0.0194	0.0181
ωR^2	0.0520	0.0415

Table A8: SHAPE measures for the Mn^{II} cations of complexes **35** and **36**. The ideal polyhedron for each complex has been highlighted in bold.

| Ideal Geometry	CShM for **35**	CShM for **36**
PP-5 Pentagon	30.22000	30.65055
vOC-5 Vacant Octahedron	7.65971	8.11395
TBPY-5 Trigonal bipyramid	**3.41483**	**3.59696**
SPY-5 Spherical square antiprism	4.25115	4.41655
JTBPY-5 Johnson trigonal biryramid	6.70155	7.49813

Figure A5: Coordination environment for the Mn^{II} cation in complexes **35** (left) and **36** (right). The ideal polyhedral are shown in blue lines.

Table A9: SHAPE measures for the Mn^{II} cations of complex **37**. The ideal polyhedron for each complex has been highlighted in bold.

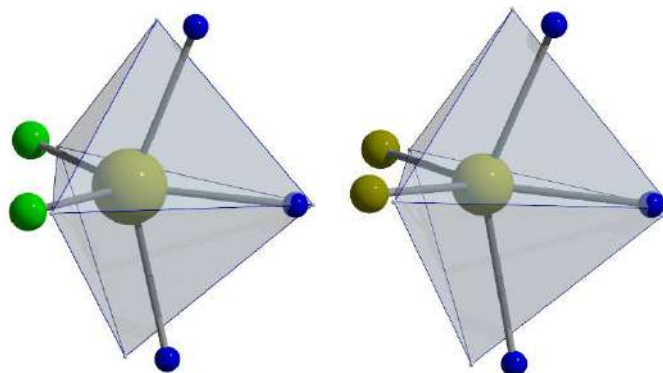| Ideal Geometry	CShM for **37**
HP-6 Haxagon	31.83886
PPY-6 Pentagonal pyramid	22.52881
OC-6 Octahedron	**2.42302**
TRP-6 Trigonal prism	10.75216
JPPY-6 Johnson pentagonal pyramid J2	26.56830
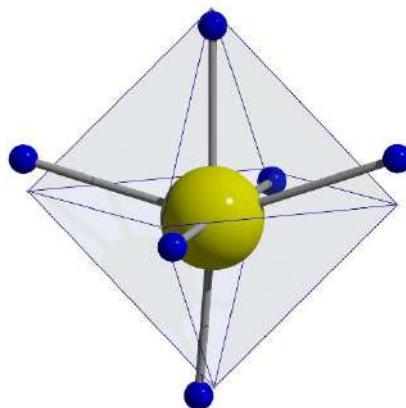
Figure A6: Coordination environment for the Mn^{II} cation in complex **37**. The ideal polyhedral are shown in blue lines.
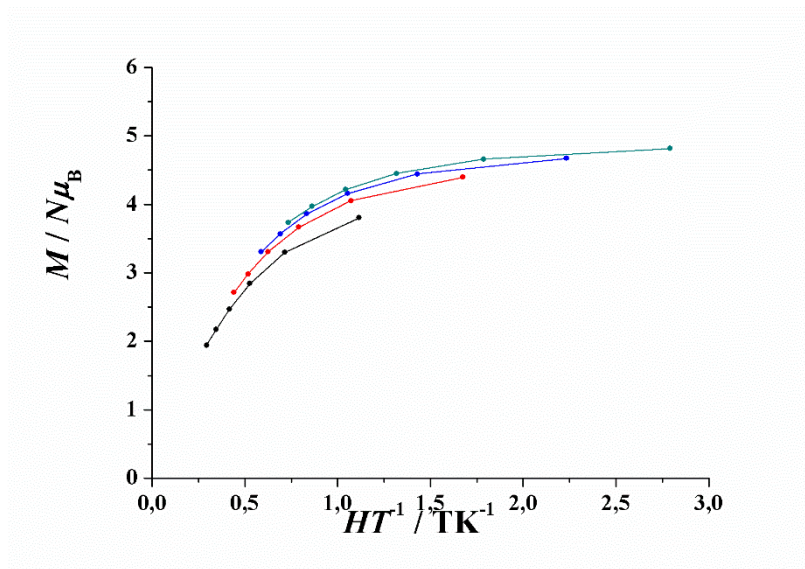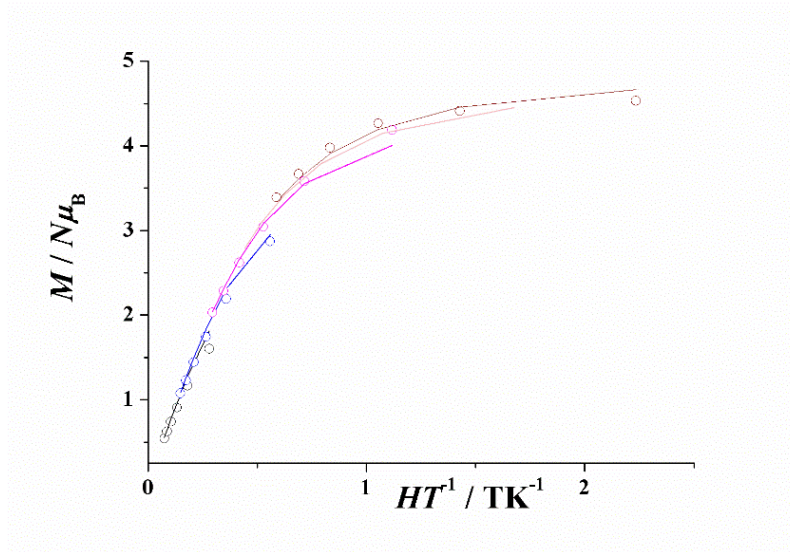
Figure A7: Reduced magnetization plot for **35** (top) and **36** (bottom).
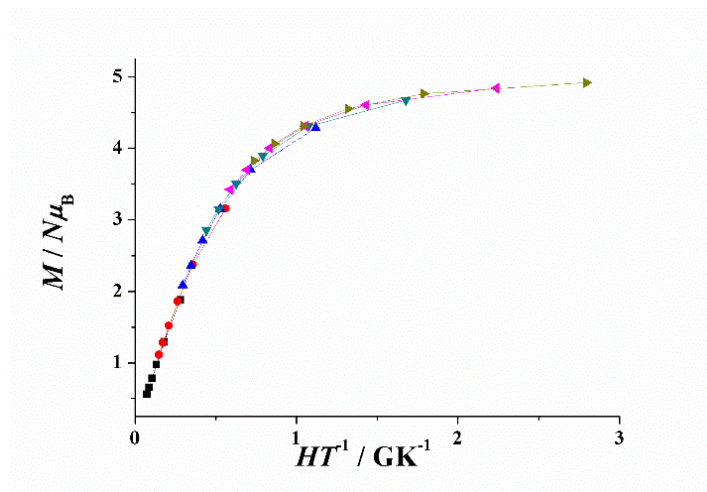
Figure A8: Reduced magnetization plot for **38**.
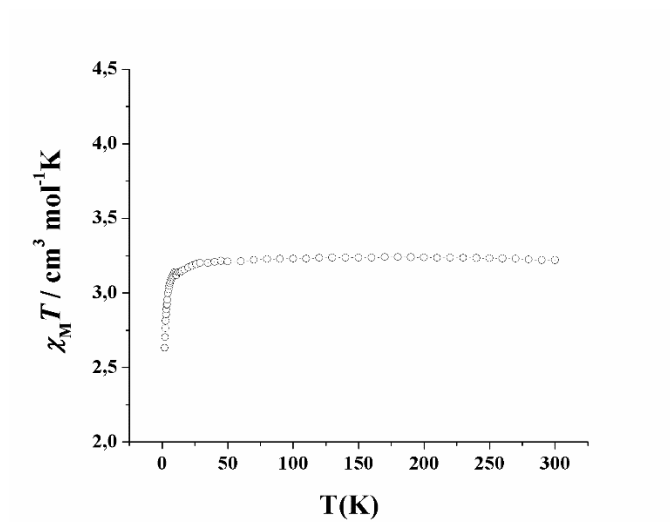
Figure A9: $\chi_M T$ plot for **39**.

Table A10. Crystal data, collection and structure refinement details for the X-ray structure determination of complexes **40**, **42** and **43**.

	40	**42**	**43**
Formula	$C_{55}H_{60}Cl_4Mn_2N_8O_3$	$C_{105}H_{100}I_8Mn_4N_{16}O$	$C_{57}H_{52}Mn_2N_{12}OS_4$
FW	1132.79	2836.96	1159.22
System	Monoclinic	Monoclinic	Triclinic
Space group	$P2_1$	C2	P1
a/Å	16.7866(10)	18.5020(11)	8.5398(4)
b/Å	8.6559(4)	9.0264(5)	10.3318(6)
c/Å	17.8003(11)	30.8068(18)	15.7479(9)
α/deg.	90	90	86.416(2)
β/deg.	98.624(2)	93.298(2)	82.774(2)
γ/deg.	90	90	75.071(2)
V/ Å^3	2557.2(2)	5136.4(5)	1331.24(13)
Z	2	2	1
T, K	100(2)	100(2)	100(2)
Θ range/deg.	1.452-30.559	1.986-30.596	2.041-30.563
Reflex. collected	53884	15581	74662
Reflex. indep.	15576	15581	16202
Parameters	652	617	687
λ(MoKα), Å	0.71073	0.71073	0.71073
ρ_{calc}, g·cm^{-3}	1.471	1.834	1.446
μ(MoK$_\alpha$), mm^{-1}	0.757	2.941	0.685
Flack param.	0.008(5)	0.05(2)	0.04(3)
R	0.0417	0.0360	0.0595
ωR^2	0.0978	0.0625	0.0769

167

Table A11: SHAPE measures for the Mn^{II} cations of complexes **40**, **42** and **43**. The ideal polyhedron for each complex has been highlighted in bold.

Ideal Geometry	CShM for **40**	CShM for **42**	CShM for **43**
HP-6 Haxagon	32.28951	32.98677	32.40280
PPY-6 Pentagonal pyramid	20.47023	22.70963	16.78661
OC-6 Octahedron	**3.52332**	**4.72181**	**4.32282**
TRP-6 Trigonal prism	8.68458	9.89633	6.98480
JPPY-6 Johnson pentagonal pyramid J2	25.248	26.66350	20.40167

Figure A10: Coordination environment for the Mn^{II} cation in complexes **40** (left), **42** (middle) and **43** (right). The ideal polyhedral are shown in blue lines.

CHAPTER 5

SRM in anisotropic systems: The case of Co(II)

Chapter 5: SRM in anisotropic systems: The case of Co(II)

This chapter comprises *Publication #6.*

In the previous Chapters, Mn(II) complexes were used in order to study the magnetic behavior of these complexes with an isotropic cation. In this case, Mn(II) was replaced with the Co(II) cation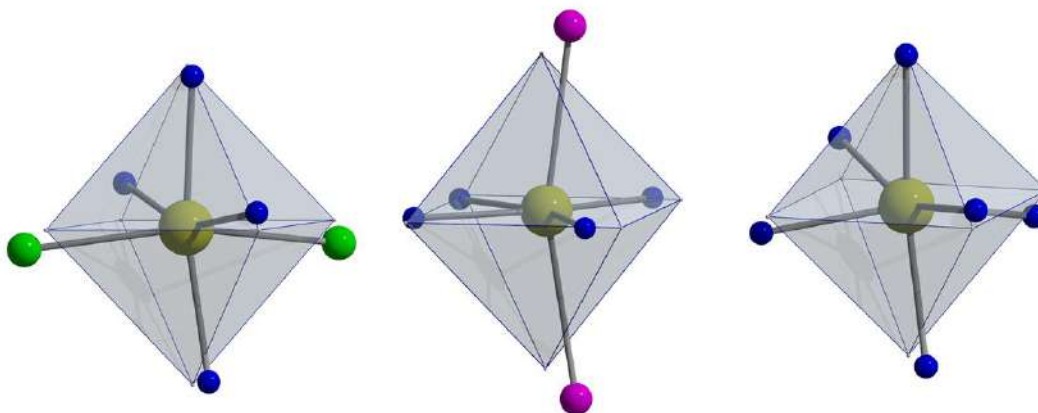, which is one of the more common 3d cations in the field of magnetism due to its anisotropic nature. The main purpose was to isolate similar systems with the previous ones, using similar organic ligands and then to study their magnetic behavior in order to realize how the nature of the cation affect the magnetism of the complexes.

Publication #6 *"Slow magnetic relaxation of cobalt(II) complexes in axial bipyramidal environment: an S = ½ spin case"* is about the syntheses and the characterization of two Ni^{II}-Co^{II} complexes and one Cu^{II}-Co^{II} complex with formulae: $[\{Ni^{II}(L4)Co^{II}(H_2O)_2(MeOH)\}\{Ni^{II}(L4)_2\}](ClO_4)_2 \cdot MeOH$ (**44·MeOH**), $[\{Ni^{II}(L9)Co^{II}(H_2O)_2(MeOH)\}\{Ni^{II}(L9)_2\}](ClO_4)_2 \cdot MeOH$ (**45·MeOH**) and $[\{Cu^{II}(L5)\}Co^{II}](ClO_4)_2 \cdot MeOH \cdot 0.5H_2O$ (**46·MeOH·0.5H₂O**), respectively. The organic ligands, whose anionic form is present in the compounds, are depicted in Fig. 91. With the organic ligand H₂L4 no crystals adequate for X-Ray diffraction were obtained. The strong anisotropy of this cation gives a behavior that has been analyzed as s pseudospin S = ½. Also, the magnetically diluted compound of **44**, **44D**, was synthesized in order to study the effect of dipole-dipole interactions. Complexes **44** and **45** were studies by means of ECD spectroscopy in order to confirm the enantiomeric nature of the reported compounds. Mirror image spectra confirmed this behavior. Interestingly, for **46** a defined *Δ* or *Λ* configuration around the Co^{II} cation has been observed.
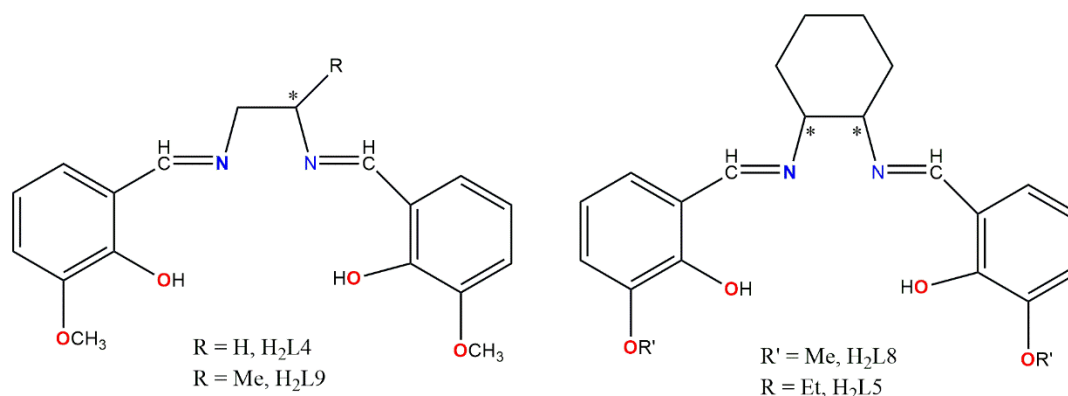
Figure 91: Organic ligands employed in *Publication #6*; with asterisk are denoted the chiral carbon centers.

The fitting of the $\chi_M T$ plots revealed the determination of $D = 84$ cm^{-1} for **44**, $D = 55$ cm^{-1} **45** and $D = -32.3$ cm^{-1} for compound **46**, resulting a strong stabilization of the $\pm 1/2$. For complex **46** it is found that a strong antiferromagnetic interaction is present between Cu^{II} and Co^{II} cations, while the magnitude of interaction was calculated as $2J = -27.4$ cm^{-1}. No ac response for all of the compounds was detected in the absence of a magnetic field. After the application of an external magnetic field complexes **44**, **44D** and **45** showed clear maxima, which allow us to determine the relaxation mechanisms and relaxation parameters. For **44** the extended ac analysis of the data showed that the mechanisms that are governed the magnetic relaxation are Direct plus Raman. This assumption is supported by ultralow frequency Raman spectroscopy (Fig. 92) in order to give insight in the lattice vibrations which helped us to prove the existence of low frequency phonons that involved in the relaxation pathways.
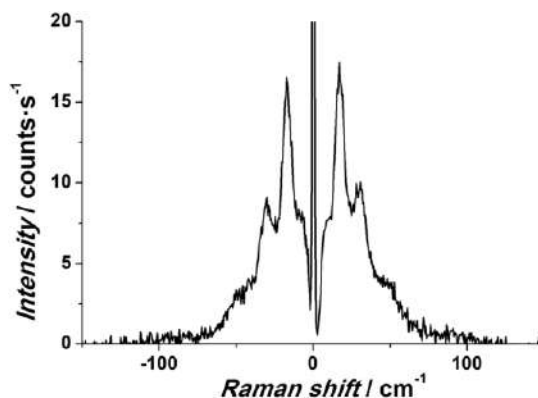
Figure 92: Ultralow frequency Raman spectrum of complex **44**.

171

PUBLICATION #6

"Slow magnetic relaxation for cobalt(II) complexes in axial bipyramidal environments: an S = ½ spin case"

Check for updates

Slow magnetic relaxation for cobalt(II) complexes in axial bipyramidal environment: an *S* = 1/2 spin case†

Evangelos Pilichos,[a] Mercè Font-Bardia,[b] Joan Cano, [ID][c] Albert Escuer [ID] *[a] and Júlia Mayans [ID] *[a]

A new family of magnetically mononuclear cobalt(II) complexes with formula [{Ni^{II}(L)Co^{II}(H$_2$O)$_2$(MeOH)}{Ni^{II}(L)}$_2$](ClO$_4$)$_2$ where H$_2$L1 = bis(*N*,*N*′-bis(3-methoxysalicylidene)ethylene-1,2-diamine) (**1**), H$_2$L2 = bis(*N*, *N*′-bis(3-methoxysalicylidene)propane-1,2-diamine) (**2**) and [{Cu^{II}(L4)}$_2$Co^{II}](ClO$_4$)$_2$ (**3**) where H$_2$L4 = bis(*N*,*N*′-bis(3-ethoxysalicylidene)cyclohexane-1,2-diamine) have been obtained employing non chiral or enantiomerically pure Schiff bases. The structural studies have been carried out by single crystal X-ray and powder diffraction. Dynamic magnetic studies indicate that some members of this family present field induced slow relaxation of the magnetization and its response has been compared with the magnetically diluted [Zn$_{0.9}$Co$_{0.1}$] complex **1D**. Ultra-low frequency Raman spectroscopy has been used to relate the slow relaxation with lattice vibrations.

Introduction

The discovery more than twenty years ago that a multinuclear transition metal cluster can exhibit slow relaxation of the magnetization was a breaking point in magnetism research and opened a new field known as molecular magnetism.[1,2] This discovery led the interest in studies related with polynuclear transition metal complexes containing different paramagnetic cations such as Mn^{III}, Fe$^{II/III}$, Co^{II} or Ni^{II},[3–8] which revealed that a high ground spin state (S) and axial zero field splitting (positive or negative), commonly known as magnetic anisotropy (*D*) should be present to achieve high energy barriers (*U*$_{eff}$) for the reversal of the magnetization. However, some years later was realized that the increase of *U*$_{eff}$ in polynuclear clusters was limited due to the inverse relationship of *D* and *S*,[9,10] and that the control of the anisotropic axes is extremely challenging. So, research was focused in mononuclear complexes with a Fe^{III}

compound[11] being the first 3d-metal single-ion magnet (SIM) reported. In this context, different strategies have been proposed to tune *D*, like the reduction and specific orientations of the coordination number, the increase of the covalence in donor atoms or performing variations in ligands substituents.[12–14]

More recently, the nature of the candidates to exhibit slow relaxation of the magnetization, for which the *D* magnitude or the barrier concept becomes not relevant, now includes isotropic systems mainly represented by cations that have a half-filled shell (Gd^{III}, Mn^{II})[15,16] or systems with *S* = 1/2 and out-of-phase response that can be reached from d^1 cations such as V^{IV} or from Kramers systems like Co^{II}. If the derived complexes exhibit large positive anisotropy (*D*) leads to a well isolated *S* = 1/2 ground state and have been proposed as qubit by means of the entanglement with the nuclear spin.[17,18]

These systems, that avoid the usual negative *D* requirement and the concomitant energy barrier between states with opposite spin orientations, are relatively common for Co^{II}, either in axially distorted octahedral environment or for penta-coordinated coordination. Complexes exhibiting axial bipyramidal geometry around the cobalt cation (*C*$_3$ symmetry) and large *D* values are not that common, and only some examples have been magnetically studied until now.[19–22]

Searching for an axial bypyramidal coordination environment around Co(II), we have explored its reactivity with the Schiff bases synthesized by the condensation of two equivalents of *o*-vanillin and one equivalent of 1,2-diethylenediamine (H$_2$L1), (*R*)- or (*S*)-1,2-propanediamine (H$_2$L2), (1*R*,2*R*), (1*S*,2*S*)-1,2-diaminocyclohexane (H$_2$L3) or two equivalents of 3-ethoxy-

^{a}Departament de Química Inorgànica i Orgànica, Secció Inorgànica and Institute of Nanoscience (IN^{2}UB) and Nanotecnology, Universitat de Barcelona, Marti i Franques 1-11, Barcelona-08028, Spain. E-mail: albert.escuer@ub.edu, julia.mayans@ub.edu
^{b}Departament de Mineralogia, Cristal lografia i Dipòsits Minerals and Unitat de Difracció de R-X, Centre Científic i Tecnològic de la Universitat de Barcelona (CCiTUB), Universitat de Barcelona, Solé i Sabarís 1-3, 08028 Barcelona, Spain
^{c}Instituto de Ciencia Molecular (ICMol), Universitat de València, 46980 Paterna, València, Spain
†Electronic supplementary information (ESI) available: Structural and magnetic data. CCDC 2157526 and 2157527. For ESI and crystallographic data in CIF or other electronic format see DOI: https://doi.org/10.1039/d2dt00880g
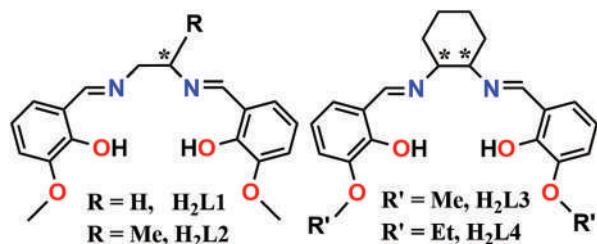
Scheme 1 Structural formula of the ligands employed in this work. Asterisks denote the chiral centres for the chiral ligands H_2L2, H_2L3 and H_2L4.

salicylaldehyde and one equivalent of (1R,2R) or (1S,2S)-1,2-diaminocyclohexane (H_2L4), (Scheme 1).

The cascade reaction of these compartmental Schiff bases with Ni^{II} followed by Co^{II} allowed to the characterization of similar complexes with H_2L1 and H_2L2 (formula [{$Ni^{II}(L)$ $Co^{II}(H_2O)_2(MeOH)$}{$Ni^{II}(L)$}$_2$](ClO$_4$)$_2$, L = L1^{2-} (**1**), L = L2^{2-} (**2**), whereas reaction of Cu^{II} with H_2L4 followed by addition of Co^{II} yielded the trinuclear system [{$Cu^{II}(L4)$}$_2$$Co^{II}$](ClO$_4$)$_2$ (**3**). The antiferromagnetic complex **3** does not show out-of-phase response, whereas complexes **1** and **2** exhibit slow relaxation of the magnetization with Single Molecular Magnet (SMM) response. The representative complex **1** has been analysed under different external applied magnetic fields and has been compared with its magnetically diluted analogue (**1D**) showing than the most appropriate relaxation path involves Direct plus spin lattice relaxations proved by ultralow frequency Raman spectroscopy.

Experimental

X-ray crystallography

Powder X-ray diffraction was performed with a PANalytical X'Pert PRO MPD θ/θ powder diffractometer of 240 millimetres of radius, in a configuration of convergent beam with a focalizing mirror and a transmission geometry with flat samples sandwiched between low absorbing films and Cu Kα radiation (λ = 1.5418 Å). Comparison between the calculated spectrum from the single crystal structure of **1** and the experimental spectrum for the diluted compound **1D** confirms the isostructurality among them, Fig. S1.†

Orange (**1** and **2R**) and red (**3SS**) prism-like specimens were used for the X-ray crystallographic analysis. The X-ray intensity data were measured on a D8 Venture system equipped with a multilayer monochromator and a Mo microfocus.

The frames were integrated with the Bruker SAINT software package using a narrow-frame algorithm. The structures were solved and refined using the Bruker SHELXTL Software Package.[23] Crystal data and refinement details for complexes **1** and **3SS** are summarized in Table 1. Acquisition data for complex **2** was performed on several crystals but its low quality does not allow to refine a crystallographically satisfactory structure. However, from the partially solved structure and the cell

Table 1 Crystal data, collection and structure refinement details for the X-ray structure determination of complexes **1** and **3SS** and the cell parameters for complex **2R**

	1	**2R**	**3SS**
Formula	$C_{56}H_{65}Cl_2Co\,N_6$ Ni_3O_{24}	$C_{59}H_{71}Cl_2Co$ $N_6Ni_3O_{24}$	$C_{196}H_{260}Cl_8Co_4$ $Cu_8N_{16}O_{78}$
FW	1512.10	1554.14	5115.82
System	Monoclinic	Triclinic	Triclinic
Space group	$P\,21/c$	$P1$	$P1$
a/Å	15.383(3)	15.537(2)	16.1923(9)
b/Å	22.053(4)	18.484(2)	17.178(1)
c/Å	18.065(3)	22.516(3)	20.1620(9)
α/°	90	89.268(5)	90.243(2)
β/°	95.410(7)	89.608(5)	90.262(2)
γ/°	90	85.969(5)	109.057(2)
V/Å^3	6100.9(9)	6450(1)	5300.7(5)
Z	4	12	1
T, K	100(2)	100(2)	100(2)
Θ Range/°	2.265–26.778		2.329–30.570
Reflex. collected	94 296		48 338
Reflex. indep.	12 976		48 338
Parameters	849		2629
λ(MoKα), Å	0.71073	0.71073	0.71073
ρ_{calc}, g cm^{-3}	1.646		1.603
μ(MoKα), mm^{-1}	1.354		1.286
Flack parameter	—		0.18(1)
R	0.0486		0.0607
ωR^2	0.1375		0.1542

parameters that compare with complex **1** (in a lower symmetry group as consequence of the employment of an enantiopure chiral ligand), the molecular structure for both complexes was proved to be similar. Further crystallographic details can be found in the corresponding CIF files provided in the ESI.†

Physical measurements

Magnetic susceptibility measurements were carried out on pressed polycrystalline samples with a MPMS5 Quantum Design susceptometer working in the range 30–300 K under magnetic fields of 0.3 T and under a field of 0.03 T in the 30–2 K range to avoid saturation effects at low temperature. Diamagnetic corrections (730, 766 and 591 cm^3 mol^{-1} for **1**, **2** and **3** respectively), were estimated from Pascal Tables.[24] Infrared spectra (4000–400 cm^{-1}) were recorded from KBr pellets on a Bruker IFS-125 FT-IR spectrophotometer. ECD spectra were recorded in 0.1 mM methanolic solutions in a Jasco-815 spectropolarimeter. Ultra-low frequency Raman spectra were recorded with a high resolution Raman T64000 (Jobin Yvon) instrument.

Syntheses

Perchlorates are potentially explosive and thus, small amounts of the compounds should be carefully handled.

[{$Ni^{II}(L1)Co^{II}(H_2O)(MeOH)$}{$Ni^{II}(L1)$}$_2$](ClO$_4$)$_2$·MeOH (1·MeOH). H_2L1 ligand was synthesized following the reported method[25] mixing o-vanillin (12 mmol/1.83 g) and ethylenediamine (6 mmol/0.36 g) in 20 mL of EtOH. The resulting yellow solution was maintained under stirring at room temperature for two hours and H_2L1 formed as a yellow powder. The solid

was filtered and washed with cold diethylether (2 × 3 mL) and air dried. Yield: 80%.

An aqueous solution (5 mL) of nickel(II) acetate tetrahydrate (0.8 mmol/0.0.199 g) was added to a suspension of H_2L1 (0.8 mmol/0.263 g) in MeOH (10 mL). The resulting solution was heated at 80 °C for 30 minutes in a microwaves furnace and a reddish precipitate of c×complex [$Ni^{II}L1$]·(H_2O) was formed,[26] collected and dried under vacuum.

A solution of [$Ni^{II}(L1)$]·(H_2O) (0.25 mmol/0.101 g) in 10 mL of CH_2Cl_2 was mixed with a methanolic solution (10 mL) of $Co(ClO_4)_2$·$6H_2O$ (0.25 mmol/0.091 g). The reaction mixture was heated in a microwaves furnace for 15 min at 70 °C resulting an orange solution. Well-shaped orange crystals of **1**, suitable for X-ray diffraction, were formed layering with diethylether after two days. IR spectrum of **1** is shown in ESI Fig. S2.† Yield: 65%. CHN for $C_{56}H_{65}Cl_2CoN_6Ni_3O_{24}$: calc: C, 44.48; H, 4.33; N, 5.56. Found C, 44.03; H, 4.37; N, 5.44.

[{$Ni^{II}(L1)Zn^{II}_{0.9}Co^{II}_{0.1}(H_2O)_2(MeOH)$}{$Ni^{II}(L1)$}$_2$]($ClO_4$)$_2$·**MeOH (1D·MeOH).** Complex **1D** was synthesized following the same procedure that yielded complex **1** but employing a mixture of $Zn(ClO_4)_2$·$6H_2O$ (0.09 mmol/0.034 g) and $Co(ClO_4)_2$·$6H_2O$ (0.120 mmol/0.044. IR spectrum of **1D** is shown in ESI Fig. S2.† Yield: 60%. CHN for $C_{56}H_{65}Cl_2Co_{0.1}Zn_{0.9}N_6Ni_3O_{24}$: calcd: C, 44.31; H, 4.32; N, 5.54. Found C, 44.93; H, 4.52; N, 5.30.

(R) and (S)-[{$Ni^{II}(L2)Co^{II}(H_2O)_2(MeOH)$}{$Ni^{II}(L2)$}$_2$]($ClO_4$)$_2$· MeOH (2R·MeOH and 2S·MeOH). A mixture of o-vanillin (1.6 mmol/0.243 g), (R)- or (S)-1,2-diaminopropane dihydrochloride (0.8 mmol/0.118 g), triethylamine (1.6 mmol/0.162 g) and nickel(II) acetate tetrahydrate (0.8 mmol/0.199 g) in 15 mL of 2 : 1 H_2O/MeOH was placed in a microwaves furnace for 30 minutes at 80 °C. A reddish precipitate of complex [$Ni^{II}(L2)$]·H_2O was collected and dried under vacuum. The fresh prepared powder of [$Ni^{II}(L2)$]·H_2O (0.25 mmol/0.104 g) was dissolved in dichloromethane/methanol (3 : 1, 15 mL) and mixed with a methanolic solution (5 mL) of cobalt (II) perchlorate hexahydrate (0.25 mmol/0.091 g). The reaction mixture was left in microwaves for 15 min at 70 °C. Slow diffusion of diethylether gave well-shaped X-ray diffraction quality crystals of **2R** or **2S** after two days. IR spectrum of **2R** is shown in ESI Fig. S3.† Yield: 52%. CHN for $C_{59}H_{71}Cl_2CoN_6Ni_3O_{24}$: calc: C, 45.60; H, 4.60; N, 5.41. Found (**2R/2S**) C, 45.46/45.70; H, 4.73/4.70; N, 5.58/5.32.

(R,R) and (S,S)-[{$Cu^{II}(L4)$}$_2Co^{II}$](ClO_4)$_2$·MeOH·0.5H₂O (3RR and 3SS·MeOH·0.5H₂O). A mixture of 3-ethoxysalicylaldehyde (0.8 mmol/0.133 g), (1R,2R) or (1S,2S)-1,2-diaminocyclohexane (0.4 mmol/0.046 g) and copper(II) acetate monohydrate (0.4 mmol/0.080 g) were dissolved in 5 mL of H_2O and 10 mL of MeOH. The solution was placed in a microwaves furnace for 30 minutes at 80 °C. A brownish precipitate of complex [$Cu^{II}(L4)(H_2O)$] was formed,[27] collected and dried under vacuum. The fresh prepared powder of [$Cu^{II}(L4)(H_2O)$] (0.25 mmol/0.123 g) was dissolved in dichloromethane/methanol (3 : 1, 15 mL) and added to a methanolic solution (5 mL) of cobalt(II) perchlorate hexahydrate (0.25 mmol/0.091 g). The reaction mixture was left in microwaves for 15 minutes at 70 °C. Slow diffusion of diethylether gave well-shaped X-ray

diffraction quality crystals of **3RR** or **3SS** were formed in few days. IR spectrum of **3SS** is shown in ESI Fig. S3.† Yield: 40%. CHN for $C_{49}H_{65}Cl_2CoCu_2N_4O_{19.5}$: calc: C, 46.01; H, 5.12; N, 4.38. Found (**3RR/3SS**) C, 45.90/45.78; H, 5.23/5.03; N, 4.42/4.50.

Results and discussion

Comments to the syntheses

The employment of hexadentate Schiff bases derived from 1,2-diamines and o-vanillin with a variety of 3d cations was studied by Mohanta *et al.*,[28–30] showing that the reaction of the [$ML(H_2O)$] (M = Cu^{II}, Ni^{II}) with perchlorates of divalent 3d cations leads to the formation of sandwich type complexes in which a central dinuclear [$M(L)M'(H_2O)_3$] unit (M = Cu^{II}, Ni^{II}, M′ = Cu^{II}, Ni^{II}, Co^{II}, Mn^{II}, Fe^{II}) is capped by two [M(L)] fragments linked by means of H-bonds. In our case, complexes **1** and **2R** exhibit a central dinuclear [$Ni(L)Co(H_2O)_2(MeOH)$] unit. The change of the water molecule, placed in an equatorial coordination site of the Co^{II} cation, by one methanol molecule excludes some of the H-bonds with the O_{alkoxo} acceptors but do not changes the overall structure.

For the Cu/Co system, the reaction of $Co(ClO_4)_2$·$6H_2O$ with the ligand obtained from the reaction of 1,2-cyclohexanediamine with o-vanillin (H_2L3) produced a crystalline compound but no adequate crystals for X-ray diffraction were obtained. In contrast, the closely related ligand H_2L4 that contains ethoxo groups instead of methoxo substituents allowed the isolation of the highly crystalline complex **3SS**.

It becomes remarkable that different products have been obtained as function of the cation placed in the inner cavity of the ligands. In fact, the reactions starting from the [Ni(L)]·(H_2O) precursors allowed the characterization of "sandwich" complexes like **1** or **2R**, whereas the reaction in the same conditions but starting from [Cu(L)]·(H_2O) precursors leads to the trinuclear CuCoCu topology, with an asymmetric linkage of the phenoxo groups that participate in the coordination sphere of the Co^{II} cation and the H-bonds that links the co-ordinated water molecules.

Trials to prepare the Zn^{II} diluted complex **1D** evidenced the preferential coordination of this cation instead the Co^{II} ion. The reaction of the [NiL1·H_2O precursor with Zn^{II}/Co^{II} perchlorates in a 10 : 1 ratio allowed the characterization of a product with very similar powder diffraction and IR spectra but with very weak magnetic ac response which is due to the very small percentage (~1%) of the Co^{II} cation. In the light of this data, the synthesis of the complex close to the 9 : 1 ratio for the Zn^{II} : Co^{II} composition (based on susceptibility and magnetization values) was performed with a lower excess of Zn^{II} (Zn^{II}/Co^{II} mixture in 3 : 4 ratio), that allowed an adequate reduction of the dipolar interactions for the magnetic measurements.

Description of the structures

[{$Ni^{II}(L1)Co^{II}(H_2O)_2(MeOH)$}{$Ni^{II}(L1)$}$_2$]($ClO_4$)$_2$·MeOH (1·MeOH). Compound **1** consists of one [$Ni(L1)Co(H_2O)_2(MeOH)$]²⁺ dinuc-

lear complex linked by means of H-bonds to two neutral [Ni(L1)] units and two perchlorate counteranions, Fig. 1. Selected bond parameters are summarized in Table 2. The nickel cations are placed in the inner N_2O_2 cavity of the deprotonated Schiff bases showing a square planar environment. The Co^{II} cation is placed in the central heterodinuclear unit linked by means of the bridging $O_{phenoxo}$ donors, one methanol and two water molecules placed in trans arrangement. In addition, the two $O_{methoxo}$ donors O(1a) and O(4a) interact weakly with the Co^{II} cation with Co–O distances larger than 2.5 Å. Thus, the environment around the Co^{II} cation can be considered as CoO_5 distorted trigonal bipyramid or alternatively as a distorted pentagonal bipyramid CoO_7 if the large Co–O(1a) and Co–O(4a) contacts are taken into account. SHAPE analysis[31] of the coordination environment of the cobalt cation shows large deviation from any regular polyhedron and strictly, its symmetry should be assumed as C_1, Table S1† and Fig. S4.†

The two water molecules coordinated to the Co^{II} cation link, by means of bifurcated H-bonds, the neutral [Ni(L1)] frag-

ments with the O-donors of the Schiff bases, ESI, Fig. S5† and Table S2,† being shorter than those involving the $O_{phenoxo}$ atoms and resulting a "sandwich" structure. The clusters of **1** are pillared forming chains that isolates the paramagnetic Co^{II} cations with Co···Co distances along the chain of 12.162(2) Å and with interchain distances of 11.457(1) Å, Fig. 1.

(*R*)-[{Ni^{II}(L2)Co^{II}(H$_2$O)$_2$(MeOH)}{Ni^{II}(L2)}$_2$](ClO$_4$)$_2$·MeOH (2*R*·MeOH). A plot of the molecular unit of **2*R*** from a partial resolution of the structure is provided in Fig. S6.† Complex **2*R*** shows an analogous sandwich structure than complex **1**, where the difference is the substitution of one H-atom of the ethylene fragment with one methyl group, which is responsible of the chiral character of the structure.

(*S*,*S*)-[{Cu^{II}(L4)}$_2$Co^{II}](ClO$_4$)$_2$·MeOH·0.5H$_2$O (3*SS*·MeOH·0.5H$_2$O). Complex **3*SS*** consists of two neutral [Cu(L4)] fragments linked to one Co^{II} cation resulting a $[\{Cu(L4)\}_2Co(H_2O)_2]^{2+}$ trinuclear unit, Fig. 2. Relevant bond parameters are summarized in Table 3. The copper cations are placed in the inner N_2O_2 cavity of the deprotonated Schiff base in a square planar environment with four copper-ligand distances being lower than 2 Å. Each neutral [Cu(L4)] fragment acts as a complex-as-ligand linking the Co^{II} cation by means of one $O_{phenoxo}$ and one O_{ethoxo} donors in a bidentate coordi-
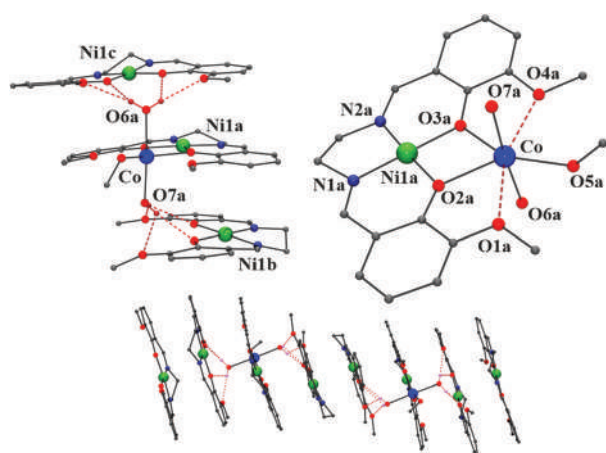

Fig. 1 Top, left, A view of the molecular unit of **1**. Top, right, partially labelled plot of the central dimeric entity. Bottom, one dimensional arrangement of pillared clusters of **1** in the network. Dark blue: cobalt, green: nickel, red: oxygen, navy: nitrogen, grey: carbon, pink: hydrogen.
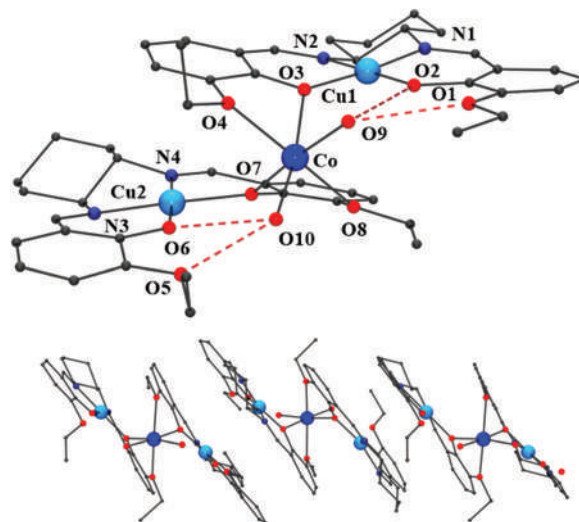

Fig. 2 Top, partially labelled plot of complex **3*SS***. Bottom, monodimensional arrangement of trimers in the network. Dark blue: cobalt, azure: copper, red: oxygen, navy: nitrogen, grey: carbon.

Table 2 Selected bond distances (Å) and angles (°) for complex **1**

Co(1a)–O(1a)	2.594(3)	Ni(1b)–N(1b)	1.843(4)
Co(1a)–O(2a)	2.125(3)	Ni(1b)–N(2b)	1.846(4)
Co(1a)–O(3a)	2.119(3)	Ni(1b)–O(2b)	1.855(3)
Co(1a)–O(4a)	2.504(3)	Ni(1b)–O(3b)	1.848(3)
Co(1a)–O(5a)	2.067(3)	Ni(1c)–N(1c)	1.853(4)
Co(1a)–O(6a)	2.064(3)	Ni(1c)–N(2c)	1.847(4)
Co(1a)–O(7a)	2.059(3)	Ni(1c)–O(2c)	1.866(3)
Ni(1a)–N(1a)	1.832(4)	Ni(1c)–O(3c)	1.846(3)
Ni(1a)–N(2a)	1.841(3)		
Ni(1a)–O(2a)	1.852(3)		
Ni(1a)–O(3a)	1.841(3)		
O(1a)–Co(1a)–O(2a)	66.04(9)	O(3a)–Co(1a)–O(5a)	145.9(1)
O(2a)–Co(1a)–O(3a)	69.3(1)	O(4a)–Co(1a)–O(5a)	80.3(1)
O(2a)–Co(1a)–O(5a)	143.3(1)	O(1a)–Co(1a)–O(5a)	78.2(1)
O(3a)–Co(1a)–O(4a)	66.9(1)	O(6a)–Co(1a)–O(7a)	175.1(1)

Table 3 Selected bond distances (Å) and angles (°) for **3*SS***

Cu(1)–O(2)	1.902(5)	Cu(2)–O(6)	1.905(5)
Cu(1)–O(3)	1.949(5)	Cu(2)–O(7)	1.958(5)
Cu(1)–N(1)	1.971(6)	Cu(2)–N(3)	1.945(6)
Cu(1)–N(2)	1.953(6)	Cu(2)–N(4)	1.956(6)
Co–O(3)	2.078(5)	Co–O(8)	2.188(6)
Co–O(4)	2.161(5)	Co–O(9)	2.014(6)
Co–O(7)	2.075(5)	Co–O(10)	1.964(6)
Cu(1)–O3–Co	126.3(3)	Cu(2)–O7–Co	125.8(3)

nation. The coordination around the Co^{II} cation is fulfilled with two water molecules, resulting a *cis*-octahedral environment. The coordination of two homochiral bidentate $L4^{2-}$ ligands leads to a Δ configuration for the Co^{II} cations. The molecule is stabilized by means of intramolecular H-bonds between the coordinated water molecules and the second pair of $O_{phenoxo}$ and one O_{ethoxo} atoms of each [Cu(L4)] fragment. In addition, the trinuclear units are linked by a large set of intermolecular H-bonds mediated by the co-crystallized solvent molecules.

Electronic circular dichroism

Chirality transfer in coordination compounds is a common feature when using enantiopure chiral ligands.[32–34] The transference of chirality for **2** and **3** from the chiral ligand to the metallic centres is not relevant for the M^{II} cations (Ni^{II}, Cu^{II}) which show an environment very close to the square planar geometry or for the trigonal bipyramidal Co^{II} cation in complexes **2**. Only for the Co^{II} cation in complexes **3** a defined Δ or Λ configuration can be observed as a consequence of its coordination with two ligands acting as bidentate. Thus, complexes **2** and **3** contains a variety of chiral centres mainly centred on the ligands. ECD spectra in methanolic solution were recorded for the enantiomeric pairs of complexes **2R**/**2S** and **3RR**/**3SS** (Fig. 3) and their mirror image confirms the enantiomeric nature of the reported complexes. The spectrum of **2R** exhibits positive Cotton effect at λ_{max} = 570(w), 410, 275, 250 and 220 and negative bands at 475, 230 and 206 nm whereas **2S** shows the same bands with opposite sign. **3RR** exhibits positive Cotton effect at λ_{max} = 485(w), 352, and 225 and negative bands at 588(w), 395, 284, 245 and 209 nm whereas **3SS** shows the same bands with opposite sign. The d–d transitions at larger wavelengths are very weak whereas the intense absorptions below 400 nm are attributed to $\pi^* \leftarrow \pi$ transitions of the ligands.
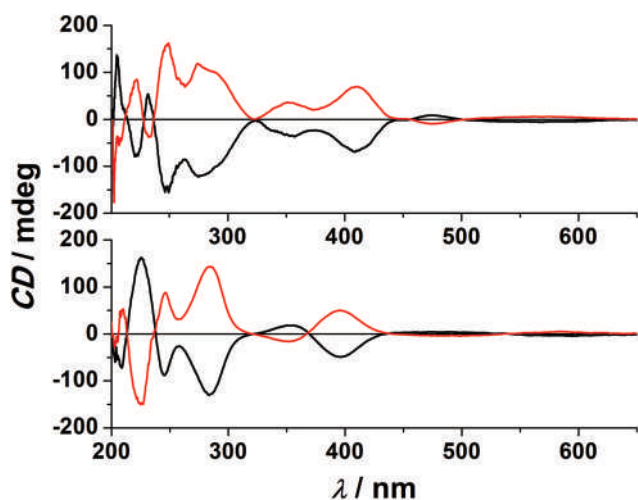
Magnetic properties

Static measurements. The magnetic susceptibility measurements for the compounds **1–3** in the form of $\chi_M T$ product *vs.* temperature were performed on polycrystalline samples in the range of 2–300 K, Fig. 4. The $\chi_M T$ values at room temperature were 3.46 cm^3 mol^{-1} K for **1**, 3.56 cm^3 mol^{-1} K for **2R** and 3.38 cm^3 mol^{-1} K for **3SS**. As expected, the $\chi_M T$ plot for **1** and **2R** are very similar, decreasing continuously upon cooling reaching the values of 2.16 and 2.03 cm^3 mol^{-1} K at 2 K, respectively. For decreasing temperature complex **3SS** shows a $\chi_M T$ decay down to a value of 0.30 cm^3 mol^{-1} K at 2 K.

Magnetization measurements for **1** and **2R** show a value of 2.32 and 2.44 $M\mu_\beta$ and an unsaturated value of 0.85 $M\mu_\beta$ for **3SS** under the maximum explored field of 5 T. Reduced magnetization experiments between 1.8–6.8 K for **1** show superimposable plots evidencing a very large D value where the only populated state is the ground effective $\frac{1}{2}m_s$ doublet, Fig. S7.†

For complexes **1** and **2R** the Ni^{II} cations are placed in a square planar environment (diamagnetic) and then, the decay of the $\chi_M T$ plot is exclusively due to the zero-field splitting of the Co^{II} cations and fit[35] of the susceptibility data revealed the determination of D = 84(1) cm^{-1}, g = 2.754(3) for **1** and D = 55(2) cm^{-1}, g = 2.777(3) for **2R**. For **3SS** the decay should be attributed to the moderately strong antiferromagnetic interaction (J) between the Cu^{II} and the Co^{II} cations mediated by the Cu–O–Co bridges. Fitting the experimental data lead to D_{ion} = −32.3(9) cm^{-1} and g = 2.430(3) while the magnitude of the interaction was calculated as $2J$ = −27.4(1) cm^{-1}.

Dynamic measurements. Preliminary alternate current measurements showed that no signals were found for the antiferromagnetically coupled complex **3**, whereas complexes **1**, **1D** and **2R** do not show out-of-phase response at zero field. However, measurements under static and increasing magnetic fields revealed well defined $\chi''_M(T)$ peaks with similar intensity in the 0.1–0.6 T range, Fig. S8.† The absence of ac response at zero field is usually attributed to quantum tunnelling of the magnetization (QTM) that usually can be suppressed by remov-

Fig. 3 Top, solution ECD spectra for the Ni/Co pair of complexes **2R** (red line) and **2S** (black line). Bottom, ECD spectra for the Cu/Co pair of complexes **3RR** (red line) and **3SS** (black line).
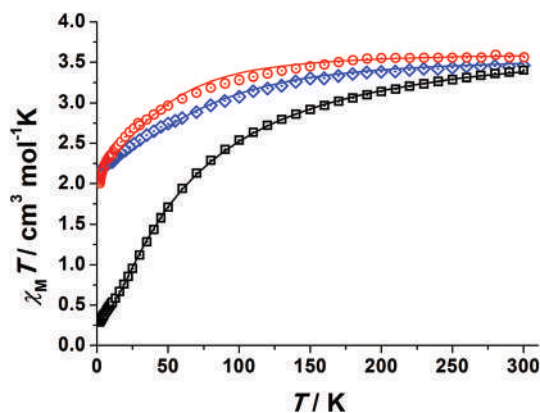

Fig. 4 $\chi_M T$ *vs.* Temperature plots for complexes **1** (blue diamonds), **2R** (red circles) and **3SS** (black squares). Solid lines show the best fit of the experimental data.

ing the $\pm m_s$ degeneration when an external dc field is applied.[36] However, this explanation cannot be applied for a $\pm 1/2$ ground Kramers doublet, as occurs in this case as a consequence of the large and positive D value in complexes **1** and **2R**.[37] The corresponding plots under different and optimal magnetic applied fields for each compound (0.2 T for **1** and **1D** and 0.1 T for **2R**) are shown in Fig. 5 and Fig. S9.† Plots of the maxima of χ''_M vs. inverse of the temperature, the so called Arrhenius plots (Fig. S10†), evidence that their dependence is not linear and only a roughly linearity can be found for the higher temperatures, indicating the presence of more than one relaxation mechanism. As a preliminary approach, the fit of the high temperature region was made using the equation $\ln(1/(2\pi\omega)) = \ln(1/\tau_0) - U_{eff}/(k_B T)$ giving low U_{eff} values, in the range of 12–30 K, and reasonable τ_0 values in the 10^{-6} to 10^{-7} range like previously reported in similar systems.[36] However, on one hand, these energy values are poorly precise due to the low number of points in the linear region and, on the other hand, the U_{eff} values, much lower than the gap with the 3/2 excited doublet, are not consistent with a thermally activated Orbach process. So, the U_{eff} values do not correspond to an archetypical over-barrier relaxation and should be attributed to an energy to achieve the next vibrational level.

A more precise analysis of the χ'_M and χ''_M behaviour was performed using the generalized Debye model,[38] where these two variables are analysed joint with τ (the relaxation rate) and α (the parameter that defines the broadness of the spectra involving the distribution in the relaxation times) represented as Argand plots (Fig. S10†).

The data extracted from the fitting is represented in the form of $\ln(\tau)$ vs. $1/T$ for complexes **1**, **1D** and **2R** (Fig. 6). For the three compounds, two different relaxations can be observed, as is confirmed in the so-called log–log plot where $\log(\tau)$ is represented in front of the $\log(T)$ (Fig. S11†). The data can be equally simulated following the combination of Orbach and Raman relaxations (eqn (1)) or following the combination of Direct and Raman relaxations (eqn (2)):

$$\tau^{-1} = \tau_0^{-1} e^{-E_a/KT} + CT^n \tag{1}$$

$$\tau^{-1} = AT + CT^n \tag{2}$$

The Orbach parameters U_{eff} and τ_0 are in good agreement with those obtained from the $\chi''_M(T^{-1})$ fit, Fig. S12,† but this relaxation mechanism is not reasonable for the $S = 1/2$ doublet and thus, the Direct plus Raman relaxation should be assumed.

The fitting parameters are summarized in Table 4, following these two different approaches mentioned above: Orbach plus Raman or Raman plus Direct. What can be seen is the difference between the values of the Raman coefficients (n) in both approximations: while the values of n in Orbach plus Raman relaxation could be attributed to optical phonons,[39] in Raman plus Direct relaxation, the values of the n parameters are an average between the expected values (2, 7–9) for Kramers ions. This could be possible probably to a mixing of different relaxation paths in the studied temperature range.

Following this second approach of Direct plus Raman relaxation, the magnetic behaviour of these two new slow relaxing compounds fully agrees with data previously reported: the low temperature region follows the Direct relaxation which can be achieved in $S = 1/2$ systems thanks to the so-called electronuc-
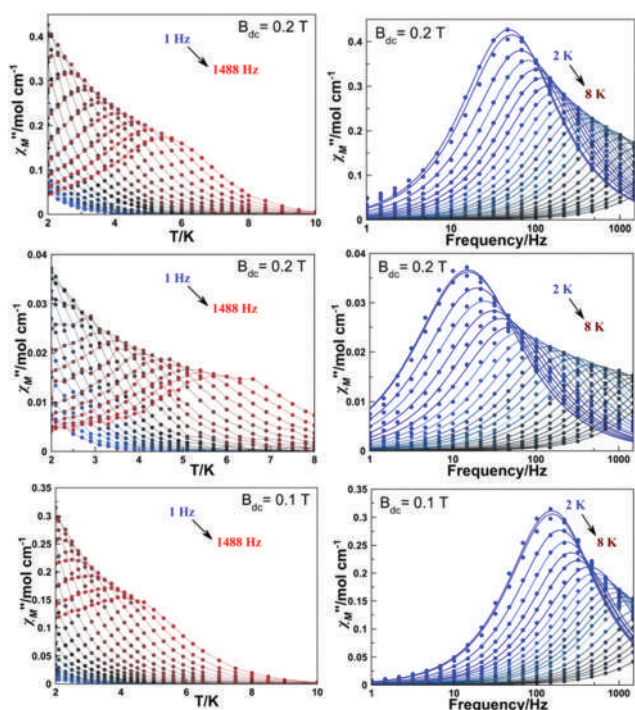

Fig. 5 Temperature (left) and frequency (right) dependence of χ''_M for complexes **1** (top), **1D** (middle) and **2R** (bottom) at different optimal applied external magnetic fields of 0.2 T for **1** and **1D** and 0.1 T for **2R**.
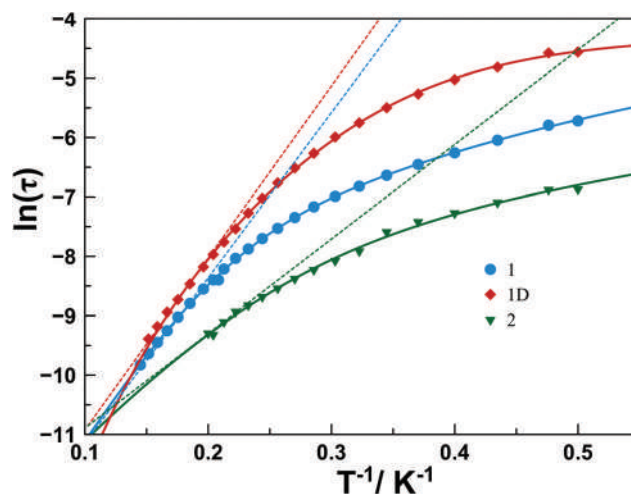

Fig. 6 Temperature dependence of the relaxation time as function of the temperature plotted as $\ln(\tau)$ vs. inverse of T. Solid lines show the best fit of the experimental data and dotted lines shows the slope of the Orbach section.

Table 4 Fitting parameters of (eqn (1)) for complexes **1**, **1D** and **2R**

Orbach+Raman

	U_{eff} (K)	τ_0 (s)	C	n
1	22.5	7.55×10^{-7}	57	2.3
1D	8.40	3.5×10^{-5}	104	3.5
2R	18.4	2.7×10^{-6}	221	2.1

Direct+Raman

	A	C	n
1	117(5)	3.8(5)	4.36(8)
1D	36(1)	0.38(3)	5.56(6)
2R	288(39)	25.0(7)	3.7(2)
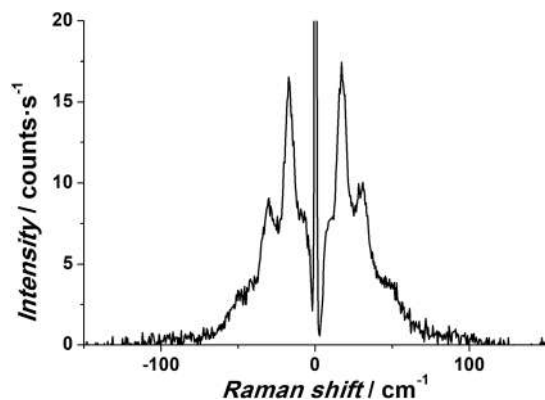
Fig. 7 Ultralow frequency Raman spectrum for complex **1** showing the absorptions at 17, 30 and the shoulders around 8 and 48 cm⁻¹.

lear coupling between the Co^II electronic spin $S = 1/2$ and the nuclear spin $I = 7/2$,[17,18] while for the high temperature region the magnetic relaxation could be achieved through spin–lattice coupling by means of a Raman relaxation with one order of magnitude larger τ for the diluted compound **1D** as consequence of the reduction of the intermolecular dipolar interactions, Fig. S13.† This intervention of the lattice can be demonstrated by the measurement of ultra-low frequency Raman spectrum for **1**, which is represented in Fig. 7. The analysis of the ultra-low Raman spectrum evidences the presence of very low frequency vibrations, appearing at 8 cm⁻¹ and 17, 30 and 48 cm⁻¹ which correspond the overtones of this first vibrational energy and are compatible with the presence of a relaxation trough spin–lattice coupling without the participation of an Orbach relaxation (see above).

Conclusions

The paper reports the structural and magnetic characterization of two [Ni$_3^{II}$Co^II] complexes that exhibit the Ni^II cations in a diamagnetic square planar environment and one [Cu$_2^{II}$Co^II] trimer antiferromagnetically coupled. The three systems were built from compartmental achiral or chiral Schiff bases that allow

the selective coordination of the Cu^II and Ni^II cations in the inner cavity of the ligands, giving different topology and nuclearities despite their similar square planar coordination. Out-of-phase signals were found for the two [Ni$_3^{II}$Co^II] systems that behaves as a Co^II mononuclear SMM taking into account the diamagnetic character of the Ni^II cation. In the light of the similar response between the non-chiral complex **1** and the closely related complex **2**, the former was selected for a wider ac study of its $S = 1/2$ analysis that show a Direct plus Raman relaxation mechanisms that for the higher temperatures can be related with the network vibrations.

Conflicts of interest

There are no conflicts to declare.

Acknowledgements

Notes and references

1 D. Gatteschi, R. Sessoli and J. Villain, *Molecular nanomagnets*, Oxford University Press, 2006.
2 R. Sessoli, D. Gatteschi, A. Caneschi and M. Novak, *Nature*, 1993, **365**, 141.
3 C. J. Milios, C. P. Raptopoulou, A. Terzis, F. Lloret, R. Vicente, S. P. Perlepes and A. Escuer, *Angew. Chem., Int. Ed.*, 2003, **43**, 210.
4 L. Gregoli, C. Danieli, A.-L. Barra, P. Neugebauer, G. Pellegrino, G. Poneti, R. Sessoli and A. Cornia, *Chem. – Eur. J.*, 2009, **15**, 6456.
5 J. Mayans, M. Font-Bardia and A. Escuer, *Dalton Trans.*, 2018, **47**, 8392.
6 S. Tripathi. A. Dey, M. Shanmugam, R. Suriya-Narayanan and V. Chandrsekhar., *Co(II) Complexes as Single-Ion Magnets*, Springer International Publishing, 2018.
7 M. Murrie, *Chem. Soc. Rev.*, 2010, **39**, 1986.
8 G. A. Craig and M. Murrie, *Chem. Soc. Rev.*, 2015, **44**, 2135.
9 O. Waldmann, *Inorg. Chem.*, 2007, **46**, 10035.
10 F. Neese and E. I. Solomon, *Inorg. Chem.*, 1998, **37**, 6568.
11 D. E. Freedman, W. H. Harman, T. D. Harris, G. J. Long, C. J. Chang and J. R. Long, *J. Am. Chem. Soc.*, 2010, **132**, 1224.
12 C.-Y. Lin, J. C. Fettinger, F. Grandjean, G. J. Long and P. P. Power, *Inorg. Chem.*, 2014, **53**, 9400.
13 S. Vaidya, A. Upadhyay, S. K. Singh, T. Gupta, S. Tewary, S. K. Langley, J. P. S. Walsh, K. S. Murray, G. Rajaraman and M. Shanmugam, *Chem. Commun.*, 2015, **51**, 3739.
14 J. M. Zadrozny, J. Telser and J. R. Long, *Polyhedron*, 2013, **64**, 209.
15 J. Mayans and A. Escuer, *Chem. Commun.*, 2021, **57**, 721.

16 E. Pilichos, M. Font-Bardia, J. Mayans and A. Escuer, *Dalton Trans.*, 2022, **51**, 1779.

17 L. Tesi, E. Lucaccini, I. Cimatti, M. Perfetti, M. Mannini, M. Atzori, E. Morra, M. Chiesa, A. Caneschi, L. Sorace and R. Sessoli, *Chem. Sci.*, 2016, **7**, 2074.

18 S. Gómez-Coca, A. Urtizberea, E. Cremades, P. J. Alonso, A. Camón, E. Ruiz and F. Luis, *Nat. Commun.*, 2014, **5**, 4300.

19 E. König, R. Schnakig and B. Kanellakopoulos, *J. Phys. Chem.*, 1975, **62**, 3907.

20 F. Shao, B. Cahier, N. Guihery, E. Riviere, R. Guillot, A.-L. Barra, Y. Lan, W. Wernsdorfer, V. E. Campbell and T. Mallah, *Chem. Commun.*, 2015, **51**, 16475.

21 F. Shao, B. Cahier, E. Rivière, R. Gullot, N. Guihéry, V. E. Campbell and T. Mallah, *Inorg. Chem.*, 2017, **56**, 1104.

22 T. J. Woods, M. F. Ballesteros-Rivas, S. Gómez-Coca, E. Ruiz and K. R. Dunbar, *J. Am. Chem. Soc.*, 2016, **138**, 16407.

23 G. M. Sheldrick, *SHELXL-2014/7: Program for the Solution of Crystal Structures*, University of Göttingen, Göttingen, Germany, 2014.

24 G. A. Bain and J. F. Berry, *J. Chem. Educ.*, 2008, **85**, 532.

25 N. F. Curtis, *J. Coord. Chem.*, 1977, **7**, 89.

26 Z. Guo, L. Li, T. Xu, J. Li and D. Wang, *Acta Crystallogr., Sect. E: Struct. Rep. Online*, 2009, **65**, m1158.

27 S. Hazra, R. Koner, M. Nayak, H. A. Sparkes, J. A. K. Howard, S. Dutta and S. Mohanta, *Eur. J. Inorg. Chem.*, 2009, 4887.

28 M. Nayak, R. Koner, H.-H. Lin, U. Florke, H.-H. Wei and S. Mohanta, *Inorg. Chem.*, 2006, **45**, 10764.

29 M. Nayak, S. Hazra, P. Lemoine, R. Koner, C. R. Lucas and S. Mohanta, *Polyhedron*, 2008, **27**, 1201.

30 S. Majumder, R. Koner, P. Lemoine, M. Nayak, M. Ghosh, S. Hazra, C. R. Lucas and S. Mohanta, *Eur. J. Inorg. Chem.*, 2009, 3447.

31 SHAPE v.2.0. M. Lunell, D. Casanova, J. Cirera, P. Alemany and S. Alvarez, Barcelona 2010. The program can be obtained by request to the authors.

32 J. Crassous, *Chem. Soc. Rev.*, 2009, **38**, 830.

33 H. Miyake, *Symmetry*, 2014, **6**, 880.

34 M. Liu, L. Zhang and T. Wang, *Chem. Rev.*, 2015, **115**, 7304.

35 N. F. Chilton, R. P. Anderson, L. D. Turner, A. Soncini and K. S. Murray, *J. Comput. Chem.*, 2013, **34**, 1164.

36 S. Hill, S. Datta, J. Liu, R. Inglis, C. J. Milios, P. L. Feng, J. J. Henderson, E. del Barco, E. K. Brechin and D. N. Hendrickson, *Dalton Trans.*, 2010, **39**, 4693.

37 A. Switlicka, B. Machura, R. Kruszynski, N. Moliner, J. M. Carbonell, J. Cano, F. Lloret and M. Julve, *Inorg. Chem. Front.*, 2020, **7**, 4535.

38 K. S. Cole and R. H. Cole, *J. Chem. Phys.*, 1941, **9**, 341.

39 L. Gu and R. Wu, *Phys. Rev. B*, 2021, **103**, 014401.

"Slow magnetic relaxation for cobalt(II) complexes in axial bipyramidal environment: an *S* = ½ spin case."

Evangelos Pilichos,[a] **Mercè Font-Bardia,**[b] **Joan Cano,**[c] **Albert Escuer,**[*a] **and Júlia Mayans** [*a]

[a] Departament de Química Inorgànica i Orgànica, Secció Inorgànica and Institute of Nanoscience (IN^{2}UB) and Nanotecnology, Universitat de Barcelona, Martí i Franquès 1-11, Barcelona-08028, Spain.

[b] Departament de Mineralogia, Cristal·lografia i Dipòsits Minerals, Universitat de Barcelona, Martí Franqués s/n, 08028 Barcelona (Spain) and Unitat de Difracció de R-X. Centre Científic i Tecnològic de la Universitat de Barcelona (CCiTUB), Solé i Sabarís 1-3. 08028 Barcelona.

[c] Instituto de Ciencia Molecular (ICMol), Universitat de València, 46980 Paterna (València), Spain

1- Characterization.

Fig. S1. Powder X-ray spectra of the reference complex **1** and its diluted analogous **1D**.
Fig. S2. IR spectra for complexes **1** and **1D**
Fig. S3. IR spectra for complexes **2** and **3**.

2-Structural aspects.

Table S1. SHAPE measures for the Co^{II} cation of complex **1**.
Fig. S4. Plot of the coordination sphere of the Co^{II} cation for complex **1**,
Fig. S5. Detail of the H-bonds promoted for complex **1**.
Table S2. Bond parameters for the bifurcated H-bonds corresponding to complex **1**.
Fig. S6. Molecular structure of complex **2R** from the partial structure resolution.

3-Magnetic data.

Fig. S7. Left, magnetization *vs.* field for complexes **1**, **2R** and **3SS**. Right, reduced magnetization for complex **1**.
Fig. S8. χ_M'' dependence of the transverse field for complexes **1** and **2R**.
Fig. S9. χ_M'(*T*) and . χ_M'(*v*) for complexes **1**, **1D** and **2R**.
Fig. S10. Argand plots for complexes **1**, **1D** and **2R.**
Fig. S11. Log-log plot for complex **1**.
Fig. S12. Plot of ln(1/2πν) vs. T^{-1} from the χ_M''(*T*) data for complexes **1**, **1D** and **2**.
Fig. S13. Plot of τ *vs.* inverse of temperature showing the low temperature increase of *t* for the diluted complex **1D**.
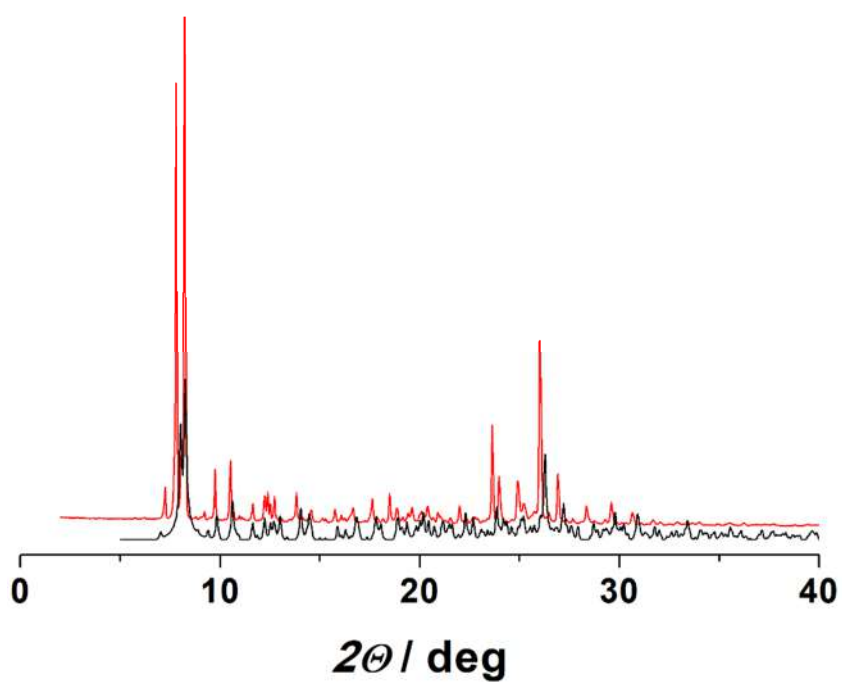
1- Characterization.

Fig. S1. Powder X-ray spectra of the reference complex **1** (black line) and its diluted analogous **1D**.
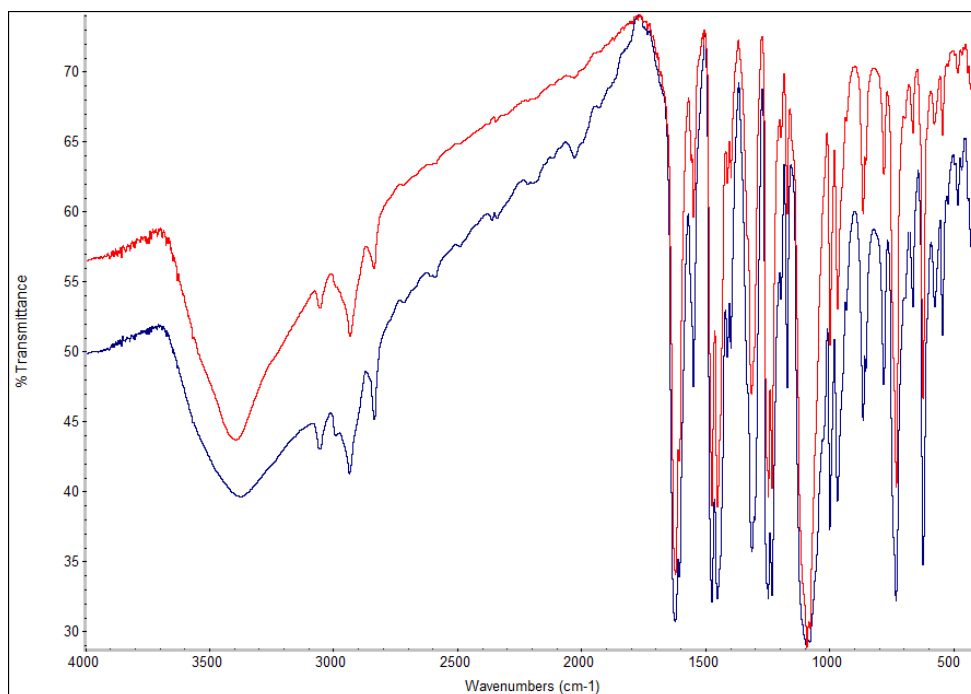

Fig. S2. IR spectra for complexes **1** (red) and **1D**. Characteristic bands: st. C-H 3000-2800 cm^{-1}; N=C iminic ~1600 cm^{-1}; st. ClO$_4^-$ 1075 cm^{-1}; δ ClO$_4^-$ 620 cm^{-1}.
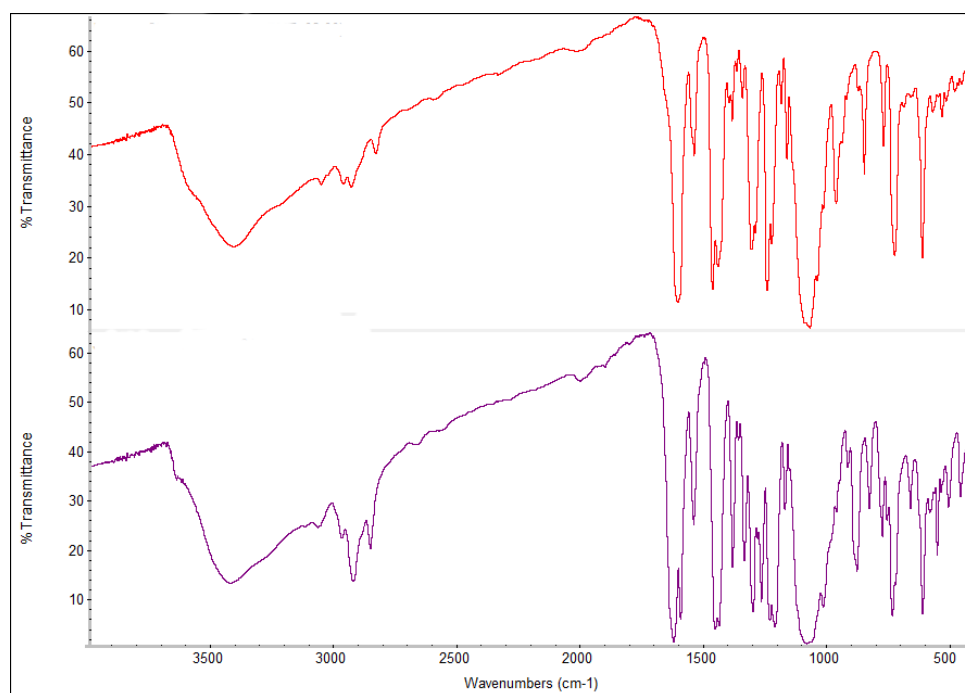
Fig. S3. IR spectra for complexes **2** (top) and **3** (bottom).

2-Structural aspects.

Table S1. SHAPE measures for the Co^{II} cation of complex **1**. $S(P) = 0$ corresponds to a structure fully coincident in shape with the reference polyhedron P, regardless of size and orientation. The closest polyhedron is highlighted in red.

S(vOC-5)	6.80	S(PBPY-7)	**1.64**
S(TBPY-5)	6.82	S(COC-7)	8.17
S(SPY-5)	6.79	S(CTPR-7)	6.59
S(JTBPY-5)	8.81	S(JPBPY-7)	3.60

Ideal ML$_5$ polyhedra: vOC-5 (C$_4$v)   Vacant octahedron; TBPY-5 (D$_3$h) Trigonal bipyramid; SPY-5 (C$_4$v) Spherical square pyramid; JTBPY-5 (D$_3$h) Johnson trigonal bipyramid J12.
Ideal ML$_7$ polyhedra: PBPY-7   (D5h)   Pentagonal bipyramid; COC-7   (C3v)   Capped octahedron; CTPR-7   (C2v)   Capped trigonal prism; JPBPY-7   (D5h)   Johnson pentagonal bipyramid J13; JETPY-7   (C3v)   Johnson elongated triangular pyramid J7.
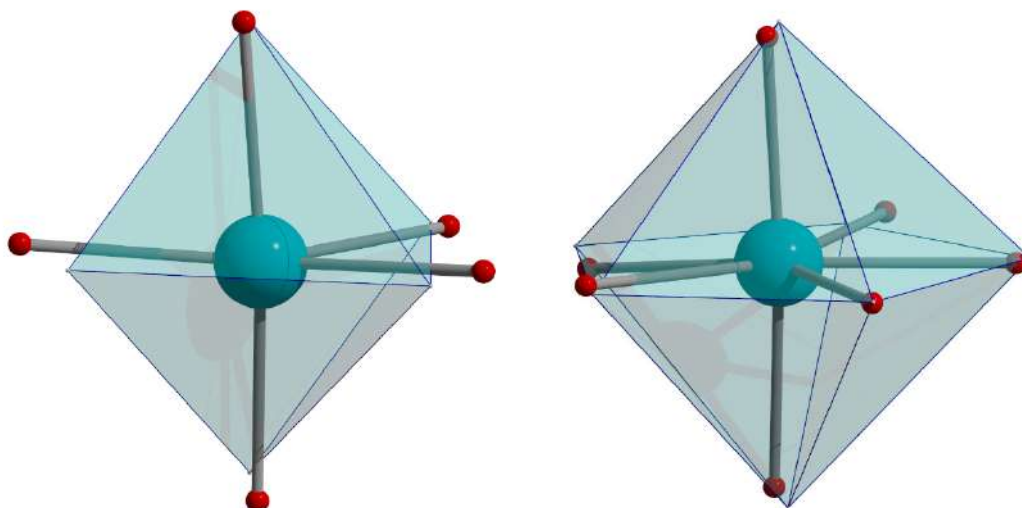
Fig. S4. Plot of the coordination sphere of the Co^{II} cation for complex **1**, referenced to the ideal polyhedra trigonal bipyramid (left) and pentagonal bipyramid (right).
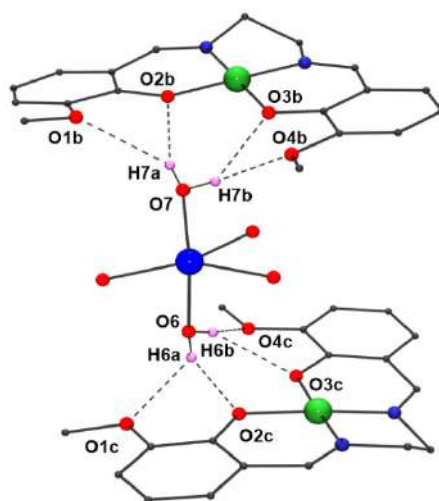

Fig. S5. Detail of the H-bonds promoted by the axially coordinated water molecules and the capping [NiL1] fragments for complex **1**.

Table S2. Bond parameters for the bifurcated H-bonds corresponding to complex **1**.

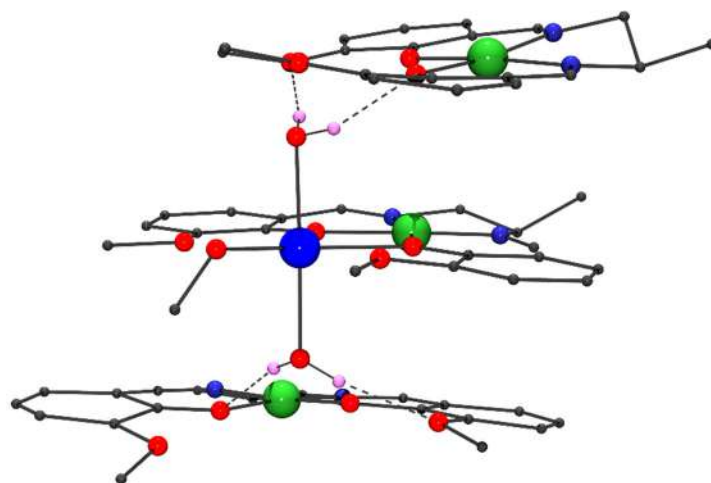|	d O$\cdots$O' (Å)		d H$\cdots$O' (Å)		O-H$\cdots$O (deg.)
O6$\cdots$O1c	2.976(4)	H6a-O1c	2.29(3)	O6-H6a$\cdots$O3c	127(2)
O6$\cdots$O2c	2.761(4)	H6a-O2c	2.10(2)	O6-H6a$\cdots$O4c	159(3)
O6$\cdots$O3c	2.848(4)	H6b-O3c	2.35(3)	O6-H6b$\cdots$O1c	135(3)
O6$\cdots$O4c	2.861(4)	H6b-O4c	2.03(2)	O6-H6b$\cdots$O2c	152(3)
O7$\cdots$O1b	3.010(4)	H7a-O1b	2.46(3)	O7-H7a$\cdots$O1b	127(3)
O7$\cdots$O2b	2.804(4)	H7a-O2b	2.04(3)	O7-H7a$\cdots$O2b	160(3)
O7$\cdots$O3b	2.860(4)	H7b-O3b	2.34(4)	O7-H7b$\cdots$O3b	123(3)
O7$\cdots$O4b	2.971(5)	H7b-O4b	2.20(4)	O7-H7b$\cdots$O4b	161(3)

Fig. S6. Molecular structure of complex **2R** from the partial structure resolution.
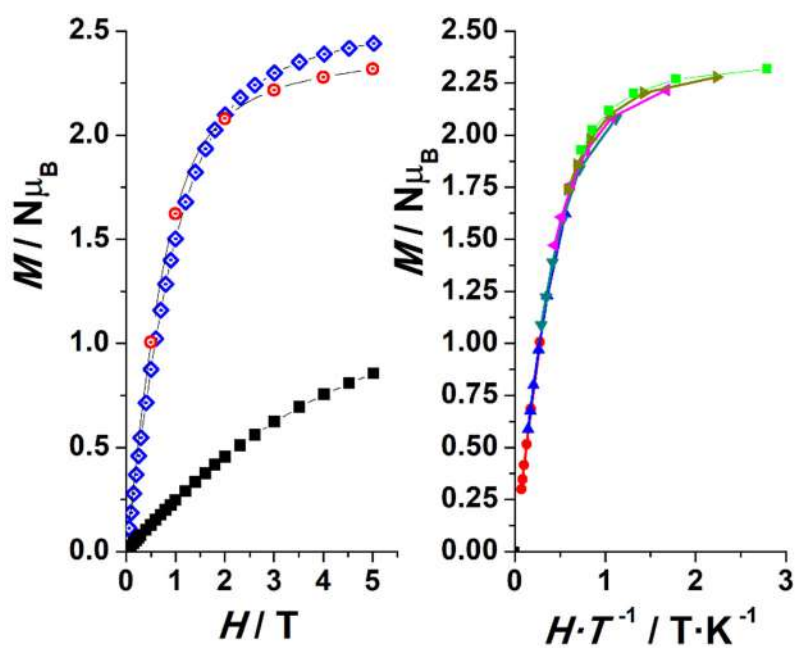
3-Magnetic data.

Fig. S7. Left, magnetization *vs*. field for complexes **1** (red circles), **2R** (blue diamonds) and **3SS** (black squares). Right, reduced magnetization for complex **1** showing the superimposable plots in the 1.8-6.8 range of temperature (increment 1 K).
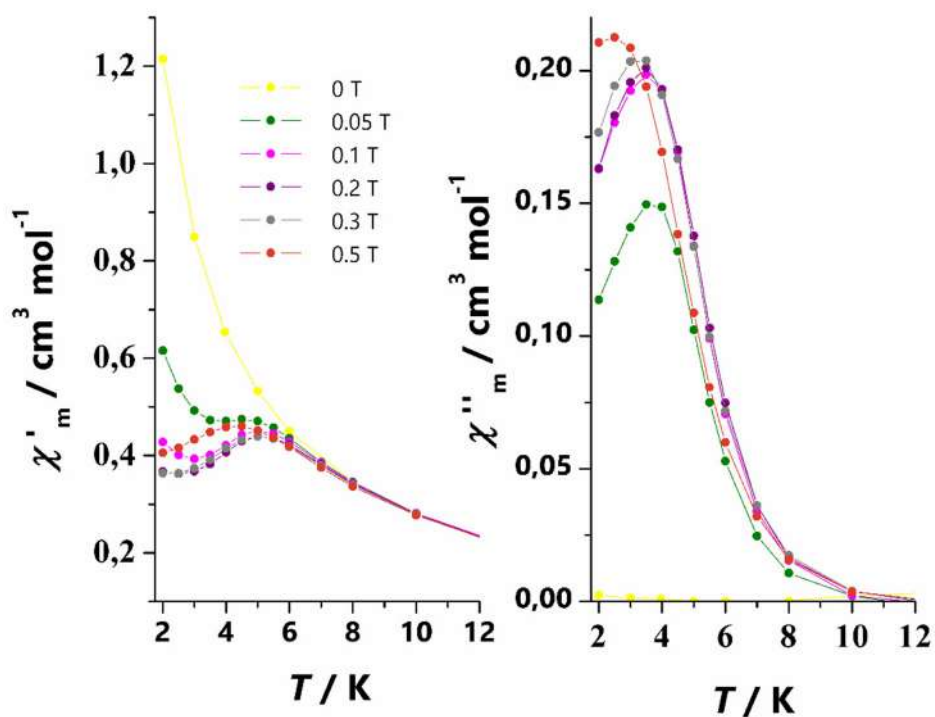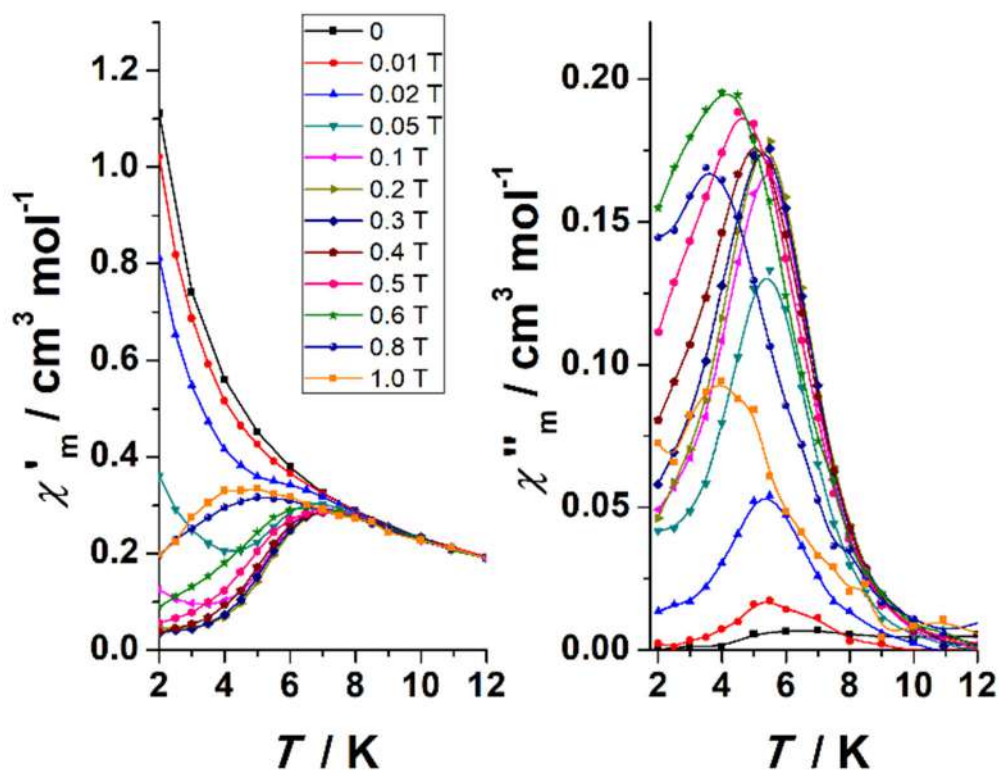
Fig. S8. χ_M'' dependence of the transverse field for complexes **1** (top) and **2R** (bottom).
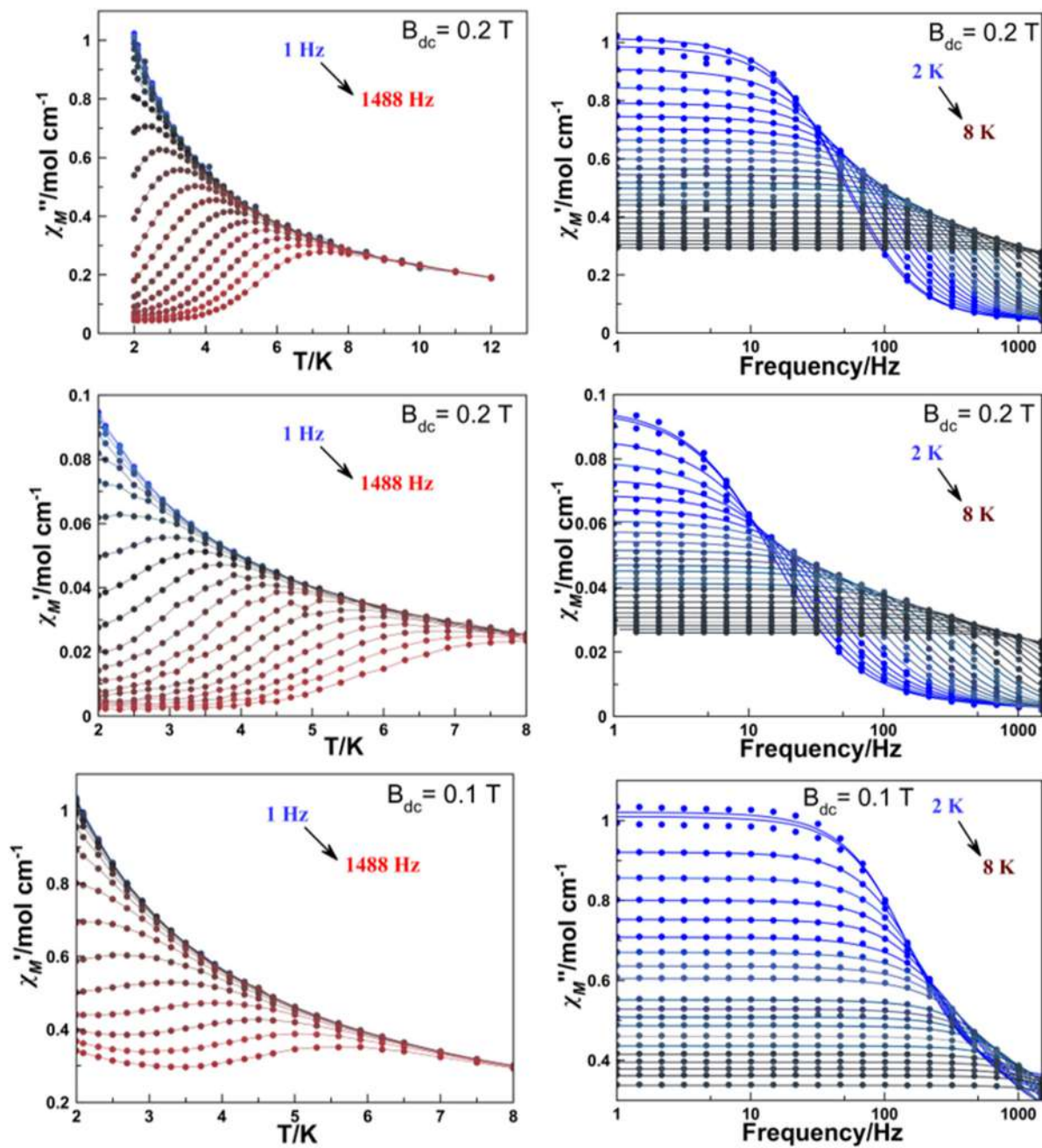
Fig. S9. $\chi_M'(T)$ and . $\chi_M'(v)$ for complexes **1**, **1D** and **2R**.
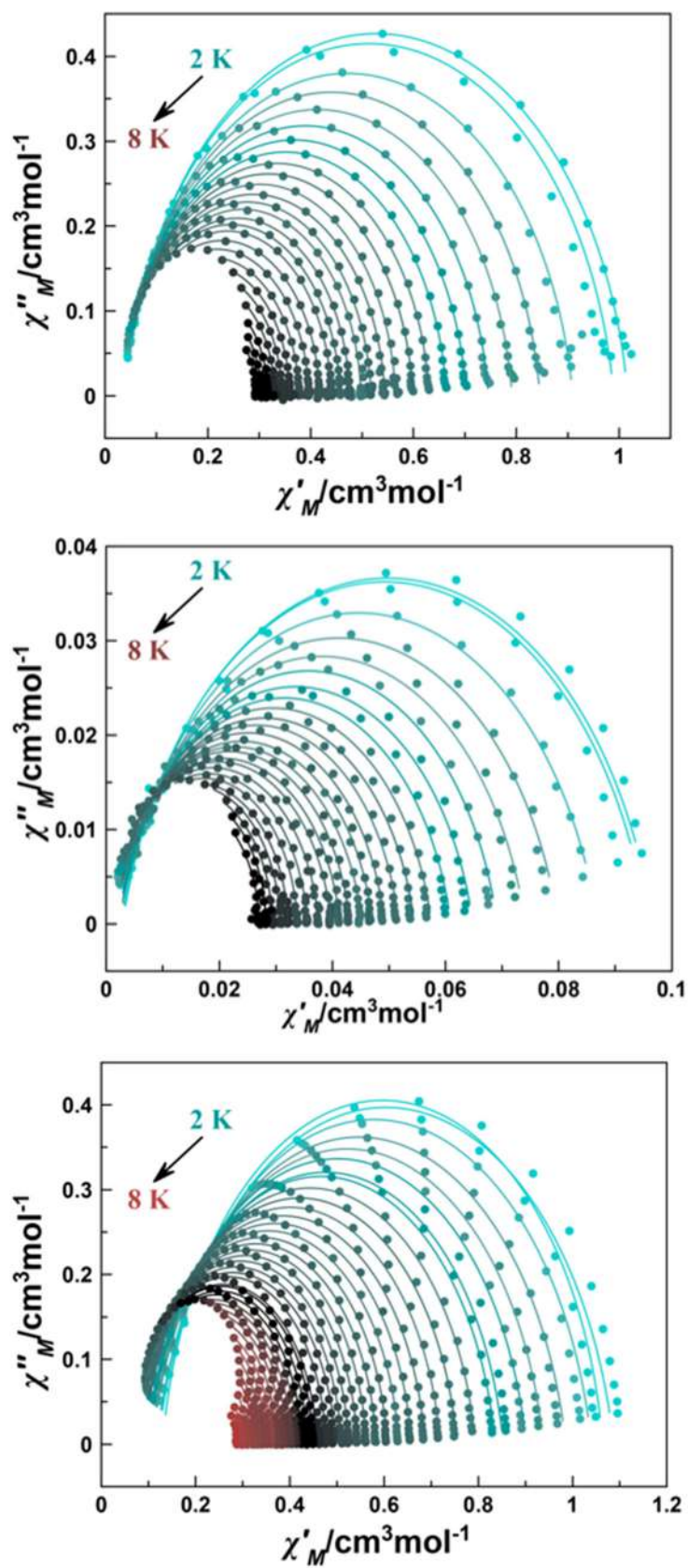
Fig. S10. Argand plots for complexes **1**, **1D** and **2R**. Solid lines show the best fit of the experimental data.
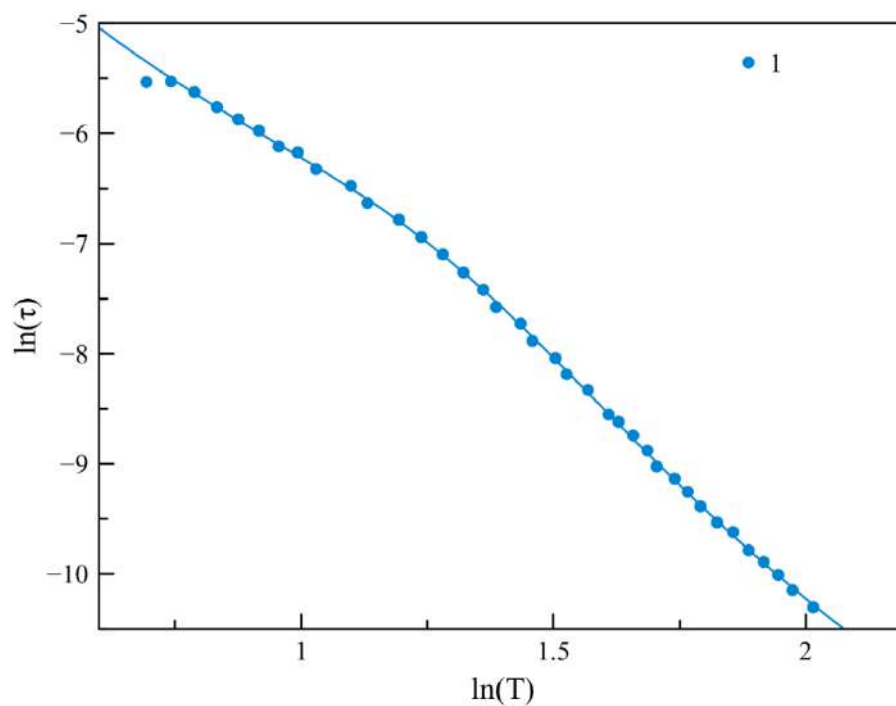
Fig. S11. Temperature dependence of the relaxation time of **1** plotted in log-log scale. The two different slopes at low and high temperature hints at dominant direct and Raman processes in the two temperature regions.
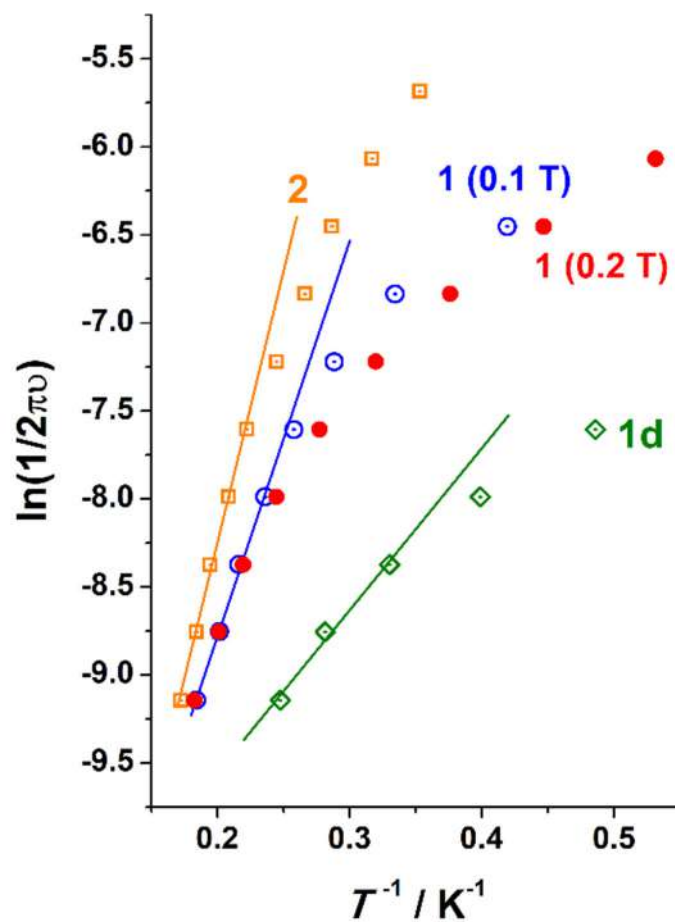
Fig. S12. Plot of $\ln(1/2\pi\nu)$ vs. T^{-1} from the $\chi_M''(T)$ data for complexes **1**, **1D** and **2R**. The data are limited to the HF region for which the maxima of χ_M'' can be observed.

Fig. S13. Plot of τ *vs*. inverse of temperature showing the lowtemperature increase of *t* for the diluted complex **1D**.

CHAPTER 6

General Discussion

Despite the relatively large number of compounds that appear in this Thesis, there are some important facts that should be mentioned. In this Chapter, the main features, observations and conclusions of each Chapter will be mentioned.

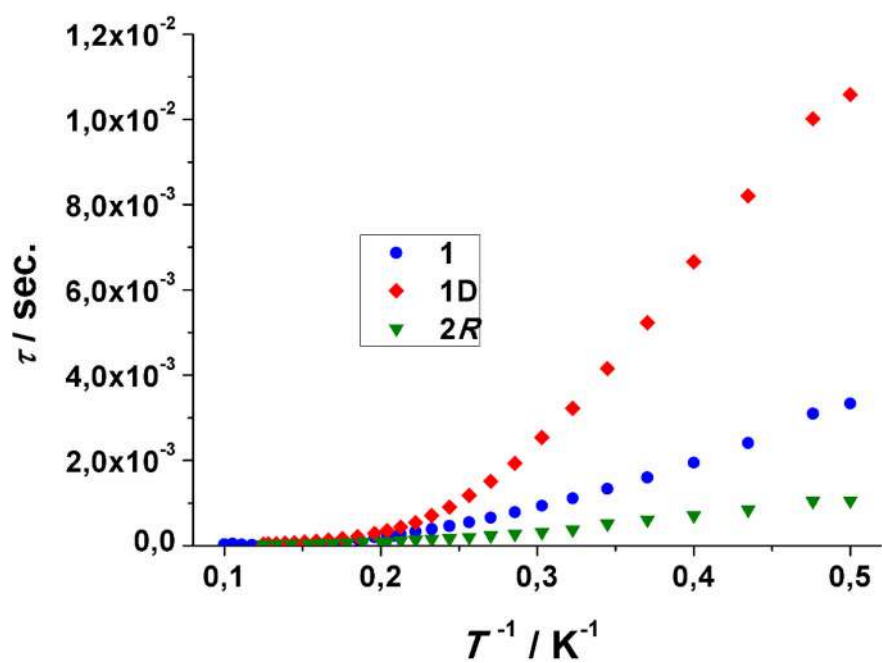In the first Chapter, lanthanide(III) cations were used as spin carriers in a series of different ligands; one neutral, N-rich double Schiff base ligand, a phosphine oxide ligand and finally a bigger, more flexible ligand. In all the cases, apart from the common building blocks for SMMs/SIMs, such as Dy^{III}, other cations, less used in this field were used. From these series there are two main conclusions that are needed to be pointed out. The first point is that, Ce^{III} has the "disadvantage" that it has a low spin value $S = \frac{1}{2}$. However, it processes enough spin-orbit coupling and magnetic relaxation can occur. The other really interesting point is the occurrence of slow relaxation of magnetization in Gd^{III} complex. The reason behind this behavior is the distortions of the geometry around the cation that can induce very low values of D. These D values, sometimes even lower than 0.1 cm^{-1}, are not detectable with any magnetometry and thus EPR experiments were necessary in order to extract this value.

Based on the fact that Gd^{III} can present slow relaxation of magnetization, we thought to try to build SMMs with other cations with isotropic or quasi-isotropic nature. So, we turned out interest to cations such as Mn^{II} and Cu^{II}. The reason to do this was to clarify if reversal of magnetization can be observed to polynuclear compounds which possess weak anisotropy with different nuclearities and ground spin states S.

In *Publication#3* the complexes **11**-**14** have four different spin states; 3/2, 2, 0 and 4, respectively. The different ground states are defined by the coupling scheme that is shown in Fig. 93. Dynamic magnetic measurements revealed that the complexes **11**, **12** and **14** show single-molecule magnet behavior. As happened with Gd^{III} complexes, the origin of the weak magnetic anisotropy is hidden in the strongly distorted hepta- or octacoordinated environment around the Mn^{II} cation. At this point it should be mentioned that, the relaxation in this kind of systems cannot happen via Orbach mechanism due to the intrinsic nature of the double-well. When the D is very weak and the spin state relatively small the barrier takes a very low value and can be overcome even at 4 K.
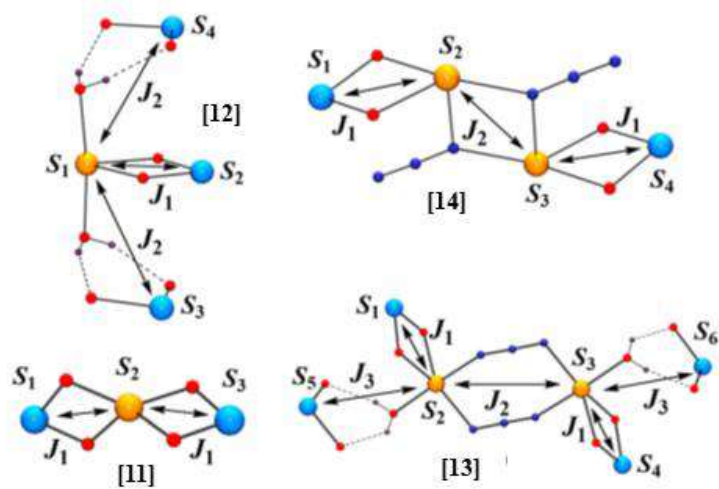
Figure 93: Coupling scheme for complexes **11**-**14.**

In the light of these results, we wanted to clarify whether the magnetic properties arise exclusively from the Mn^{II} cations. Thus, we used similar ligands in order to synthesize Ni^{II}-Mn^{II} complexes where the Ni^{II} cation would be in a square planar environment and thus diamagnetic. Fig. 94 shows the ligands were used for this purpose. As can be observed there two cavities in all cases, where the inner cavity N_2O_2 provides the planarity needed for Ni^{II} cation to adopt the square planar geometry.
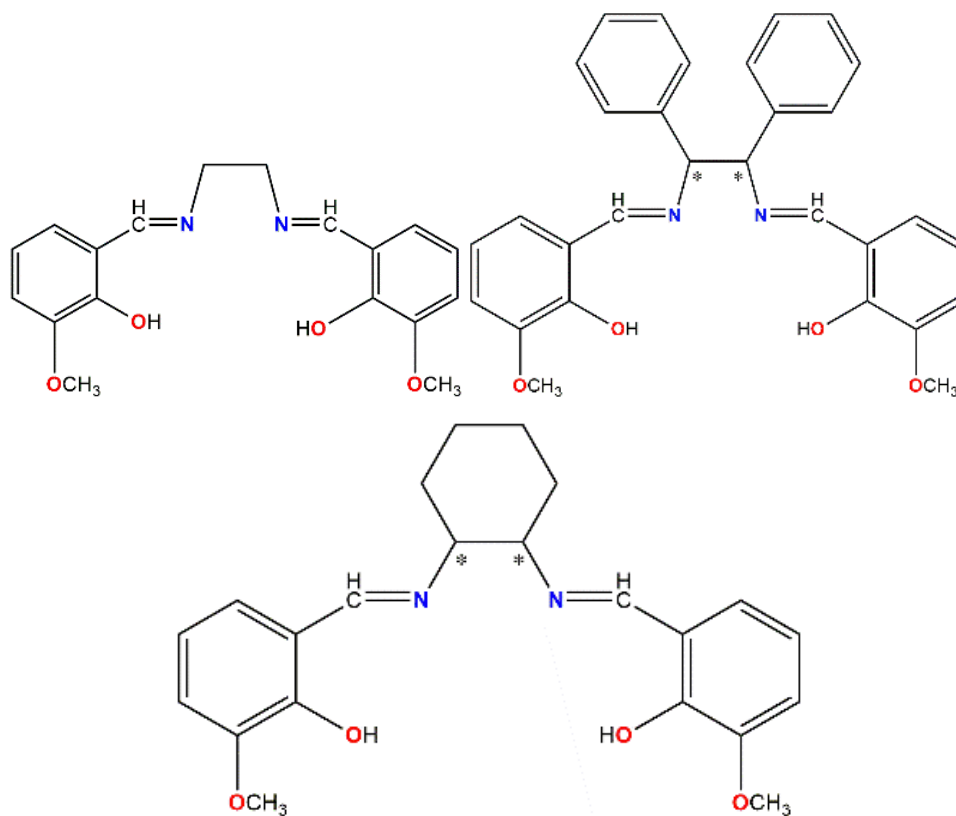
Figure 94: Structural formula of ligands employed in Chapter 4.

The Mn^{II} cation showed different coordination numbers, ranging from four to eight, with strongly distorted geometries. Also, in order to increase the nuclearity of the complexes azido ligands were used. Indeed, in complex **30** the end-to-end coordination mode of the azides led to isolation of a dinuclear complex (Fig. 95) that, until today, presents the higher spin ground state ($S = 5$) in the family of isotropic SMMs. All the complexes that synthesized showed slow relaxation of magnetization that governed from Direct and Raman mechanisms.
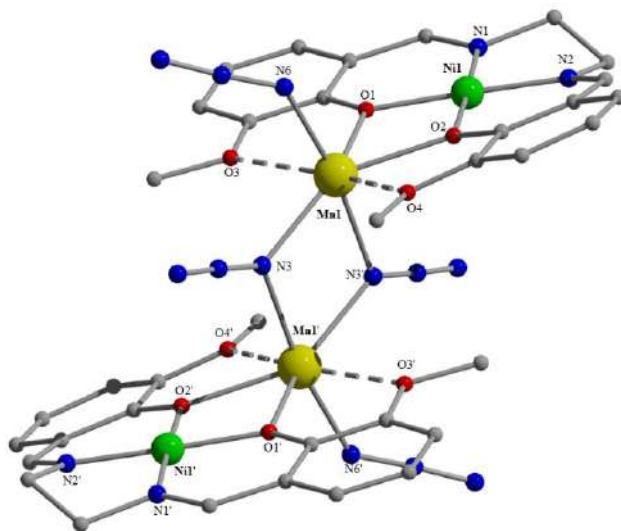
Figure 95: Partially labeled plot of complex **30**.

At this point, we can conclude that when the Mn^{II} cation is positioned in a strongly distorted environment then a small anisotropy is induced and slow relaxation of magnetization could be observed. Also, we can conclude that in order to observe relaxation there is no need to have in a compound another paramagnetic and/or anisotropic cation,

However, still there is no clear explanation in the question why this is happening. In a try to search in depth the Mn^{II} magnets, we synthesized mononuclear coordination compounds in order to make sure that the magnetism is exclusively due to manganese and secondly to decide which is the decisive factor for the presence of magnetic relaxation.

In Section 4.3, we studied three series of Mn^{II} complexes where a clear tendency was observed: when chloro ligands were bound to the metal center then relaxation of magnetization occurred; when heavier atoms were coordinated this behavior disappeared. Thus, in order to have a clear picture we used a flexible, neutral ligand (L13) and the only changes we made were in the coordination sphere of Mn^{II} using Cl^-, Br^-, I^- and SCN^- as terminal ligands. By doing this we ensure that the complexes would have same vibrational modes and the only thing that changes is the ligand field promoted by the ligands. Magnetic studies revealed that the *D* value increases with the atomic number of the terminal ligand ($D_{Cl} \ll D_{Br} < D_I$). Also, dynamic measurements showed that only the complexes with Cl^- and SCN^- ligands responded in the ac experiments.

181

The above mentioned experimental facts proved for the first time that relaxation that occurs in these systems is independent of the ligand field promoted by the ligands. Instead, the presence of very low D values is enough to induce mixing of the m_s states and relaxation can be observed. On the other hand, when D is larger (such as the cases of Br⁻ and I⁻ complexes) the m_s doublets are enough separated to give a barrier with (DS^2-1/4) value of just few wavenumbers that can be overcome even at low temperature.

Finally, working with a more anisotropic cation, such as Co[II], the magnetic behavior of complexes **44**-**46** showed some interesting features. Reduced magnetization measurements for **44** (Fig. 96) showed superimposable plots, which evidence the presence of very high magnetic anisotropy. Indeed, D value found to be equal to 84 cm⁻¹. That means, that the m_s doublets are well separated and the only populated state is the effective m_s = ½ doublet. In this case, the alternate current measurements were fitted in the same manner as the complexes of Mn[II], i.e. Direct plus Raman relaxation mechanisms. The same behavior showed also complex **45**. In Table 14, there is a summary with the parameters for all the complexes that present these two processes.
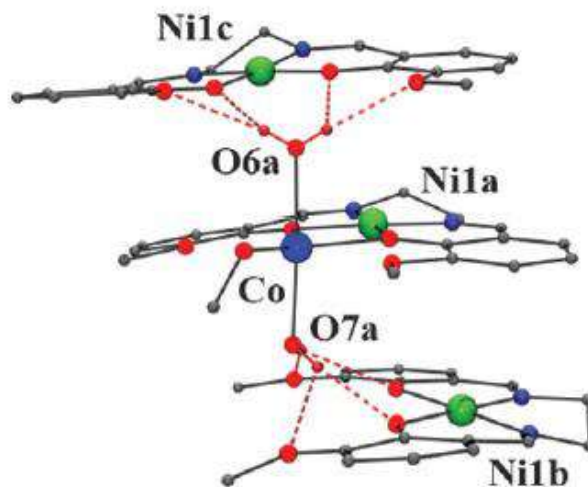
Figure 96: Partially labeled plot of complex **44**.

Table 14: Fitting parameters for the compounds that relax via Raman, Direct and QTM relaxation mechanisms.

Complex	C	n	QT	A
20	2.011	4.38	9745	-
21	0.001	8.4	-	20714
22 (3500 G)	$2.9 \cdot 10^{-4}$	9.1	-	1847
22 (6000 G)	0.95	5.23	-	6232
24 (3000 G)	56.0	2.84	-	411
24 (6000 G)	2.10	3.82	-	592
25	0.17	6.0	-	16956
27 (3500 G)	0.03	6.7	-	6558
27 (6000 G)	0.95	5.2	-	6232
28	0.0004	9.38	-	40877
29	0.0032	5.7	-	2839
30 (1500 G)	0.134	4.57	$5.83 \cdot 10^{3}$	$1.72 \cdot 10^{3}$
30 (3000 G)	1.321	3.72	$4.57 \cdot 10^{3}$	$4.3 \cdot 10^{3}$
30 (5000 G)	0.3217	4.46	-	767
31	1.343	4.61	-	2489
32	30.363	2.78	-	560
35	0.005	6.38	-	4126
38	0.026	2.87	-	2.163
43	0.036	5.1	-	2380
44	3.8	4.36	-	117
44-Diluted	0.38	5.56	-	36
45	25	3.7	-	288

CONCLUSION

The main conclusions of this Thesis are the following:

- Lanthanide(III) cations are the widely used in the field of molecular magnetism; especially the trivalent cations of Dy^{III} and Tb^{III} are the most used for the building of SMMs. However, the isotropic member of the family, Gd^{III} ($^8S_{7/2}$ and $g_J = 2$), can present field-induced relaxation of magnetization, when the cation shows strongly distorted geometries which can induce weak anisotropy. This small anisotropy, can break the degeneracy of the ground state and lead to SRM.

- Schiff base ligands found to be adequate for this purpose, as they can induce the desired distortions to the cation.

- Due to the small anisotropy, the energy barriers that derive from these systems are very low in magnitude, and can be overcome even at very low temperatures. Thus, over-barrier relaxation mechanism (Orbach relaxation) is not operative, and different spin-phonon mechanisms have to be taken into consideration.

- SRM can be extended also to Mn(II) systems; the distorted environment of the cation can induce a weak anisotropy and under an applied field to SMM/SIM behavior.

- The factor that governs the relaxation of magnetization is the presence of small D; in this case the m_s doublets are mixed and in the presence of an applied field SRM can occur. However, since the barriers are very small, like in the cases of Gd(III), the mechanisms that govern the relaxation are Direct and Raman.

- Due to the fact that D is very small, conventional magnetic measurements cannot give reliable results. Thus, EPR becomes of paramount importance due to its high sensitivity.

RESUM EN CATALÀ

La tesis doctoral "Synthesis and Magnetic Studies of QuasiIsotropic Coordination Compounds with 3d and 4f cations" ha estat duta a terme al laboratori de Magnetisme Molecular del Departament de Química Inorgànica i Orgànica de la Universitat de Barcelona.

La present tesis doctoral estudia la coordinació de lligands tipus Base de Schiff a diferents cations paramagnètics per a estudiar els seu comportament magnetoquímica i la seva relaxació lenta de la magnetització (SMR). Tots els compostos que es presenten han estat sintetitzats, caracteritzats estructuralment i magnèticament.

Un dels paradigmes de la relaxació lenta de la magnetització ha estat sempre la necessària existència d'una elevada anisotropia magnètica (parametritzada com a D o *axial zero field splitting*) de la quan en depèn la barrera d'energia potencial necessària per a presentar SMR.

La present tesi doctoral, ajuda a demostrar que aquest paràmetre D pot ser gairebé negligible i dóna lloc al que hem anomenat *quasi-isotropic slow relaxation of the magnetization systems*, ja que els sistemes que aquí es discuteixen estan derivats de cations paramagnètics isotròpics (i per tant amb una D gairebé negligible) i tot i així presenten comportament SMR.

Els cations escollits per a estudiar la propietat de relaxació lenta en sistemes isotròpics han estat els cations amb capes semiplenes com el Mn^{II} i Gd^{III}. El Gd^{III} presenta una distribució electrònica dels seus electrons f completament esfèrica i per tant sense possibilitat d'anisotropia, mentre que el Mn^{II} ha permès manipular la seva geometria i camp cristal·lí per demostrar que (i) a mida que s'augmenta la seva anisotropia mitjançant la introducció de diferents àtoms donadors en la seva esfera de coordinació va perdent caràcter de SMR i (ii) que a mida que augmenta la distorsió del seu entorn de coordinació també augmenta el seu caràcter SMR.

Les mesures acurades del comportament SMR s'han realitzat amb SQUID. Degut a que aquesta classe de SMR no pot transcórrer a través de la barrera d'energia potencial, mesures específiques d'espectroscòpies d'ultra baixa freqüència han demostrat que, efectivament, els mecanismes de relaxació magnètica no transcorren a través d'una barrera energètica. Els valors de les anisotropies magnètiques dels compostos (axial i romboèdrica) s'han dut a terme mitjançant mesures d'EPR.

LITERATURE

[1] O. Kahn. *Molecular magnetism.* VCH, Weinheim, **1993**.

[2] R. Bagai, G. Christou. *Chem. Soc. Rev.* **2009**, 38, 1011.

[3] G.A. Bain, J.F. Berry. *J. Chem. Educ.* **2008**, 85, 4, 532.

[4] C. Benelli, D. Gatteschi. *Intorduction to Molecular Magnetism: From Transition Metals to Lanthanides.* Wiley-VCH, Weinheim, **2015**.

[5] P.W. Anderson. *Magnetism.* **1963**, 1, 25.

[6] J. S. Miller, A.J. Epstein. *Agew. Chem. Int. Ed. Engl.* **1994**, 33, 385.

[7] D. Gatteschi, R. Sessoli, J. Villain. *Molecular Nanomagnets.* Oxford University Press, Oxford, **2006**.

[8] J. V. Yakhmi. *Bull. Mater. Sci.* **2009**, 3, 217.

[9] a) J. S. Miller, J. C. Calabrese, H. Rommenlmann, S. R. Chittipeddi, J. H. Zhang, W.M. Reiff, A.J. Epstein. *J. Am. Chem. Soc.* **1987**, 109, 769; b) A.J. Banister, N. Bricklebank, I. Lavender, J. Rawson, C. Gregory, B.K. Tanner, W. Clegg. *Ang. Chem. Int. Ed.* **1996**, 35, 2533.

[10] F. Donati,S. Rusponi, S. Stepanow, C. Wackerlin, A. Singha, L. Persichetti, R. Baltic, K. Diller, F. Patthey, E. Fernandes, J. Dreiser, Z. Sljivancanin, K. Kummer, C. Nistor, P. Gambarella, H. Brune. *Science* **2016**, 352, 318

[11] R. Sessoli, H.-L. Tsai, A.R. Schake, S. Wang, J.B. Vincent, K. Folting, D. Gatteschi, G. Christou, D.N. Hendrickson. *J. Am. Chem. Soc.* **1993**, 115, 1804.

[12] G. Christou, D. Gatteschi, D.N. Hendrickson, R. Sessoli. *MRS Bulletin* **2000**, 66.

[13] T. Lis. *Acta Cryst.* **1980**, B36, 2042.

[14] R. Sessoli, D. Gatteschi, A. Caneschi, M.A. Novak. *Nature* **1993**, 365, 141.

[15] D. Gatteschi, L. Sorace. *J. Solid State Chem.* **2001**, 159, 253.

[16] D. P. Di Vincenzo. *Fortschr. Phys.* **2000**, 48, 9.

[17] D. Aravena, E. Ruiz. *Dalton Trans.* **2020**, 49, 9916.

[18] J. R. Friedman, M.P. Sarachik, J. Tejada, J. Maciejewski, R. Ziolo. *J. Appl. Phys.* **1996**, 79, 6031.

[19] J. R. Friedman, M.P. Sarachik, J. Tejada, J. Maciejewski, R. Ziolo. *Phys, Rev. Lett.* **1996**, 76, 3830.

[20] L. Thomas, F. Lionti, R. Ballon, D. Gatteschi, R. Sessoli, B. Barbara. *Nature* **1996**, 383,45.

[21] A. Lunghi, F. Totti, R. Sessoli, S. Sanvito. *Nature Commun.* **2017**, 8, 14620.

[22] R. Orbach. *Proc. R. Soc. Lond.* **1961**, 24, 458.

[23] G. A. Craig, M. Murrie. *Chem. Soc. Rev.* **2015**, 44, 2135.

[24] S. T. Liddle, J. van Slageren. *Chem. Soc. Rev.* **2015**, 44, 6655.

[25] D. Gatteschi, R. Sessoli. *Ang. Chem. Int. Ed.* **2003**, 42.

[26] J. M. Frost, K.L.M. Harriman, M. Murugesu. *Chem. Sci.* **2016**, 7, 2470.

[27] a) D.M. Low, L.F. Jones, A. Bell, E.K. Brechin, T. Mallah, E. Riverie, S.J. Teat, E.J.L. McInnes. *Ang. Chem. Int. Ed.* **2003**, 42, 3781; b) A.M. Ako, I.J. Hewitt, V. Mereacre, R. Clerac, W. Wernsdorfer, C.E. Anson, A.K. Powell. *Ang. Chem. Int. Ed.* **2006**, 45, 4926.

[28] O. Waldmann. *Inorg. Chem.* **2007**, 46, 10035.

[29] W.H. Harman, T.D. Harris, D.E. Freedman, H. Fong, A. Chang, J.D. Rinehart, A. Ozarowski, M.T. Sougrati, F. Grandjean, G.J. Long, J.R. Long, C.J. Chang. *J. Am. Chem. Soc.* **2010**, 132, 18115.

[30] K.H.J. Buschow, F.Rd. Bower. *Physics of magnetism and magnetic materials* **2003**, Kluwer, Academic/Plenum Publishers, New York.

[31] M. Getzlaff. *Fundamentals of magnetism.* **2008**, Springer, Berlin.

[32] R. Marin, G. Brunet, M. Murugesu. *Angew. Chem. Int. Ed.* **2021**, 60, 1728.

[33] D. N. Woodruff, R.E.P. Winpenny, R.A. Layfield. *Chem. Rev.* **2013**, 113 (7), 5110.

[34] J. Tang, P. Zhang. *Lanthanide Single Molecule Magnets* **2014**, Springer-Verlag Berlin Heidelberg.

[35] J.D. Rinehart, J.R. Long. *Chem. Sci.* **2011**, 2, 2078.

[36] N. Ishikawa, M. Sugita, T. Ishikawa, S.-Y. Koshihara, Y. Kazin. *J. Am. Chem. Soc.* **2003**, 125, 8694.

[37] J. R. Lakowicz. *Principles of Fluorescence Spectroscopy.* **2006**, Spring, New York.

[38] W. H. Melhuish. *Pure Appl. Chem.* **1984**, 56, 231.

[39] S. Cotton. *Lanthanide and Actinide Chemistry.* **2006**, Wiley & Sons, Ltd, Sussex.

[40] a) R.E.P Winpenny. *Adv. Inorg. Chem.* **2001**,1; b) R.E.P. Winpenny. *J. Chem. Soc., Dalton Trans.* **2002**, 1.

[41] a) E.K. Brechin. *Chem. Comm.* **2005**, 5141; b) G.S. Papaefstathiou, S.P. Perlepes. *Comments Inorg. Chem.* **2002**, 23, 249.

[42] P.S. Perlepe, L. Cunha-Silva, V. Bekiari, K.J. Gangou, S.J. Teat, A. Escuer, T.C. Stamatatos. *Dalton Trans.* **2016**, 45,10256.

[43] S. Hill, N. Anderson, A. Wilson, S. Takahashi, K. Petnkhov, N.E. Chakov, M. Murugesu, J.M. North, E. del Barco, A.D. Kent, N.S. Dalal, G. Christou. *Polyhedron* **2005**, 24, 2284.

[44] P.N. Baxter, J.-M. Lehn, J. Fisher, M.-T. Youinou. *Ang. Chem. Int. Ed. Engl.* **1994**, 33, 2284.

[45] a) M. Fujita. *Chem. Soc. Rev.* **1998**, 417, 27; b) S.R. Seidl, P.J. Stang. *Acc. Chem. Res.* **2002**, 35, 972; c) S. Leininger, B. Oleuyuk, P.J. Stang. *Chem. Rev.* **2000**, 100, 853.

[46] R.E.P. Winpenny. *Comprehensive Coordination Chemistry II.* **2004**, Vol. 7, Elsevier, Amsterdam.

[47] C.M. da Silva, D.L. da Silva, L.V. Modolo, R.B. Alves, M.A. de Resende, C.V.B. Martins, A. da Fatima. *J. Adv. Res.* **2011**, 2,1.

[48] R.M. Clarke, T. Storr. *Dalton Trans.* **2014**, 43, 9380.

[49] P.G. Cozzi. *Chem. Soc. Rev.* **2004**, 33, 410.

[50] A.H. Blatt, N. Gross. *J. Org. Chem.* **1964**, 29(11), 3306.

[51] J. M. Lehn. *Supramolecular Chemistry, Concepts and Perspectives.* **1995**, VCH, Weinheim.

[52] K.L. Wolf, H. Frahm, H. Harm. *Z. Phys. Chem.* **1937**, Abt. B36, 237.

[53] a) D.J. Cram, J.M. Cram. *Acc. Chem. Res.* **1978**, 11,8; b) D.J. Cram, J.M. Cram. *Acc. Chem. Res.* **1971**, 4, 204.

[54] J.M. Lehn. *Acc. Chem. Res.* **1978**, 11,49.

[55] C.J. Pedersen. *J. Am. Chem. Soc.* **1967**, 89, 7017.

[56] D.K. Cabbines, D.W. Margerum. *J. Am. Chem. Soc.* **1969**, 91, 6540.

[57] A. Werner. *Z. Anorg. Allg. Chem.* **1893**, 3, 267.

[58] A.F. Cotton, G. Wilkinson, C.A. Murillo, M. Bochmann. *Advanced Inorganic Chemistry.* **1999**, John Wiley & Sons, 5th Edition, Inc., UK.

[59] A.C. Benniston, S. Melnic, C. Turta, A.B. Arauzo, J. Bartolome, E. Bartolome, R.W. Harrington, M.R. Probert. *Dalton Trans.* **2014**, 43, 13349.

[60] C. Rajnak, J. Titis, J. Moncol, R. Micova, R. Boca. *Inorg. Chem.* **2019**, 58(2), 991.

[61] T.T. da Cunha, V.M.M. Barbosa, W.X.C. Oliveira, E.F. Pedroso, D.M.A. Garcia, W.C. Nunes, C.L.M. Pereira. *Inorg. Chem.* **2020**, 59(18), 12983.

[62] K. Uchida, G. Cosquer, K. Sugisaki, H. Matsuoka, K. Sato, B.K. Breedlove, M. Yamashita. *Dalton Trans.* **2019**, 48, 12023.

[63] M. Orendac, L. Sedlakova, E. Cizmar, A. Orendacova, A. Feher. *Phys. Rev. B.* **2010**, B81, 214410.

[64] L. Bin, W.B. Wu, W. ZheMing, G. Song. *Sci. China Chem.* **2012**, 55(6), 926.

[65] R. J. Holmberg, L.T. Anh Ho, L. Ungur, I. Korobkov, L.F. Chibotaru, M. Murugesu. *Dalton Trans.* **2015**, 44, 20321.

[66] A. Aranzo, A. Lazarescu, S. Shova, E. Bartolome, R. Cases, J. Luzon, J. Bartolome, C. Turta. *Dalton Trans.* **2014**, 43, 12342.

[67] D.C. Izuogu, T. Yoshida, H. Zhang, G. Cosquer, K. Katoh, S. Ogata, M. Hasegawa, H. Nojiri, M. Damjanovic, W. Wernsdorfer, T. Uruga, T. Ina, B.K. Breedlove, M. Yamashita. *Chem. Eur. J.* **2018**, 24, 9285.

[68] Y. Horri, K. Katoh, Y. Miyazaki, M. Damjanovic, T. Sato, L. Ungur, L.F. Chibotaru, B.K. Breedlove, M. Nakano, W. Wernsdorfer, M. Yamashita. *Chem. Eur. J.* **2020**, 26, 8076.

[69] M.J. Martinez-Perez, S. Cardona-Serra, C. Schlegel, F, Moro, P.J. Alonso, H. Prima-Garcia, J.M. Clemente-Juan, M. Evangelisti, A. Gaita-Ariño, J. Sese, J. van Slageren, E. Coronado, F. Luis. *Phys. Rev. Let.* **2012**, 108, 247213.

[70] J. Mayans, A. Escuer. *Chem. Comm.* **2021**, 57, 721.

[71] M.A. Dunston, D.S. Brown, L. Sorace, R.A. Mole, C. Boskovic. *Chem. Asian J.* **2022**, 17, e2022325.

[72] M. Orts-Arroyo, R. Rabelo, A. Carrasco-Berlanga, N. Moliner, J. Cano, M. Julve, F. Lloret, G. De Munno, R. Ruiz-Garcia, J. Mayans, J. Martinez-Lillo, I. Castro. *Dalton Trans.* **2021**, 50, 3801.

[73] E. Moreno-Pineda, W. Wernsdorfer. *Nat. Rev. Phys.* **2021**, 3, 645.

[74] H.B.G. Casimir, D. Bijl, F.K. du Prè. *Physica (The Hague)*, **1941**, 8, 449.

[75] K.S. Cole, R.H. Cole. *J. Chem. Phys.* **1941**, 9, 341.

[76] C. Dekker, A.F.M. Arts, H.W. de Wijn. *Phys. Rev. B.* **40**, 11243.

[77] M.M. Roessler, E. Salvadori. *Chem. Soc. Rev.* **2018**, 47, 2534.

[78] H.-P. Jia, W. Li, Z.-F. Ju, J. Zhang. *Inorg. Chemm. Comm.* 2007, 10, 397.

[79] N.F. Chilton, R.P. Anderson, L.D. Turner, A. Soncini, K.S. Murray. *J. Comput. Chem.* **2013**, 34, 1164.

[80] a) C. Pichon, P. Mialane, R. Riviere, G, Blain, A. Dolbecq, J. Marrot, F. Secheresse, C. Duboc. *Inorg. Chem.* **2007**, 46, 7710; b) C. Duboc. *Chem. Soc. Rev.* **2016**, 45, 5834; c) C. Duboc, T. Phoeung, S. Zein, J. Pecaut, M.N. Collomb, F. Neese. *Inorg. Chem.* **2007**, 46, 10750.

[81] R.M. Wood, D.M. Stucker, L.M. Jones, W.B. Lynch, S.K. Misra, J.H. Freed. *Inorg. Chem.* **1999**, 38, 5384.

[82] C. Mantel, C. Baffret, I. Romero, A. Deronzier, J. Pecaut, M.-N. Collomb, C. Duboc. *Inorg. Chem.* **2004**, 43, 6455.

[83] L. Gu, R. Wu. *Phys. Rev. B* **2021**, 103, 014401.